INSIGHTS INTO THE INTERACTIVE EFFECTS OF TEMPERATURE AND IRON ON SOUTHERN OCEAN PHYTOPLANKTON

by

Loay J. Jabre

Submitted in partial fulfillment of the requirements
for the degree of Doctor of Philosophy

at

Dalhousie University
Halifax, Nova Scotia
August 2023

To my parents, who sacrificed everything just so I can have this one thing

TABLE OF CONTENTS

LIST OF TABLES

LIST OF FIGURES

ABSTRACT

The photosynthetic conversion of CO_2 into organic matter by phytoplankton sustains marine food webs, influences the long-term burial of atmospheric carbon, and underpins many other critical Earth system processes. Seasonal phytoplankton blooms in the Southern Ocean contribute to a large portion of global phytoplankton metabolism, but are substantially limited by low iron availability and cold temperatures. In this thesis, I investigate how changes in iron and temperature influence Southern Ocean phytoplankton metabolic processes and explore implications for marine primary productivity and biogeochemistry. I first conducted laboratory culture experiments using a model Southern Ocean diatom to examine the effects of iron and temperature on growth rates and physiology. I found an interactive iron-temperature relationship, where warming decreased iron demand in this species, allowing cells to maintain half maximal growth at lower iron concentrations. I then used metatranscriptomic data from field experiments in the Ross Sea to ask questions about the cellular mechanisms that underpin enhanced growth under warming and low iron. I found that some diatom taxa grow better under warmer low-iron conditions due to their ability to use iron-conserving metabolic processes, thereby reducing cellular iron demand. Lastly, I combined metaproteomics with elemental measurements from two different shipboard experiments in the Weddell Sea to examine how iron and temperature-driven changes in phytoplankton growth could influence ecological and biogeochemical processes. Consistent with the previous laboratory and field experiments, here concurrent warming and increased iron availability amplified phytoplankton growth and nutrient consumption. I also identified taxon-specific and community-wide proteomic characteristics that connect phytoplankton growth and physiology with the stoichiometry of macro and micro-nutrient consumption. In sum, the findings presented in this thesis show that iron and temperature interactively affect phytoplankton growth through specific cellular mechanisms that have consequences for primary productivity and elemental stoichiometry in a changing ocean.

LIST OF ABBREVIATIONS USED

Chl-a	Chlorophyll-a
F_v/F_m	Photosynthetic efficiency of PSII
HCl	Hydrochloric acid
HNLC	High (macro)nutrient - low chlorophyll
ICP-MS	Inductively coupled plasma mass spectrometry
IUE	Iron use efficiency
LC-MS-MS	Liquid chromatography - tandem mass spectrometry
LED	Light-emitting diode
LHC	Light harvesting complex
MCL	Markov cluster
metaP	Metaproteomics
metaT	Metatranscriptomics
mRNA	Messenger ribonucleic acid
MS1	Precursor ion scan
MS2	Fragment ion scan
ORF	Open reading frame
PAR	Photosynthetically active radiation
PN	Particulate nitrogen
POC	Particulate organic carbon
PSI	Photosystem I
PSII	Photosystem II
rRNA	ribosomal ribonucleic acid
RuBisCO	Ribulose-1,5-bisphosphate carboxylase/oxygenase
SO	Southern Ocean
TIC	Total ion current
TMC	Trace metal clean
σ_{PSII}	Functional absorption cross-section of PSII

ACKNOWLEDGEMENTS

Over the last few years I have had the freedom to think about the ocean, to be curious, and at times even stress about experiments. To be able to ponder the world and to get stressed by matters that aren't life or death is a true privilege that many do not have. I am beyond lucky to have had this privilege, and to have parents who afforded it to me. A million thank yous will never be enough, but nevertheless, thank you to my mom and dad who uprooted their lives on multiple occasions and did everything they could to send me to school. I am grateful to my brothers 3oday and Kosay who picked up the phone at times when I really needed it, and for keeping me humble, also at times when I really needed it. I am grateful to my little sister Shaza who makes me see the world in a new light every day.

I owe a huge thank you to my advisor, Erin Bertrand, for being the most amazing mentor anyone can ask for. Erin, your guidance, understanding and support throughout the ups and downs of this PhD journey are what kept me going. Thank you for setting the bar high, and for creating countless opportunities for me to explore, collaborate, and learn new things. I am thankful to my committee members, Julie LaRoche, Zoe Finkel and Hugh MacIntyre, who not only provided me with much needed advice and encouragement, but also opened their labs and allowed me to use many of their instruments throughout my work.

I am also so fortunate to have had the most incredible lab mates and friends in the Bertrand Lab. Thank you Elden Rowland for being the mass spec guru I so much needed, and for sharing your lunch with me pretty much every day. Cat Bannon, thank you for all the laughs, your friendship, and for inspiring me to be a better scientist. Megan Roberts, working with you has been a real blessing. You somehow always managed to put a smile on my face - let's make this cruise happen! Scott Pollara, thank you for all the thoughtful discussions, the amazing food, and for showing me that haptophytes can also be cool. Scott McCain, I have learned so much from you, and I am so grateful that we've crossed paths! Graduate school would not have been the same without you. Thank you Sonja, Lena, Isaiah, Patrick, Ryan, Anna, Julia, Gianpaolo, Kiran, Maria, Albury, Tor, Insa and everyone else in the Bertrand Lab for being absolute gems.

Thank you to Joerg Behnke for teaching me the trace metal culturing ways. Thank you

to Yana and Gordon for showing me how to be a graduate student and for your friendship over the years. Thank you to Sophia Stone who advocated fearlessly for graduate students in our department and for making our lives better. Thank you Louis for the awesome early morning chats, for being interested in my research, and for making sure to always tell me that there's light at the end of the tunnel. Thank you to all my fellow graduate students, BOGS, the faculty and staff at Dalhousie University who made my graduate experience a memorable one.

I am also grateful for the many collaborations and interactions I've had outside of Dalhousie - Thank you Rob Middag and group for the collaborations and the MetalGate cruise opportunity. Thank you Andy Allen and group for the collaborations we've had and for hosting me at JCVI. Thank you Mak Saito and group for hosting me at WHOI.

I am especially thankful to my partner Sara Ericsson. Thank you for the patience, your editorial services, and the unlimited support during this journey. I could not have done it without you.

Thank you to the Simons Foundation and the Nova Scotia Graduate Scholarship for funding my graduate studies, and to the Kimberly Foundation's Hugh Morris Experiential Learning Fellowship for granting me the opportunity to chase my curiosities.

CHAPTER 1

INTRODUCTION

Phytoplankton are a diverse group of tiny photosynthetic organisms that inhabit the sunlight layers of the oceans. They contribute to half of global primary productivity (Field et al., 1998) and assimilate dissolved carbon (C), nitrogen (N), phosphorus (P), and other elements into their cells as particulate matter. By doing this, phytoplankton fuel higher trophic levels, influence elemental cycling in the ocean (Arrigo, 2005), and contribute to the export and long-term storage of atmospheric carbon in the deep ocean (Eppley and Peterson, 1979; Volk and Hoffert, 1985). Our descriptions of marine ecosystems, biogeochemical cycles, and many important Earth processes therefore hinge on understanding phytoplankton biology and ecology.

Light, nutrients, and thermal energy (temperature) are among the primary factors that influence phytoplankton growth in the ocean. Light provides energy for photosynthetic carbon fixation, nutrients are used for constructing cellular building blocks (proteins, lipids, nucleic acids etc.), and temperature regulates particle movement and enzymatic reaction rates. While each of these drivers can be studied in much detail through many different lenses, in this thesis I focused specifically on the micronutrient iron and temperature. Both iron availability and temperature are important drivers of phytoplankton growth that are predicted to change in future oceans (Boyd et al., 2015b). Here, I examined how these drivers interactively affect phytoplankton growth, metabolic processes, and elemental stoichiometry.

1.1 Iron, temperature and phytoplankton growth

Iron – Advancements in ultra-clean research methods over the last few decades have shed light on the importance of trace metals for phytoplankton metabolism, and their influence on ocean biogeochemistry (Sunda, 2012). Iron is one of the most abundant trace metals within phytoplankton cells due to its use in several critical metabolic processes such as photosynthesis (e.g. PSI, PSII, electron transport proteins), nitrogen fixation (e.g. nitrogenase), nitrogen assimilation (e.g. nitrate reductase) and oxidative stress management (e.g. iron-superoxide dismutase) (Schoffman et al., 2016; Sunda, 1989; Raven et al., 1999; Twining and Baines, 2013; Raven, 2013b). Despite its high requirement within phytoplankton, iron is largely insoluble in the contemporary ocean and its supply to ocean microbes is often less than demand. This makes iron a limiting nutrient in approximately 30% of the world's oceans, including in regions like the Equatorial Pacific and the Southern Ocean (Martin and Fitzwater, 1988; Martin et al., 1990, 1991; Behrenfeld et al., 1996). These iron-limitted regions are typically characterized by an excess of macronutrients relative to the amount of biomass that could be assimilated using these macronutrients, and are referred to as high nutrient-low chlorophyll (HNLC) regions.

Many phytoplankton taxa can use various mechanisms to mitigate periodic or chronic iron limitation. They can reduce cellular iron demand by optimizing their photosynthetic architecture (Strzepek et al., 2011, 2012, 2019) or by replacing iron-containing proteins with non-iron requiring functional homologs. For example, some phytoplankton groups can substitute iron-containing ferredoxin with flavodoxin (LaRoche et al., 1996; Pankowski and McMinn, 2009b), cytochrome c_6 with plastocyanin (Peers and Price, 2006), or iron-superoxide dismutases (SOD) with manganese-SOD (Peers and Price, 2004). There is also evidence for increased expression of iron uptake proteins under iron limitation (Morrissey et al., 2015; Kazamia et al., 2018; McQuaid et al., 2018; Behnke and LaRoche, 2020), and use of iron luxury uptake and storage when iron is abundant (Marchetti et al., 2009).

Temperature – Thermal energy, or temperature, exerts direct and indirect control over phytoplankton metabolism and growth. Temperature regulates the kinetics of particle movement, which ultimately controls enzymatic reaction rates. This influences metabolic processes like carbon fixation (e.g. RuBisCO turnover rates) (Jordan and Ogren, 1984; Young et al., 2015), protein translation rates (Farewell and Neidhardt, 1998), nutrient

diffusion and uptake (Reay et al., 1999; Gao et al., 2000), and eventually growth rates (Eppley, 1972). Temperature also affects the physical properties of macromolecules, such as phospholipid membrane fluidity and protein structure stability, which leads to changes in their functional qualities and biochemical kinetics.

Phytoplankton acclimate to temperature changes by using a variety of physiological and morphological mechanisms, which ultimately influence their elemental composition, and their success in the environment (Zinser et al., 2007; Rose et al., 2009; Lomas et al., 2021). For example, phytoplankton can reduce ribosomal protein investment to compensate for increased translation efficiency under warming (Toseland et al., 2013), or decrease their cell size possibly to increase buoyancy in warmer less dense water, and to increase nutrient uptake due to enhanced surface area:volume ratio (Atkinson et al., 2003).

Indirectly, changes in ocean temperature can influence other environmental conditions like ice formation/melting and water column stratification (Li et al., 2020). This could lead to cascading effects on nutrient availability, sunlight exposure, grazing pressures, etc. I did not investigate these secondary effects in this thesis.

Iron-temperature interactions – Iron and temperature are typically considered as independent, multiplicative factors in most current marine ecosystem models that are embedded in coupled carbon–climate Earth system models (Laufkötter et al., 2015). That is, a change in temperature does not affect how iron influences phytoplankton growth, and vice versa, in models that seek to understand how phytoplankton impact global climate and other key biogeochemical processes. Yet, temperature has the potential to impact how cells use iron. For instance, temperature impacts the reaction rates of many iron-containing enzymes (see review by Hutchins and Sañudo-Wilhelmy (2022)), which may influence how iron is used within phytoplankton cells. Warming generally increases the turnover rates of iron-containing enzymes (until optimum), which can increase their iron use efficiency (IUE). It can then be inferred that fewer iron-containing enzymes, and ultimately less iron, may be needed to achieve equal or even increased activity under warming. This idea was recently tested in two N-fixing cyanobacteria (*Trichodesmium* and *Crocosphaera*), which allocate a major portion of their intracellular iron pool to temperature-sensitive N-fixing enzymes. These studies showed that warming increased the amount of fixed N per amount of iron. That is, warming increased cellular IUE, and led to decreased iron:N stoichiometry

(Jiang et al., 2018; Yang et al., 2021). By enhancing the IUE of nitrogen fixation, warming may then influence the stoichiometry of nutrient supply in the marine environment, which in turn influences phytoplankton biology and ecological processes.

In contrast to nitrogen fixers, a major portion of the iron pool within non-diazotrophic phytoplankton is found in temperature-insensitive photosynthetic proteins, with some iron used in temperature-sensitive enzymes (Raven et al., 1999). This suggests that there may be a marked difference in how temperature influences iron:nutrient stoichiometry in the different cellular constituents of these phytoplankton. For example, the IUE of nitrate uptake and assimilation may increase under warming due to the temperature sensitivity of the enzymes involved in this process –such as nitrate reductase (Kudo et al., 2000; Gao et al., 2000; Di Martino Rigano et al., 2006). Warming might contribute to a reduction in iron:N by increasing the amount of N taken up by the cell (Reay et al., 1999), or by decreasing the number of iron-containing N assimilation proteins, or both. The IUE of carbon fixation may remain constant under warming, given that the iron-containing proteins involved in photosynthesis (e.g. proteins in light-dependent reactions) are generally temperature insensitive (Raven and Geider, 1988). This could contribute to a stable iron:C as more iron-containing temperature-insensitive proteins may be needed to match the increased turnover rate in light-independent photosynthetic reactions (e.g. RuBisCO turnover rates). With ocean temperatures changing at rates faster than originally predicted by climate models (Cheng et al., 2019), and changes in iron availability predicted for many ocean regions (Boyd et al., 2015b), an important question arises: How do changes in both iron and temperature influence phytoplankton growth and subsequent ecological and biogeochemical processes? In this thesis, I explored this question specifically from the perspective of the Southern Ocean.

1.2 Southern Ocean

The Southern Ocean is the oceanographic region that surrounds the Antarctic continent and is a site where both iron and temperature play critical roles in controlling phytoplankton growth. Here, old deep water from other ocean basins is upwelled, supplying the region with high concentrations of nutrients that drive primary productivity. A portion of this water is then subjected to winter cooling and increased salinity through brine rejection

when ice is formed, which increase density and cause this water to sink into the Antarctic Bottom Waters. This drives the export of carbon and other nutrients that are assimilated by surface microbial communities into the deep ocean. The other portion of this upwelled water flows northward, where it delivers the remaining unconsumed nutrients to lower latitudes. Through this conveyor belt, the Southern Ocean plays a vital role in global ocean circulation and influences oceanic nutrient distribution, carbon export, and Earth's climate (Fig. 1.1) (Murphy et al., 2021; Meijers et al., 2023).

In the Southern Ocean, wind-driven deposition of iron-rich dust is especially low (Jickells et al., 2005; Mahowald et al., 2005), and sediment/shelf release of iron is constrained to coastal regions (Moore and Braucher, 2008). Further, iron supply to the surface after deep winter mixing is counteracted by detrainment and precipitation (Tagliabue et al., 2014), which reduce the iron:macronutrient ratio in upwelled water. This causes the available iron at the surface to be quickly consumed by microbial communities without sufficient replacement from other sources. As a result, phytoplankton growth in much of the Southern Ocean becomes largely iron limited, leaving behind high concentrations of unused macronutrients at the surface. This makes the Southern Ocean the largest HNLC region in the world, spanning approximately 20 million km^2.

The Southern Ocean can be divided into several geographic sectors / ecological provinces. These mainly include the West Antarctic Peninsula, Weddell Sea, South Indian Sector, Ross Sea, and Amundsen Sea. The Ross Sea and the Weddell Sea are the most productive regions in the Southern Ocean, contributing to annual primary production of 503 Tg C $year^{-1}$ and 477 Tg C $year^{-1}$ respectively (Arrigo et al., 2008). This is approximately half of all annual primary production in the region. Within the Weddell Sea, the Weddell Gyre sustains high levels of primary productivity and plays an important role in deep water formation, thereby influencing the flow of heat, nutrients, and carbon throughout the world's oceans (Vernet et al., 2019; Moreau et al., 2023). In the Ross Sea, McMurdo Sound receives relatively high aeolian dust deposition (compared to other Southern Ocean regions) and experiences deep mixing, which provide favorable conditions for intense seasonal phytoplankton blooms (de Jong et al., 2013).

Both iron availability and temperature are predicted to change across the Southern Ocean over the next century, but there still remains large model uncertainties and substantial

variability in how different Southern Ocean regions will experience the effects of a changing climate (Turner et al., 2005; Boyd et al., 2015b; Tagliabue et al., 2016; Moore et al., 2018). For example, warming by 0.5-2 °C is predicted to occur in the Ross Sea surface waters by 2100 (Moore et al., 2018; Boyd et al., 2015b), but little warming is expected to occur at the Weddell Sea surface (Strass et al., 2020). However, rapid warming of Weddell Sea deep water has been observed, which can have large implications for nutrient export and global ocean circulation patterns (Strass et al., 2020). Projections of iron supply remain uncertain (Tagliabue et al., 2016), but a general trend of increasing iron availability throughout the Southern Ocean is predicted (Boyd et al., 2015b; Moore et al., 2018; Henley et al., 2020).

Various phytoplankton groups including many diatoms species and *Phaeocystis* sp. have adapted to grow in the Southern Ocean, and bloom in large amounts, with high spatial and temporal variability, during the spring and summer months when light and temperature are conducive to growth. Phytoplankton blooms in the Southern Ocean alone contribute to a quarter of all oceanic primary production and carbon uptake, and are therefore an integral component of ocean metabolism and biogeochemical cycling (Takahashi et al., 2002). Changing environmental conditions in the Southern Ocean will inevitably influence phytoplankton community composition, primary productivity, and ultimately nutrient and carbon export in the region. It is now more important than ever to examine how Southern Ocean phytoplankton could respond to change, and to understand how this may influence ecological and biogeochemical processes at regional and global scales.

1.3 Phytoplankton research in the omics era

Our understanding of phytoplankton has improved tremendously since early descriptions by Haeckel and Leeuwenhoek (Haeckel, 1904; Dobell, 1932). Over the last two centuries, researchers and explorers have passively and purposefully studied phytoplankton in the field and in laboratories. New technological advances were embraced, and a large toolbox of instrumentation, workflows, and analyses became a central part of biological oceanography. Some of these tools include fluorometry (Holm-Hansen et al., 1965; Krause and Weis, 1991), flow cytometry (Trask et al., 1982), remote sensing (Blondeau-Patissier et al., 2014), advanced imaging (Engel et al., 2015; Kraft et al., 2022), and cell culturing methods (Andersen, 2005), to name a few. As more and more data accumulated, various

models of phytoplankton growth and ecology began to emerge, placing phytoplankton as a central component of global primary productivity and other ecological and biogeochemical processes.

The advent of high-throughput DNA sequencing allowed us to better understand the evolutionary origins of phytoplankton, and to explore taxonomic and functional diversity within the ocean at an unprecedented scale (Louca et al., 2016; Delmont et al., 2022). We now have large collections of assembled and functionally annotated transcriptomes from many marine eukaryotes (Keeling et al., 2014), and fully sequenced genomes of several phytoplankton species (Armbrust et al., 2004; Mock et al., 2017), allowing for molecular and gene manipulation studies. Transcriptome sequencing methods, which generally measure gene expression at the mRNA level, have been pivotal in helping us understand complex cellular pathways, and in examining how different genes/cellular processes are used by phytoplankton (e.g. Allen et al. (2008); Marchetti et al. (2012); Moreno et al. (2018)). However, the relationship between gene expression at the transcript level (e.g. mRNA abundance) and functional protein abundance is complex and often lacks a clear correlation (Liu et al., 2016; Cheng et al., 2018). This makes transcriptomic studies difficult to connect directly with cellular and ecosystem processes.

Mass spectrometry-based proteomics workflows are becoming increasingly common for measuring gene expression at the protein level (Han et al., 2008; Hettich et al., 2013; Nunn et al., 2013; Saito et al., 2019; Wu et al., 2019; McCain et al., 2022). Measurements of cellular proteins reflect phenotype more accurately than mRNA transcripts, and can be useful for relating gene expression to observable metabolic processes like carbon fixation, nutrient uptake, and growth rates (Gao et al., 2000; Young et al., 2015; McCain et al., 2021; Hutchins and Sañudo-Wilhelmy, 2022). Proteins are also major reservoirs of trace metals, nitrogen and phosphorus (Geider and La Roche, 2002; Twining and Baines, 2013), and their quantification can be useful for inferring the stoichiometry and distribution of various elements within phytoplankton cells. As such, proteomics measurements can connect molecular processes at the cellular scale with physiological and ecosystem processes. The integration of omics data with physiological measurements (e.g. growth rates, elemental composition, etc.) could be useful for developing a deeper understanding of phytoplankton biology and ecology in the ocean.

1.4 Thesis overview

The first two data chapters in this thesis (Chapters 2 and 3) have been peer reviewed and published, and the third data chapter (Chapter 4) will be submitted for peer review in the near future. Although each of these chapters can be regarded as a standalone body of work, together, they revolve around the central theme of understanding the interactive effects of iron and temperature on phytoplankton growth and ecology in the Southern Ocean.

In Chapter 2, I examined the effects of iron and temperature on the growth and photophysiology of a prominent polar diatom *Fragilariopsis cylindrus*. I used trace-metal-clean methods to grow this diatom in the laboratory and examined its growth rates and photophysiology under a matrix of iron and temperature conditions. Here, I found an interactive effect of iron and temperature on growth, where warming allowed this species to reduce its iron demand and increase its growth rate under limiting iron concentrations. This chapter was published in Limnology and Oceanography Letters (Jabre and Bertrand, 2020).

In Chapter 3, I used metatranscriptomics data from an iron-temperature incubation experiment conducted in McMurdo Sound, Ross Sea (Fig. 1.1), to examine the cellular processes that underpin phytoplankton growth under changing iron and temperature conditions. Here I found that one phytoplankton group (*Pseudo-nitzschia*) is more adapted to grow under warmer, low-iron conditions by managing cellular iron requirements and efficiently increasing photosynthetic capacity. This chapter was published in PNAS (Jabre et al., 2021).

In Chapter 4, I used the metatranscriptomes from Chapter 3 as a reference for metaproteomic analyses of samples taken from iron-temperature incubations in the Weddell Sea (Fig. 1.1). I combined these metaproteomic measurements with measurements of growth and elemental stoichiometry to ask questions about how changes in phytoplankton growth and metabolism can influence ecological processes. Here, I found links between the abundance of various proteins, phytoplankton growth, and elemental stoichiometry under different environmental conditions.

In Chapter 5, I summarize the findings in this thesis, and provide some thoughts on using omics in the quest for better understanding the oceans around us. All the literature

cited throughout this thesis has been combined into a References section at the end of the document.

I also note that the work conducted in this thesis combines highly interdisciplinary experimental approaches and methodologies. This required extensive collaborations during field work, and for conducting various types of measurements. As such, it is important to acknowledge that many people have contributed to the work presented here. I have included specific co-author contributions at the beginning of each chapter.

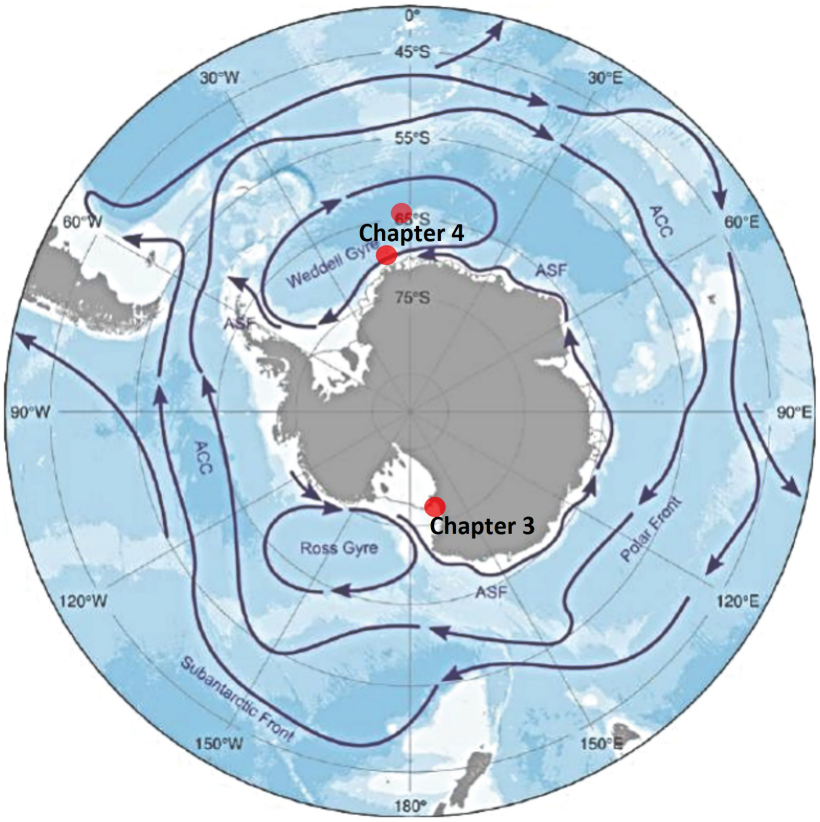

Figure 1.1: Map of major Southern Ocean circulation features adapted from De Broyer et al. (2014), showing locations of the ice edge sampling site discussed in Chapter 3 (McMurdo Sound sea ice edge), and field locations of incubations discussed in Chapter 4 (Weddell Sea).

CHAPTER 2

INTERACTIVE EFFECTS OF IRON AND TEMPERATURE ON THE GROWTH OF *Fragilariopsis cylindrus*

This chapter has been published in Limnology and Oceanography Letters. Volume 5. Issue 5. 2020. doi: https://doi.org/10.1002/lol2.10158

2.1 Author Contribution Statement

The published manuscript was co-authored by: Loay J. Jabre and Erin M. Bertrand.

L.J.J and E.M.B designed the study. L.J.J performed culture work, data collection, and analysis. L.J.J and E.B.M contributed to data interpretation and the writing of the manuscript.

2.2 Abstract

Iron and temperature are important drivers controlling phytoplankton growth in the Southern Ocean (SO). Most studies examining phytoplankton responses to these variables consider them independently, testing responses to changing temperature under constant iron and vice versa. Consequently, we lack a phenomenological and mechanistic understanding of how concurrent changes in these variables influence primary productivity. Here, we used a matrix of three temperatures and eight iron levels to examine changes in growth rate, photophysiology, and size in *Fragilariopsis cylindrus*. Temperature and iron interactively influenced growth; warming decreased iron demand, allowing cells to maintain half-maximal growth rate at lower iron concentrations. We also observed possible mechanisms underpinning this phenomenon: warming increased light-harvesting cross section and reduced cell size, thereby increasing light energy availability and iron uptake efficiency. These results suggest that interactive iron-warming effects could lead to larger increases in SO phytoplankton growth than those currently predicted by marine ecosystem models.

2.3 Scientific Significance Statement

Understanding how phytoplankton growth could react to future climate conditions will improve our knowledge of important marine ecosystem processes such as nutrient cycling and the ocean's ability to absorb atmospheric CO_2. We currently do not understand how the projected simultaneous changes in two major drivers of phytoplankton growth, temperature and iron, will influence phytoplankton productivity in the future. In this study, we show that an ecologically important polar diatom can maximize growth under warming conditions by reducing its iron requirements. We observe morphological and physiological characteristics that may permit this species to take advantage of increased thermal energy under low iron.

2.4 Introduction

Diatom assemblages, which include *Fragilariopsis cylindrus*, contribute to the Southern Ocean's (SO) ability to absorb 40% of all anthropogenic CO_2 (Frölicher et al., 2015). Future climate scenarios forecast changes in the SO environment, including average warming trends and uncertain modifications in iron availability (Turner et al., 2005; Tagliabue et al., 2017; Moore et al., 2018). Iron and temperature are two important drivers of phytoplankton growth; iron-specific growth rates increase with iron concentration until saturation (Sunda and Huntsman, 1995b; Hutchins et al., 2002) and temperature-specific growth rates increase with warming until optimum (Eppley, 1972). Most studies examining phytoplankton responses to these two variables examine them independently, and the few studies seeking to examine responses of temperature and iron simultaneously have featured experimental designs that test temperature responses under two iron conditions, replete and limiting (e.g. Zhu et al., 2016; Boyd, 2019). While these studies have yielded important insights into interactions between temperature and iron, they lack power to examine changes in growth kinetics and trends in the underpinning physiological responses. Consequently, we still lack a framework describing if temperature and iron interactively or independently influence growth. In an independent (additive or multiplicative) relationship, a change in one variable (i.e., temperature) does not influence how another variable (i.e., iron) affects growth. In an interactive relationship, a change in one variable influences another variable's effect on growth. Understanding temperature-iron relationships in phytoplankton is imperative for understanding controls on SO primary productivity on physiological time scales.

Marine ecosystem models (MEMs) that simulate primary productivity typically assume that temperature (T_F^P) and nutrients (N_{lim}) influence growth in an independent, multiplicative manner (Laufkötter et al., 2015) (Eq. 2.1), where μ = specific growth rate (d^{-1}), μ_{max}= maximum growth rate, T_F^P= temperature coefficient = Q_{10} relationship, N_{lim}= nutrient factor = Monod function, and L_{lim}= light factor = function of light saturation (Eq. 2.1).

$$\mu = \mu_{max}.T_F^P.N_{\text{lim}}.L_{\text{lim}} \tag{2.1}$$

These models are based largely on work describing an independent temperature-macronutrient utilization relationship (Goldman and Carpenter, 1974; Ahlgren, 1987; Marañón et al., 2018), even though temperature has been shown to influence macronutrient utilization in several phytoplankton groups (Rhee and Gotham, 1981; Bestion et al., 2018). Moreover, MEMs do not incorporate temperature-micronutrient (e.g., iron) interactions, yet evidence shows that warming can influence iron utilization in *Trichodesmium* (Jiang et al., 2018).

An interactive temperature-iron relationship is possible due to phytoplankton's ability to adjust morphological and physiological characteristics in response to environmental change. For example, cell size ubiquitously decreases at a rate of 2.5% $°C^{-1}$ warming in many protist taxa (Atkinson et al., 2003), whereas cell volume increases with iron availability (Allen et al., 2008). Iron and temperature also influence photosynthetic parameters where photosynthetic efficiency increases with iron availability and light harvesting capacity increases with temperature (Maxwell et al., 1994; Strzepek et al., 2019). Changes in morphology and physiology could influence iron uptake rates, iron use efficiencies, and energy production, all of which can affect growth under different temperature and iron regimes.

The inability of current model formulations to capture potentially important interactive effects may contribute to their uncertainties (Laufkötter et al., 2015) and could hamper our ability to accurately predict future marine primary productivity. Our goal here is to characterize the short-term temperature effects on phytoplankton growth using an experimental design that would facilitate the examination of changes in growth kinetic responses to iron availability under different temperatures. We grew the polar diatom, *F. cylindrus*, under a gradient of ecologically relevant temperatures (1 °C, 3 °C, 6 °C) and eight iron conditions, and measured its growth rate, size, and photosynthetic health (F_v/F_m). Our results reveal a change in the kinetic constants that describe the relationship between iron availability and growth, and demonstrate that *F. cylindrus* can sustain half maximal growth rate at much lower iron concentrations under elevated temperature.

2.5 Methods

2.5.1 Experimental setup

We grew *F. cylindrus* (NCMA-1102, see Supporting Information Methods) in ethylenediaminetetraacetic acid (EDTA)-buffered media under a range of total iron concentrations (Fe_{Total}: 0, 3.75, 10, 15, 20, 35, 50, 100, and 500 nmol L^{-1}) at 1 °C, 3 °C, and 6 °C. *F. cylindrus* is successful in a wide span of SO environments including cold (< 0 °C) high-salinity sea ice to warmer ($\sim$5 °C) lower salinity open waters (Sackett et al., 2013), making it an ecologically and biogeochemically important species. The growth temperatures we used encompass a typical range of water temperatures during the current Antarctic growth season and possible future temperatures under warming (Boyd et al., 2015b). Iron treatments ranged from severely limiting to replete, and were chosen based on previous work by (Pankowski and McMinn, 2009b). Average dissolved free inorganic iron concentrations [Fe'] were calculated by applying temperature-adjusted dissociation factors from Sunda and Huntsman (2003) to Eq. 2.2 from Sunda et al. (2005) (see Supporting Information Methods, Table S2.2, and Fig. S2.5).

$$[Fe'] = \frac{[FeEDTA^*].(K'_{dark} + I_{hv}K_{hv}h/24)}{[EDTA^*]} \tag{2.2}$$

Irradiance was supplied through white LED lights (LEDMO-EZ550) and was kept constant at $\sim$50 μmol photosynthetically active radiation m^{-2} s^{-1}. Cells were first acclimated to all iron concentrations until growth rates were stable at 3 °C (5 transfers 15–20 generations). Cells from each iron concentration - except 0 nmol L^{-1} Fe, which failed to grow - were further acclimated to 1 °C and 3 °C through a full growth cycle and then used to inoculate triplicate 28 mL polycarbonate tubes (Nalgene) for each iron concentration at either 1 °C and 3 °C. Following this, cultures that had been kept at 3 °C were used to inoculate six replicates at 6 °C, N_{total} = 96. Overall, cells were exposed to the experimental iron conditions for at least 20 generations, and to the temperature conditions for 4-8 generations. Cell cultures were mixed daily by inverting the tubes, and their location in the incubator was randomized regularly throughout the experiment.

2.5.2 Media preparation

Synthetic ocean water was prepared in a trace-metal-clean manner following the Aquil* recipe (Price et al., 1988; Sunda et al., 2005). Vitamins and macronutrients were prepared and added to the media following the Aquil* recipe (Sunda et al., 2005). An iron-free, EDTA-buffered trace metal mixture (modified from Sunda and Huntsman (1995a) was added to the media with various concentrations of Fe_3Cl (Fe_{Total}) dissolved in acidified ultrapure water to attain the desired iron treatments (see Supporting Information Methods). Media preparation and cell culture work were conducted in a purpose-built clean room under positive pressure high efficiency particulate (HEPA) filtered air. Labware was rigorously cleaned through a series of soaks in 0.1% Citranox solution and 1.2 mol L^{-1} trace-metal grade HCl, followed by rinsing with ultrapure pH3 Milli-Q water.

2.5.3 Growth rates

In vivo relative chlorophyll a fluorescence units (RFUs) were measured directly from 28 mL culture tubes using a 10-AU Fluorometer (Turner Designs). Cell counts were also measured on the day of inoculation and 2–3 times throughout exponential growth using a BD Accuri™ C6 flow cytometer (BD Biosciences). RFUs correlated linearly with cell counts, R^2 = 0.96 (Fig. S2.6), and were measured more frequently to reduce possible iron contamination from subsampling. Specific growth rates (d^{-1}) were calculated using linear regression of ln RFUs during the exponential growth phase over time using R package "growthrates." Table S2.3 provides R^2 values for the growth rate model fits.

Relative cell size was determined during mid-exponential growth by converting raw forward scatter, a proxy used to estimate cell size (van Tol et al., 2017), from the flow cytometer into estimated cell diameter (ECD). Three different size calibrations beads (diameters: 0.75, 3.0, and 10 μm) were measured on the flow cytometer under the same settings as the cell cultures, and a linear regression of forward scatter vs. diameter was used to calculate ECD. A spherical dimension was assumed for all cells.

2.5.4 Photophysiology

Photochemical efficiency of PSII (F_v/F_m), relative functional absorption cross-section of PSII (σ_{PSII}), and PSII reaction center abundance (RC_{II}) were measured using a FIRe

Fluorometer System (Satlantic). Measurements were conducted during mid-exponential growth after 30 min of dark acclimation at the respective culture temperatures. The generated fluorescence profiles were fitted using Fireworx code (Barnett, 2017), (F_v/F_m) was calculated as the ratio of variable to maximum fluorescence, where $F_v = F_m - F_o$, and σ_{PSII} was estimated using the slope between F_0 and F_m. RC_{II} was calculated as F_v/cells μL^{-1} to account for varying cell densities under the different treatments (Oxborough et al., 2012).

2.5.5 Curve fitting and statistical analysis

All statistical analyses were conducted using R version 3.6.0. and are discussed at significance level of $p < 0.05$. To characterize the temperature and iron effects on growth, we fitted growth rates vs. iron to a Monod equation (Eq. 2.3) using a nonlinear mixed effects model via "SSmicmen" in R package "nlme," where μ_{max} = maximum growth rate and K_{Fe} = iron half-saturation coefficient.

$$\mu = \frac{\mu_{max}.[Fe]}{K_{Fe} + [Fe]} \tag{2.3}$$

We then investigated the temperature effect on model coefficients (μ_{max} and K_{Fe}) by treating temperature as a fixed three level factor (1, 3, 6) and replicates as random effects. Nested models containing temperature effect on both, one, or none of the parameters were compared through likelihood ratio tests and Akaike information criterion (AIC) scores, and parameter estimates were determined using maximum likelihood (see Tables S2.4 and S2.5). To characterize temperature and iron effects on size, data were fitted to a logistic model (Eq. 2.4) using "SSlogis" in R package "nlme" where $Size_{max}$ = maximum size, Fe_{mid} = inflection point, and $Size_{scale}$ = scaling parameter describing how quickly size approaches maximum. Model selection and parameterization were carried out using the method described above (see, Tables S2.6 and S2.7).

$$Size = \frac{Size_{max}}{1 + e^{(Fe_{mid} - Fe)/Size_{scale}}} \tag{2.4}$$

Temperature and iron effects on F_v/F_m were also characterized via "SSmicmen" in "nlme" using the method described above (Tables S2.8 and S2.9). The most appropriate "nlme" models were initially chosen based on lowest AIC scores following methods from Schaum et al. (2017).

2.6 Results

2.6.1 Growth kinetics

Growth rates ranged from 0.33 $\pm$ 0.19 d^{-1} (mean $\pm$ standard error) at iron-replete 6 °C, to no measurable growth in the 0 nmol L^{-1} Fe_{Total} treatment (i.e., dead cultures), which caused the 0 nmol L^{-1} iron treatment to be excluded from further data analysis (Fig. 2.1). The iron half-saturation coefficient, K_{Fe}, decreased significantly (likelihood ratio test comparing models with and without temperature effect on K_{Fe} , p = 0.021) with warming following the Monod function $K_{Fe} = (20.38T)/(-0.69 + T)$, where T = temperature in °C. Maximum growth rate, μ_{max}, also increased linearly with temperature (likelihood ratio test comparing models with and without temperature effect on μ_{max}, $p < 0.001$), where μ_{max} = 0.03*T + 0.16 (Fig. 2.2A, B; Tables S2.4, S2.5). The linear nature of the μ_{max}-temperature relationship indicates that our growth temperatures were below T_{opt} for *F. cylindrus*, which is typically 7–9 °C (Mock and Hoch, 2005).

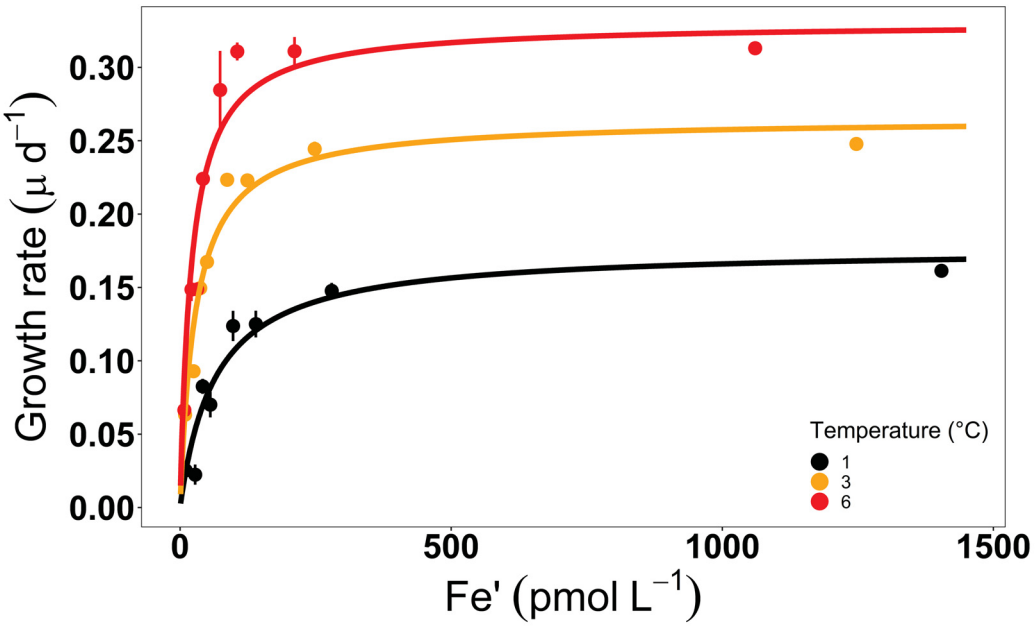

Figure 2.1: Growth rates of *F. cylindrus* under various temperatures and dissolved free iron (Fe') concentrations fitted using a Monod function. Each point at 1 °C and 3 °C represents measurements of three independent biological replicates. Each point at 6 °C represents measurements of six independent biological replicates. $N_{total} = 96$, error bars represent 95% confidence intervals.

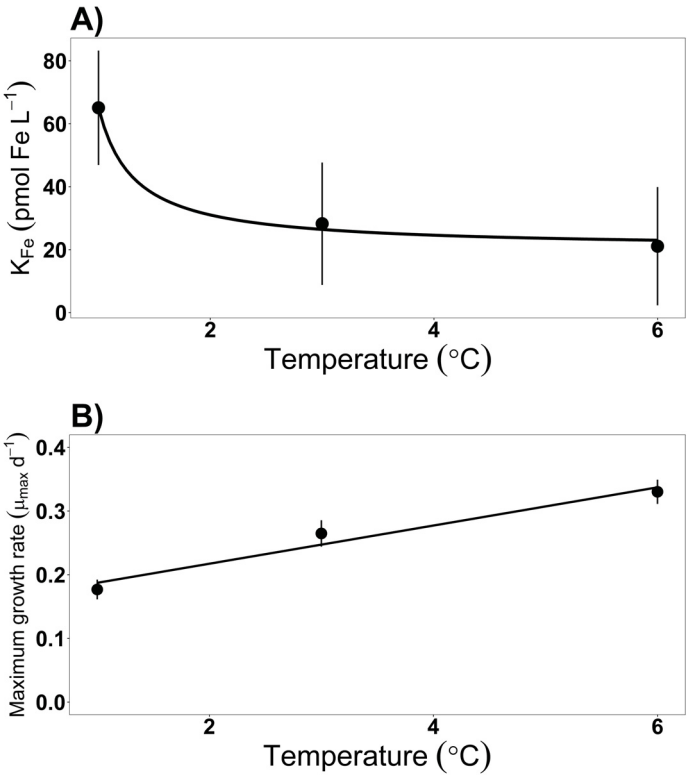

Figure 2.2: (A) Changes in iron half saturation coefficient K_{Fe} with temperature. K_{Fe} is fitted using the Monod function $K_{Fe} = (20.38 * T)/(-0.69 + T)$, where T = temperature in °C, and residual standard error (RSE) = 2.63. (B) Changes in maximum growth rate, μ_{max}, with temperature. μ_{max} is fitted using the linear equation $\mu_{max} = (0.03 * T) + 0.16$. In both (A) and (B), error bars represent 95% confidence intervals, line fits were estimated using R package nlMS (Table S2.10).

2.6.2 Size

ECD ranged from 3.7 $\pm$ 0.04 µm in the most severely iron-limited cultures at 6 °C to 6.29 $\pm$ 0.08 µm in iron-replete cultures at 1 °C (Fig. 2.3A). Warming significantly reduced maximum size (likelihood ratio test comparing models with and without temperature effect on $Size_{max}$, $p < 0.0001$) and increased the rate at which cells became smaller under low iron (likelihood ratio test comparing models with and without temperature effect on $Size_{scale}$, p = 0.002, Tables S2.6, S2.7). Additionally, cells in iron replete treatments (Fe_{Total} $>$ 50 nmol L^{-1}), reduced in size at a rate of 2.09% $\pm$ 0.29% 1°C^{-1} warming, while iron stressed cells (3.75 nmol L^{-1} $<$ Fe_{Total} $<$ 50 nmol L^{-1}), reduced in size at a rate of 4.52% $\pm$ 0.11% 1 °C^{-1} warming (Fig. 2.3B).

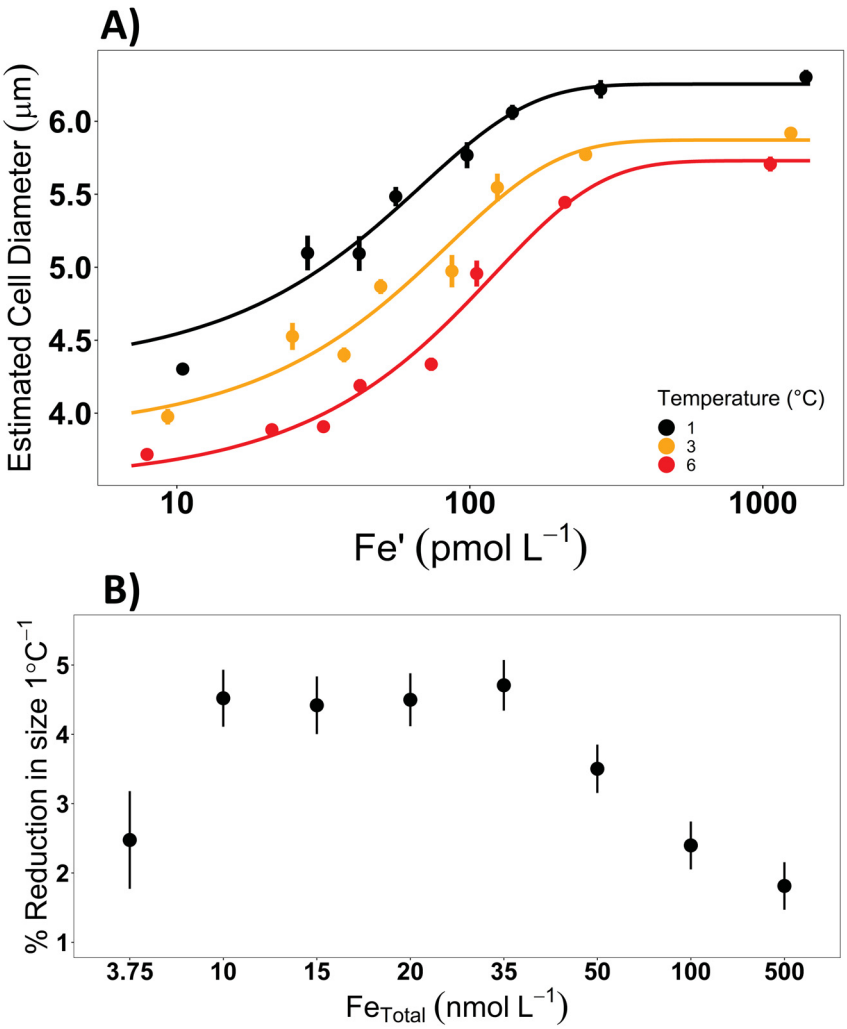

Figure 2.3: (A) Estimated cell diameter vs. dissolved free iron concentrations (Fe') at the three tested temperatures. Each point represents measurements of three independent biological replicates, $N_{total} = 72$. X-axis is log-transformed for clarity. (B) The percent reduction in ECD per 1 °C warming under various total iron (Fe_{Total}) conditions. This was calculated using the slope values of $\Delta ECD/\Delta temperature$ under the various iron conditions. In both (A) and (B), error bars represent 95% confidence intervals.

2.6.3 Photophysiology

F_v/F_m values ranged from 0.23 $\pm$ 0.03 in the most iron limited cultures, indicating severe iron stress, to 0.47 $\pm$ 0.01 in iron replete cultures at 6 °C, a typical value for unstressed *F. cylindrus* (Arrigo et al., 2010) (Fig. 2.4A). Warming increased maximum F_v/F_m values under iron replete conditions but not under iron stress (likelihood ratio test comparing models with and without temperature effect on $F_v/F_{m\text{-max}}$, $p < 0.0001$ and $F_v/F_{m\text{-lowrion}}$,

p = 0.27, respectively, Tables S2.8, S2.9). σ_{PSII} showed a decreasing trend with iron availability at 3 °C and 6 °C and increased with warming only under iron-limited conditions (Fig. S2.7). RC_{II} increased significantly with iron availability, and decreased at 6 °C under iron replete conditions (multiple linear regression using "lm" function, p = 0.001 and p = 0.01, respectively; R^2 = 0.81) (Fig. S2.8).

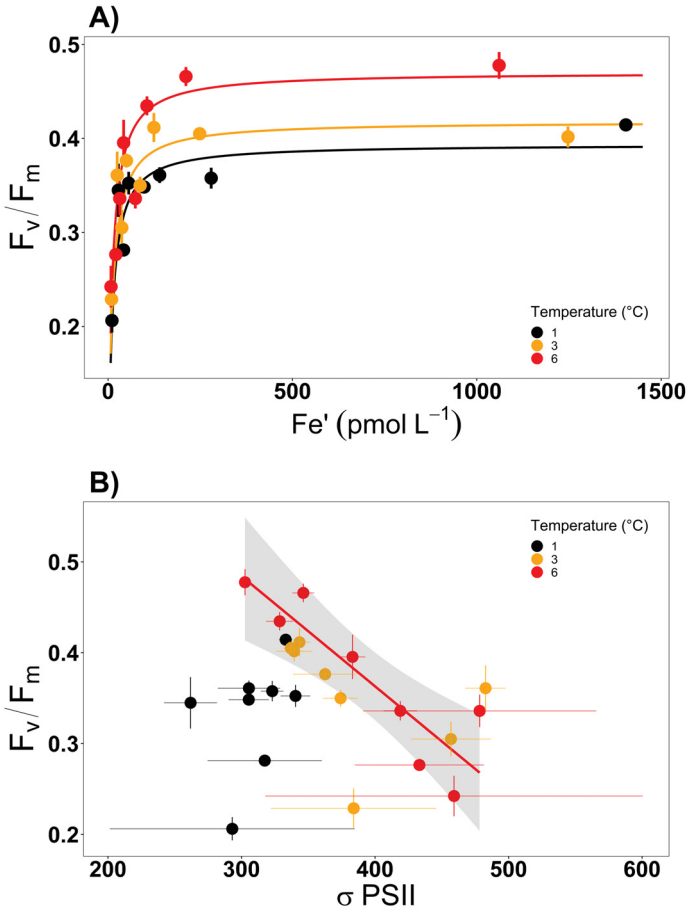

Figure 2.4: (A) Photochemical efficiency of PSII, F_v/F_m, vs. dissolved free iron concentrations (Fe') at the three tested temperatures. (B) F_v/F_m plotted against relative functional absorption cross-section of PSII (σ_{PSII}) at the three tested temperatures. There was no significant relationship between F_v/F_m and σ_{PSII} at 1 °C or 3 °C, but a significant inverse relationship was observed at 6 °C where $F_v/F_m = -0.001\sigma_{PSII} + 0.85$, $R^2 = 0.79$. Gray shading represents 95% confidence range of the linear fit at 6 °C. In both (A) and (B), each point represents measurements of three independent biological replicates, $N_{total} = 72$, and error bars represent 95% confidence intervals.

2.7 Discussion

The increase in growth rate with warming and increasing iron availability we observed has been well documented previously, and is captured in models that use an independent relationship between dependencies on iron and temperature (Laufkötter et al., 2015). However, we show an interactive temperature-iron relationship, where warming decreases the iron half-saturation coefficient (K_{Fe}), indicating that cells need less iron to sustain growth under warming. This interaction causes an increase in the nutrient(iron) term — $N_{lim(Fe)}$ — (Eq. 2.1) even when iron is not increased. To quantify the effect of temperature on $N_{lim(Fe)}$, we can incorporate the temperature-K_{Fe} relationship into the Monod equation (Eq. 2.3) to include a temperature-Fe interactive term (Eq. 2.5). Where μ = specific growth rate (d^{-1}), $\mu_{maxTemp} = 0.03T + 0.16$, [Fe] = iron concentration (pmol L^{-1}) and K_{FeTemp} = temperature adjusted $K_{Fe} = (20.38 * T)/(-0.69 + T)$, T = temperature in °C.

$$N_{\text{lim(Fe)}} \equiv \mu = \frac{\mu_{maxTemp} \cdot [Fe]}{K_{FeTemp} + [Fe]} \tag{2.5}$$

An increase in $N_{lim(Fe)}$ with warming under low iron could translate to higher *F. cylindrus* primary productivity rates than current models predict. This short-term interactive response to temperature and iron could have important ramifications in the SO where iron is limiting throughout most of the year, and would be especially important if the response is maintained in the long term.

Our findings differ from studies where warming did not enhance phytoplankton growth under macronutrient limitation (Marañón et al., 2018). This discrepancy may be due to the different fundamental roles these two types of nutrients play within cells: macronutrients function as molecular "building blocks," while iron functions as a cofactor in many enzymes used as "workers" to assemble these blocks. Under macronutrient limitation, warming increases enzymatic (worker) efficiency, but cell growth would be limited by the lack of building blocks. Conversely, in an iron-limited, macronutrient replete environment, warming increases enzymatic efficiency and thus decreases the number of iron-containing workers required to maintain growth. This would only be beneficial in regions like the SO, where there is an abundance of macronutrient building blocks.

While the efficiency of iron-containing enzymes has been shown to increase with warming (Di Martino Rigano et al., 2006; Jiang et al., 2018), iron quota measurements and proteomic surveys under various temperature and iron conditions are needed to further examine this hypothesis.

The interactive temperature-iron relationship we show is also influenced by the degree of iron limitation. Growth rate increase due to warming was an order of magnitude lower under severely iron-limiting treatments (Fe_{Total} <10 nmol L^{-1}) compared to moderately stressed and replete iron conditions (Table 2.1). The negligible temperature effect on growth at extremely low iron may be due to severe stress (F_v/F_m = 0.23) and failure to meet the minimum iron quota required to sustain basic metabolic function. Consequently, studies using only iron replete and deplete conditions could fail to observe much of the important interactive effects of temperature and iron on growth.

Table 2.1: Increase in growth rate ($\Delta\mu$, d^{-1}) per 1 °C warming at very low, intermediate, and replete iron conditions.

Fe_{Total}	**$\Delta\mu$ (d^{-1}) per 1 °C**
Very low (<10 nmol L^{-1})	0.004 ± 0.003
Intermediate (35 nmol L^{-1})	0.029 ± 0.006
Replete (>50 nmol L^{-1})	0.028 ± 0.003

We observed several morphological and physiological characteristics that may allow *F. cylindrus* to reduce K_{Fe} and take advantage of warming. Photosynthetic efficiency (F_v/F_m) did not improve with warming under low iron, which suggests that other photosynthetic mechanisms may be responsible. The increase in σ_{PSII} under warmer, low-iron conditions (Fig. S2.7) improves light harvesting and increases the energy available for photosynthesis. This decreases the demand for iron-containing photosynthetic proteins, as reflected in the reduced abundance of PSII reaction centers (RC_{II}) at 6 °C (Supporting Information Fig. S2.8). However, larger σ_{PSII} reduce the efficiency of light energy transfer to photosynthetic reaction centers, creating an inverse relationship between σ_{PSII} and F_v/F_m in SO algae grown at ∼4 °C (Strzepek et al., 2019). This inverse relationship was only apparent under elevated temperature in our experiment (Fig. 2.4B, Table S2.11),

which further suggests that warming may assist iron-limited photosynthesis by increasing light harvesting.

The decrease in iron requirement with temperature was accompanied by a decrease in cell size. Smaller cells grow more favorably under iron limitation due to increased surface area to volume ratios and reduced nutrient and energy quotas per cell, allowing faster division/growth rates (Hudson and Morel, 1990; Finkel et al., 2010). A decrease in size under increased temperature could then be a beneficial strategy to maximize growth while reducing iron demand. This would be especially advantageous in the SO, where higher water temperatures occur later in the summer and coincide with major iron drawdown by algal blooms (Wu et al., 2019). The decrease in size with temperature observed here (2.1% decrease $^{\circ}C^{-1}$ warming) follows an established temperature-size rule in nutrient replete environments (Atkinson et al., 2003). Our results expand on this rule by showing that the decrease in size is magnified two-fold under iron-limited growth conditions (4.5% decrease $^{\circ}C^{-1}$ warming). This phenomenon further reduces iron demand per cell and enables increased growth with warming. However, since smaller cells also contain less carbon, it is possible that iron demand per carbon (Fe : C ratio) did not change. Interrogation of Fe:C ratios is required to understand the implications of these trends for iron use efficiency.

Our data show that temperature and iron interactively, not independently, influence the growth rates of *F. cylindrus*; the initial slope of the exponential phase of growth rate curves (Fig. 2.1) becomes steeper at higher temperatures, indicating a reduction in K_{Fe}. This allows *F. cylindrus* to increase its iron-limited growth at a rate faster than is predicted by current models under warming. Regardless of mechanisms underlying this temperature-iron interaction, the morphological and physiological flexibility we observed here will influence the abundance and ecological role of *F. cylindrus* in SO microbial communities. This temperature-iron interaction may also be amplified in diatoms with lower iron demand than *F. cylindrus* (e.g., *Pseudo-nitzschia subcurvata*, Zhu et al. (2016)). The resulting increase in primary productivity under warming would contribute to further drawdown of macronutrients and increase the SO trapping effect, where nutrients are exported and prevented from being redistributed to fuel productivity at lower latitudes (Moore et al., 2018). With increasing sea surface temperature trends, an interactive temperature-iron relationship could have important ramifications for SO primary productivity and global biogeochemistry.

2.8 Data Availability Statement

Data and metadata are available at https://doi.org/10.5061/dryad.np5hqbzq3.

2.9 Acknowledgments

We thank Julie LaRoche for access to the flow cytometer and Hugh MacIntyre for access to fluorometers throughout the project. We also thank Zoe Finkel, Andrew Irwin, Zhengke Li, H.M., J.L.R, David Hutchins, and Scott McCain for meaningful discussion and feedback. This work was funded by the Nova Scotia Graduate Scholarship to L.J., NSERC Discovery Grant RGPIN-2015-05009 to E.B., an NSERC Canada Research Chair to E.B., and Simons Foundation Grant 504183 to E.B.

2.10 Conflict of Interest

None declared.

2.11 Supporting Information

2.11.1 Supporting Methods

***Fragilariopsis cylindrus* additional information**

We used an axenic monoculture of *F. cylindrus* (NCMA-1102) isolated from the Weddell Sea, Southern Ocean, in 1979). This strain is available at Bigelow's National Center for Marine Algae and Microbiota (https://ncma.bigelow.org/ccmp1102) and is widely used as a model organism for cold water diatoms and in trace metal studies. We have been maintaining this strain in our laboratory at 3 °C for several years (stock culture), and used one inoculum from the stock culture to inoculate all our initial replicates.

Calculation of average dissolved inorganic iron concentrations [Fe']

Iron's speciation in EDTA-buffered media affects its bioavailability and is influenced by pH, light and temperature (Sunda and Huntsman, 2003). It is therefore important to calculate the concentration of free, dissolved (the most bioavailable form of) iron in experiments with varying environmental conditions - like temperature in our experiment. We calculated [Fe'] at 1 °C, 3 °C and 6 °C (Table S2.2) by applying temperature-adjusted dissociation factors from (Sunda and Huntsman, 2003) to the following equation from Sunda et al. (2005).

$$[Fe'] = \frac{[FeEDTA^*].(K'_{dark} + I_{hv}K_{hv}h/24)}{[EDTA^*])} \tag{2.6}$$

Where:

$[FeEDTA^*]$: Total iron concentration added to the media = 3.75 x 10^{-9}, 10 x 10^{-9}, 15 x 10^{-9}, 20 x 10^{-9}, 35 x 10^{-9}, 50 x 10^{-9}, 100 x 10^{-9} and 500 x 10^{-9} mol L^{-1}.

$[K'_{dark}]$: Dissociation constant in the dark, not influenced by temperature = 9.55 x 10^{-8} (Figure S2.5).

$[I_{hv}]$: Light intensity relative to which K_{hv} was measured = 50 µmol PAR m^{-2} s^{-1} / 500 µmol PAR m^{-2} s^{-1} = 0.1

$[K_{hv}]$: Dissociation constant in the light, decreases with temperature (Figure S2.5). Using a linear relationship between K_{hv} and temperature, we estimate K_{hv} values of 1.99 x 10^{-6}, 1.65 x 10^{-6} and 1.25 x 10^{-6} at 1 °C, 3 °C, 6 °C respectively (Figure S2.5).

h: Number of light hours = 22 hours.

$[EDTA^*]$: Free EDTA concentration = Total EDTA concentration minus total concentration of trace metals (Fe, Mn, Cu, Ni, Se, Zn, Co, Mo) = 9.955 x10^{-5}, 9.954 x10^{-5}, 9.954 x10^{-5}, 9.953 x10^{-3}, 9.952 x10^{-5}, 9.950 x10^{-5}, 9.945 x10^{-5}, 9.905 x10^{-5} mol L^{-1} at iron concentrations 3.75 x 10^{-9} $\rightarrow$ 500 x 10^{-9} mol L^{-1} respectively.

Table 2.2: Average dissolved inorganic iron concentrations [Fe'] at each temperature and total iron treatment.

	1 °C	**3 °C**	**6 °C**
Fe_{Total}(mol L^{-1})	**Fe' (pmol L^{-1})**		
3.75 x 10^{-9}	10.48	9.31	7.91
1.0 x 10^{-8}	27.95	24.82	21.11
1.5 x 10^{-8}	41.92	37.24	31.66
2.0 x 10^{-8}	55.89	49.65	42.22
3.5 x 10^{-8}	97.84	86.91	73.89
5.0 x 10^{-8}	139.79	124.17	105.58
1.0 x 10^{-7}	279.72	248.47	211.26
5.0 x 10^{-7}	1404.25	1247.34	1060.59

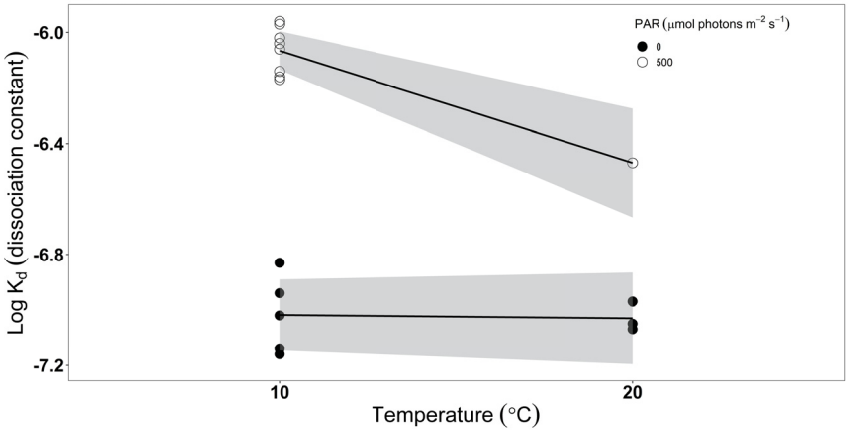

Figure 2.5: Dissociation constant (K_d) for dark and light conditions ($N_{total} = 17$) plotted against temperature. K_d is not influenced by temperature in the dark (PAR = 0 μmol m^{-2} s^{-1}) but decreases with temperature in the light (PAR = 500 μmol m^{-2} s^{-1}). Data were obtained from Sunda and Huntsman (2003)

Media preparation

Synthetic ocean water was prepared following the Aquil* recipe and was treated with Chelex® to remove metal contaminants (Price et al., 1988; Sunda et al., 2005). Vitamins and nutrient stocks were added to the media following the Aquil* recipe (Sunda et al., 2005). An iron-free, EDTA-buffered trace metal mixture (modified from Sunda and Huntsman (1995a)) was added to the media with various concentrations of Fe_3Cl dissolved in acidified ultrapure water to attain the desired iron treatments.

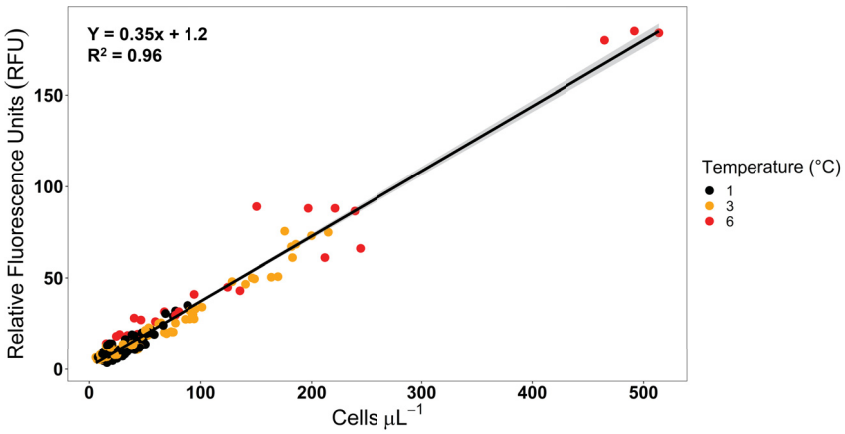

Figure 2.6: Relative fluorescence units (arbitrary units) vs cell density (cells μL^{-1}). $RFU = 0.35 * cells\,\mu L^{-1} + 1.2$, R^2 = 0.96. Points represent cultures from all temperature and iron treatments during lag and exponential growth phases, $N_{total} = 235$. The strong linear correlation between RFUs, a measure of chlorophyll-a fluorescence, and cell density shows that RFU measurements can be used as a proxy for cell density in our experiment. RFUs were measured non-invasively on a 10-AU Fluorometer (Turner Designs) using the entire 28 mL culture tube. Cells μL^{-1} were measured by sampling the cultures under sterile, trace-metal-clean conditions, and then counting the number of cells on a BD Accuri C6 flow cytometer coupled with BD CSampler^{TM} (BD Biosciences).

Table 2.3: R^2 values from the linear regression used to calculate specific growth rates (d^{-1}) for all replicates at all iron and temperature treatments. Growth rates were calculated via linear regression of ln RFUs during the exponential growth phase over time using R package "growthrates v 0.7.2".

Total Iron	**Replicate**	**1 °C** R^2	**3 °C** R^2	**6 °C** R^2
3.75	A	0.34	0.88	0.98
10	A	0.20	0.63	1.00
15	A	0.87	0.93	1.00
20	A	0.76	0.86	0.99
35	A	0.94	0.95	0.98
50	A	0.97	0.95	0.97
100	A	0.95	0.99	0.97
500	A	0.94	1.00	0.98
3.75	B	0.44	0.77	1.00
10	B	0.30	0.73	1.00
15	B	0.76	0.91	1.00
20	B	0.84	0.88	0.98
35	B	0.96	0.98	0.98
50	B	0.96	0.98	0.96
100	B	0.95	0.99	0.95
500	B	0.95	1.00	0.98
3.75	C	0.36	0.72	0.97
10	C	0.12	0.74	0.98
15	C	0.53	0.95	0.99
20	C	0.44	0.92	0.98
35	C	0.75	0.98	0.98
50	C	0.88	0.97	0.98
100	C	0.91	1.00	0.98
500	C	0.96	1.00	0.98
3.75	D			0.84
10	D			0.97
15	D			0.97

20	D	0.98
35	D	0.99
50	D	0.98
100	D	0.99
500	D	1.00
3.75	E	0.86
10	E	0.97
15	E	0.98
20	E	0.97
35	E	0.98
50	E	0.99
100	E	0.99
500	E	0.99
3.75	F	0.76
10	F	0.99
20	F	0.95
35	F	0.95
50	F	1.00
100	F	1.00
500	F	0.99

Curve fitting methods and statistical analysis

Growth rate:

Curve fitting began by first using the most complex Monod model (see methods) where growth rate was treated as a function of iron concentration, temperature (three level fixed effect) influenced all model parameters (μ_{max} and K_{Fe}) and replicates treated as random effects on all model parameters. Random effects with very low variance were removed from the model. Nested models including a temperature effect only on μ_{max} and only on K_{Fe} were then compared to the most complex model using likelihood ratio tests via the 'anova' function in R package 'nlme'. Here, the full model was significantly different from the other two models ($p < 0.05$) and had the highest log-likelihood score and lowest AIC score (Table S2.4). This indicates that temperature significantly influenced both μmax and K_{Fe}. Parameter estimates for the fixed effects were then determined using maximum likelihood (Table S2.5), and were used to fit the curves in Figure 2.1.

Table 2.4: Output from the likelihood ratio tests used to determine the temperature-iron effect on growth rate model parameters. Full = most complex model with temperature influencing all the parameters, parameter dropped = removing the temperature effect on that parameter. P-value < 0.05 indicates a significant temperature effect on the dropped parameter.

	Model	df	AIC	BIC	logLik	Test	L.ratio	p-value	Parameter Dropped
Growth_1_full	1	8	-406.68	-385.92	211.34				
Growth_2	2	6	-402.94	-387.37	207.47	1 vs 2	7.74	0.021	K_{Fe}
Growth_3	3	6	-390.03	-374.46	201.02	1 vs 3	20.65	< 0.0001	μ_{max}

Table 2.5: Parameter estimates for fixed effects from the non-linear model for growth rate determined using maximum likelihood.

Temperature effect on:	Estimate $\pm$ 1SE	p-value
K_{Fe}	1 °C: 65.068 $\pm$ 18.174 3 °C: 28.243 $\pm$ 19.432 6 °C: 21.108 $\pm$ 18.781	0.021
μ_{max}	1 °C: 0.177 $\pm$ 0.016 3 °C: 0.265 $\pm$ 0.021 6 °C: 0.330 $\pm$ 0.190	< 0.0001

Cell size:

Curve fitting began by first using the most complex logistic model (see methods) where size was treated as a function of iron concentration, temperature influenced all model parameters ($Size_{max}$ = maximum size, Fe_{mid} = Inflection point, and $Size_{scale}$ = scaling parameter), and replicates treated as random effects on all model parameters. Random effects with very low variance were removed from the model. Nested models where the temperature effect was removed for each of the model parameters were then compared to the most complex model using a likelihood ratio test via the 'anova' function in R package 'nlme'. Here, removing the temperature effect on the Fe_{mid} parameter had no significant effect ($p = 0.135$), while models with no temperature effect on $Size_{max}$ and Scal were significantly different from the most complex model ($p < 0.05$) and had higher AIC and lower log likelihood scores (Table S2.6). This indicates that temperature only significantly influences the maximum size ($Size_{max}$) and how quickly maximum size is reached when iron is added ($Size_{scale}$). Parameter estimates for the fixed effects were then determined using maximum likelihood (Table S2.7), and were used to fit the lines in Figure 2.2A.

Table 2.6: Output from the likelihood ratio tests used to determine the temperature-iron effect on size model parameters. Full most complex model with temperature influencing all the parameters, parameter dropped removing the temperature effect on that parameter. P-value < 0.05 indicates a significant temperature effect of the dropped parameter.

	Model	df	AIC	BIC	logLik	Test	L.Ratio	p-value	Parameter Dropped
Size_1_full	1	11	-49.61	-24.88	35.81				
Size_2	2	9	-28.94	-8.70	23.47	1vs2	24.68	< 0.0001	$Size_{max}$
Size_3	3	9	-58.22	-37.99	38.11	1vs3	4.61	0.135	Fe_{mid}
Size_4	4	7	-41.25	-21.02	29.63	1vs4	12.36	0.002	$Size_{scale}$

Table 2.7: Parameter estimates for fixed effects from the non-linear model for size determined using maximum likelihood.

Temperature effect on:	**Estimate $\pm$ 1SE**	**p-value**
$\mathbf{Size_{max}}$	1 °C: 6.252 $\pm$ 0.084 3°C: 5.864 $\pm$ 0.130 6 °C: 5.730 $\pm$ 0.143	< 0.0001
$\mathbf{Fe_{mid}}$	-40.078 $\pm$ 5.677	0.135
$\mathbf{S_{cal}}$	1 °C: 52.482 $\pm$ 5.733 3 °C: 62.449 $\pm$ 6.319 6 °C: 86.327 $\pm$ 9.290	0.002

F_v/F_m:

Curve fitting here began by first using the most complex Monod model where F_v/F_m rate was treated as a function of iron concentration, temperature influenced all model parameters (F_v/F_m-max and K_{Fe} = F_v/F_m-lowiron), and replicates treated as random effects on all model parameters. Random effects with very low variance were removed from the model. Nested models including a temperature effect only on F_v/F_m-max and only on K_{Fe} were then compared to the most complex model using a likelihood ratio test via the 'anova' function in R package 'nlme'. Here, the full model was not significantly different from the model with no temperature effect on F_v/F_m-lowiron (p 0.269) and was only significantly different from the model with no temperature effect on F_v/F_m-max (P 0.0001) (Table S2.8). This indicates that temperature does not influence F_v/F_m measurements at lower iron concentrations (initial slope of the Monod function), and only influences F_v/F_m when iron is replete (F_v/F_m-max). Parameter estimates for the fixed effects were then determined using maximum likelihood (Table S2.9), and were used to fit the lines in Figure 2.4A.

Table 2.8: Output from the likelihood ratio tests used to determine the temperature effect F_v/F_m model parameters. Full = most complex model with temperature influencing all the parameters, parameter dropped = removing the temperature effect on that parameter. P-value < 0.05 indicates a significant temperature effect of the dropped parameter.

	Model	**df**	**AIC**	**BIC**	**logLik**	**Test**	**L.ratio**	**p-value**	**Parameter Dropped**
Fv/Fm_1_full	1	8	-275.03	-256.82	145.51				
Fv/Fm_2	2	6	-276.41	-262.75	144.21	1 vs 2	2.62	0.269	$F_v/F_{m-lowiron}$
Fv/Fm_3	3	6	-246.99	-233.33	129.49	1 vs 3	32.04	< 0.0001	F_v/F_{m-max}

Table 2.9: Parameter estimates for fixed effects from the non-linear model for F_v/F_m determined using maximum likelihood.

Temperature effect on:	**Estimate ± 1SE**	**P-value**
$F_v/F_{m-lowiron}$	10.107 ± 1.729	0.269
F_v/F_{m-max}	1 °C: 0.394 ± 0.009 3 °C: 0.418 ± 0.013 6 °C: 0.470 ± 0.013	< 0.0001

Table 2.10: Model fit comparisons examining the relationship between temperature and iron growth kinetics with seven different models using R package nlMS v 1.1. The best fitting model was chosen based on lowest AIC score. N.A = no convergence. Norm = normally distributed, no norm = non-normal distributed.

Model		**Figure 2A** $\mathbf{K_{Fe}}$ **vs Temperature**	**Figure 2B** μ_{max} **vs Temperature**
	AIC	28.06	-19.26
linear	**RSE**	16.57	0.01
	residuals	norm	norm
Quadratic	**AIC**	N.A	N.A
	RSE	N.A	N.A
	residuals	N.A	N.A
Cubic	**AIC**	0.00	0.00
	RSE	0.00	0.00
	residuals	no norm	no norm
Logistic	**AIC**	N.A	N.A
	RSE	N.A	N.A
	residuals	N.A	N.A
Exponential	**AIC**	26.31	-12.97
	RSE	12.37	0.02
	residuals	norm	norm
Power	**AIC**	N.A	N.A
	RSE	N.A	N.A
	residuals	N.A	N.A
Monod	**AIC**	17.019	-7.55
	RSE	2.63	0.04
	residuals	norm	norm
Best fit		**Monod**	**Linear (R^2 = 0.95)**

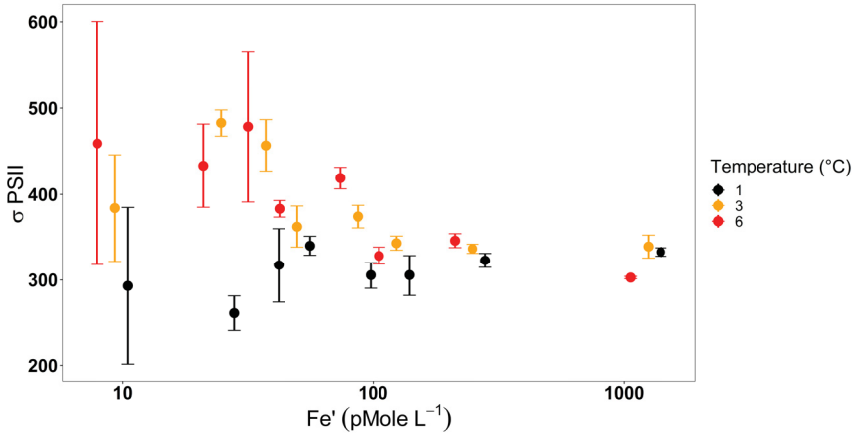

Figure 2.7: Relative functional absorption cross-section of PSII (σ_{PSII}) vs dissolved free iron concentrations Fe' at the three tested temperatures. σ_{PSII} decreases with iron availability only at 3 °C and 6 °C. Warming increases σ_{PSII} only under iron limited conditions ($<$ 50 pM). Each point represents measurements of three independent biological replicates, $N_{total} = 72$, and error bars represent 95% confidence intervals.

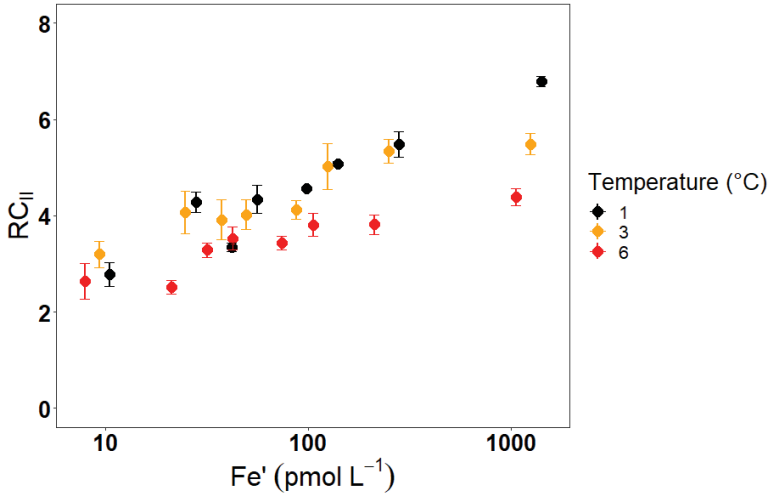

Figure 2.8: PSII reaction center abundance, RC_{II} (unitless), vs dissolved free iron concentrations (Fe') at the three tested temperatures. RC_{II} shows increasing trends with iron availability and a decrease at 6 °C. Each point represents measurements of three independent biological replicates, $N_{total} = 72$, and error bars represent 95% confidence intervals.

Table 2.11: Model statistics and parameter estimates from the linear model fit for the effects of temperature and σ_{PSII} on F_v/F_m.

	1 °C	**3 °C**	**6 °C**
Intercept $\pm$ **SE**	0.062 $\pm$ 0.3	0.54 $\pm$ 0.16	0.848 $\pm$ 0.1
σ_{PSII} $\pm$ **SE**	0.0009 $\pm$ 0.001	-0.0005 $\pm$ 0.0004	-0.001 $\pm$ 0.0003
RSE	0.06	0.061	0.043
R^2	-0.03	0.043	0.79
F-statistic	0.82	1.32	22.94
p-value	0.39	0.29	0.003

CHAPTER 3

MOLECULAR UNDERPINNINGS AND BIOGEOCHEMICAL CONSEQUENCES OF ENHANCED DIATOM GROWTH IN A WARMING SOUTHERN OCEAN

This chapter has been published in Proceedings of the National Academy of Sciences (PNAS).
Volume 118. Issue 30. 2021. doi.org/10.1073/pnas.2107238118

3.1 Author Contribution Statement

The published manuscript was co-authored by:
Loay J. Jabre, Andrew E. Allen, J. Scott P. McCain, John P. McCrow, Nancy Tenenbaum, Jenna L. Spackeen, Rachel E. Sipler, Beverley R. Green, Deborah A. Bronk, David A. Hutchins, and Erin M. Bertrand

L.J.J led the data analysis and manuscript writing, with input from all co-authors. A.E.A., D.A.H., and E.M.B. designed the research experiments. A.E.A., N.T., J.L.S., R.E.S., D.A.B., D.A.H., and E.M.B. performed field experiments and analytical measurements. A.E.A. contributed reagents and analytical tools.

3.2 Significance

Phytoplankton contribute to the Southern Ocean's (SO) ability to absorb atmospheric CO_2 and shape the stoichiometry of northward macronutrient delivery. Climate change is altering the SO environment, yet we know little about how resident phytoplankton will react to these changes. Here, we studied a natural SO community and compared responses of two prevalent, bloom-forming diatom groups to changes in temperature and iron that are projected to occur by 2100 to 2300. We found that one group, *Pseudo-nitzschia*, grows better under warmer low-iron conditions by managing cellular iron demand and efficiently increasing photosynthetic capacity. This ability to grow and draw down nutrients in the face of warming, regardless of iron availability, has major implications for ocean ecosystems and global nutrient cycles.

3.3 Abstract

The Southern Ocean (SO) harbors some of the most intense phytoplankton blooms on Earth. Changes in temperature and iron availability are expected to alter the intensity of SO phytoplankton blooms, but little is known about how these changes will influence community composition and downstream biogeochemical processes. We performed light-saturated experimental manipulations on surface ocean microbial communities from McMurdo Sound in the Ross Sea to examine the effects of increased iron availability (+2 nM) and warming (+3 and +6 °C) on nutrient uptake, as well as the growth and transcriptional responses of two dominant diatoms, *Fragilariopsis* and *Pseudo-nitzschia*. We found that community nutrient uptake and primary productivity were elevated under both warming conditions without iron addition (relative to ambient -0.5 °C). This effect was greater than additive under concurrent iron addition and warming. *Pseudo-nitzschia* became more abundant under warming without added iron (especially at 6 °C), while *Fragilariopsis* only became more abundant under warming in the iron-added treatments. We attribute the apparent advantage *Pseudo-nitzschia* shows under warming to up-regulation of iron-conserving photosynthetic processes, utilization of iron-economic nitrogen assimilation mechanisms, and increased iron uptake and storage. These data identify important molecular and physiological differences between dominant diatom groups and add to the growing body of evidence for *Pseudo-nitzschia*'s increasingly important role in warming SO ecosystems. This study also suggests that temperature-driven shifts in SO phytoplankton assemblages may increase utilization of the vast pool of excess nutrients in iron-limited SO surface waters and thereby influence global nutrient distribution and carbon cycling.

3.4 Introduction

The Southern Ocean (SO) occupies less than 10% of Earth's ocean surface area but plays a major role in driving global climate and biogeochemical cycles. It connects the Pacific, Atlantic, and Indian ocean basins, supplies nutrients to lower latitudes, and absorbs a considerable portion of global heat and CO_2 (Frölicher et al., 2015; Moore et al., 2018). SO ecological processes are driven by seasonally productive phytoplankton assemblages that require sufficient light, macronutrients (e.g., nitrogen, phosphorus), micronutrients (e.g., iron, vitamin B_{12}), and suitable temperatures to grow. These phytoplankton sequester atmospheric CO_2 through the biological pump, sustain food webs, and influence the stoichiometry of nutrient supply to lower latitudes. Despite large regional variations, climate change models project overall warming in the SO, with current average sea surface temperatures (0 to 4 °C) predicted to increase by 1 to 2 °C in 2100 and 6 °C by 2300 (Moore et al., 2018; Turner et al., 2005; Boyd et al., 2015b; IPCC, 2019). Additionally, small increases in iron supply (e.g., increased iron flux, by 0.01 nM and 0.02 nM day^{-1} by 2100 and 2300, respectively) are projected for the SO (Moore et al., 2018; Turner et al., 2005; Boyd et al., 2015b) (Table S3.1), but large uncertainties remain in model projections of SO iron supply, which are complicated by the diversity of supply mechanisms and other physical/chemical factors (Tagliabue et al., 2016; Hutchins and Boyd, 2016). Temperature and iron can be major drivers of SO phytoplankton growth (Eppley, 1972; Martin et al., 1990), yet we still have a limited understanding of how changes in these factors will influence the cellular mechanisms that govern phytoplankton dynamics and biogeochemistry in the SO.

Low iron availability limits phytoplankton growth and is the primary cause of the high-(macro)nutrient low-chlorophyll (HNLC) conditions in the SO (Martin et al., 1990; de Baar et al., 1990). Despite this, diatoms are highly successful in these environments and contribute substantially to primary productivity throughout the region. Low-iron–adapted diatoms utilize several strategies to survive chronic, episodic, or seasonal iron limitation. For example, they can reduce photosynthetic iron demand by substituting iron-containing ferredoxin with flavodoxin (Pankowski and McMinn, 2009b) or cytochrome c_6 with plastocyanin (Peers and Price, 2006). Increased light harvesting cross-section has also been

observed in several iron-stressed diatoms, allowing for more light energy capture to facilitate photosynthesis (Strzepek et al., 2019; Jabre and Bertrand, 2020). Diatoms may also use iron-free rhodopsin to supplement photosynthetic energy capture (Marchetti et al., 2015), have transport mechanisms that can be up-regulated to maximize iron acquisition (Morrissey et al., 2015; Kazamia et al., 2018; McQuaid et al., 2018), and some species contain iron storage proteins (ferritin) to buffer the sporadic availability of this micronutrient (Marchetti et al., 2009).

Temperature influences intracellular transport processes and enzymatic turnover rates and ultimately plays an important role in controlling phytoplankton growth and physiology (Raven and Geider, 1988). Temperature has also been shown to limit SO phytoplankton growth in the field and the laboratory. Warming incubations that simulate projected sea surface temperature changes by the year 2100 to 2300 (0 °C versus +4 °C) in iron-limited, diatom-dominated SO microbial communities resulted in increased nutrient drawdown and improved the growth of several diatom groups (Rose et al., 2009), with similar results reported in iron-limited laboratory diatom cultures grown under the same temperature treatments (Zhu et al., 2016). Warming (up to a critical threshold) improves iron use efficiency (Sunda and Huntsman, 2011; Jiang et al., 2018; Yang et al., 2021), increases the turnover rate of iron-containing enzymes such as nitrate reductase (Gao et al., 1993; Di Martino Rigano et al., 2006), and may thus cause increased utilization of SO nitrate even in the absence of iron addition (Hutchins and Boyd, 2016; Spackeen et al., 2018a). Some Antarctic diatoms such as *Fragilariopsis cylindrus* also exhibit reduced cell size under elevated temperature, which can decrease cellular iron quotas, increase surface area to volume ratios, and facilitate nutrient uptake and growth (Jabre and Bertrand, 2020). Other studies have shown a reduction in the upper thermal limit of Antarctic diatom growth (e.g., centric diatoms *Chaetoceros neglectus*, *Chaetoceros flexuosus*, *Thalassiosira antarctica*) under reduced iron availability (Boyd, 2019; Andrew et al., 2019), and some diatoms like the pennate *F. cylindrus* still require iron supplementation ($>$ 10 nM EDTA-buffered iron) to benefit from warming (3 °C and 6 °C compared to 1 °C), even when iron-conserving mechanisms are used (Jabre and Bertrand, 2020). Additionally, concurrent increases in temperature and iron have been shown to have larger synergistic effects on growth and nutrient utilization compared to the individual effects of each factor (Hutchins and Boyd, 2016; Rose et al., 2009; Zhu et al., 2016). Here, we define "synergistic" as a

nonlinear, multiplicative response, which exceeds the sum of the individual effects of iron and temperature (Boyd and Hutchins, 2012).

Despite shared adaptations across various taxa, diatoms are an extremely diverse group of phytoplankton. Within the SO, major diatom groups have different morphological and physiological traits, with unique optimal growth temperatures and different tolerances to low iron (Strzepek et al., 2019; Boyd, 2019; Hutchins et al., 2001; Sackett et al., 2013; Coello-Camba and Agustí, 2017; Tréguer et al., 2018). The molecular mechanisms that underpin these differences are still poorly understood and are overlooked by the majority of current marine ecosystem models, which consider all diatoms as one group (Laufkötter et al., 2015). This oversimplification cannot capture how environmentally mediated changes in diatom community composition and structure (e.g., communities with different sinking rates) may affect important ecological processes, as well as nutrient and carbon biogeochemistry (Assmy et al., 2013).

Here, we present an experimental manipulation study performed at the sea ice edge (IE) in the Ross Sea of the SO. Coastal areas of the SO, including the sea IE, are highly productive, and the Ross Sea alone contributes to 25% of all SO primary productivity (Arrigo et al., 2008), making this area of the SO ecologically and biogeochemically important. This region has also been shown in previous growing seasons (e.g., 2013, 2014 (Bertrand et al., 2015)) to be iron limited, suggesting that despite its coastal nature, phytoplankton here experience similar nutritional stressors found throughout the Ross Sea and broader SO. We investigated the growth, nutrient drawdown, and transcriptional responses of an SO microbial community to warming and changes in iron availability, mimicking changes that are projected to occur between the years 2100 and 2300 (Moore et al., 2018; Turner et al., 2005; Boyd et al., 2015b). We show that nutrient drawdown increases in response to temperature and iron, both independently and synergistically, and that two closely related diatom groups, *Fragilariopsis* spp. and *Pseudo-nitzschia* spp., respond differently to changes in temperature and iron. These two bloom-forming taxa (Mangoni et al., 2017) contribute substantially to diatom assemblages in the SO and strongly influence the ecology and biogeochemistry of the region (Rose et al., 2009; Kang and Fryxell, 1992; Quéguiner, 2013). *Pseudo-nitzschia* cell numbers increased more than *Fragilariopsis* under warming alone, while the latter required iron addition to benefit from

increased temperature. Our metatranscriptome data suggest that the growth of *Pseudo-nitzschia* under warming is likely facilitated by temperature-responsive light harvesting and iron management strategies that were not utilized by *Fragilariopsis*. This ability to grow and draw down nutrients in the face of warming, regardless of iron availability, could have major implications for the ecological and biogeochemical response of the HNLC SO to a changing climate.

3.5 Results and Discussion

We incubated SO surface water under constant growth-saturating light (65 to 85 μE m^{-2} sec^{-1}) with and without 2 nM iron addition at three temperatures (-0.5 °C, 3 °C, 6 °C) to simulate increased iron availability and a range of SO surface water temperatures, spanning from current to projected conditions 100 to 300 y from now (Moore et al., 2018; Turner et al., 2005; Boyd et al., 2015b) (Table S3.1). We then examined the microbial community after 24 h (T1) and again after 5 (T5) and 7 d (T7). Unless otherwise stated, a temperature effect (i.e., effect of increased temperature) on the various measured parameters refers to an effect at both 3 °C and 6 °C (see Materials and Methods Summary for details).

Increasing temperature and iron separately caused a significant but small increase in community (> 0.7 μm) primary productivity measured as bicarbonate uptake (Fig. 3.1A, Fig. S3.6, two-way ANOVA, temperature effect P = 1.1 x 10^{-6}, Fe effect P = 2.4 x 10^{-6}), as well as an increase in community nitrate uptake rates (Fig. 3.1A, Fig. S3.6, two-way ANOVA, temperature effect P = 0.001, Fe effect P = 7.9 x 10^{-5}), nitrate consumption (Fig. 3.1B, Fig. S3.6, two-way ANOVA, temperature effect P = 2.9 x 10^{-11}, Fe effect P = 1.2 x 10^{-12}), and phosphorus consumption (Fig. 3.1B, Fig. S3.6, two-way ANOVA, temperature effect P = 2.3 x 10^{-6} , Fe effect P = 1.0 x 10^{-6}). Incubations under concurrent warming and iron addition showed a synergistic increase in primary productivity (Fig. 3.1A, two-way ANOVA, temperature x Fe effect P = 4.7 x 10^{-5}), nitrate uptake rates (Fig. 3.1A, two-way ANOVA, temperature x Fe effect P = 0.007), nitrate consumption (Fig. 3.1B, Fig. S3.6, two-way ANOVA, temperature x Fe effect P = 6.0 x 10^{-9}), and phosphorus consumption (Fig. 3.1B, Fig. S3.6, two-way ANOVA, temperature x Fe effect P = 7.5 x 10^{-5}). This synergistic iron–temperature effect has been observed previously (Rose et al., 2009; Spackeen et al., 2018a) and suggests that future warming conditions can

strongly influence SO productivity and nutrient drawdown, especially if combined with a concurrent increase in iron availability.

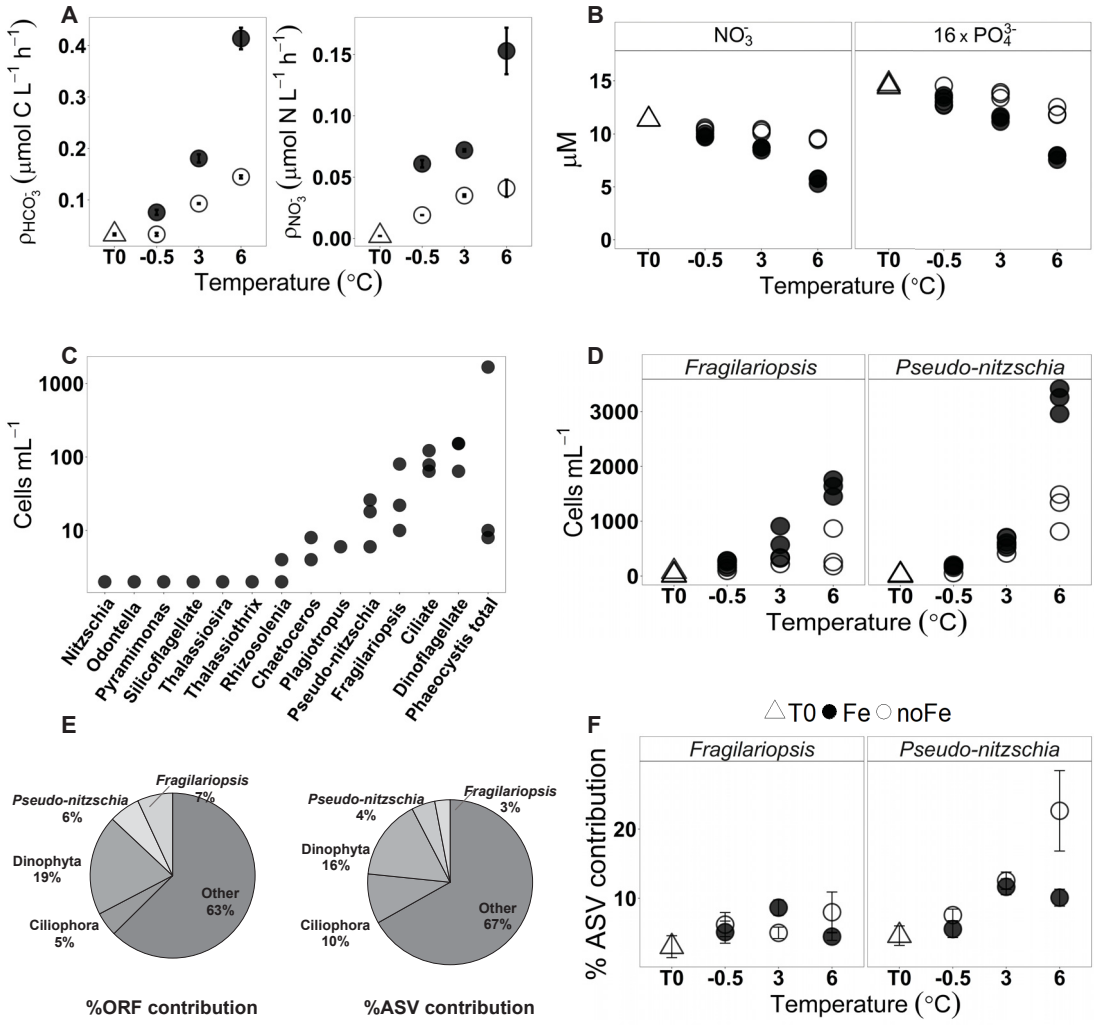

Figure 3.1: (A) Absolute bicarbonate and nitrate uptake rates at T0 (prior to the incubations) and T7 for each temperature and iron condition. Uptake rates were measured in duplicate from a single incubation bottle per treatment. (B) Dissolved nitrate and phosphate concentrations in triplicate incubation bottles at T0 and T7. Phosphate concentration is scaled (16×) for better visual comparison with nitrate. (C) Initial (T0) cell counts of eukaryotic taxa identified by light microscopy, n = 3, taxa are arranged from low to high abundance. The large variation in *Phaeocystis* cell counts at T0 likely resulted from random variability in colony abundance and size in the relatively small-volume samples used for microscopic cell counts. Cell counts for other taxonomic groups under the different temperature and iron treatments are shown in Fig. S3.7. (D) Measurements of *Fragilariopsis* and *Pseudo-nitzschia* cell counts at T0 and T7 in triplicate incubation bottles for each temperature and iron condition. (E) Pie charts representing percent contribution of taxa to the total reads mapped to ORFs and to the total 18S rRNA Amplicon Sequence Variant (ASV) abundance at T0. "Other" represents all other taxonomic groups, including prokaryotes and viruses. (F) Percent contribution of *Fragilariopsis* and *Pseudo-nitzschia* to the total ASV abundance at T0 and T5 for each temperature and iron condition. Each point represents triplicate means; error bars represent ±1 SD and fall within the bounds of the symbol when not visible.

Microscopy observations showed that *Phaeocystis*, dinoflagellates, ciliates, *Fragilariopsis*, and *Pseudo-nitzschia* were among the most abundant eukaryotic taxa at the beginning of the incubation experiment (the in situ community) and after temperature and iron incubations (Fig. 3.1C, Fig. S3.7). We focused our analyses here on the responses of the two most abundant diatom groups in our samples, *Fragilariopsis* (identified by light microscopy and 18S ribosomal RNA sequencing as mostly *Fragilariopsis kerguelensis* and *Fragilariopsis cylindrus*) and *Pseudo-nitzschia* (identified by light microscopy, 18S ribosomal RNA sequencing, and a protein Basic Local Alignment Search Tool (BLAST-p) analysis of *Pseudo-nitzschia* transcriptomes as mostly *Pseudo-nitzschia subcurvata*) (Table S3.2 and S3.3, and Full Materials and Methods). *Pseudo-nitzschia* but not *Fragilariopsis* cell counts increased significantly under warming without added iron (Fig. 3.1D, two-way ANOVA, temperature effect P = 0.003 and P = 0.5, respectively) and showed the largest increase in abundance throughout the incubations, compared to other plankton groups (Fig. S3.7). Additionally, concurrent warming and iron supplementation caused an increase in *Fragilariopsis* (Fig. 3.1D, two-way ANOVA, temperature x Fe effect P = 0.001) and a much larger synergistic increase in *Pseudo-nitzschia* cell counts (Fig. 3.1D, , two-way ANOVA, temperature x Fe effect P = 1.13 x 10^{-6}). This highlights the ability of *Pseudo-nitzschia* to increase its growth under warmer conditions, regardless of iron availability.

We used metatranscriptomics to comprehensively capture gene expression patterns and examine the molecular processes underpinning the distinct growth responses of *Fragilariopsis* and *Pseudo-nitzschia* to shifts in iron availability and temperature (Fig. 3.2). Metatranscriptomics allows for the interrogation of cellular pathways utilized across various taxa and can be used to infer metabolic states under different environmental conditions (Bertrand et al., 2015; Marchetti et al., 2012; Cohen et al., 2018a). Here, we identified transcripts belonging to viruses, prokaryotes, and eukaryotes (Fig. S3.8); with dinoflagellates, ciliates, *Pseudo-nitzschia*, and *Fragilariopsis* contributing 37% of the total reads mapped to open reading frames (ORFs) (Fig. 3.1E). The contribution of *Phaeocystis* to the metatranscriptome was lower than anticipated based on microscopy, possibly due to difficulty in harvesting cells/colonies without rupturing them (Kiene and Slezak, 2006). Kyoto Encyclopedia of Genes and Genomes (KEGG) Orthology (KO) term enrichment analysis on ORFs belonging to *Fragilariopsis* and *Pseudo-nitzschia* showed that pathways

corresponding to photosynthesis, nitrogen metabolism, and genetic information processing/translation were highly differentially expressed in both taxa following temperature and iron increase (Fig. S3.9, S3.10). We explored these pathways in more detail by grouping individual ORFs into clusters of similar sequences using Markov clustering (MCL) (Enright, 2002) (Materials and Methods Summary). Several clusters contained differential expression patterns that were similar in *Fragilariopsis* and *Pseudo-nitzschia* under iron addition (63 clusters) and temperature increase (212 clusters). However, a larger number of clusters were uniquely differentially expressed in either *Fragilariopsis* or *Pseudo-nitzschia* under these conditions (Fig. 3.3A), suggesting that *Fragilariopsis* and *Pseudo-nitzschia* utilize different molecular strategies to respond to changes in temperature and/or iron.

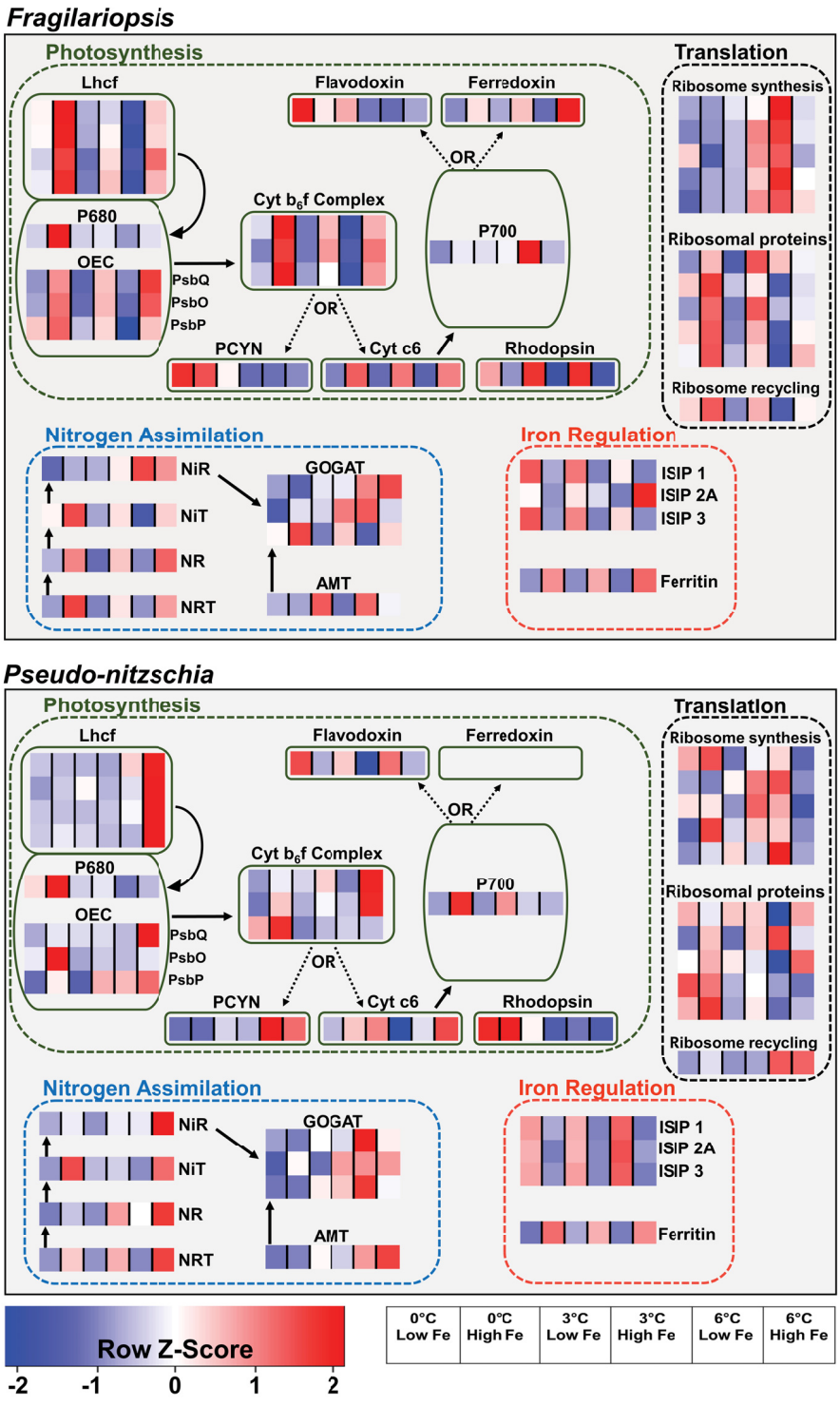
Fragilariopsis
Photosynthesis
Lhcf
Flavodoxin
Ferredoxin
OR
Cyt b6f Complex
P680
OEC
PsbQ
PsbO
PsbP
P700
OR
PCYN
Cyt c6
Rhodopsin
Translation
Ribosome synthesis
Ribosomal proteins
Ribosome recycling
Nitrogen Assimilation
NiR
NiT
NR
NRT
GOGAT
AMT
Iron Regulation
ISIP 1
ISIP 2A
ISIP 3
Ferritin
Pseudo-nitzschia
Photosynthesis
Lhcf
Flavodoxin
Ferredoxin
OR
Cyt b6f Complex
P680
OEC
PsbQ
PsbO
PsbP
P700
OR
PCYN
Cyt c6
Rhodopsin
Translation
Ribosome synthesis
Ribosomal proteins
Ribosome recycling
Nitrogen Assimilation
NiR
NiT
NR
NRT
GOGAT
AMT
Iron Regulation
ISIP 1
ISIP 2A
ISIP 3
Ferritin
Row Z-Score
-2
-1
0
1
2
0°C Low Fe
0°C High Fe
3°C Low Fe
3°C High Fe
6°C Low Fe
6°C High Fe

Figure 3.2

Figure 3.2: Schematic representations of *Fragilariopsis* and *Pseudo-nitzschia* cells showing cellular processes, with each process comprised of several transcript clusters (MCL clusters). Photosynthesis: Lhcf = light harvesting complexes-f, OEC = oxygen evolving complex, Cyt b_6f complex = cytochrome b_6f complex, PCYN = plastocyanin, Cyt c_6 = cytochrome c_6. Nitrogen Assimilation: NRT = nitrate transporter, NR = nitrate reductase, NiT = nitrite transporter, NiR = nitrite reductase, AMT = ammonium transporter, GOGAT = glutamine oxoglutarate aminotransferase cycle. Iron Regulation: ISIP = iron starvation induced protein. Each row in a heatmap represents one MCL, each column represents a temperature and iron treatment at T5 with each block representing three biological replicate means with individual replicates shown in Fig. S3.14. Heatmaps were constructed using taxon-normalized RPKM values. Empty heatmap placeholders represent clusters found in *Fragilariopsis* but not *Pseudo-nitzschia*. Arrows represent energy/electron flow in photosynthetic light reactions and steps involved in nitrogen assimilation using nitrate or ammonium.

3.5.1 Photosynthesis

Iron addition resulted in up-regulation of iron-containing cytochrome b_6f complex transcripts and down-regulation of flavodoxin transcripts in both *Fragilariopsis* and *Pseudo-nitzschia* (Fig 3.2, 3.3). This indicates that both diatoms in our study were undergoing some degree of iron stress at the time of sampling; ambient dissolved iron concentrations at the time of sampling were growth limiting at 0.47 nM (Wu et al., 2019), and iron-containing photosynthetic processes including the electron transport chain can account for up to 40% of cellular iron quotas (Raven et al., 1999) and are typically down-regulated under low iron (LaRoche et al., 1996; Allen et al., 2008). Here, we did not detect the expression of iron-dependent electron acceptor ferredoxin (PetF) in *Pseudo-nitzschia*, regardless of iron status. Antarctic *Pseudo-nitzschia* species may have constitutively reduced dependence on PetF (Pankowski and McMinn, 2009a; Moreno et al., 2018) to minimize photosynthetic iron demand.

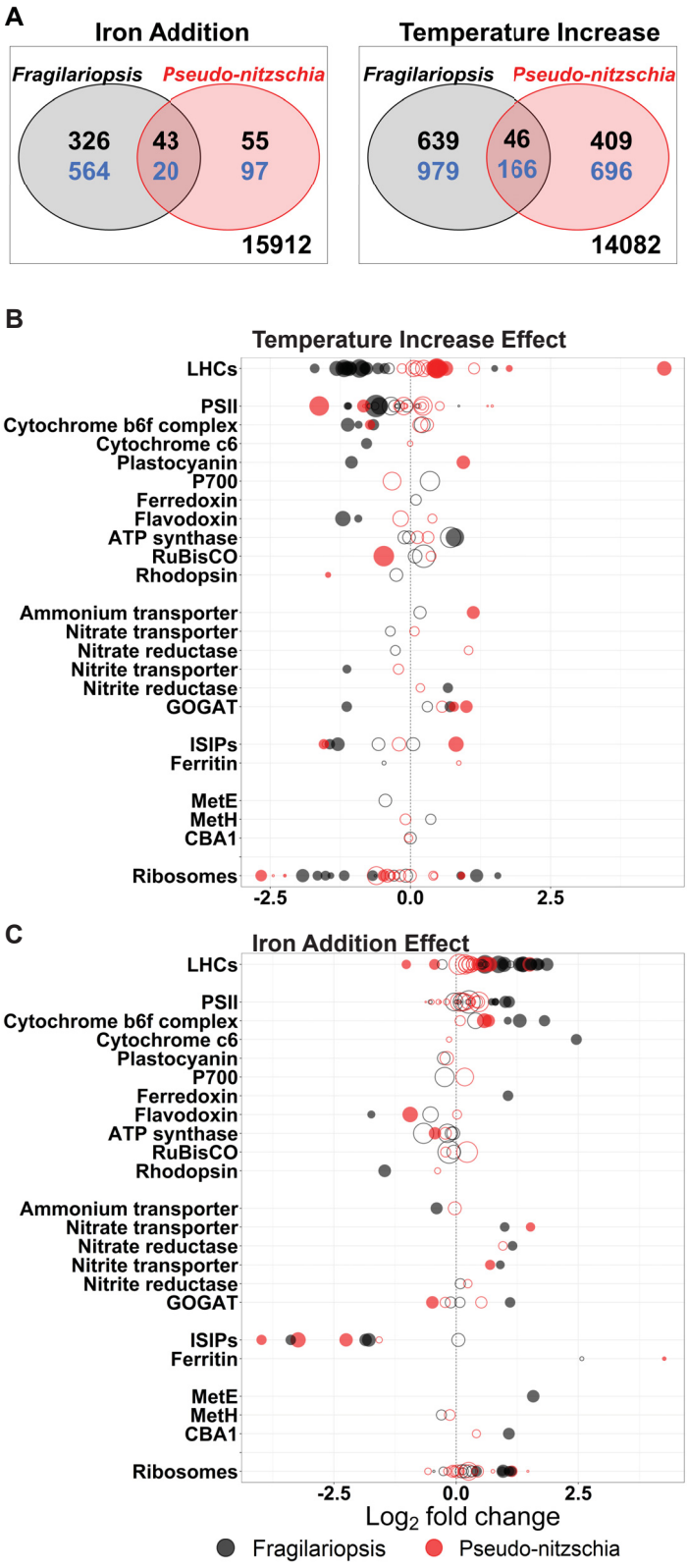
A
Iron Addition
Fragilariopsis
Pseudo-nitzschia
326
564
43
20
55
97
15912
Temperature Increase
Fragilariopsis
Pseudo-nitzschia
639
979
46
166
409
696
14082
B
Temperature Increase Effect
LHCs
PSII
Cytochrome b6f complex
Cytochrome c6
Plastocyanin
P700
Ferredoxin
Flavodoxin
ATP synthase
RuBisCO
Rhodopsin
Ammonium transporter
Nitrate transporter
Nitrate reductase
Nitrite transporter
Nitrite reductase
GOGAT
ISIPs
Ferritin
MetE
MetH
CBA1
Ribosomes
-2.5
0.0
2.5
C
Iron Addition Effect
LHCs
PSII
Cytochrome b6f complex
Cytochrome c6
Plastocyanin
P700
Ferredoxin
Flavodoxin
ATP synthase
RuBisCO
Rhodopsin
Ammonium transporter
Nitrate transporter
Nitrate reductase
Nitrite transporter
Nitrite reductase
GOGAT
ISIPs
Ferritin
MetE
MetH
CBA1
Ribosomes
-2.5
0.0
2.5
Log2 fold change
Fragilariopsis
Pseudo-nitzschia

Figure 3.3

Figure 3.3: (A) Venn diagram showing the number of transcript clusters that are significantly up (black) or down (blue) regulated with iron addition or temperature increase in *Fragilariopsis* and *Pseudo-nitzschia*. The intersection represents clusters up, or down, regulated in both *Fragilariopsis* and *Pseudo-nitzschia*. The number outside of the circles represents the number of clusters from both taxa that were not differentially expressed. In both taxa, warming caused more clusters to be differentially expressed than iron addition. (B) Differential expression (DE) of various clusters under increased temperature. DE was calculated using the quasi-likelihood test (glmQLFTest) in EdgeR, and fold change was calculated for high-temperature (6 °C) versus low-temperature (-0.5 °C) treatments at T5. (C) DE of various clusters after iron addition. DE was calculated using the quasi-likelihood test (glmQLFTest) in EdgeR, and fold change was calculated for iron-added versus no iron-added treatments at T5. In both B and C, positive and negative Log_2 fold change values represent up and down regulation, respectively. Filled circles are clusters with statistically significant DE (adjusted P value < 0.05). Point size represents total normalized transcript abundance under all iron and temperature treatments.

3.5.2 Light-Harvesting Complexes

Most members of the light-harvesting complex (LHC) superfamily primarily absorb and direct light energy to photosynthetic reaction centers where charge separation occurs, but some of them (Lhcx clade) are also involved in stress responses and photoprotection (Zhu and Green, 2010; Buck et al., 2019). Expression patterns of transcripts belonging to the major Lhcf group and photosystem I (PSI)-associated Lhcr groups were markedly different between the two taxa under the different temperature and iron treatments (Fig. 3.4). In *Fragilariopsis*, there was a general pattern of decreased expression with warming and marked up-regulation with iron addition. In contrast, *Pseudo-nitzschia* showed a pattern of increasing expression with elevated temperatures. Up-regulation of Lhcf and Lhcr groups contributes to increased light harvesting efficiency and provides more energy for downstream temperature-dependent catalytic processes. This also alleviates photosynthetic iron demand by reducing the number of iron-containing photosynthetic components required to process light energy (Schuback et al., 2015). Increased light harvesting cross-section has been measured under warming (3 °C and 6 °C compared to 1 °C) in iron-stressed *F. cylindrus* in the laboratory (Jabre and Bertrand, 2020). However, these environmental data indicate that *Pseudo-nitzschia* may be even better equipped to use this mechanism to support growth under low iron in the SO, provided that the LHC up-regulation observed here reflects an increase in light harvesting cross-section, which remains speculative at this time. Several Lhcf and Lhcr clusters were also up-regulated in both *Fragilariopsis* and *Pseudo-nitzschia* after iron addition. Given that iron addition is expected to decrease light harvesting cross-section (Strzepek et al., 2019; Jabre and Bertrand, 2020; Greene et al., 1992; Strzepek et al., 2012), it might be predicted that iron addition could decrease the demand for Lhcf and Lhcr expression. However, this impact appears to be overridden by increased demand for LHC expression resulting from iron-induced increases in photosynthetic unit (PSU) abundance. Additional measurements of light absorption cross-section and photosynthetic efficiency could provide further insight into how light harvesting responds to changes in LHC expression under different iron and temperature conditions.

Each transcript cluster belonging to the Lhcx clade was down-regulated after 24 h of incubation at all temperatures and iron conditions in both *Fragilariopsis* and *Pseudo-nitzschia* (Fig. 3.4). Lhcxs are highly sensitive to environmental change, including

fluctuations in light and nutrient levels (Zhu and Green, 2010; Buck et al., 2019; Taddei et al., 2016). Given these expression patterns and previous observations of Lhcx regulation, the Lhcx transcripts detected here may be responding to changes in the light levels that cells would have undergone during sample collection—brief exposure to unattenuated daylight during sampling, followed by lower light intensities in the incubations. Notably, expression of these Lhcx clades showed only minimal responses to iron addition.

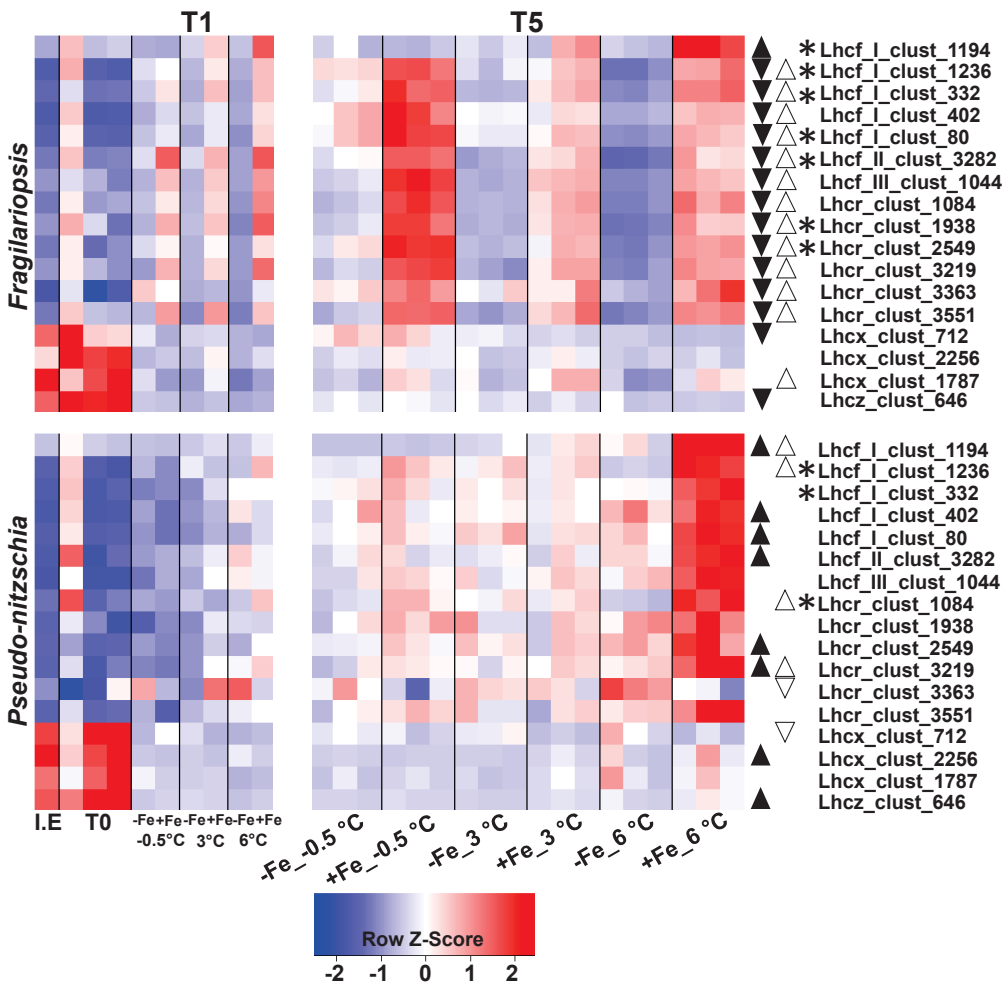

Figure 3.4: Heatmaps of MCL clusters of LHCs Lhcf, Lhcr, Lhcx, and Lhcz in *Pseudo-nitzschia* and *Fragilariopsis* measured after 24 h (T1) and 5 d (T5) of incubation under the various iron and temperature treatments. Heatmaps were constructed using taxon-normalized RPKM values. I.E represents IE samples; T0 represents in situ samples processed immediately before any incubations. Each block is one biological replicate measurement. Black and white up/down pointing triangles represent transcripts that were significantly (glmQLFTest-EdgeR $P < 0.05$) up- or down-regulated due to warming or iron addition (respectively) at T5. Stars represent transcripts that were significantly (glmQLFTest-EdgeR $P < 0.05$) up-regulated due to an interactive iron–temperature effect at T5.

3.5.3 Plastocyanin

Plastocyanin is a copper-containing protein that acts as an electron shuttle in the electron transport chain and plays an important role in reducing iron requirements in phytoplankton by substituting for cytochrome c_6 (Peers and Price, 2006; Wu et al., 2019; Schoffman

et al., 2016). Here, iron addition had no significant effect on plastocyanin transcript expression, while warming caused its up-regulation in *Pseudo-nitzschia* and down-regulation in *Fragilariopsis* (Fig. 3.3). Plastocyanin expression has been observed to be insensitive to iron availability in low-iron–adapted diatoms (Marchetti et al., 2012). However, our data suggest that *Pseudo-nitzschia* plastocyanin transcripts are phylogenetically distinct from those of *Fragilariopsis* and may play a temperature-responsive role to support growth under elevated temperatures (Fig. S3.11). Plastocyanin transcript abundance in *Pseudo-nitzschia* was higher at 3 °C and 6 °C compared to −0.5 °C at T1, showing a rapid response to warming (Fig. S3.11). This, in combination with the strong and immediate response of LHCs may give *Pseudo-nitzschia* a photosynthetic advantage over *Fragilariopsis* across a wide range of likely warming scenarios in the SO.

3.5.4 Nitrogen Metabolism

KO term enrichment analysis showed that transcripts encoding nitrogen metabolism were enriched in *Pseudo-nitzschia* and depleted in *Fragilariopsis* after temperature increase (Figs. S3.9, S3.10). Nitrogen is required for protein synthesis and would be necessary to support the observed increase in *Pseudo-nitzschia* cell counts under warming, and notably, dissolved nitrogen drawdown was enhanced due to warming alone and elevated further upon iron addition (Fig. 3.5 A, B). However, nitrogen acquisition and assimilation from nitrate requires iron (Schoffman et al., 2016), and the observed *Pseudo-nitzschia* growth under elevated temperature would necessitate iron-economic nitrogen metabolism. Our data show that ammonium transporter transcripts were up-regulated in *Pseudo-nitzschia* but not in *Fragilariopsis* under warming (Fig. 3.3B, 3.5C, D), indicating that *Pseudo-nitzschia* is better equipped to utilize ammonium as an additional and/or alternative nitrogen source in response to elevated nitrogen demand, which is likely a result of increased growth in response to warming. Elevated ammonium transporter expression would provide *Pseudo-nitzschia* with an additional nitrogen source at a lower iron cost for use in amino acid synthesis and growth (Schoffman et al., 2016; Raven, 1988; Smith et al., 2019). In fact, community ammonium drawdown at 6 °C was greater than at lower temperatures, regardless of iron status (Fig. 3.5B), consistent with the notion that ammonium use at high temperature and low iron could have contributed to the success of *Pseudo-nitzschia*. The ability to uptake and utilize ammonium rapidly, relative to nitrate, also allows diatoms to

grow faster when ammonium is available (Parslow et al., 1984; Tada et al., 2009). However, the high *Pseudo-nitzschia* growth we observed cannot be supported by ammonium alone; total community ammonium drawdown comprised only $25.2 \pm 2.4\%$ of dissolved inorganic nitrogen (nitrate + ammonium) drawdown in the 6 °C no added iron treatment and $7.9 \pm 1.0\%$ of dissolved inorganic nitrogen drawdown in the added iron 6 °C treatment (Fig. 3.5A, B). Nitrate drawdown was responsible for the majority of dissolved nitrogen uptake regardless of iron status, though significantly (two-way ANOVA, $P = 9.6 \times 10^{-11}$) more so under elevated iron. This suggests that *Pseudo-nitzschia* may have utilized additional parsimonious mechanisms such as internal protein recycling to further reduce nitrogen requirements and thereby reduce iron demand (Nunn et al., 2013). While nitrate drawdown was elevated at high temperatures both with and without added iron (Fig. 3.5A), neither *Pseudo-nitzschia* nor *Fragilariopsis* changed their expression of nitrate transporters in response to elevated temperature. Both diatom groups up-regulated nitrate transporters in response to iron addition regardless of temperature (Fig. 3.3, Fig. 3.5E, F). Similarly, nitrate reductase transcript expression was up-regulated in response to iron addition but not elevated temperature (Fig. 3.3, Fig. 3.5G, H). However, the observed elevation in nitrate drawdown and nitrate uptake rates with warming (Fig. 3.1, Fig. 3.5), in the absence of a change in gene expression, is consistent with the well-characterized temperature dependence of nitrate reductase activity Gao et al. (2000). This suggests that the enhanced nitrate assimilation under elevated temperature was indeed accomplished without the increase in iron demand required to produce additional copies of active nitrate reductase.

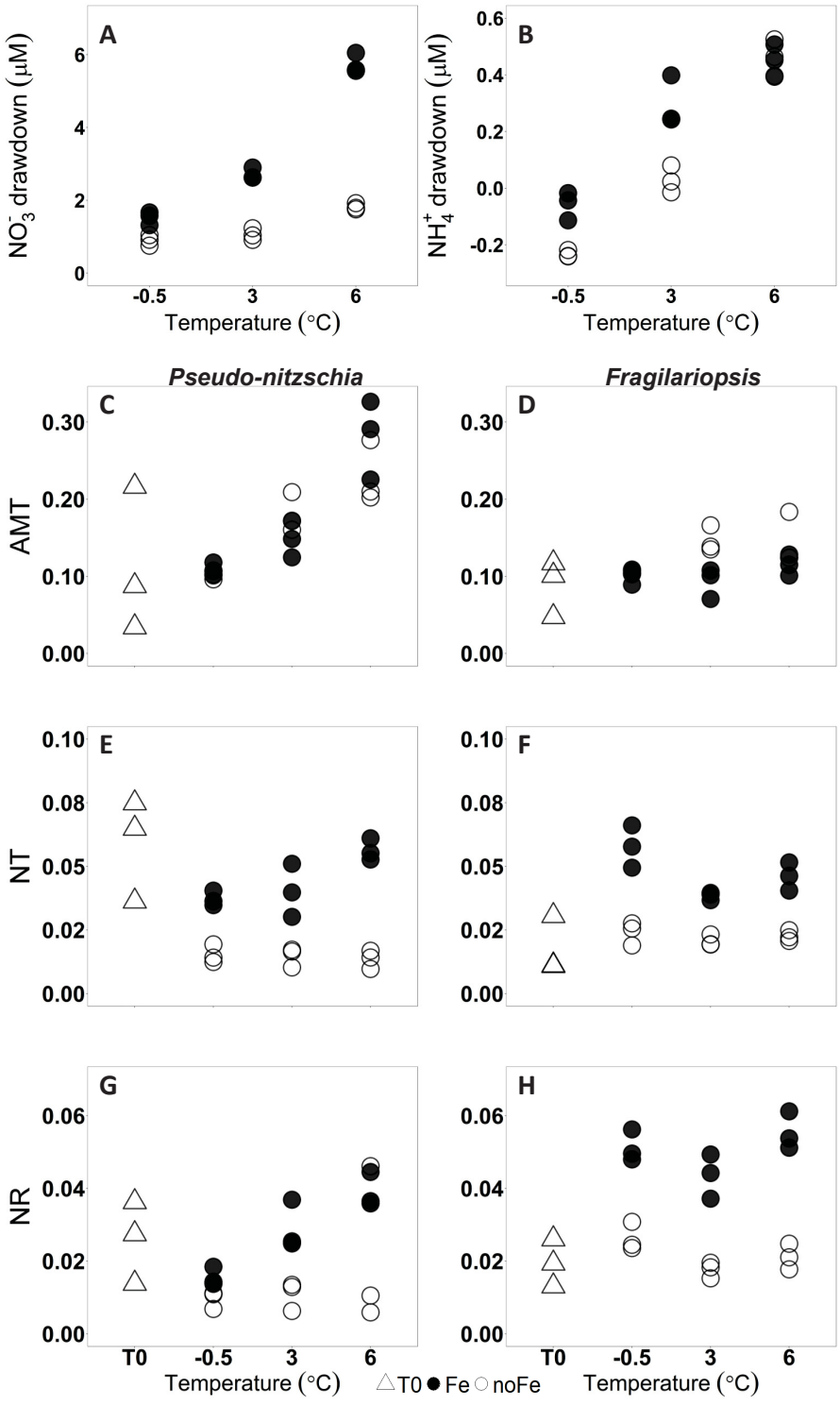

Figure 3.5: (A and B) Total nitrate and ammonium drawdown from beginning to end of the experiment (difference in concentration between T7 and T0). (C–H) Taxon-normalized RPKM expression values for clusters belonging to ammonium transporters (AMT), nitrate transporters (NT), and nitrate reductase (NR) in both *Pseudo-nitzschia* and *Fragilariopsis* prior to incubation (T0) and at T5 with and without added iron at −0.5, 3, and 6 °C.

3.5.5 Genetic Information Processing/Translation

Protein synthesis is an energetically costly process that is required for metabolism and growth. Increased kinetic energy due to warming enhances translation efficiency, reduces the total RNA per cell, and reduces the number of ribosomes required to maintain protein synthesis rates (Toseland et al., 2013). Consistent with this response, we observed that several transcript clusters corresponding to ribosomes were down-regulated in both *Fragilariopsis* and *Pseudo-nitzschia* under warming (Fig. 3.2, Fig. 3.3). Warming also caused up-regulation of transcripts encoding ribosomal recycling proteins only in *Pseudo-nitzschia* (Fig. 3.2), which can reduce nitrogen demand and the energetic costs associated with ribosomal synthesis. While the reduction in phosphorus-rich ribosome abundance is thought to increase cellular N:P ratios, leading to increased nitrogen demand in warmer ocean regions (Toseland et al., 2013), our bulk nutrient drawdown ratios (Fig. S3.6) show that N:P drawdown is not significantly influenced by warming (two-way ANOVA, P = 0.07). This suggests that the increasing dominance of diatoms, with their considerably lower N:P ratios than other SO plankton groups such as *Phaeocystis* (Zhu et al., 2016; Arrigo et al., 1999), is likely an overall driver of N:P ratios and can counterbalance the expected reduction in cellular phosphate demand at high temperature from reduced ribosome content. It is also possible that temperature changes alone, without additional interactive effects due to changes in other variables such as CO_2 and light, might not cause a strong increase in N:P ratios (Boyd et al., 2015a).

3.5.6 Micronutrient Acquisition, Trafficking, and Storage

Increased iron uptake, storage, and intracellular transport are strategies to improve growth under low iron availability. In the laboratory, Zhu et al. (2016) report higher iron uptake rates in *P. subcurvata* than in *F. cylindrus* under warming. Our data show down-regulation of iron stress-induced proteins (ISIP1, ISIP2A, ISIP3) in both *Pseudo-nitzschia* and *Fragilariopsis* after iron addition, and ISIP2A up-regulation only in *Pseudo-nitzschia* after warming (Fig. 3.2, Fig. 3.3). ISIPs are involved in iron acquisition and storage systems in diatoms, and specifically, ISIP2A contributes to nonreductive iron uptake (Morrissey et al., 2015; Kazamia et al., 2018; McQuaid et al., 2018; Allen et al., 2008). No previous studies have inspected ISIP2A response to temperature, but it is likely that the apparent temperature response of ISIP2A contributes to the ability of *Pseudo-nitzschia* to acquire

and utilize iron to support growth under warming. Additionally, transcripts for ferritin, an iron storage protein (Marchetti et al., 2009), were significantly up-regulated only in *Pseudo-nitzschia* after iron addition (Fig. 3.3). Several studies have reported ferritin up-regulation in *Pseudo-nitzschia* under iron-replete conditions (Cohen et al., 2018a,b), and *Fragilariopsis* can also utilize ferritin to store iron (Marchetti et al., 2009). However, consistent with low *Fragilariopsis* ferritin expression under iron-replete conditions in the field (Lampe et al., 2018), our study shows that *Fragilariopsis* ferritin transcripts were not significantly up-regulated after iron addition (Fig. 3.3). These trends suggest that in addition to reducing iron demand, *Pseudo-nitzschia* was better able to increase iron uptake and utilized stored ferritin-bound iron to support growth under warming. This suggests that *Pseudo-nitzschia* may be particularly well suited to environments with episodic iron availability.

In addition to iron, cobalamin has also been shown to be a critical micronutrient driver of phytoplankton growth and community composition in the SO (Bertrand et al., 2015). *Fragilariopsis* and *Pseudo-nitzschia*'s cobalamin acquisition and stress response machinery also showed markedly different responses to iron and warming (Fig. 3.3, Fig. S3.12), suggesting that these two diatoms may employ different strategies to cope with low cobalamin availability (Supplemental Results and Discussion).

3.5.7 Synergistic Responses and Gene Expression

The observed synergistic iron–temperature effects on growth and nutrient drawdown were not accompanied by a synergistic effect on gene expression (Fig. S3.8, S3.15). For example, we did not observe an interactive iron–temperature effect on the expression of genes involved in nitrogen uptake, yet nitrate and ammonium drawdown increased synergistically due to iron and temperature increase (Fig. 3.1). It is unlikely that synergistic nutrient drawdown was influenced by synergistic gene expression in taxa other than *Fragilariopsis* and *Pseudo-nitzschia*. Except for the prokaryotic Alteromonadales group, we observed relatively little or no interactive iron–temperature effect on gene expression in all the taxa we assessed (Fig. S3.8). This suggests that improved enzymatic efficiency under warming can accelerate metabolic functions, even without a proportional increase in transcript abundance. It is worth noting that, without extensive genetic manipulation and biochemical

investigations using monocultures in controlled conditions, observational studies like this lack the ability to disentangle causal relationships between gene expression patterns and physiology/growth. Nevertheless, observations of gene expression trends under different environmental conditions provide insight into the cellular mechanisms that facilitate growth and those which underpin differences between ecologically important groups.

3.5.8 Ecological and Biogeochemical Relevance

Most recent model projections show warming trends across the SO with sea surface temperatures increasing by 1 to 2 °C by 2100 and 6 °C by 2300 (Moore et al., 2018; Boyd et al., 2015b; Rickard and Behrens, 2016). *Fragilariopsis* grows in a wide range of environments throughout the SO but is most successful in high-salinity, high-iron sea ice while *Pseudo-nitzschia* is most successful in warmer low-salinity, low-iron meltwaters (Sackett et al., 2013; Petrou et al., 2011; Petrou and Ralph, 2011). The growth and gene expression patterns we observed in both diatoms may then be driven by niche-specific adaptations due to competition for resources. Our results are consistent with a 2013 incubation study conducted at the IE in the Ross Sea where *Pseudo-nitzschia* dominated the community after warming (Spackeen et al., 2018a), suggesting that Antarctic *Pseudo-nitzschia* are better equipped to dominate in a warmer (4 °C compared to 0 °C) ocean and even more so if iron availability increases. A shift into a *Pseudo-nitzschia* dominated community raises concerns for domoic acid (DA) production and its toxic effects in mammals and other trophic levels (Liu et al., 2007; Scholin et al., 2000). A search for DA biosynthesis transcripts (Brunson et al., 2018) did not yield strong evidence for expression of the DA biosynthesis gene cluster in this experiment (Tables S3.4, S3.5). However, other studies have measured DA concentrations as high as 220 ng L^{-1} in the SO (Silver et al., 2010; Geuer et al., 2019), but the temporal, spatial, and environmental factors that elicit DA production remain unclear. Further work is required to investigate whether resident *Pseudo-nitzschia* can produce the toxin under conditions not examined in our study or if DA producing *Pseudo-nitzschia* are likely to migrate into a warmer SO.

A change in SO phytoplankton community structure could have important biogeochemical ramifications on local and global scales. Changes in cell size, frustule thickness, and metabolic functions under changing temperature and iron conditions could influence

ecosystem and biogeochemical processes by altering sinking rates, grazing pressures, and cellular nutrient quotas (Assmy et al., 2013; Quéguiner, 2013; Boyd et al., 2015a). Warming-induced increases in the expression of ISIP2A, as well as iron-conserving plastocyanin, LHCs, and nitrogen assimilation processes suggest the involvement of a suite of mechanisms that support growth under warming. These cellular changes resulted in increased nutrient drawdown in our multiday experiment, even in the face of iron limitation. Such warming-enhanced SO nutrient drawdown could have profound consequences for northward nutrient supply, especially if cells are able to utilize these parsimonious processes over weeks or months and if the trends we observe in this coastal experiment hold true across broad swaths of the SO. As more nutrients such as nitrogen and phosphorous are consumed by phytoplankton and exported out of the surface ocean around Antarctica, less nutrients will be available to fuel productivity at lower latitudes (Moore et al., 2018). Here, we have identified molecular mechanisms that appear to enable diatoms, particularly *Pseudo-nitzschia*, to accomplish enhanced growth and nutrient drawdown with rising temperatures under low-iron conditions. These mechanisms, up-regulation of iron-conserving photosynthetic processes, utilization of iron-economic nitrogen assimilation mechanisms, and increased iron uptake and storage, underpin what may be a pattern of increasing nutrient utilization in the SO and decreasing availability of nutrients for lower latitudes.

3.6 Materials and Methods Summary

Seawater was collected at a 3-m depth at the IE from McMurdo Sound, Antarctica on January 15, 2015 (165°24.7985' E, 77°37.1370' S) using previously described trace-metal-clean techniques (Bertrand et al., 2015). Triplicate bottles of each treatment (temperature: -0.5 °C $\pm$ 0.2 °C, 3 $\pm$ 0.5 °C, and 6 $\pm$ 0.5 °C; iron: not added [+0 nM], added [+2 nM]) were incubated indoors at a constant irradiance of 65 to 85 μE m^{-2} sec^{-1}. This incubation irradiance is generally growth saturating for Antarctic phytoplankton (Strzepek et al., 2012; Arrigo et al., 2010) and falls within observational bounds of mean mixed layer light levels (Mangoni et al., 2019). Metatranscriptome samples were taken at the sea IE, in the laboratory immediately following bottle incubation setup (T0), on January 16 (T1), and again on January 20 (T5). Cell counts were measured on T0 and January 22 (T7). Dissolved nutrients (nitrate, phosphate, silicate) were measured on T0, T1, T3, T5, and T7,

and ammonium was measured on T0 and T7. Primary productivity (bicarbonate uptake) and nitrate uptake rates were measured on T0, T1, T3, and T7 (Fig. S3.6).

For metatranscriptomics, the microbial community was harvested on 0.2 μm Sterivex filters, total RNA was extracted using TRIzol reagent (Thermo Fisher Scientific), and ribosomal RNA was removed with Ribo-Zero Magnetic kits (Illumina). The resulting messenger RNA (mRNA) was purified and subjected to amplification and complementary DNA (cDNA) synthesis, using the Ovation RNA-Seq System V2 (TECAN). One microgram of the resulting cDNA pool was fragmented to a mean length of 200 base pairs, and libraries were prepared using Truseq kit (Illumina) and subjected to paired-end sequencing via Illumina HiSeq. Illumina paired reads were filtered to eliminate primer sequences and quality trimmed to Phred Q33, and rRNA was identified and removed using riboPicker (Schmieder et al., 2012). Transcript contigs were assembled de novo using CLC Assembly Cell (https://www.qiagenbioinformatics.com/), and ORFs were predicted using FragGeneScan (Rho et al., 2010). ORFs were annotated for putative function using hidden Markov models and BLAST-p against PhyloDB (Bertrand et al., 2015) and filtered to eliminate those with low mapping coverage (<50 reads total over all samples) and proteins with no BLAST hits and no known domains. ORFs were assigned to taxonomic groups of interest (Fig. S3.7) based on best Lineage Probability Index (LPI) taxonomy (Bertrand et al., 2015; Podell and Gaasterland, 2007). Reads per kilobase mapped (RPKM) expression values for each ORF were calculated and taxon normalized using a normalization factor representing the summed taxonomic group contribution to total nuclear-assigned reads per sample. ORFs were clustered into orthologs and protein families using MCL (Enright, 2002). Group normalized cluster (average/total) RPKM expression values were calculated by pooling the taxon-normalized expression values for each group within a cluster. Cluster annotations were aggregated by annotation type (KEGG, KO, euKaryotic Orthologous Groups [KOG], KOG class, Pfam, TIGRfam, Enzyme Commission [EC], Gene Ontology [GO]), and a single annotation was chosen to represent each cluster based on the lowest Fisher's exact test P value (fisher.test in R).

Differential gene expression at T5 (foldchange magnitude and adjusted P value) was calculated using empirical Bayes quasi-likelihood F-tests (glmQLFTest in edgeR) on taxon-normalized expression values to account for the change in abundance under the different iron and temperature treatments. A P value cut off of 0.05 was used for statistical

significance. Iron effect was determined by comparing all -Fe treatments at T5 to all +Fe treatments at T5. Temperature effect was determined by comparing all -0.5 °C to 3 °C treatments at T5 and -0.5 °C to 6 °C at T5. A gene was considered up-regulated with temperature if it was up-regulated in both -0.5 °C versus 3 °C and -0.5 °C versus 6 °C tests.

Stable isotope tracer techniques, using ^{15}N-labeled nitrate and ^{13}C-labeled bicarbonate (Cambridge Isotope Laboratories), were used to determine uptake rates, similar to methods previously described in Ross Sea nutrient utilization studies (Spackeen et al., 2018a). Tracer amounts of labeled substrates were added to bottles containing the initial IE community (T0) and to subsampled volume from treatments at T1, T3, and T7. After incubations (6 h), the microbial communities ($>$0.7 μm) were collected on glass fiber filters (Whatman GF/F; combusted at 450 °C for 2 h) and stored frozen. Isotopic enrichments of ^{15}N and ^{13}C were measured on a Europa 20/20 isotope ratio mass spectrometer, and absolute uptake rates (μM h^{-1}) were calculated according to (Dugdale and Wilkerson, 1986). Complete methods and uptake rate measurements from all time points can be found in Fig. S3.6).

3.7 Data Availability

The data reported in this paper have been deposited in the National Center for Biotechnology Information sequence read archive (BioProject accession no. PRJNA637767; RNA-Seq BioSample accession nos. SAMN15154229–SAMN15154256, 18S ribosomal RNA (rRNA) amplicon BioSample accession nos. SAMN18528738–SAMN18528777). Contigs, assembled ORFs, 18S rRNA abundance, and MCL cluster abundance and differential expression analysis results are available at:
http://datadryad.org/stash/dataset/doi:10.5061/dryad.cjsxksn3j.

3.8 Acknowledgments

We are grateful to Antarctic Support Contractors, especially Ned Corkran, for facilitating fieldwork. We thank Jeff Hoffman, Zhi Zhu, and Quinn Roberts for assistance in the field, Hong Zheng for her work in the laboratory, and Pratap Venepally for assistance with bioinformatic analyses. This study was funded by NSF Antarctic Sciences Awards 1103503 (to E.M.B.), 0732822 and 1043671 (to A.E.A.), 1043748 (to D.A.H.), 1043635 (to D.A.B.); Gordon and Betty Moore Foundation Grant GBMF3828 (to A.E.A.); NSF Ocean Sciences Award NSF-OCE-1136477 and NSF-OCE-1756884 (to A.E.A.) and NSF-OCE-1638804 and NSF-OCE-1851222 (to D.A.H.); Nova Scotia Graduate Scholarship to L.J.J.; National Sciences and Engineering Research Council of Canada - Canada Graduate Scholarship and Transatlantic Ocean System Science and Technology scholarship to J.S.P.M.; NSERC Discovery Grant RGPIN-2015-05009 to E.M.B.; Simons Foundation Grant 504183 to E.M.B.; and Canada Research Chair support to E.M.B.

3.9 Conflict of Interest

None declared.

3.10 Supporting Information

3.10.1 Full Materials and Methods

Experimental Design - The planktonic microbial community was sampled at 3-m depth via diaphragm pump from the sea ice edge in McMurdo Sound, Antarctica on January 15, 2015 (165°24.7985'E, 77°37.1370'S) from 11:00 - 12:15 using trace metal clean techniques previously described (Bertrand et al., 2015). In-situ water temperature at the time of sampling was -1 °C. The community was protected from light upon sampling using dark trash bags, stored at 0 °C until 17:00 and then split into trace-metal cleaned polycarbonate bottles (two 1.1L and one 2.7L per treatment), with and without iron supplementation at three different temperatures. Bottles were kept at -0.5 ± 0.2 °C, 3 ± 0.5 °C or 6 ± 0.5 °C at constant 65-85 uE m^{-2} sec^{-1} irradiance in indoor incubators for a total of 7 days. For iron supplmentation, 2 nM iron was added as $Fe(NO_3)_3$ from an ultrapure analytical standard solution, 1001 mg L^{-1} in 2% nitric acid. This was diluted to a working stock in pH 2.5 milli Q water with hydrochloric acid, resulting in a negligible nitrate addition to iron amended bottles.

Metatranscriptome Sampling and Assembly - Four separate metatranscriptome samples were taken from the initial community, one at the sea ice edge (IE; approximately 2L) and triplicates in the laboratory during bottle incubation setup (T0, approximately 2L). Subsamples of single replicates from each experimental treatment were harvested on January 16th (T1) and subsamples of each replicate (n = 3 for each experimental treatment) were taken again on January 20th (T5). Each was harvested onto 0.2 μm Sterivex^{TM} filters. RNA was extracted and sequenced via paired end Illumina HiSeq. Total RNA was extracted using Trizol reagent (Thermo Fisher Scientific). Ribosomal RNA was removed with Ribo-Zero Magnetic kits (Illumina). A mixed Removal Solution was prepared from plant, bacterial, and human/mouse/rat Removal Solution at a ratio of 2:1:1. The resulting rRNA subtracted RNA was purified and subjected to amplification and cDNA synthesis, using the Ovation RNA-Seq System V2 (TECAN). One microgram of the resulting high-quality cDNA pool was fragmented to a mean length of 200 bp, and libraries were prepared using Truseq kit (Illumina) from the -repair step in the manufacturers protocol and subjected to paired-end sequencing via Illumina HiSeq.

Illumina paired reads were filtered to eliminate primer sequences and quality trimmed to Phred Q33, and rRNA identified and removed using riboPicker (Schmieder et al., 2012) (average 13.5% rRNA). Transcript contigs were assembled de novo, in a combined assembly, using CLC Assembly Cell (http://www.clcbio.com) and ORFs predicted using FragGeneScan (Rho et al., 2010). Reads were mapped to ORFs using CLC (73% read mapping), and ORFs were annotated for putative function using hidden Markov models and BLAST-p against PhyloDB (Bertrand et al., 2015). ORFs were filtered to eliminate those with low mapping coverage ($<$ 50 reads total over all samples), proteins with no BLAST hits, and no known domains (See Tables S3.7, S3.8, S3.9). The remaining set of ORFs were assigned to chloroplast, mitochondrial or nuclear origin based on the best BLAST-p hit above e-value 1e-3 to an organism with known organellular peptide sequences (nuclear by default), and used for further comparative analysis.

Taxonomic groups of interest were defined (Fig. S3.7) and each ORF was assigned to a group based on best LPI taxonomy (Bertrand et al., 2015; Podell and Gaasterland, 2007). A total of 64,487 ORFs were assigned to *Fragilariopsis* and 28,650 ORFs were assigned to *Pseudo-nitzschia*. Reads per kilobase mapped (RPKM) expression values for each ORF were calculated and taxon normalized using a normalization factor representing the summed taxonomic group contribution to total nuclear-assigned reads per sample. For example, the taxon-normalized expression of an ORF assigned to *Fragilariopsis* in a particular library is given as reads mapped to that ORF/ORF length/total *Fragilariopsis* nuclear assigned reads in that library. ORFs were clustered into orthologs and protein families using MCL (Enright, 2002). MCL clustering was run in label mode (parameter -abc), with the default inflation setting 2.0 (parameter -I), on ratios of best BLAST-p bitscore to self-hit bitscore using BLASTALL (e-value: 1e-3). Group normalized cluster (average/total) RPKM expression values were calculated by pooling the taxon-normalized expression values for each group within a cluster. These taxon-normalized RPKM values were used to examine gene and cluster abundance. Cluster annotations were aggregated by annotation type (Kegg, KO, KOG, KOG class, Pfam, TIGRfam, EC, GO) and a single annotation chosen to represent each cluster based on the lowest Fisher's exact test p-value (fisher.test in R) given the 2-way contingency table for each annotation coverage of each cluster.

***Pseudo-nitzschia* BLAST-p analyses -** A subset of TFG peptide sequences, assembled from meta-transcriptome sequences and annotated as most-likely from *Pseudo-nitzschia* (n= 27,420), as described above, were used in BLAST-p analysis against peptide databases from culture-based transcriptomes of several *Pseudo-nitzschia* species (Table S3.3). All the peptide matches that passed an E value threshold of 1E-05 were collected separately for each *Pseudo-nitzschia* species. Their distribution profiles in percent identity and the alignment length are summarized in Table S3.3.

18S rRNA Sequencing - 1-10 ng of total RNA was used to generate cDNA using the Life Technologies SuperScript III First Strand Synthesis system with random hexamer primers. The cDNA was diluted 10-fold and had final concentrations ranging from 10-50 ng/μl. Amplicon libraries targeting the V9 region of the 18S gene were generated as described here: https://www.protocols.io/view/amplicon-library-preparation-bmuck6sw. Briefly, cDNA was amplified via a one-step PCR using the TruFi DNA Polymerase PCR kit (Azura, Raynham, MA, USA). The 1389F (TTGTACACACCGCCC) and 1510R (CCTTCYGCAGGTTCACCTAC) primer set was used (Amaral-Zettler et al., 2009). Each reaction was performed with an initial denaturing step at 95 °C for 1 minute followed by 30 cycles of 95 °C for 15 seconds, 56 °C for 15 seconds, and 72 °C for 30 seconds. 2.5 μL of each PCR reaction was ran on a 1.8% agarose gel confirm amplification. PCR products were purified using Beckman Coulter AMPure XP beads following the standard 1x PCR clean-up protocol. PCR quantification was performed in duplicate using Invitrogen Quant-iT PicoGreen dsDNA Assay kit. Samples were then pooled in equal proportions followed by another 0.8x AMPure XP bead purification. The Pool was evaluated on an Agilent 2200 TapeStation and quantified with Qubit HS dsDNA. Sequencing was performed at the University of California, San Diego Sequencing Core on a single Illumina MiSeq lane (2 x 150bp) with a 15% PhiX spike-in.

Amplicons were analyzed with QIIME2 v2019.4 (Bolyen et al., 2019). Briefly, demultiplexed paired-end reads were trimmed to remove adapter and primer sequences with cutadapt (Martin, 2011). Trimmed reads were then denoised with DADA2 to produce amplicon sequence variants (ASVs) (Callahan et al., 2016). Each pool was denoised with DADA2 individually to account for different error profiles in each run. Taxonomic

annotation of ASVs was conducted with the q2-feature-classifier classify-sklearn naïve-bayes classifier (Bokulich et al., 2018; Pedregosa et al., 2011) PR2 v4.12.0 (Guillou et al., 2012) for 18S amplicons.

ISIP1 taxonomic re-assignment - *Pseudo-nitzschia* and *Fragilariopsis* ISIP1 genes could not be differentiated using BLAST-p. Instead, nucleotide ISIP1 sequences were compared to a reference database of ISIP1 genes from *F. cylindrus*, *F. kergulensis*, *P. granii*, *P. heimii*, *P. multistriata* and *P. fraudulenta* using BLAST-n. ISIP1 sequences were assigned to *Fragilariopsis* or *Pseudo-nitzschia* based on lowest e-value score. These sequences were then manually placed in clusters and their abundance was normalized to each taxon as previously described.

Query for Domoic Acid Biosynthesis (DAB) Genes - BioEdit v7.2 was used to conduct a local BLAST-p search for DAB genes in our data using Blosum62 similarity matrix. Amino acid query sequences from *Pseudo-nitzschia multiseries* DAB-A (GenBank: AYD91073.1), DAB-B (GenBank: AYD91072.1), DAB-C (GenBank: AYD91075.1) and DAB-D (GenBank: AYD91074.1) (Brunson et al., 2018) were used.

LHC assignments - All *Fragilariopsis* and *Pseudo-nitzschia* ORFs annotated as 'chlorophyll binding' or 'light harvesting proteins' were selected for further inspection. For *Fragilariopsis* LHCs, a BLAST-p was performed against *F. cylindrus* CCMP1102 and annotations were retrieved for the top BLAST hit for each amino acid sequence. *Pseudo-nitzschia* LHC sequences were identified by comparison with those collected during the annotation of the *Pseudo-nitzschia multiseries* CLN-47 genome. The protein sequences of both diatoms were assigned to the Lhcf, Lhcr, Lhcx or Lhcz groups following a previous diatom LHC classification based on maximum-likelihood phylogenetic trees and published as Supp. Information 11 and Supp. Fig. 20 of Mock et al. (2017) and in Hippmann et al. (2017). The dominant Lhcf clade was further subdivided into Lhcf_I, Lhcf_II (diatom-specific), and Lhcf_III groups. PID numbers and the clusters to which they were assigned (see above) can be found in Table S3.6.

Plastocyanin Tree - Previously identified plastocyanin sequences were retrieved from

MMETSP (*Fragilariopsis kerguelensis* _0735, *Pseudo-nitzschia heimii* _1423, Coscinodiscus wailesii_1066), JGI (*Fragilariopsis cylindrus* _272258), NCBI (*Thalassiosira oceanica* _EJK71623.1), Moreno et al. (2018) (P*seudo-nitzschia subcurvata*), and Cohen et al. (2018a) (*Pseudo-nitzschia granii*), and aligned with plastocyanin sequences from *Pseudo-nitzschia* and *Fragilariopsis* in our dataset using Clustal Omega in SeaView v5.0 (Fig. S3.13). A maximum-likelihood phylogeny was then estimated using PhyML with LG model and 100 bootstrap iterations in SeaView v5.0, and the resulting tree was edited using FigTree v1.4.4.

Nutrient Measurements - Samples from initial (T0) and subsequent time points (T1, T3, T5, and T7) were collected, passed through a GF/F filter (Whatman; 0.7 μm nominal pore size; combusted at 450 °C for 2 hours), and filtrate was stored frozen (-40 °C) until further analysis. A Lachat QuickChem 8500 autoanalyzer was used to measure duplicate concentrations of dissolved nitrate, phosphate and silicate (detection limit 0.03 μmol N L^{-1}, 0.03 μmol P L^{-1} and 0.05 μmol Si L^{-1}; (Parsons et al., 1984)). Samples for ammonium, collected on T0 and T7, were measured in triplicate on a Shimadzu UV-1601 spectrophotometer using the manual phenol-hypochlorite method (detection limit 0.05 μmol N L^{-1}; (Koroleff, 1983).

Uptake Measurements - Nitrate and bicarbonate uptakes were assessed using the initial community (T0) collected from the ice edge and during T1, T3, and T7 of the experiment. Uptake rates were measured using ^{15}N and ^{13}C stable isotope tracer techniques, and substrates used included ^{15}N-labeled potassium nitrate ($K_{15}NO_3$-; 98%) and ^{13}C-labeled sodium bicarbonate ($NaH_{13}CO_3$-; 99%; both substrates came from Cambridge Isotope Laboratories, Andover, MA). Uptake experiments at T0 were done in triplicate using 1 L polyethylene terephthalate glycol-modified bottles. At T1, T3, and T7 a single replicate of each treatment was subsampled, and uptake experiments were done in duplicate in 230 mL polycarbonate conical bottles (all bottles were acid washed with 10% hydrochloric acid and thoroughly rinsed with ultrapure water). After tracer level additions (less than 10% of background concentrations) of ^{15}N and ^{13}C-labled substrates were made, bottles were returned to their respective incubators for approximately 6 hours. Incubations were terminated by filtering microbial communities ($>$ 0.7 μm) onto combusted (450 °C for 4

hours) Whatman GF/F filters. During T0 incubations, two microbial size fractions (0.7 – 5.0 μm collected on GF/F filters and $>$ 5.0 μm collected on Sterlitech silver membrane filters) were added together to represent the $>$ 0.7 μm microbial community. Filters were kept fozen (-40 °C) inside 1 mL cryo vials until particulate nitrogen and carbon concentrations and isotopic enrichment of ^{15}N and ^{13}C were measured on a Europa 20/20 isotope ratio mass spectrometer. Absolute uptake rates for ^{15}N-labeled nitrate and ^{13}C-labeled bicarbonate were calculated according to (Dugdale and Wilkerson, 1986; Hama et al., 1983) respectively. Nitrate uptake rates were not corrected for isotope dilution because concentrations of nitrate were greater than 5.5 μmol N L^{-1} at all time points, and isotope dilution is generally negligible when concentrations are high (Baer et al., 2017).

Cell Counts - Phytoplankton cell count samples from the initial (T0) and final days (T7) of the experiment were preserved with 1% glutaraldehyde, stored refrigerated in the dark and later enumerated in the lab on a Sedgwick Rafter counting chamber using an inverted compound light microscope (Accu-Scope 3032), as in (Tatters et al., 2018). All plankton taxa were identified to the lowest taxonomic level possible according to (Tomas, 1997; Scott and Marchant, 2005), with special attention to the diatom genera *Fragilariopsis* and *Pseudo-nitzschia*.

Statistical Analysis - We analyzed differential gene expression at T5 within observed taxa to determine which genes are responsive to Fe and temperature treatments in each group. First, we normalized reads mapped to each ORF by the abundance of nuclear reads assigned to that taxonomic group in total, which controls for changes in community composition across treatments. We then used a generalized linear model with one categorical explanatory variable, with each category representing a unique experimental treatment. To examine the effect of Fe, temperature, and their interaction on gene expression, we specified model contrasts. For Fe, we tested the difference between the sum of coefficient estimates for all Fe treatments, minus the sum of coefficient estimates for all -Fe treatments. We followed a similar approach for temperature, where we tested the difference between the sum of coefficient estimates for one temperature treatment versus another temperature treatment. For both approaches, we divided these differences by the number of treatments in the sum (i.e. 3 for Fe test and 2 for each temperature test). To test for statistical

significance, we used empirical Bayes quasi-likelihood F-tests (glmQLFTest in edgeR). To examine the interaction between Fe and temperature, we set up a contrast to compare the difference between +/-Fe treatments at constant temperature, and then compared this difference to a distinct temperature treatment. The test for a significant interactive effect is based on the difference of these differences – i.e. is the expression of a gene to Fe altered due to warming? Throughout, we used a p-value cut off of 0.05 for statistical significance.

To examine the effects of iron on gene differential expression and fold-change magnitude, -Fe treatments for all temperatures at T5 (-Fe -0.5 °C, -Fe 3 °C, -Fe 6 °C) were compared to +Fe treatments for all temperatures at T5 (+Fe -0.5 °C, +Fe 3 °C, +Fe 6 °C). For temperature effect, -0.5 °C was compared to 3 °C at all iron conditions at T5 (+Fe and -Fe at -0.5 °C vs +Fe and -Fe at 3 °C) and -0.5 °C was compared to 6 °C at all iron conditions at T5 (+Fe and -Fe at -0.5 °C vs +Fe and -Fe at 6 °C). For a gene to be considered upregulated with temperature, it had to be upregulated in both -0.5 °C vs 3 °C and -0.5 °C vs 6 °C (same rule applied for down regulation). If a gene is upregulated in one temperature comparison and downregulated in the other, it was not considered differentially expressed. Fold-change for temperature effect was calculated from -0.5 °C (+Fe and -Fe) vs 6 °C (+Fe and -Fe).

K.O. term enrichment analysis was performed on significantly upregulated (enriched) and downregulated (depleted) ORFs separately using KEGG enrichment functions in the GOstats R package (Falcon and Gentleman, 2007). A hypergeometric distribution test was used to test for significant enrichment and depletion at $p < 0.05$. K.O. terms associated with less than 10 ORFs were excluded from the results.

3.10.2 Supplemental Results and Discussion

Cobalamin Metabolism - Exogenous vitamin B_{12} (cobalamin) acts as a cofactor in the cobalamin-requiring methionine synthase enzyme (MetH) found in all diatoms to synthesize the essential amino acid methionine and facilitate one-carbon metabolism (Bertrand et al., 2012). Under low cobalamin availability, however, certain diatoms including *Fragilariopsis* but not *Pseudo-nitzschia*, are capable of synthesizing methionine from homocysteine using a less efficient cobalamin-independent methionine synthase (MetE) (Ellis et al., 2017; Bertrand et al., 2012). Diatoms also upregulate CBA1, a cobalamin acquisition related protein, under cobalamin deprivation (Ellis et al., 2017; Bertrand et al., 2012). Following the initial 24-hour incubation period, CBA1 and MetH were upregulated in *Pseudo-nitzschia* after warming at 6 °C (Fig. S3.12), but were not significantly influenced by iron or temperature following 5-day incubations (Fig. 3.3, S3.12). In contrast, MetE and CBA1 transcripts were significantly upregulated in *Fragilariopsis* following iron additions after 5-day incubations (Fig. 3.3, S3.12), suggesting rearranged metabolism to cope with cobalamin deprivation that likely emerged in response to iron addition (Bertrand et al., 2015).

Rapid cobalamin uptake by *Pseudo-nitzschia*, facilitated by upregulation of CBA1 after 24 hours, may give it a competitive advantage when cobalamin is available. However, the ability of *Pseudo-nitzschia* to maintain vigorous growth without significantly elevating CBA1 expression after 5 days is notable, and suggests that these two diatoms may employ different strategies to cope with low cobalamin availability. *Fragilariopsis* appears to reduce cobalamin demand through the use of MetE while increasing investment in acquisition with CBA1. In contrast, *Pseudo-nitzschia* may 1) have a MetH enzyme that is more efficient at elevated temperatures compared to *Fragilariopsis*, 2) employ salvage and repair of degraded cobalamin complexes (Cohen et al., 2018a) or 3) rely on bacteria in close physical association for cobalamin supply. Our data show that the overall expression of genes encoding cobalamin salvage and remodeling proteins were not influenced by iron status or temperature in *Pseudo-nitzschia* (Fig. S3.12), despite previous evidence of their upregulation with iron addition in North Pacific diatoms including P. granii (Cohen et al., 2017, 2018a). Further work comparing cobalamin uptake and methionine synthase kinetics between *Pseudo-nitzschia* and *Fragilariopsis*, and examining their relationships with cobalamin producing and consuming bacteria, could provide further insight into how

these taxa cope with episodic decreases in cobalamin availability.

3.10.3 Supplemental Figures

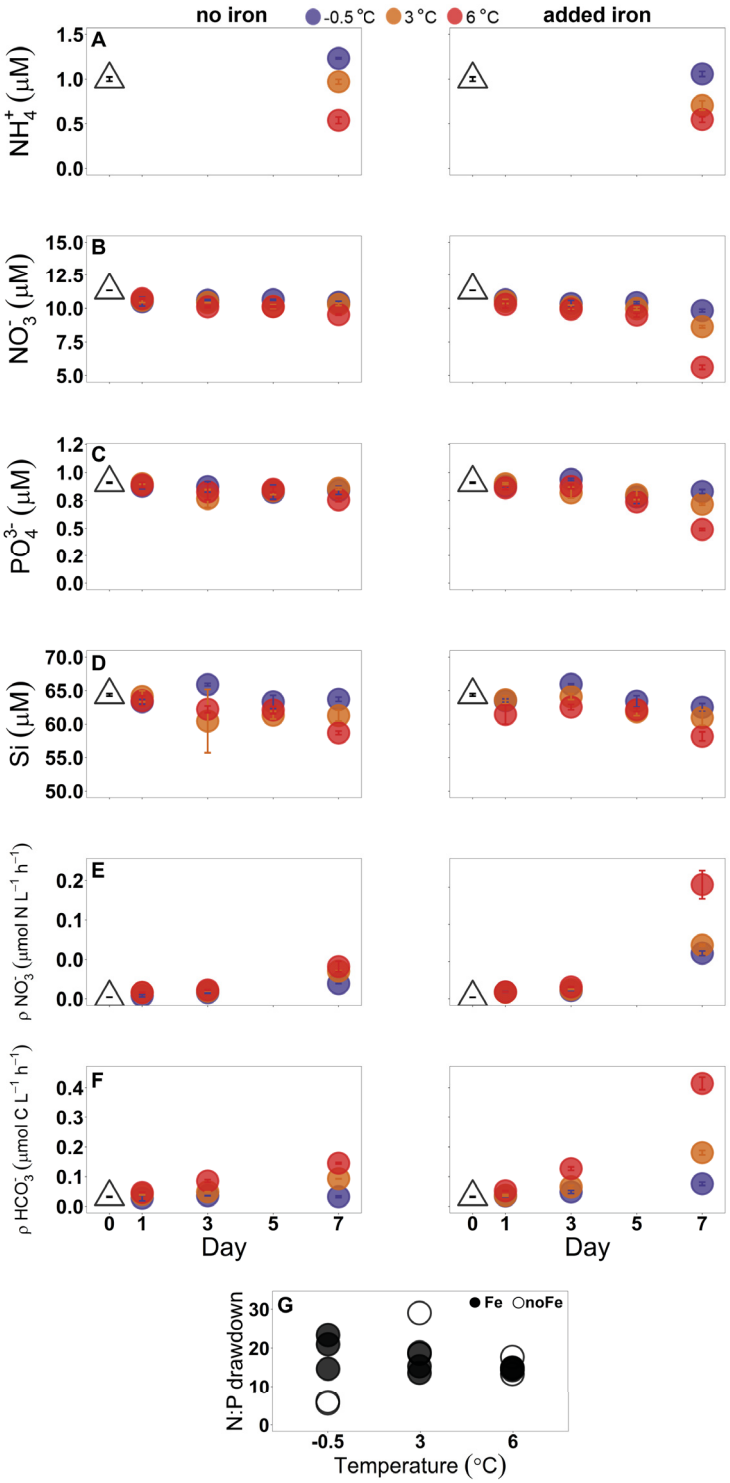

Figure 3.6

Figure 3.6: A-D) Dissolved nutrient concentrations prior to incubations (day 0), and after 1, 3, 5 and 7 days of incubation with and without added iron at -0.5, 3, and 6 °C. Each point represents a mean value, where n = 2 on day 1, and n = 3 on days 0, 3, 5, 7. In A-J, error bars represent ± 1 SD, and fall within the bounds of the symbol when not visible. E,F) Nitrate and bicarbonate uptake rates prior to incubations (day 0), and after 1, 3, and 7 days of incubation with and without added iron at -0.5, 3, and 6 °C. Each point represents a mean value, where n = 2 on days 1, 3, 7 and n = 3 on day 0. G) Dissolved nitrogen (nitrate + ammonium) : phosphate drawdown ratio at T7. Draw down is calculated as the difference in concentration between T7 and T0.

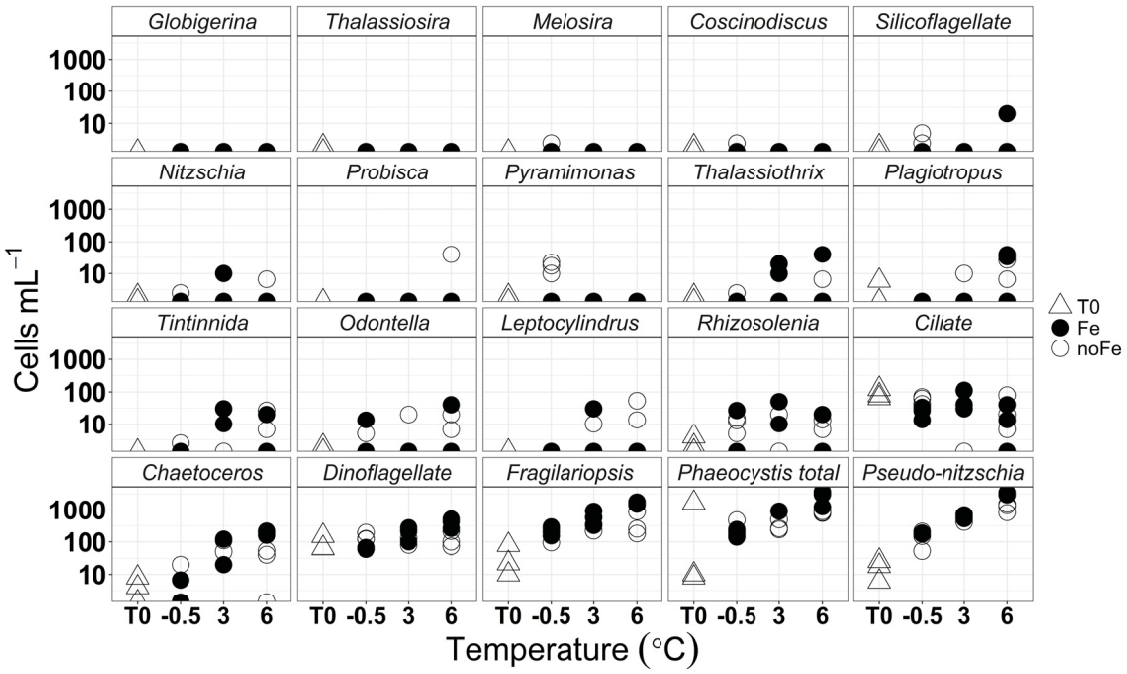

Figure 3.7: Triplicate cell count measurements of initial (T0) samples and after 7-day incubations with and without iron addition at -0.5, 3 and 6 °C. Cells from the various taxonomic groups were counted and identified using light microscopy. The large variation in *Phaeocystis* cell counts at T0 could have resulted from difficulties in enumeration of colonial and single cell forms in the samples, and variability in colony abundance and size in the relatively small-volume samples used for microscopic cell counts.

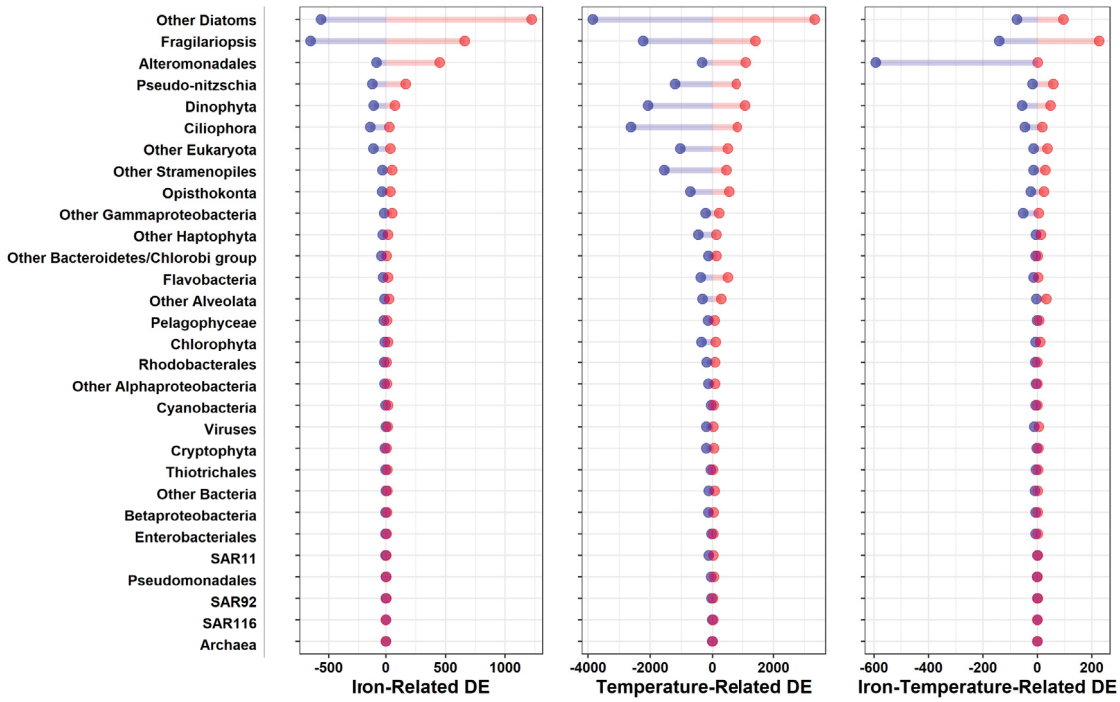

Figure 3.8: Number of significantly differentially expressed open reading frames (ORFs) belonging to the 30 taxonomic groups identified in the metatranscriptome dataset. Red = upregulation, blue = downregulation. Differential taxon-normalized expression was calculated using the quasi likelihood test (glmQLFTest) in EdgeR, and p-value cut-off of 0.05 was used for statistical significance. Iron-related DE represents differential expression patterns observed with and without iron addition at T5, temperature-related DE represents differential expression patterns observed due to warming at T5, Iron-Temperature-related DE represents interactive iron-temperature effect on gene expression (Methods).

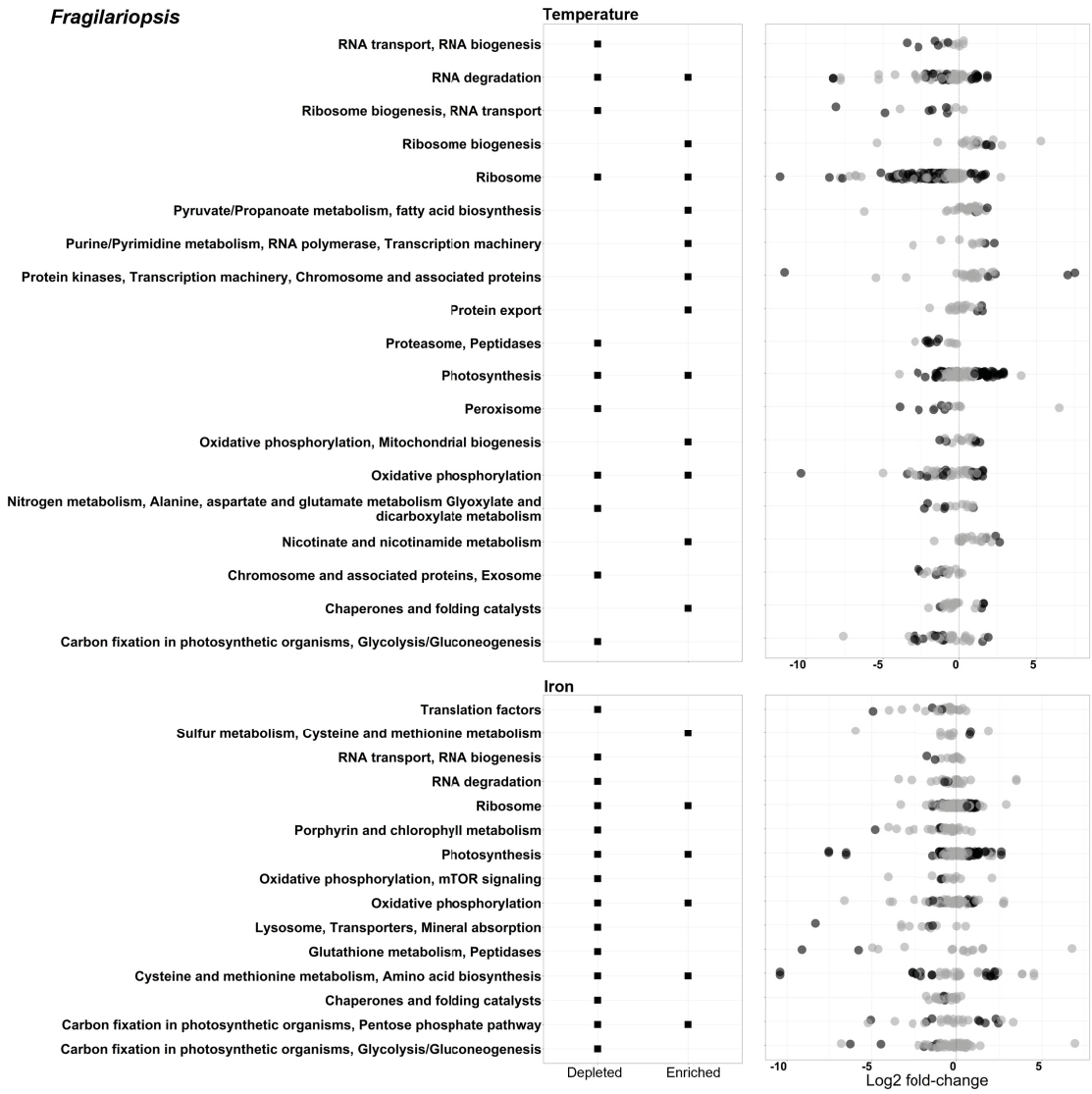

Figure 3.9: KEGG Orthology (K.O.) term enrichment analysis using all *Fragilariopsis* ORFs that were annotated with a K.O. number. Black squares correspond to 'C' level annotations that were significantly ($p < 0.05$) upregulated (Enriched) and/or downregulated (Depleted) at T5 by temperature increase or iron addition. Circles correspond to the individual ORFs used in the analysis for each annotation. Black circles represent statistically significant ($p < 0.05$) up or down regulated ORFs (positive and negative Log_2 fold-change values, respectively). Temperature fold change was calculated using -0.5 °C vs 6 °C treatments. Iron fold-change was calculated using -Fe vs +Fe treatments at all temperatures (Methods).

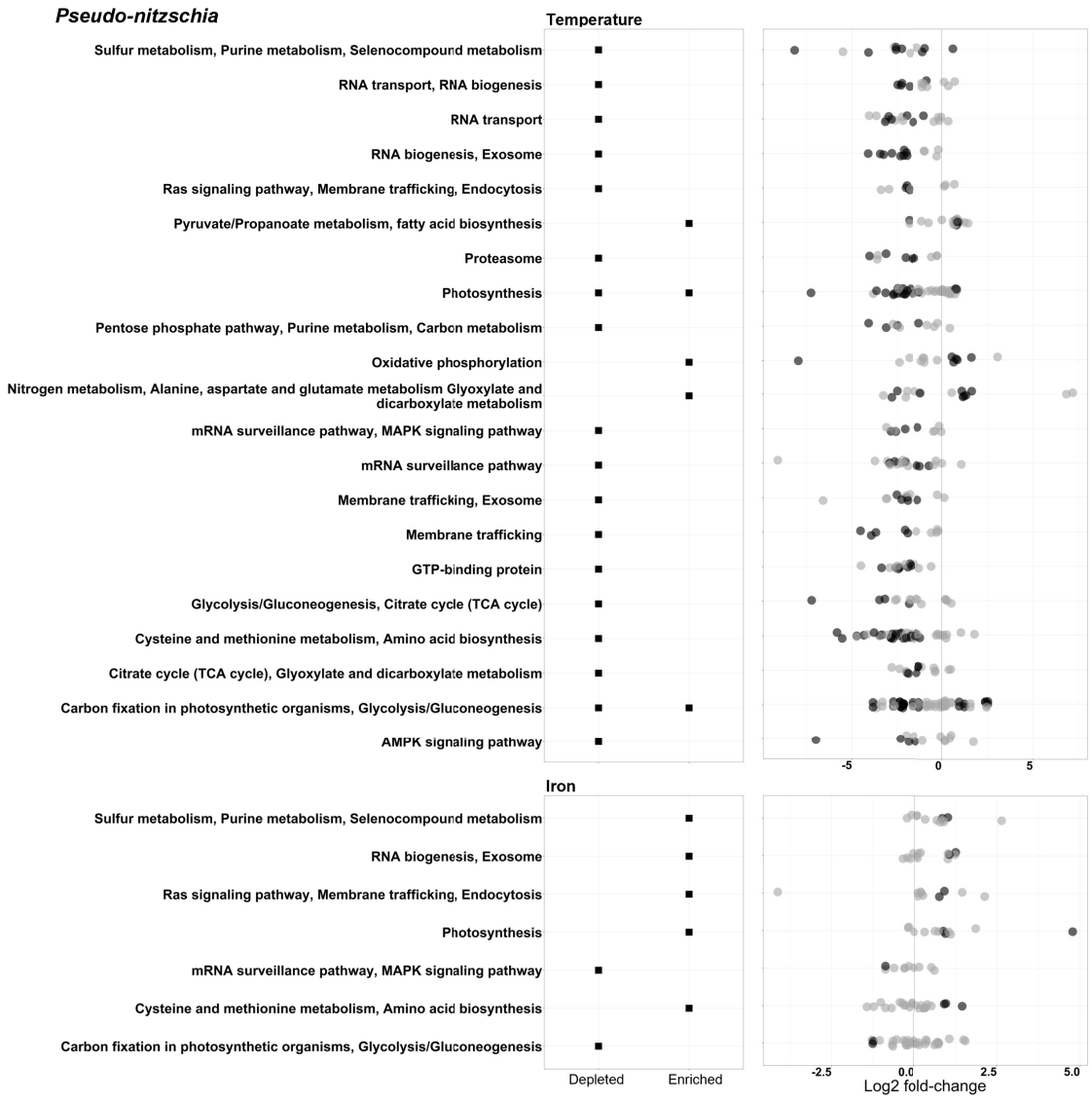

Figure 3.10: KEGG Orthology (K.O.) term enrichment analysis using all *Pseudo-nitzschia* ORFs that were annotated with a K.O. number. Black squares correspond to 'C' level annotations that were significantly ($p < 0.05$) upregulated (Enriched) and/or downregulated (Depleted) at T5 by temperature increase or iron addition. Circles correspond to the individual ORFs used in the analysis for each annotation. Black circles represent statistically significant ($p < 0.05$) up or down regulated ORFs (positive and negative Log_2 fold-change values, respectively). Temperature fold-change was calculated using -0.5 °C vs 6 °C treatments. Iron fold-change was calculated using -Fe vs +Fe treatments at all temperatures (Methods).

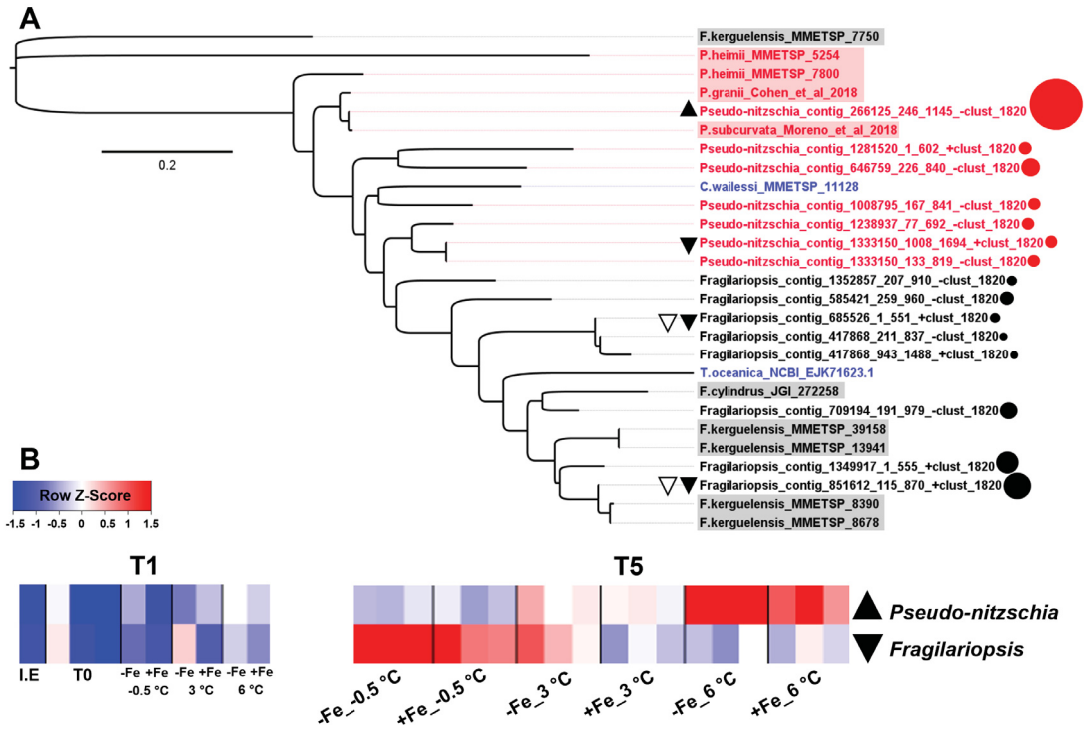

Figure 3.11: Phylogenetic tree of the plastocyanin sequences (ORFs) comprising the plastocyanin MCL cluster from both *Pseudo-nitzschia* (red) and *Fragilariopsis* (black). Non-highlighted branch tips represent ORFs in our dataset, with corresponding point size representing mean taxon-normalized ORF expression. Highlighted branch tip labels represent previously identified plastocyanin sequences retrieved from the MMETSP dataset (*Fragilariopsis kerguelensis* _0735, *Pseudo-nitzschia heimii*_1423, *Coscinodiscus wailesii* _1066), JGI (*Fragilariopsis cylindrus* _272258), NCBI (*Thalassiosira oceanica* _EJK71623.1), Cohen et al. 2018 (*Pseudo-nitzschia granii*), and Moreno et al. 2018 (*Pseudo-nitzschia subcurvata*). B) Heatmaps of MCL clusters representing and plastocyanin (cluster_1820) in *Pseudo-nitzschia* and *Fragilariopsis* measured after 24 hours (T1) and 5 days (T5) of incubation under the various iron and temperature treatments. I.E represents ice edge samples, T0 represents in-situ samples before any incubations. Each block is one biological replicate measurement. Black-filled up or down pointing triangles represent transcripts that were significantly (glmQLFTest-EdgeR $p < 0.05$) up or down regulated due to warming at T5.

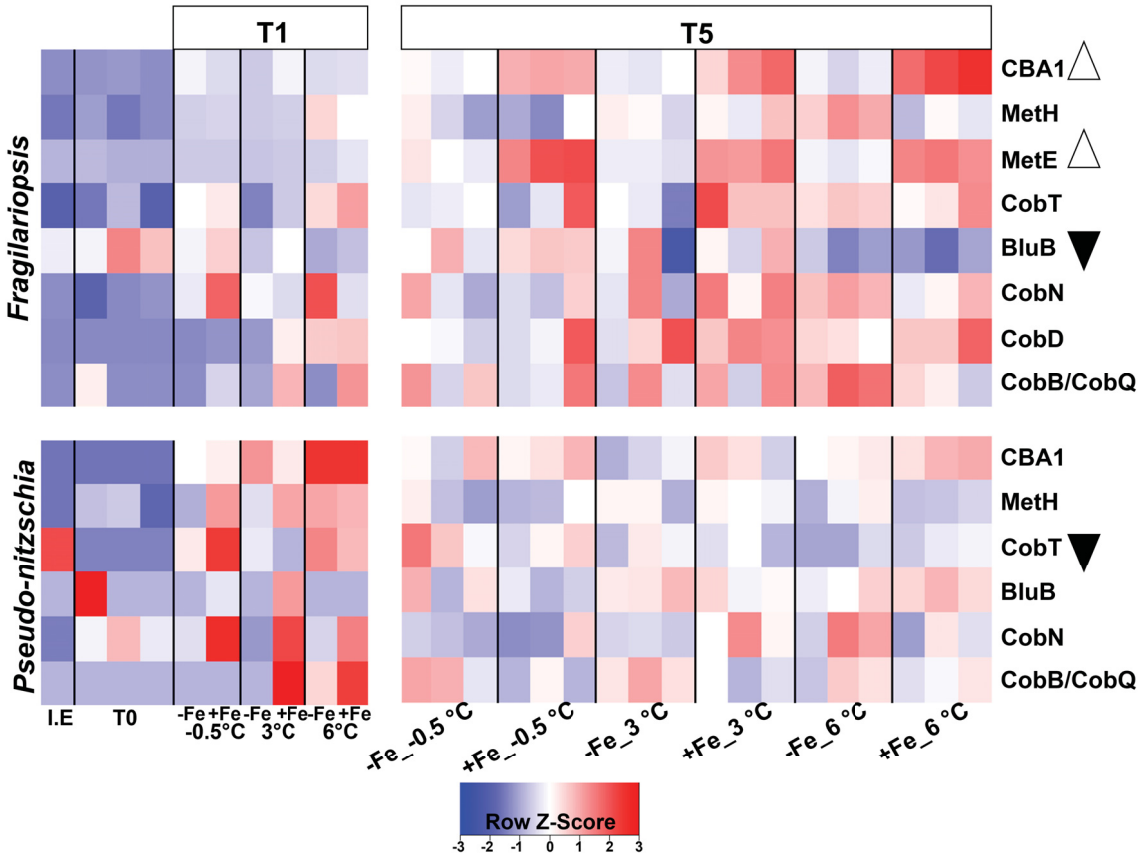

Figure 3.12: Heatmaps of MCL clusters involved in B_{12} metabolism in *Fragilariopsis* and *Pseudo-nitzschia* measured after 24 hours or 5 days of incubation under various iron and temperature treatments. I.E represents ice edge samples, T0 represents in-situ samples processed in the laboratory before any incubations and each block is one biological replicate measurement. CBA1: cobalamin acquisition protein 1; MetH: cobalamin-requiring methionine synthase; MetE: cobalamin-independent methionine synthase; CobT, CobN: cobaltochelatase; BluB: gene involved in DMB production; CobB/CobQ: cobyrinic acid a,c-diamide synthase/ adenosylcobyric acid synthase. Open triangles represent clusters that were significantly (glmQLFTest-EdgeR $p < 0.05$) up regulated due to iron addition at T5. Black-filled triangles represent clusters that were significantly (glmQLFTest-EdgeR $p < 0.05$) down regulated due to warming at T5.

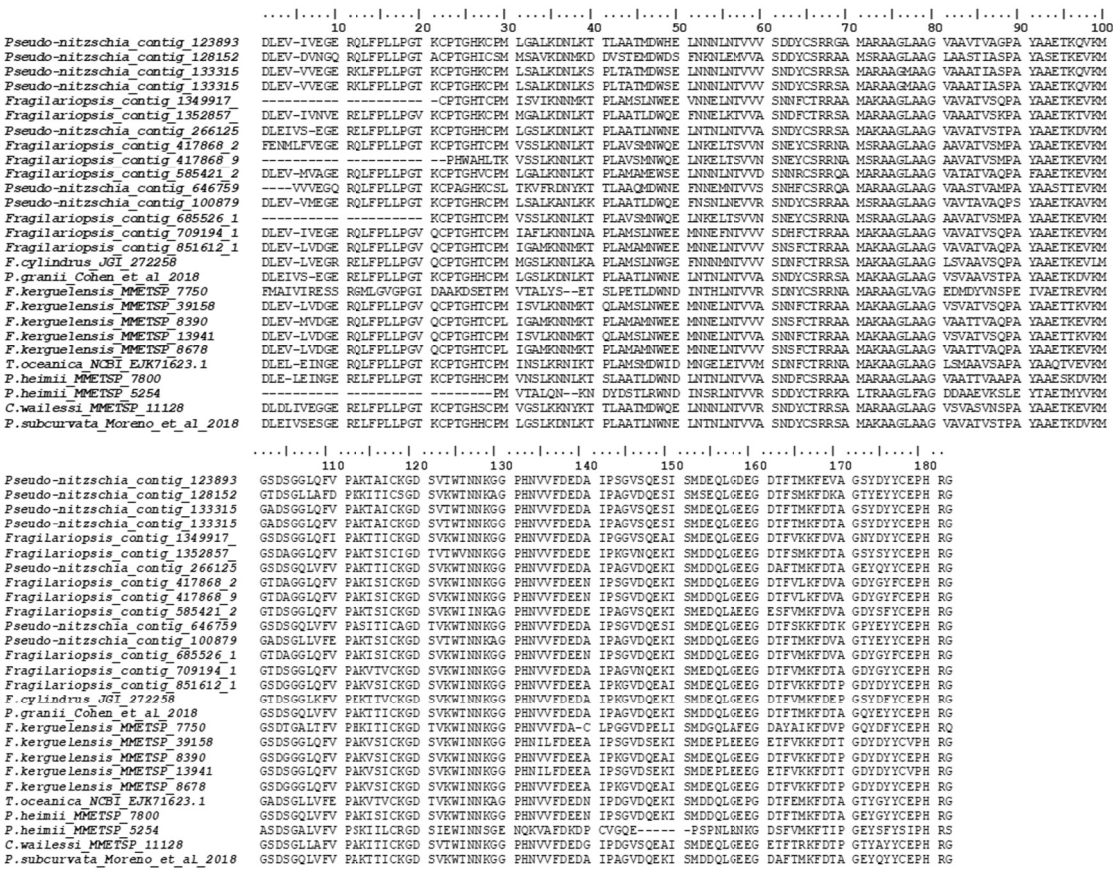

Figure 3.13: Alignment of *Pseudo-nitzschia* and *Fragilariopsis* plastocyanin sequences from our metatranscriptome data and previously identified plastocyanin sequences retrieved from the MMETSP dataset (*Fragilariopsis kerguelensis* _0735, *Pseudo-nitzschia heimii*_1423, *Coscinodiscus wailesii* _1066), JGI (*Fragilariopsis cylindrus* _272258), NCBI (*Thalassiosira oceanica* _EJK71623.1), Cohen et al. 2018 (*Pseudo-nitzschia granii*), and Moreno et al. 2018 (*Pseudo-nitzschia subcurvata*). The alignment was conducted using Clustal Omega in SeaView v5.0. and was used to construct the maximum-likelihood phylogenetic tree for plastocyanin in Figure S3.11.

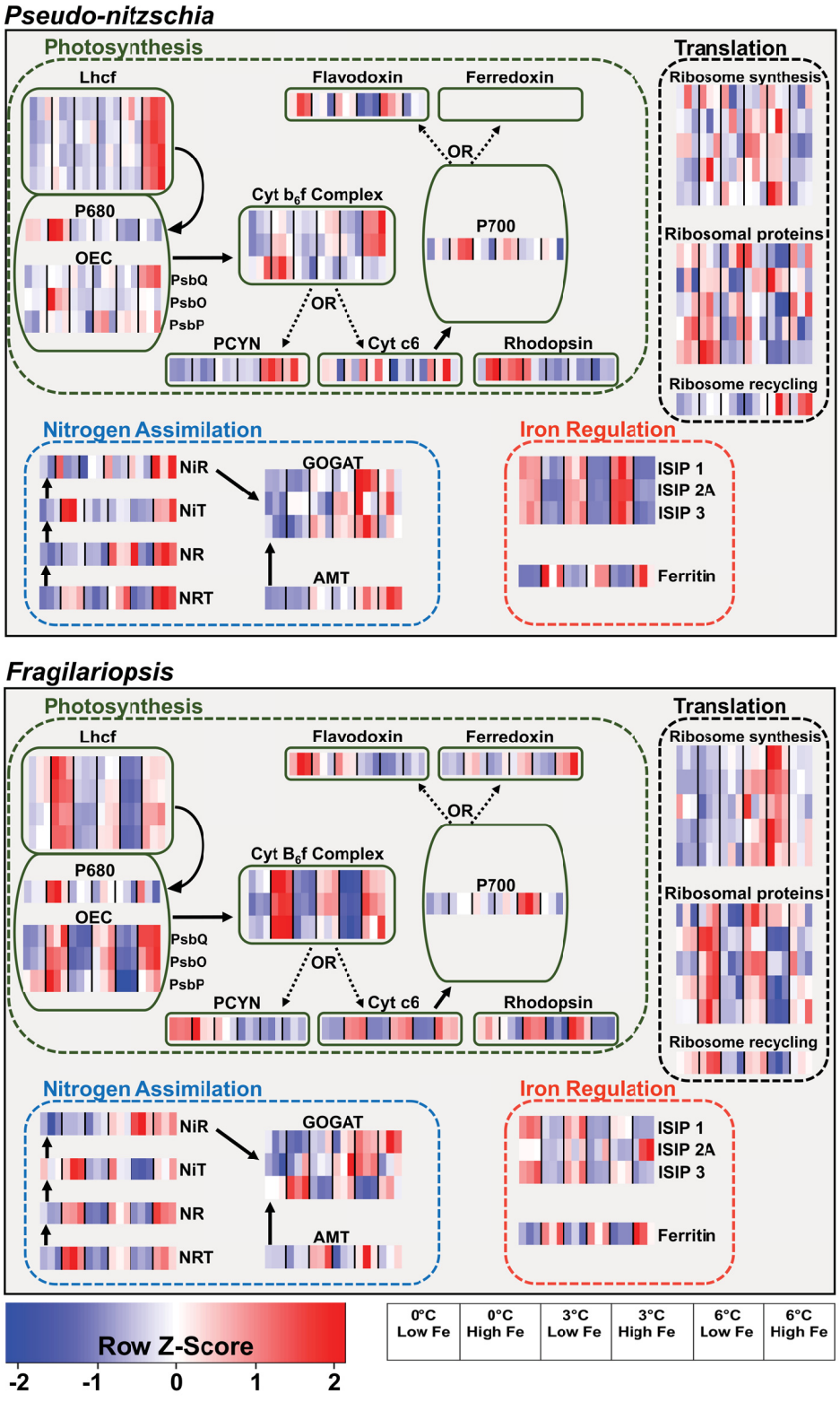
Pseudo-nitzschia
Photosynthesis
Translation
Lhcf
Flavodoxin
Ferredoxin
OR
Cyt b6f Complex
P680
P700
OEC
PsbQ
PsbO
PsbP
OR
PCYN
Cyt c6
Rhodopsin
Ribosome synthesis
Ribosomal proteins
Ribosome recycling
Nitrogen Assimilation
Iron Regulation
NiR
NiT
NR
NRT
GOGAT
AMT
ISIP 1
ISIP 2A
ISIP 3
Ferritin
Fragilariopsis
Photosynthesis
Translation
Lhcf
Flavodoxin
Ferredoxin
OR
Cyt B6f Complex
P680
P700
OEC
PsbQ
PsbO
PsbP
OR
PCYN
Cyt c6
Rhodopsin
Ribosome synthesis
Ribosomal proteins
Ribosome recycling
Nitrogen Assimilation
Iron Regulation
NiR
NiT
NR
NRT
GOGAT
AMT
ISIP 1
ISIP 2A
ISIP 3
Ferritin
Row Z-Score
-2
-1
0
1
2
0°C Low Fe
0°C High Fe
3°C Low Fe
3°C High Fe
6°C Low Fe
6°C High Fe

Figure 3.14

Figure 3.14: Schematic representations of *Pseudo-nitzschia* and *Fragilariopsis* cells showing cellular processes, with each process comprised of several protein clusters (MCL clusters). Lhcf = light harvesting complexes-f, OEC = oxygen evolving complex, Cyt b_6f complex = cytochrome b_6f complex, PCYN = plastocyanin, Cyt c_6 = cytochrome c_6, NRT = nitrate transporter, NR = nitrate reductase, NiT = nitrite transporter, NiR = nitrite reductase, AMT = ammonium transporter, GOGAT = glutamine oxoglutarate aminotransferase cycle, ISIP = iron starvation induced protein. Each row in a heatmap represents one Markov cluster (MCL), each column represents a temperature and iron treatment at T5 with each block representing one biological replicate. Heatmaps were constructed using taxon-normalized RPKM values. Empty heatmap placeholders represent clusters found in *Fragilariopsis* but not *Pseudo-nitzschia*. Arrows represent energy/electron flow in photosynthetic light reactions, and steps involved in nitrogen assimilation using nitrate or ammonium.

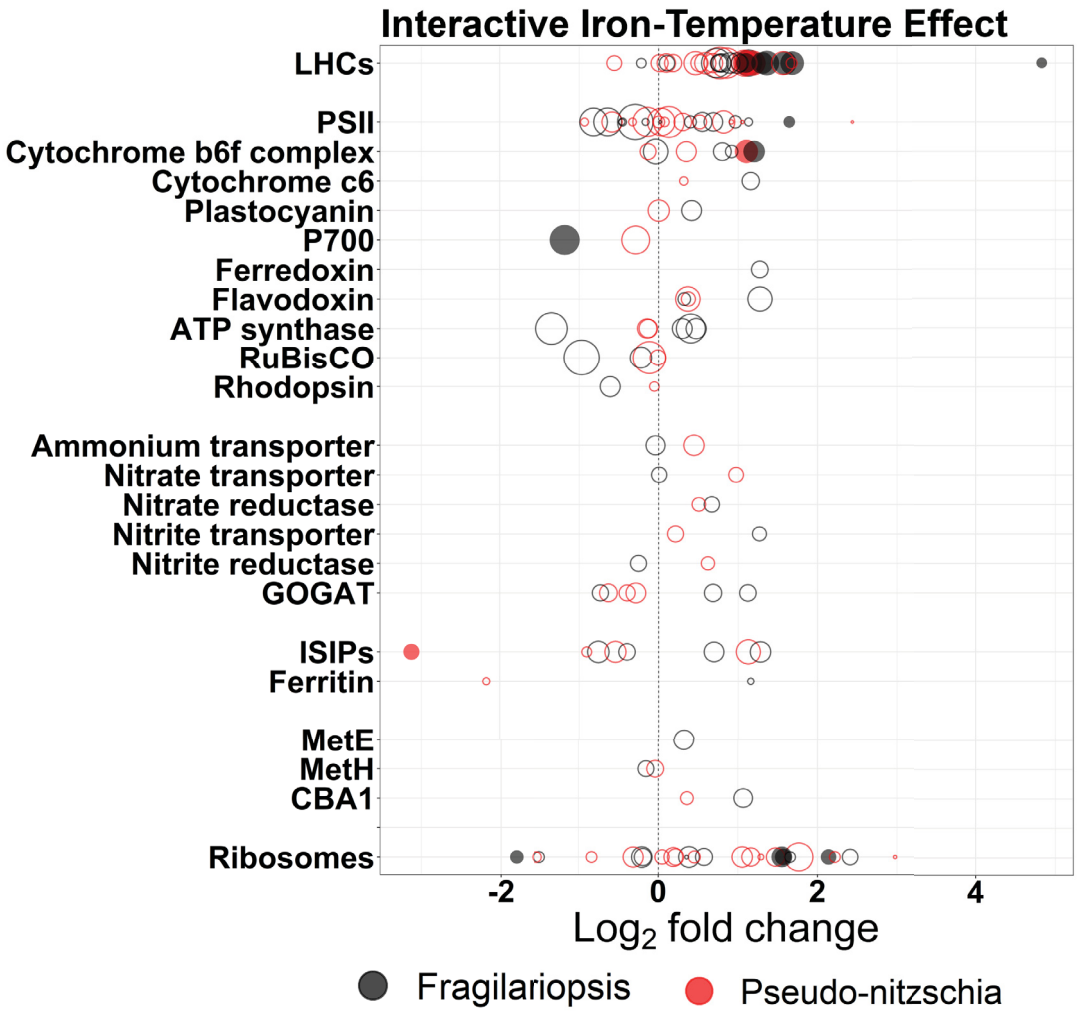

Figure 3.15: Interactive iron-temperature effect on differential expression (DE) of various clusters. Differential expression was calculated using the quasi-likelihood test (glmQLFTest) in EdgeR and fold-change was calculated for iron-effect at -0.5 °C vs iron-effect at 6 °C treatments at T5. Positive and negative Log_2 fold change values represent up and down regulation, respectively. Filled circles are clusters with statistically significant DE (adjusted p-value <0.05). Point size represent total normalized transcript abundance under all iron and temperature treatments.

3.10.4 Supplemental Tables

Table 3.1: Projected changes in sea surface temperature and iron availability in the Southern Ocean.

	Temperature	**Iron**
2100	+1.5 – 2 °C (1, 2)	+ 0.01 nM m^{-1}(upwelled water) day^{-1} (2)
	+0.5 – 1.5 °C (3)	-0.002 – -0.006 nM (3)
2300	+6 °C (2)	+ 0.02 nM m^{-1}(upwelled water) day^{-1} (2)

1 - (Boyd et al., 2015b), **2 -** (Moore et al., 2018), **3 -** (Boyd et al., 2008)

Table 3.2: Top ten BLAST-n search results against NCBI's nr/nt database for both *Pseudo-nitzschia* and *Fragilariopsis* 18S rRNA query sequences. UE = Uncultured Eukaryote.

18S rRNA sequence	Matched Taxa	Query Cover	E-Value	% Identity	Accession
Pseudo-nitzschia	*P. subcurvata*	100%	1e-59	100%	KX253952.1
	UE	100%	1e-59	100%	KJ758369.1
	UE	100%	1e-59	100%	KJ758245.1
	Pseudo-nitzschia sp.	100%	1e-59	100%	GU373970.1
	UE	100%	1e-59	100%	AY672814.1
	UE	100%	1e-58	99.23%	HM581774.1
	P. seriata	100%	1e-58	99.23%	GU373969.1
	P. cupsidata	100%	1e-51	96.15%	JN091719.1
	P. lineola	100%	1e-51	96.15%	JN091717.1
	P. turgidula	100%	1e-51	96.15%	FJ222752.1
Fragilariopsis	*F. cylindrus*	100%	1e-59	100%	LC189084.1
	UE	100%	1e-59	100%	KJ758397.1
	UE	100%	1e-59	100%	KJ758375.1
	UE	100%	1e-59	100%	KJ758350.1
	UE	100%	1e-59	100%	KJ758343.1
	UE	100%	1e-59	100%	KJ758332.1
	UE	100%	1e-59	100%	KJ758252.1
	UE	100%	1e-59	100%	KJ758212.1
	UE	100%	1e-59	100%	KJ758191.1
	UE	100%	1e-59	100%	KJ758103.1

Pseudo-nitzschia 18S rRNA nucleotide query sequence:

GTCGCACCTACCGATTGAATGGTCCGGTGAAGCCTCGGGATTGTGGCT GGTTTC-CTTTATTGGAATCTGCCACAGAACCTGTCTAAACCTTATCATTTA GAGGAAGGT-GAAGTCGTAACAAGGTTTCC

Fragilariopsis 18S rRNA nucleotide query sequence:

GTCGCACCTACCGATTGAATGGTCCGGTGAGGCCTC GGGATTGTGGTTAGTTTC-CTTTATTGGAAGTTAGTCCGA GAACTTGTCCAAACCTTATCATTTAGAGGAAG-GTGAAGTCGTAACAAGGTTTCC

Table 3.3: Summary statistics for BLAST-p analyses comparing *Pseudo-nitzschia* peptide sequences from this study and *Pseudo-nitzschia* peptides from various publicly available culture-based transcriptomes. Summary statistics include: number of sequences with better than E = 1E-5 (of the n= 27,420 peptide sequences queried), their match identities and their alignment lengths (1st Quartile, Median, Mean, and 3rd Quartile). Results from *Pseudo-nitzschia subcurvata* are highlighted in bold.

		Match Identities				**Alignment Length**			
	No. matches	***1st Qu.***	***Median***	***Mean***	***3rd Qu.***	***1st Qu.***	***Median***	***Mean***	***3rd Qu.***
Pseudo-nitzschia arenysensis	23588	56.25	69.58	68.1	81.44	123	195	197	270
Pseudo-nitzschia australis Strain 10249 10AB	21615	51.52	65.9	64.5	78.43	122	193	198	269
Pseudo-nitzschia delicatissima B596	*23087*	56.02	70	68	81.51	126	198	199	272
Pseudo-nitzschia delicatissima Strain UNC1205	20019	55.98	71.17	68.4	82.58	110	175	181	247
Pseudo-nitzschia fraudulenta Strain WWA7	20896	51.82	67.63	65.8	80.83	117	185	190	261
Pseudo-nitzschia granii	*12444*	55.28	85.71	75.3	94.82	69	98	110	138
Pseudo-nitzschia heimii Strain UNC1101	*22041*	53.76	68.28	66.4	80.49	122	193	197	270
Pseudo-nitzschia multiseries	*22510*	55.47	69.28	67.5	81.18	108	173	181	249
Pseudo-nitzschia pungens	*22333*	51.52	65.53	64.5	78.28	116	188	193	268
Pseudo-nitzschia pungens cf. cingulata	21727	50.41	64.67	63.8	77.83	121	193	197	271
Pseudo-nitzschia subcurvata (Moreno et al 2017)	***24647***	**93.47**	**98.44**	**90.4**	**99.57**	**119**	**179**	**188**	**255**

Table 3.4: BLAST-p search results for sequences encoding domoic acid biosynthesis proteins (DabA, B, C, D) retrieved from GenBank, against all ORFs from this study. No matches were found for DabA and DabB encoding genes and no significant eukaryotic matches were found for DabC encoding genes. Score and e-values were calculated using the Blosum62 similarity matrix. E-value 1e-30 was used as the cut-off for DabD results. These DabD results are further explored in Table S3.5.

Query Gene	Matched Sequence (ORF ID)	Score	E-value	Taxa	Hypothesized annotation
DAB-A AYD91073.1	-	-	-	-	-
DAB-B AYD91072.1	-	-	-	-	-
DAB-C AYD91075.1	contig_254441_113_1024_+	63	6e-010	Flavobacteria	2OG-Fe(II) oxygenase family
	contig_1174518_67_906_+	61	6e-010	Alteromonadales	2OG-Fe(II) oxygenase family
	contig_732674_1_798_-	56	9e-008	Alteromonadales	2OG-Fe(II) oxygenase family
	contig_633551_118_1041_+	56	9e-008	Flavobacteria	2OG-Fe(II) oxygenase family
	contig_627399_1_787_-	54	5e-007	Cyanobacteria	2OG-Fe(II) oxygenase family
	contig_1862_1_732_-	54	5e-007	Other Bacteria	2OG-Fe(II) oxygenase family
	contig_660976_1_1043_+	52	2e-006	Other Stramenopiles	2OG-Fe(II) oxygenase family
	contig_253357_26_973_+	52	2e-006	Flavobacteria	2OG-Fe(II) oxygenase family
DAB-D AYD91074.1	contig_596040_24_938_-	231	9e-061	*Pseudo-nitzschia*	Cyt P450, CYP4/CYP19/CYP26
	contig_625510_955_1881_-	225	6e-059	*Pseudo-nitzschia*	Cyt P450, CYP4/CYP19/CYP26
	contig_82244_85_1023_+	156	5e-038	*Fragilariopsis*	Cyt P450, CYP4/CYP19/CYP26
	contig_596040_947_1648_-	152	9e-037	*Fragilariopsis*	Cyt P450, CYP4X1
	contig_82244_1395_1877_+	145	7e-035	*Fragilariopsis*	Cyt P450
	contig_680152_23_630_-	132	6e-031	Cyanobacteria	Cyt P450
	contig_1109498_1_752_-	130	3e-030	Other Diatom	Cyt P450

Table 3.5: Reciprocal BLAST-p search results for ORFs with similarity to DabD-encoding genes against NCBI's nr database.

ORF ID	Top four BLAST-p hits	Taxa	Query Cover	E-Value	% Identity	Accession
contig_596040_24_938_-	- Cytochrome P450	*F. cylindrus*	99%	2e-133	64.62%	OEU10111.1
	- Unnamed protein	*P. multistriata*	99%	4e-71	42.95%	VEU44693.1
	- DabD	*P. multiseries*	98%	4e-70	42.43%	AYD91074.1
	- Alkane-1-monooxygenaze	*F. solaris*	96%	2e-61	39.86%	GAX28661.1
contig_625510_955_1881_-	- Cytochrome P450	*F. cylindrus*	94%	1e-111	56.48%	OEU10111.1
	- DabD	*P. multiseries*	95%	3e-67	41.81%	AYD91074.1
	- Unnamed protein	*P. multistriata*	95%	3e-63	41.14%	VEU44693.1
	- Alkane-1-monooxygenaze	*F. solaris*	94%	6e-58	40.61%	GAX28661.1
contig_82244_85_1023_+	- Cytochrome P450	*F. cylindrus*	99%	0.0	96.43%	OEU10111.1
	- Alkane-1-monooxygenaze	*F. solaris*	88%	5e-46	35.21%	GAX23170.1
	- Alkane-1-monooxygenaze	*F. solaris*	88%	2e-45	35.92%	GAX28661.1
contig_596040_947_1648_-	- DabD	*P. multiseries*	93%	3e-41	32.00%	AYD91074.1
	- Cytochrome P450	*F. cylindrus*	93%	1e-114	77.06%	OEU10111.1
	- Alkane-1-monooxygenaze	*F. solaris*	84%	4e-41	40.8%	GAX28661.1
	- Alkane-1-monooxygenaze	*F. solaris*	84%	2e-40	40.5%	GAX23170.1
contig_82244_1395_1877_+	- DabD	*P. multiseries*	84%	8e-40	37.81%	AYD91074.1
	- Cytochrome P450	*F. cylindrus*	100%	4e-110	99.37%	OEU10111.1
	- Hypothetical protein	*T. oceanica*	98%	3e-43	49.68%	EJK45228.1
	- DabD	*P. multiseries*	99%	1e-38	47.47%	AYD91074.1
contig_680152_23_630_-	- Unnamed protein	*P. multistriata*	98%	2e-37	45.86%	VEU44693.1
	- TPA: cytochrome P450	Porticoccaceae	100%	5e-130	86.07%	HAZ79708.1
	- Hypothetical protein	Porticoccaceae	100%	2e-128	86.07%	MAY69286.1
	- Cytochrome P450	Porticoccaceae	100%	7e-102	69.65%	WP_155531439.1
contig_1109498_1_752_-	- Hypothetical protein	SAR92	99%	1e-101	69.50%	KRP17789.1
	- Cytochrome P450	*F. cylindrus*	92%	7e-58	43.25%	OEU10111.1
	- DabD	*P. multiseries*	91%	1e-32	29.34%	AYD91074.1
	- Unnamed protein	*P. multistriata*	91%	6e-31	29.75%	VEU44693.1
	- Alkane-1-monooxygenaze	*F. solaris*	87%	1e-24	30.38%	GAX28661.1

Table 3.6: Protein ID (PID) assignments for ORFs in the various *Pseudo-nitzschia* spp. and *Fragilariopsis* spp. light harvesting complex (LHC) clusters. PIDs were assigned by performing a BLAST-p search against *Pseudo-nitzschia multiseries* (CLN-47) and *Fragilariopsis cylindrus* (CCMP 1102). LHC groups were assigned based on previous diatom LHC classifications in Mock et al. (2017) (Supp.Info.11) and Hippmann et al. (2017).

Cluster	*Pseudo-nitzschia PID*	*Fragilariopsis* PID	LHC Group
clust_1044	258347, 261276	169285, 205888	Lhcf_III
clust_1084	247179, 263274	195639, 261294	Lhcr
clust_1194	257565, 303201, 304112, 306047	195777	Lhcf_I
clust_1236	41763, 197371, 302398,310027	170761, 174589, 269349, 269868, 271557	Lhcf_I
clust_1787	238335, 257821	188478, 271659	Lhcx
clust_1938	318557	270184	Lhcr
clust_2256	66239, 238335	269313, 272562	Lhcx
clust_2549	307175	273003, 271559	Lhcr
clust_3219	301726	270606	Lhcr
clust_3282	307174	271561, 273005	Lhcf_II
clust_332	257565, 306047, 306447	267329, 271330, 271332	Lhcf_I
clust_3363	264176	260998	Lhcr
clust_3551	325841	210115, 213124	Lhcr
clust_402	191001, 300768, 303201, 304112, 305325, 307376	267576, 267702, 267837, 268624, 269543, 269567	Lhcf_I
clust_646	14959, 178030, 234364, 318210	177731, 187698, 195639, 270940	Lhcz
clust_712	66239, 264022, 307174	218498, 271659, 272024	Lhcx
clust_80	191001, 255698, 300768, 300769, 303058, 303201,305325, 305720, 307376	143190, 174589, 207327, 267576, 271931, 268626	Lhcf_I

Table 3.7: Summary statistics for both assembled contigs and predicted ORFs for all replicates and treatments combined.

Assembly	Assembled Contigs	Predicted ORFs from contigs
# contigs ($\geq$ 0 bp)	1315493	2265230
# contigs ($\geq$ 1000 bp)	233450	26705
# contigs ($\geq$ 5000 bp)	1445	0
# contigs ($\geq$ 10000 bp)	106	0
# contigs ($\geq$ 25000 bp)	3	0
# contigs ($\geq$ 50000 bp)	0	0
Total length ($\geq$ 0 bp)	937746248	689493243
Total length ($\geq$1000 bp)	359162487	29719929
Total length ($\geq$ 5000 bp)	9769226	0
Total length ($\geq$ 10000 bp)	1394315	0
Total length ($\geq$ 25000 bp)	84630	0
Total length ($\geq$ 50000 bp)	0	0
# contigs	795370	384770
Largest contig	33111	3999
Total length	754213377	276614610
GC (%)	43.32	45.72
N50	969	732
N75	710	600
L50	251690	153883
L75	480396	258428
# N's per 100 kbp	91.56	4.23

 # contigs ($\geq$ x bp): total number of contigs of length $\geq$ x bp.

Total length ($\geq$ x bp): total number of bases in contigs of length $\geq$ x bp.

 # contigs: total number of contigs in the assembly for contigs size $\geq$ 500 bp.

Largest contig is the length of the longest contigs in the assembly.

Total length is the total number of bases in the assembly for using contigs size $\geq$ 500 bp. **GC (%):** total number of G and C nucleotides in the assembly, divided by the total length of the assembly.

N50: length for which the collection of all contigs of that length or longer covers at least half (50%) the total base content of the Assembly. It serves as a median value for assessing whether the Assembly is balanced towards longer contigs (higher N50) or shorter contigs (lower N50). N75 is used for the same purpose but the length is set at 75% of total base content instead of 50%.

L50: number of contigs equal to or longer than the N50 length. In other words, L50, is the minimal number of contigs that contain half the total base content of the Assembly. L75 is used for the same purpose in reference to the N75 length.

 # N's per 100 kbp: average number of uncalled bases per 100,000 assembly bases.

Table 3.8: Total number of raw and trimmed reads, mRNA and rRNA contribution to the trimmed reads, number of mapped mRNA reads, and total number of predicted ORFs for all individual replicates and treatments.

Treatment	Raw Reads	Trimmed Reads	mRNA	rRNA	% rRNA	Mapped Reads	% Mapped Reads	# ORFs
Ice Edge	28492536	27232733	25443952	1788781	6.6%	18226962	71.6%	826190
T0_A	45575920	38947343	33358200	5589143	14.4%	23296503	69.8%	852002
T0_B	19375404	17965033	15308130	2656903	14.8%	10733771	70.1%	577573
T0_C	46579930	38952747	28025278	10927469	28.1%	20712096	73.9%	638446
T1_-Fe_-0.5 °C	21205314	19401307	17366099	2035208	10.5%	12812358	73.8%	576148
T1_+Fe_-0.5 °C	38041776	35740347	32575458	3164889	8.9%	23588683	72.4%	1025062
T1_-Fe_3 °C	35349994	32732641	28188283	4544358	13.9%	20572627	73.0%	916171
T1_+Fe_3 °C	34477352	33059336	29594763	3464573	10.5%	21540022	72.8%	1008607
T1_-Fe_6 °C	32027512	30406112	26596077	3810035	12.5%	18668646	70.2%	887919
T1_+Fe_6 °C	29129438	27409840	23359243	4050597	14.8%	17033876	72.9%	825869
T5_-Fe_-0.5 °C_A	37671290	33464510	28737672	4726838	14.1%	20375592	70.9%	986301
T5_-Fe_-0.5 °C_B	30654564	29139435	26199569	2939866	10.1%	18903422	72.2%	1031680
T5_-Fe_-0.5 °C_C	40290894	36930817	32542651	4388166	11.9%	23560702	72.4%	1128714
T5_+Fe_-0.5 °C_A	39948682	38527552	34406982	4120570	10.7%	25220490	73.3%	1080944
T5_+Fe_-0.5 °C_B	38691956	35399483	29137122	6262361	17.7%	21608015	74.2%	1003994
T5_+Fe_-0.5 °C_C	36287660	34523817	30608808	3915009	11.3%	22940050	75.0%	1013086
T5_-Fe_3 °C_A	34696294	33814638	30373744	3440894	10.2%	22017380	72.5%	1161828
T5_-Fe_3 °C_B	31585290	30088753	27450391	2638362	8.8%	19637249	71.5%	1084754
T5_-Fe_3 °C_C	35546072	32177978	27306946	4871032	15.1%	18999285	69.6%	853823
T5_+Fe_3 °C_A	28153060	26415130	24099272	2315858	8.8%	17773329	73.8%	803545
T5_+Fe_3 °C_B	46637782	41924346	34537148	7387198	17.6%	26251536	76.0%	975259
T5_+Fe_3 °C_C	22038026	20474922	17797508	2677414	13.1%	13314623	74.8%	636362
T5_-Fe_6 °C_A	34470852	32034859	28986089	3048770	9.5%	21576040	74.4%	954425
T5_-Fe_6 °C_B	28342516	27016685	22841677	4175008	15.5%	16929366	74.1%	692317
T5_-Fe_6 °C_C	35887516	35118299	28397352	6720947	19.1%	20889743	73.6%	971567
T5_+Fe_6 °C_A	31556152	29705369	26100052	3605317	12.1%	19817298	75.9%	733987
T5_+Fe_6 °C_B	40514850	38946408	35004303	3942105	10.1%	26683763	76.2%	971080
T5_+Fe_6 °C_C	24900074	23356091	19248203	4107888	17.6%	14118461	73.4%	647783

Table 3.9: Number of reads assigned to *Fragilariopsis* and *Pseudo-nitzschia* for all treatments and replicates.

Treatment	***Fragilariopsis***	***Pseudo-nitzschia***
Ice Edge	604153	149926
T0_A	792326	265315
T0_B	324368	87393
T0_C	444067	132386
T1_-Fe_-0.5 °C	525883	141403
T1_+Fe_-0.5 °C	1389023	422961
T1_-Fe_3 °C	1032805	285845
T1_+Fe_3 °C	1298385	452981
T1_-Fe_3 °C	1270679	501788
T1_+Fe_3 °C	896978	305966
T5_-Fe_-0.5 °C_A	2366719	872030
T5_-Fe_-0.5 °C_B	1783721	642148
T5_-Fe_-0.5 °C_C	2192675	875719
T5_+Fe_-0.5 °C_A	2618615	833378
T5_+Fe_-0.5 °C_B	2381675	694578
T5_+Fe_-0.5 °C_C	3172422	1140824
T5_-Fe_3 °C_A	2433791	1503958
T5_-Fe_3 °C_B	1871392	1150238
T5_-Fe_3 °C_C	1348818	715756
T5_+Fe_3 °C_A	2531661	1003347
T5_+Fe_3 °C_B	3390565	1619939
T5_+Fe_3 °C_C	2199219	909139
T5_-Fe_6 °C_A	2406422	2404759
T5_-Fe_6 °C_B	2216364	2339347
T5_-Fe_6 °C_C	3528660	2814964
T5_+Fe_6 °C_A	2772000	1577368
T5_+Fe_6 °C_B	4251421	2819891
T5_+Fe_6 °C_C	2445033	1409944

CHAPTER 4

METAPROTEOMIC INSIGHTS INTO ELEMENTAL STOICHIOMETRY IN A CHANGING SOUTHERN OCEAN

This chapter will be submitted for peer review in the near future.

4.1 Author Contribution Statement

This manuscript will be co-authored by:
Loay J. Jabre, Mathijs van Manen, Charlotte Eich, Willem van de Poll, Elden Rowland, Corina Brussaard, Rob Middag and Erin M. Bertrand.

L.J.J performed data analyses and wrote the manuscript with input from all authors. L.J.J processed the protein samples and analyzed the metaproteomics data with E.M.B and E.R; E.M.B, R.M, and C.B designed the experiment with input from all authors. M.M, C.E, E.M.B, and R.M collected all the samples aboard RV Polarstern. M.M took the elemental measurements. W.v.d.P took the pigment measurements. C.E took the flow cytometry measurements. E.M.B, R.M and C.B supervised the project and acquired the funding.

4.2 Abstract

Changes in iron (Fe) availability and temperature occur at various spatial and temporal scales across the Southern Ocean (SO). We currently have a limited understanding of how phytoplankton interact with these changes, which restricts our descriptions and predictions of ecological and biogeochemical processes. Here we performed shipboard incubations in the Weddell Sea and examined the phytoplankton communities' responses to alterations in Fe and temperature. We combined elemental measurements with metaproteomics to explore taxon-specific and whole-community characteristics that underpin fitness and elemental stoichiometry under change. Fe addition (+2 nM) increased growth and macronutrient consumption, but warming alone (+2 °C) did not. When Fe and temperature were increased concurrently, the increase in growth and macronutrient drawdown was amplified beyond that observed under Fe addition alone. We found that increased ribosomal abundance coincided with increased growth under high Fe conditions, but less so with concurrent warming. This is consistent with the growth rate hypothesis and shows evidence for translation compensation. However, ribosomal abundance was decoupled from N:P, which suggests other factors, besides ribosomal abundance, are important drivers of changes in N:P stoichiometry. Further, we quantitatively linked the abundance of metalloproteins with the accumulation of metal cofactors. Notably, we associated the complete consumption of manganese mainly with its use in manganese-cluster proteins under high Fe, and increased use in other proteins like superoxide dismutase under low Fe. Our results identify important mechanisms that modulate the stoichiometry of nutrient use in phytoplankton, and highlight proteomic traits that can be used to improve our understanding of carbon and nutrient cycling in the SO and beyond.

4.3 Introduction

Phytoplankton drive productivity in higher trophic levels (Pauly and Christensen, 1995), influence elemental cycling in the ocean (Arrigo, 2005), and contribute to the export and long-term burial of atmospheric carbon (Eppley and Peterson, 1979; Volk and Hoffert, 1985). Knowledge of phytoplankton elemental composition and its controls is therefore critical for understanding marine ecosystems and biogeochemical cycles. Cellular proteins, which are used to maintain various metabolic processes, are important drivers of phytoplankton elemental composition. In addition to being the main reservoirs of nitrogen (N) in phytoplankton, proteins can influence elemental composition in several ways. Many proteins are involved in nutrient transport and underpin the uptake of various elements from the environment into the cell. Proteins are also the primary reservoirs of trace metals within phytoplankton (Twining and Baines, 2013) as many proteins require metal cofactors to function. Further, ribosomal RNA-protein complexes ($protein_1$:$RNA_{1.8}$ by weight), which are used for protein synthesis in every living organism, are phosphorus (P) rich and their prevalence within cells can make them a major reservoir of P (Geider and La Roche, 2002). Studying the proteome landscape of phytoplankton cells is a promising avenue for examining the underpinnings of phytoplankton elemental composition, and may ultimately improve our understanding of elemental stoichiometry in the ocean.

Iron (Fe) and temperature are important drivers of phytoplankton growth and could individually, or together, limit primary production in the Southern Ocean (SO) where both Fe availability and temperature are low. Fe is used as a cofactor in many proteins involved in photosynthesis, respiration, nutrient uptake and oxidative stress management (Raven, 2013b). Temperature directly influences enzymatic turnover rates, including the rates of many Fe-containing enzymes, and therefore plays an important role in influencing phytoplankton metabolism and growth (Eppley, 1972; Raven and Geider, 1988). Fe and temperature can also interactively influence phytoplankton growth and physiology. For example, warming can improve Fe use efficiency which leads to enhanced nitrogen fixation even when Fe availability is low (Jiang et al., 2018; Yang et al., 2021). Warming can also improve growth rates and primary production under low Fe availability by reducing Fe demand (Rose et al., 2009; Jabre and Bertrand, 2020; Jabre et al., 2021), and concurrent increases in Fe and temperature have been shown to have a synergistic influence on growth,

where the effect of warming and increased Fe together exceeds the sum of the individual effects of either variable (Rose et al., 2009; Jabre et al., 2021; Boyd and Hutchins, 2012). The majority of these Fe-temperature interaction studies have been conducted in temperate regions, or in the Ross Sea, SO. It is therefore important to understand how fluctuations in Fe and temperature could influence phytoplankton growth and ecology in other regions like the Weddell Sea, SO.

Within the SO, the Weddell Sea is a globally important site for deep water formation, where cold dense water sinks into the Antarctic Bottom Water, exporting large amounts of heat and carbon from the atmosphere, as well as other elements, in the process (Orsi et al., 1999; Meijers et al., 2023). A fraction of Weddell Sea surface water is also advected northward, carrying macronutrients that fuel primary productivity at lower latitudes (Sarmiento et al., 2004). Evidence shows rapid warming of Weddell Sea deep water, with large implications for nutrient export and global ocean circulation patterns (Quéré et al., 2007; Strass et al., 2020). In contrast to the rapidly warming deep water, no significant warming has been observed in Weddell Sea surface water for the past few decades, and surface warming is not predicted to be as severe by the end of the century (Turner et al., 2005; Conil and Menéndez, 2006; Strass et al., 2020). The Weddell Sea surface is however subject to short-term temperature fluctuations caused by various weather processes like polar cyclones (Jena et al., 2022). In addition, Fe availability in the Weddell Sea may also change under both future climate scenarios and in the short term, but our understanding, and consequently our predictions, of these processes are highly variable (Tagliabue et al., 2016). Both the amount and stoichiometry of nutrients that are exported to the deep ocean or advected northward from the SO are influenced by phytoplankton growth, and the elemental requirements of different phytoplankton groups under different environmental conditions.

Trait-based approaches for studying phytoplankton have contributed greatly to our understanding of phytoplankton biology and ecology. Functional traits can be defined as "morphological, physiological or phenological features measurable at the individual [or community] level, and influence organismal fitness" (Violle et al., 2007). Some established traits include cell size, photosynthetic capacity, elemental composition, and more recently, genomic composition and gene expression at the transcript level (Litchman and Klausmeier, 2008; Finkel et al., 2010; Coles et al., 2017). These approaches have yielded extensive

insights into the controls of phytoplankton growth and metabolic processes. Additionally, their utility for quantifying the connection between gene expression, growth, and ecological processes shows promise but has not been developed. This, in addition to our limited understanding of how different phytoplankton groups interact with environmental change, has constrained our ability to integrate additional flexibility into Earth system models to increase their descriptive and predictive capacity.

Recently, McCain et al. (2022) introduced coarse-grained protein allocation as a possible way to define new traits. A proteomic trait can be defined as "a characteristic of an organism at the proteome-level, that includes both the abundance and identity of a protein (or group of proteins), and is connected to organismal fitness or performance" (McCain et al., 2022). Some of these proposed traits include ribosomal protein allocation, and the proportion of the proteome that does not change in response to a variable environment. Proteomic measurements in phytoplankton may therefore add another dimension to traditional trait-based approaches, where the abundance of certain proteins can be linked to meaningful cellular characteristics, and ultimately ecological and biogeochemical processes.

Untargeted metaproteomics workflows can characterize a suite of proteins/protein groups within a single mass spectrometry experiment, making them valuable for examining proteomic traits within phytoplankton communities (Hettich et al., 2013). However, without quantifiable peptide standards (which are costly and reduce throughput), the relative abundance measurements produced with these methods can be subject to biases arising from heterogeneous sample complexity and changes in community composition between samples. Further, the signal intensity (i.e. relative abundance) arising from different peptides within a sample is influenced by a variety of factors like the chemical properties of the peptide, in addition to the actual abundance of the peptide being measured. One way to mitigate the variability surrounding individual peptide measurements is to use a 'coarse-grained' approach where peptides are binned into larger protein groups (e.g. all peptides from different photosynthetic proteins are considered a 'photosynthetic protein' group), and/or only using proteins with a sufficient number of matching peptides (McCain et al., 2022). Coarse graining reduces biases, and allows us to meaningfully compare the relative abundance of different protein groups within and between samples, and might make it possible to convert relative abundance measurements into absolute protein amounts.

Ribosomal abundance is a potentially valuable proteomic trait as ribosomes play an important role in organismal growth and elemental stoichiometry. The growth rate hypothesis postulates that increased growth rate requires increased ribosomal abundance, which in turn increases cellular rRNA and P content, and decreases cellular N:P (Sterner and Elser, 2002). This hypothesis has been mainly formulated from observations of laboratory cultures of non-photoautotrophs, and skepticism remains about its general applicability in phytoplankton (Flynn et al., 2010). A better understanding of how ribosomal investment influences phytoplankton growth may therefore be fruitful for understanding and predicting primary productivity and N:P stoichiometry in a changing ocean. The abundance of different metalloproteins may also be a useful proteomic trait as these proteins are highly responsive to change and could impact organismal success under different environmental conditions (Twining and Baines, 2013; Schoffman et al., 2016). Metalloproteins can also be directly linked to trace metal stoichiometry since the majority of the cellular trace metal reservoir is bound to proteins (Twining and Baines, 2013). Our knowledge of trace metal interactions within phytoplankton has been focused on on Fe-containing metalloproteins and their contribution to cellular Fe, mainly due to a high metabolic requirement for Fe within phytoplankton and its potential for being a limiting nutrient in much of the world's oceans (Martin et al., 1991; Moore et al., 2001). However, other trace metals like manganese, copper, and zinc also play critical roles in phytoplankton metabolism and could have complex metabolic interactions with Fe in phytoplankton cells (Peers and Price, 2004; Schoffman et al., 2016). Challenges in conducting ultra-clean work in the field have made it difficult to verify laboratory observations of trace metal utilization in phytoplankton under different environmental conditions. Examining metalloproteins in the field could improve our understanding of trace-metal use within phytoplankton cells and across phytoplankton communities under change.

The response of phytoplankton growth to environmental change influences primary productivity, the biological carbon pump, and the cycling of nutrients in the ocean. Understanding phytoplankton elemental composition and its stoichiometric controls can provide insight into the underpinnings of phytoplankton growth and consequent effects on ecological and biogeochemical processes (Kwiatkowski et al., 2018). In this study, we incubated phytoplankton communities in the Weddell Sea for eight days under a matrix

of high and low Fe and temperature conditions and examined the proteomic profiles of these communities using metaproteomics. We identified possibly useful proteomics traits for understanding how changes in Fe and temperature influence growth and elemental stoichiometry.

4.4 Results and Discussion

4.4.1 Initial environmental conditions

We incubated phytoplankton communities from two different locations in the Weddell Sea (Figure 4.1A) under a matrix of in situ and increased Fe and temperature conditions. The water temperature at sampling depth was warmer at the BA1 location compared to the BA2 location, measuring -0.3 $\pm$ 0.3 °C and -1.4 $\pm$ 0.3 °C, respectively (Figure S4.6). We could not confidently compare DFe concentrations between the two locations due to Fe contamination in some of our T0 samples, but our measurements suggest that Fe availability was very low at both sites ($<$ 0.1 nM) (Figure 4.1B). The initial dissolved trace metal concentrations of manganese (DMn), cadmium (DCd), zinc (DZn), and copper (DCu) were generally lower in BA1 than in BA2 (Figure 4.1B, Figure S4.7). The initial dissolved nitrate (NO_3^-), phosphate (PO_4^{3-}) and silicate (Si) (measured as silicic acid, $Si(OH)_4$) were also slightly lower in BA1 than in BA2 (Figure 4.1 C, D, Figure S4.7). These differences in dissolved nutrients were likely driven by distance from shore, where BA2 would have been exposed to a larger influx of nutrient and metal-rich water from the ice edge, or from upwelling in shallower waters. We note that in both bioassays, macronutrient concentrations were high at T0 and remained high after eight days of Fe-temperature incubations.

4.4.2 Metaproteomics overview

We used mass spectrometry-based metaproteomics to examine phytoplankton community composition and functional traits. Here we provide a general overview of our metaproteomics data, and assess their suitability for addressing our research questions.

Our quality control analyses of the raw mass spectrometry (Figure S4.8, S4.9, S4.10) showed that samples corresponding to injections 48-58 (Table S4.2) exhibited lower Total

Ion Current (TIC) and matched peptide abundance, and reduced number of MS scans relative to the other samples. This indicates poorer sample quality relative to other samples, which was likely caused by a fire in an adjacent laboratory and subsequent power outage that occurred while these specific samples were being prepared. Upon closer examination, we found that the protein expression patterns within these samples were consistent with other biological replicates of the same treatments. We therefore determined that despite the compromised sample preparation quality, these samples remained informative and suitable for subsequent analyses. We emphasize here that comprehensive data quality assessments are crucial for identifying anomalous samples that may bias downstream bioinformatics and data inference.

Next, we evaluated whether a metatranscriptome database created from Ross Sea samples (Jabre et al., 2021) was suitable for use in peptide matching in these samples. Having a suitable database is a critical factor in metaproteomics experiments as database choice influences the number of unique peptides (and ultimately proteins) that can be observed, and affects the perceived abundance of these peptides (Eng et al., 2011; Tanca et al., 2016; Kumar et al., 2017; McCain et al., 2022). Using this unmatched database, we found 37,472 unique peptides across all samples (Figure 4.11), approximately 2x more than previously observed using this same database on Ross Sea protein samples collected with the samples used to prepare this metatranscriptome (McCain et al., 2022). This difference is likely due to our measurement of a larger number of samples under different environmental conditions, and the inclusion of variable peptide modifications in the database search parameters, which allowed for more flexibility in finding chemically modified peptides. We were also able to match 15-35% of TIC and 20-50% of all peptide-like feature abundance (Figure S4.12), which is consistent with good database suitability (McCain et al., 2022) despite our database not being sample-specific (paired). The relatively low eukaryotic microbial diversity throughout the SO (Raes et al., 2018) may have been advantageous in our case, as it may reduce the disparity between proteomics samples and reference databases derived from spatially and temporally separated locations within the SO.

We examined the correlations between three different abundance metrics that were calculated independently of database influence (TIC and peptide-like feature abundance) and after database searching was completed (matched peptide abundance) (Figure S4.12).

We found a strong correlation between matched peptide abundance and TIC (R^2 = 0.97), and between matched peptide abundance and peptide-like feature abundance (R^2 = 0.96), with no notable outliers (Figure S4.12). This suggests that our database suitability was consistent across all samples. We also observed a strong correlation between peptide-like feature abundance and TIC (R^2 = 0.99) (Figure S4.12) which indicates that contamination levels were also consistent across samples.

The strong correlations between database dependent and database independent abundance metrics provided us with the flexibility to select between database-dependent or database-independent normalization factors for normalizing peptide abundance. Unless otherwise stated, we normalized peptide abundance using database-dependent and sample-specific normalization factors. That is, we normalized the abundance of proteins of interest by the total abundance of all matched peptides in each sample (see Materials and Methods section for more details).

4.4.3 Growth and nutrient drawdown

We observed clear signatures of Fe limitation in both bioassay experiments, consistent with the low DFe measurements. When we supplemented the community with Fe, the photosynthetic efficiency of PSII, measured as F_v/F_m , was significantly increased (BA1, BA2 $p < 0.001$) (Figure 4.1E) . F_v/F_m has been used extensively as a general indicator of Fe stress in cultures and in the field (Greene et al., 1992; Olson et al., 2000; Jabre and Bertrand, 2020), but may be influenced by other stressors like low Mn-availability (Wu et al., 2019) (Figure S4.13). The addition of Fe significantly enhanced phytoplankton net growth, measured as the accumulation of total chlorophyl-a (chl-a) (BA1, BA2 p = 0.002) and particulate organic carbon (POC) (BA1, BA2 $p < 0.001$) (Figure 4.1F,G) . As expected, this increase in growth coincided with increased drawdown of NO_3^-, (BA1, BA2 $p < 0.001$) and PO_4^{3-} (BA1, BA2 $p < 0.001$) in both bioassays (Figure 4.1), and Si in BA1 ($p < 0.001$) (Figure S4.7). Fe-limited phytoplankton growth has been well documented in the SO, and is one of the main reasons why the SO is considered a high (macro)nutrient – low chlorophyl (HNLC) region (de Baar et al., 1990; Martin et al., 1990; Boyd et al., 2000).

Warming, without Fe addition, did not cause notable changes in F_v/F_m, (BA1 p = 0.40, BA2 p = 0.79) consistent with SO phytoplankton culture results (Jabre and Bertrand

2019), and had no effect on chl-a (BA1 p = 0.97, BA2 p = 0.83), or POC (BA1 p = 0.18, BA2 p = 0.17) (Figure 4.1). It also did not significantly influence the drawdown of NO_3^- (BA1 p = 0.29, BA2 p = 0.68) or PO_4^{3-} (BA1 p = 0.19, BA2 p = 0.33) (Figure 4.1). Warming has been shown to increase Fe-limited phytoplankton growth and nitrogen fixation in the absence of added Fe (Rose et al., 2009; Jiang et al., 2018; Jabre and Bertrand, 2020; Yang et al., 2021; Jabre et al., 2021), yet it did not benefit the Fe-limited the phytoplankton communities in our bioassays. This could be attributed to the slight increase in temperature we used (+2 °C) compared to other studies (+ >3 °C), which may not have been sufficient to improve Fe-use efficiency. This suggests that small changes in temperature without increased Fe availability may not cause large ecological or biogeochemical impact in the Weddell Sea, unlike other sectors in the SO like the Ross Sea or the Antarctic Peninsula, where larger temperature changes are predicted (Vaughan et al., 2003; Turner et al., 2005). Further, taxonomic composition may also influence the average community's response to warming, where for example, a phytoplankton community with a high fraction of temperature-responsive pennate diatoms could appear to benefit from slight warming.

Despite no notable temperature effect under low Fe, we observed a significant synergistic Fe-temperature influence on chl-a (BA1 p = 0.02; BA2 $p < 0.001$) and POC accumulation (BA1, BA2 $p < 0.001$), and on the drawdown of NO_3^- (BA1, BA2 $p < 0.001$) and PO_4^{3-} (BA1 p = 0.01, BA2 $p < 0.001$) (Figure 4.1). That is, when warming occurred concurrently with Fe addition, a larger increase in growth and nutrient drawdown was observed relative to the individual effects of Fe addition and warming. This is consistent with an interactive Fe-temperature effect (Rose et al., 2009; Jabre et al., 2021), and suggests that in the event of increased Fe availability, growth and nutrient consumption in SO surface waters could be magnified even under slight warming. Increased nutrient consumption from the SO surface water could reduce nutrient supply to lower latitudes where these nutrients fuel primary productivity (Primeau et al., 2013; Moore et al., 2018).

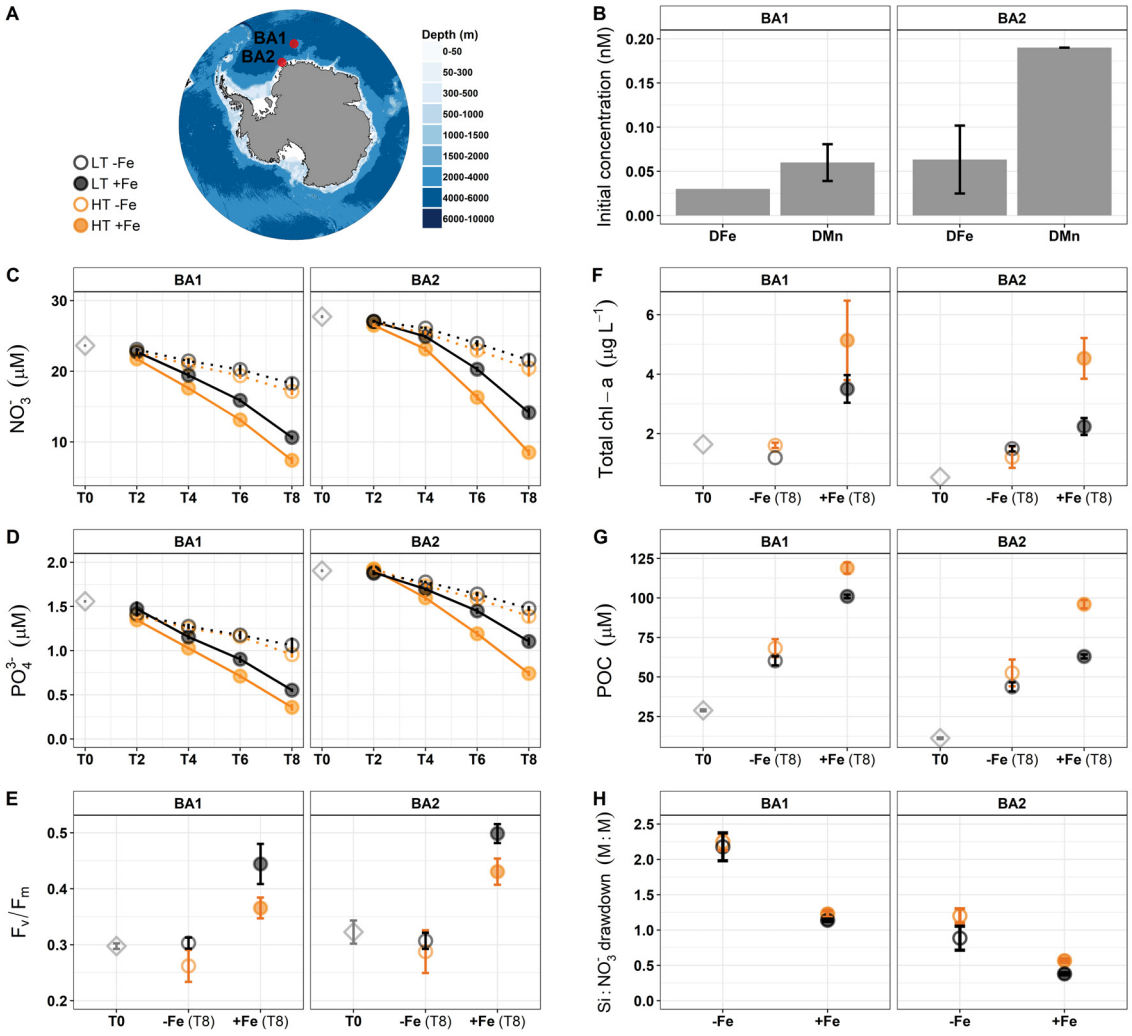

Figure 4.1: A) Locations of bioassay1 (BA1) and bioassay2 (BA2) in the Weddell Sea, Southern Ocean. B) Initial (T0) dissolved iron (DFe) and manganese (DMn) concentrations at both bioassay locations. Only one replicate was available for DFe measurements in BA1 due to contamination of the sample. C) Dissolved nitrate (NO_3^-) concentrations on T0 and every other day of the incubation period. D) Dissolved phosphate (PO_4^{3-}) concentrations on T0 and every other day of the incubation period. Note that both NO_3^- and PO_4^{3-} were still in excess at the end of both bioassay incubations regardless of treatment. E) Photosynthetic efficiency of PSII (F_v/F_m , unitless) on T0 and after 8 days of iron-temperature incubations (T8). F) Total chlorophyl a (chl-a) concentrations on T0 and T8. G) Particulate organic carbon (POC) concentrations on T0 and T8. F) H) Ratio of silicic acid (Si) to nitrate (NO_3^-) drawdown (M:M) calculated using Si and NO_3^- measurements between T2 and T8 of iron-temperature incubations. Error bars represent ± 1 SD and fall within the bounds of points when not visible.

4.4.4 Si:NO_3^- drawdown

We examined the ratio of Si drawdown relative to NO_3^- (Si: NO_3^-) and found generally higher Si: NO_3^- drawdown in BA1 than in BA2 (Figure 4.1H). This suggests that Si-requiring organisms, like diatoms, were more abundant in BA1 than in BA2, and that non-Si requiring organisms formed a larger portion of the phytoplankton community in BA2 compared to BA1. We also found that Fe addition significantly decreased Si:NO_3^- drawdown in both bioassays (BA1, BA2 $p < 0.001$) and warming slightly increased this ratio only in BA2 ($p = 0.02$). Note that the lowest Si:NO_3^- drawdown ratios we observed in BA1 and BA2 were $\sim$1 and $\sim$0.5, respectively, in the Fe-replete treatments. The decrease in Si: NO_3^- with Fe addition might indicate a reduction in the diatom fraction of the phytoplankton community. However, this is likely not the case here – see community composition discussions below. Another reason for this is that diatom Si consumption is influenced by Fe availability. Diatoms consume Si and N in roughly equimolar amount (Si:N $\approx$ 1) when grown under nutrient replete conditions (Brzezinski, 1985), but increase their Si consumption relative to N (Si:N $>$ 1) when grown under Fe limitation (Hutchins and Bruland, 1998; Takeda, 1998). The decrease in Si:NO_3^- drawdown after Fe addition was therefore likely caused by an alleviation of Fe-limited diatom growth in both bioassay experiments. Enhanced frustule silicification under low Fe could be advantageous to diatoms as it protects against grazing (Assmy et al., 2013; Ryderheim et al., 2022), and increases sinking to deeper waters (Petrucciani et al., 2023) where trace metal availability may be higher. As such, changes in Fe availability could influence food web dynamics by altering grazer composition and grazing strategies, and may have serious implications for carbon and nutrient export by influencing sinking rates (Waite and Nodder, 2001). The relationship between Si drawdown and Fe availability could also influence the stoichiometry of Si transfer out of the SO, with consequences for nutrient limitation and phytoplankton community composition.

4.4.5 Phytoplankton community composition

We performed NMDS ordination analyses on pigments, flow cytometry, and metaproteomics data to examine general similarities and dissimilarities between samples from the two bioassay experiments. All three data types showed that T0 samples in BA1 clustered separately from the T0 samples in BA2 (Figure 4.2A, B, C). In the flow cytometry and protein data, samples from BA1 and BA2 remained distinctly clustered regardless of treatment, but Fe supplementation caused additional clustering within each experiment. In the pigment data, Fe addition led to a more pronounced clustering pattern, where Fe-replete BA1 and BA2 samples clustered together, and separately from the low Fe samples. Temperature did not cause a notable impact on sample clustering. All together, these clustering patterns indicate that the microbial communities were distinct at the two bioassay locations, and that Fe addition caused a bigger change in community composition relative to temperature.

Pigment-based community composition – We then explored these broad community composition trends in more detail using the pigment and metaproteomics measurements. For this, we calculated community composition as a fraction of total chl-a concentration using pigments (i.e., taxon-specific pigment(s) / total chl-a), or as a fraction of total matched protein abundance using metaproteomics (i.e., taxon-specific protein abundance / abundance of all matched proteins).

Our pigment data identified diatoms and haptophytes as the most abundant taxa in both bioassays, collectively accounting for 92-98% of total chl-a. The diatom fraction was higher in BA1 (63-81%) relative to BA2 (38-71%), while the haptophyte fraction was lower in BA1 (18-36%) relative to in BA2 (29-50%). In both bioassays, Fe addition caused a significant increase in the diatom fraction (BA1, BA2 $p < 0.001$) and a significant decrease in the haptophyte fraction (BA1, BA2 $p < 0.001$). There was no significant temperature effect on pigment taxonomic composition (Figure 4.2D).

Protein-based community composition – We analyzed our protein data at a taxonomic resolution comparable to pigments, and at a finer resolution to examine the phytoplankton communities in more detail. Our protein data also identified diatoms and haptophytes as the most abundant taxa in both bioassays, collectively accounting for 41-68% of the total matched protein abundance (hereafter interchangeably referred to as total protein,

but not to be confused with bulk protein concentrations measured through bicinchoninic acid assay (BCA) or estimated from particulate nitrogen (PN)). Similarly, the diatom contribution to total protein was higher BA1 (30-52%) relative to BA2 (21-33%), while the haptophyte contribution was lower in BA1 (8-12%) relative to in BA2 (22-40%). In contrast to the pigment data, however, Fe addition caused no significant change in the diatom fraction in either bioassay (BA1 p = 0.52; BA2 p = 0.59) and caused significant increase in the haptophyte fraction in BA2 (BA1 p = 0.63; BA2 p = 0.04). We did not observe a significant temperature effect on protein taxonomic composition (Figure 4.2E). We note here that 8-13% of matched peptides that could not be resolved beyond the eukaryote level were histone peptides (Figure S4.15), which are highly conserved across species. If these peptides were to be assigned a specific taxonomy, they could increase the relative abundance of each taxonomic group but would unlikely influence the taxonomic composition.

Both pigment and metaproteomics data (Figure 4.2) are consistent with the Si:NO_3^- consumption measurements (Figure 4.1H), showing that diatoms were a larger portion of the phytoplankton community in BA1 relative to BA2, and that haptophytes were a larger portion of the phytoplankton community in BA2 relative to BA1 (Figure 4.2D, E). However, the contrast in how pigment and protein measurements show the effect of Fe addition on community composition is notable, and may stem from fundamental biological differences in how these pools of cellular materials respond to change. Pigment measurements describe pigment-containing (i.e., photosynthetic) organisms, and can therefore be biased by changes in pigment content of these organisms. For example, phytoplankton can have vastly different intracellular pigment concentrations when grown under Fe-limited vs Fe-replete conditions (Kosakowska et al., 2004; van Oijen et al., 2004; DiTullio et al., 2007; van Leeuwe and Stefels, 2007). Conversely, protein measurements can capture all proteins (photosynthesis-related or not) in both photosynthetic and non-photosynthetic organisms. Our results show that in conditions where intracellular pigment concentrations can be severely impacted, such as changing Fe availability, metaproteomics may provide a more accurate representation of community biomass composition. Integrating high-throughput microscopy cell counts and biovolume estimates with pigments and metaproteomics measurements could provide better insight into microbial community composition under change (see Pierella Karlusich et al. (2022) for discussion on using high-throughput

imaging in plankton surveys).

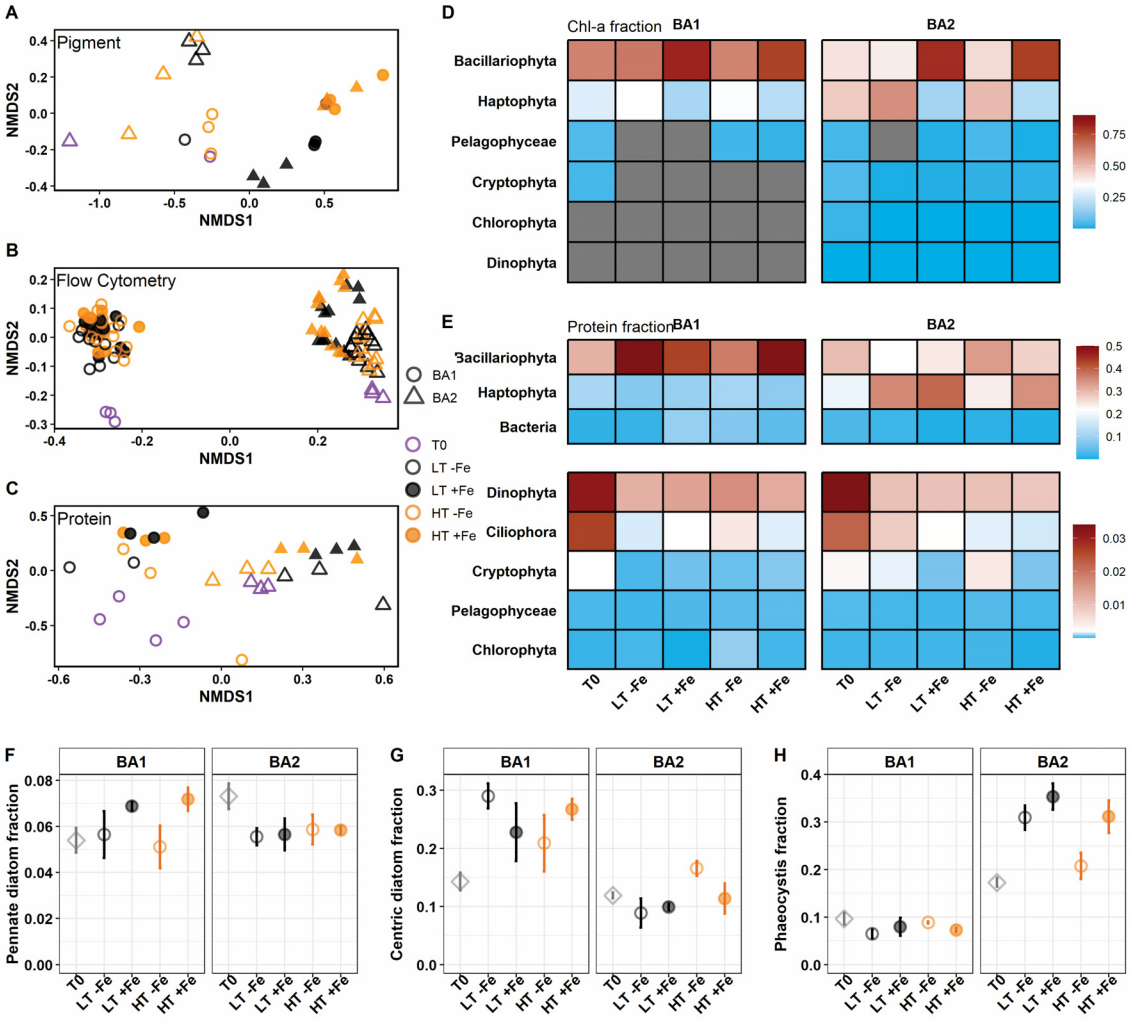

Figure 4.2: Phytoplankton community composition is unique at each bioassay location, with diverse taxonomic responses to changes in iron and temperature. A) Non-metric multi-dimensional scaling (NMDS) plot using pigment abundance measurements at T0 and T8. NMDS model stress value = 0.03. B) NMDS plot using size-fractioned flow-cytometry measurements at T0, T2, T4, T8. NMDS model stress value = 0.07. C) NMDS plot using peptide abundance values at T0 and T8. NMDS model stress value = 0.12. Figure S4.14 shows the NMDS model fit tests for A, B, and C. D) Heatmap showing the fractional contribution of various phytoplankton taxonomic group pigments to total chlorophyll a. E) Heatmap showing the fractional contribution of various phytoplankton and other taxonomic group peptides to total peptide abundance. We changed the scale in lower panel in E) for clarity. In D and E, each square represents the mean of triplicate measurements. F) The pennate diatom fraction of total protein abundance. G) The centric diatom fraction of total protein abundance. H) The *Phaeocystis* sp. fraction of total protein abundance. Total protein abundance was calculated as the sum of all matched peptide intensities. Error bars represent $\pm$ 1 SD and fall within the bounds of points when not visible.

Community composition at a higher resolution – Upon further examination of the diatom and haptophyte protein groups, we found that diatom protein was primarily composed of centric diatoms (predominantly *Chaetoceros* sp. and *Thalassiosira* sp.) and to a lesser extent pennate diatoms (predominantly *Fragilariopsis* sp. and *Pseudo-nitzschia* sp.) (Figure 4.2F, G, H, Figure S4.15), and haptophyte protein was primarily composed of *Phaeocystis* sp. (Figure S4.15). This is consistent with previous observations showing that several diatom taxa and *Phaeocystis* dominate phytoplankton blooms at different times and locations throughout the SO (Kang and Fryxell, 1993; DiTullio and Smith Jr., 1996; Arrigo et al., 1999; Rose et al., 2009; Jabre et al., 2021). *Phaeocystis* typically appears in early spring when the water is colder and more turbulent, and trace metal availability is higher, and diatoms typically dominate later in the season when trace metals are more depleted and the water is warmer and more stratified (DiTullio and Smith Jr., 1996; Liu and Smith, 2012; Smith et al., 2013). This may explain why *Phaeocystis* was more abundant in BA2 (colder, higher dissolved trace metal concentrations) than in BA1 in our experiments, even though BA2 was initiated 12 days later (Figure 4.2).

We found that Fe addition significantly increased the pennate diatom protein fraction in BA1 ($p = 0.04$) but not in BA2 ($p = 0.95$) and did not influence the centric diatom fraction in either bioassay (BA1 $p = 0.89$, BA2 $p = 0.31$). Pennate diatoms typically dominate phytoplankton blooms after Fe fertilization in HNLC regions (de Baar et al., 2005), likely due to their ability to quickly uptake nutrients, and to maintain baseline metabolism when Fe is sparse through reducing intracellular Fe demand (Jabre et al., 2021) and using ferritin Fe stores (Marchetti et al., 2009). Ferritin may also play an important role in buffering intracellular free Fe (Botebol et al., 2015), which is toxic if not packaged properly (Halliwell and Gutteridge, 1992). Centric diatoms, which generally lack ferritin (Lampe et al., 2018), may be more susceptible to the toxic effects of free Fe after pulsed Fe inputs, which may be another reason why pennates, but not centric diatoms, were able to take advantage of Fe addition in BA1. We also observed a significant increase in the *Phaeocystis* protein fraction after Fe addition in BA2 ($p = 0.03$), but not in BA1 ($p = 0.81$); the opposite of what we observed for pennate diatoms. This suggests that some taxonomic groups are more adapted for growth under certain environmental conditions (e.g., the preference of *Phaeocystis* to grow in colder water relative to pennate diatoms), which gives them a competitive advantage or disadvantage when environmental conditions

are shifted.

Together, these results highlight that 1) there are important variations in how different phytoplankton taxa respond to change (e.g. pennate vs centric diatom response to Fe addition), and 2) these variations may get concealed when community composition is considered at a taxonomic level that is too broad (e.g., diatoms as a whole). This led us to ask: how do proteomic traits vary in different taxa and how do these traits influence organismal success under change? To answer this, we focused our analyses on three main functional protein groups: ribosomes, RuBisCO, and photosynthetic proteins, within pennate diatoms, centric diatoms, and *Phaeocystis*.

4.4.6 Proteomic traits vary across taxa and influence organismal fitness under change

The taxon-normalized photosynthetic protein fraction (light-reaction photosynthetic proteins) generally increased after Fe addition in both pennate and centric diatoms, but remained stable in *Phaeocystis* regardless of treatment. Similarly, the RuBisCO fraction increased after Fe addition in pennate and centric diatoms, specifically in BA2, but remained stable under change in *Phaeocystis*. We note that centric diatoms invested substantially more in RuBisCO protein than pennate diatoms (20-30% vs 2-6%, respectively). The ribosomal protein fraction was similar across taxa at T0, and notably increased after Fe addition in pennate diatoms, and in *Phaeocystis* in BA2 (Figure 4.3 A-I).

These protein allocation characteristics reveal diverse strategies among taxa which could underpin their success under different environmental conditions. The relative stability of photosynthetic proteins and RuBisCO in *Phaeocystis* impose a lower regulatory cost than in other taxa, which may allow it to thrive better under dynamic/turbulent coastal environments without the need to constantly regulate its proteome (Nissen and Vogt, 2021; McCain et al., 2022). This may have also given *Phaeocystis* a competitive advantage in BA2, where near-coastal conditions are more likely to fluctuate than in the open ocean (BA1).

Overall, the protein allocations to RuBisCO (Figure S4.16) were generally higher (10-17%) than expected based on (Losh et al., 2013) ($< 6\%$) who used western blotting to measure RuBisCO as a proportion of total protein in plankton communities off the

coast of California. However, given that 1) Rubisco concentrations vary widely among phytoplankton taxa, likely reflecting taxonomic variations in RuBisCO kinetic properties and carbon concentrating mechanisms, and 2) our experiments were conducted in a polar region where RuBisCO carboxylation rates are limited by the cold (Young et al., 2015), it is not surprising that we measured higher RuBisCO fractions than would be expected in temperate regions. The 5-10 fold difference in RuBisCO investment in pennate diatoms compared to centric diatoms (Figure 4.3B, E) is nevertheless noteworthy. Laboratory evidence points to a positive correlation between N allocation to RuBisCO (i.e. RuBisCO fraction) and cell size in centric diatoms, possibly to counteract the decline in RuBisCO turn over rate with size (see Wu et al. (2014) for discussion). It may be that larger centric diatoms (*Thalassiosira* and *Chaetoceros*) dominated our centric diatom protein fraction, which, when combined with generally higher RuBisCO abundance in cold environments, would have contributed to a large investment in RuBisCO protein in centric diatoms.

The increased ribosomal fraction in pennate diatoms but not centric diatoms after Fe addition suggests that pennates have more flexible proteomes that could be tuned to different environmental conditions. This may aid in more rapid pennate diatom growth and blooming under favorable conditions. Here we observed larger increase in total pennate diatom protein under high Fe relative to centric diatom protein (Figure S4.17), likely indicative of increased pennate diatom growth. Further, we only observed an increase in *Phaeocystis* ribosomal investment after Fe addition in BA2, where we also observed an increase in total *Phaeocystis* protein (Figure S4.17). This may be consistent with the growth rate hypothesis, where increased ribosomal investment is linked to increased organismal growth. Together, these data suggest that proteomic traits could shed light on organismal fitness under environmental change.

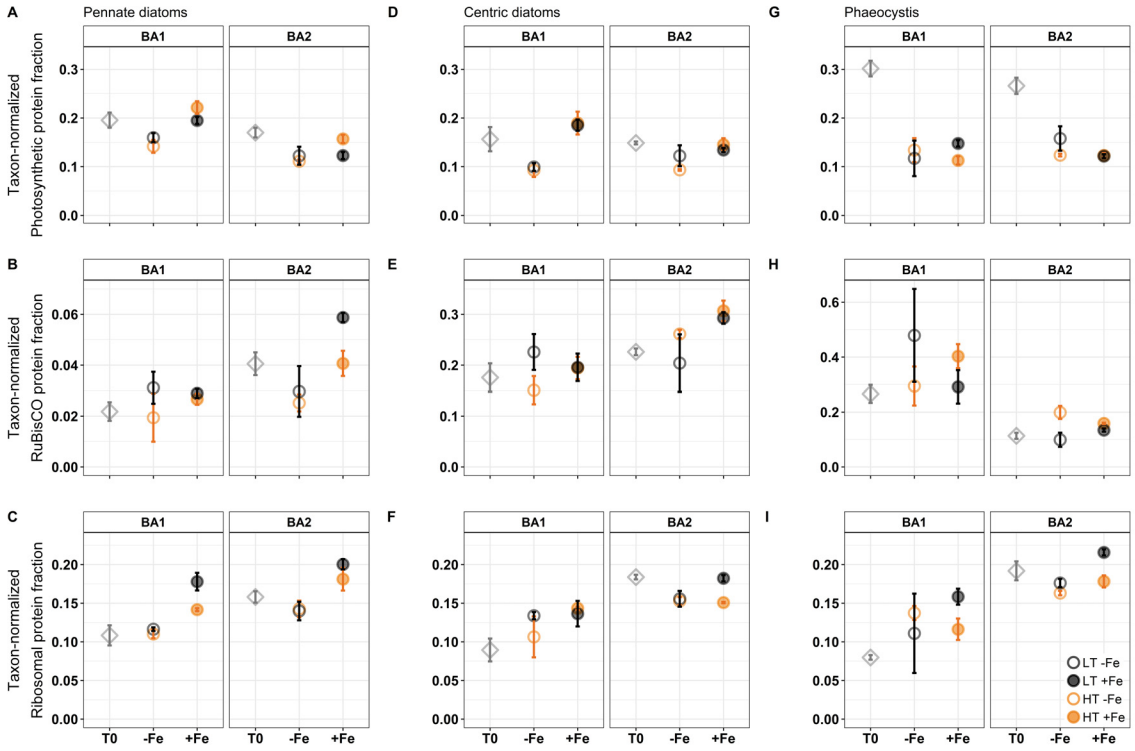

Figure 4.3: Taxon-specific photosynthetic protein, RuBisCO and ribosomal protein allocation at T0 and after 8 days of iron-temperature incubations. A) Pennate diatom photosynthetic protein fraction of total pennate diatom protein. B) Pennate diatom RuBisCO protein fraction of total pennate diatom protein C) Pennate diatom ribosomal protein fraction of total pennate diatom protein. D) Centric diatom photosynthetic protein fraction of total centric diatom protein. E) Centric diatom RuBisCO protein fraction of total centric diatom. F) Centric diatom ribosomal protein fraction of total centric diatom protein. G) *Phaeocystis* photosynthetic protein fraction of total *Phaeocystis* protein. H) *Phaeocystis* RuBisCO protein fraction of total *Phaeocystis* protein. I) *Phaeocystis* ribosomal protein fraction of total *Phaeocystis* protein. Total taxon protein abundance was calculated as the sum of all taxon-specific peptide intensities. Error bars represent $\pm$ 1 SD and fall within the bounds of points when not visible.

The elemental composition of phytoplankton cells is influenced by their macromolecular composition (Finkel et al., 2016), including highly dynamic proteins that underpin specific elemental quotas. Here, we focused on a few of these proteins that may play important roles in influencing elemental stoichiometry: ribosomes, which may regulate P quotas and N:P stoichiometry, and several metalloproteins which contribute to various trace-metal quotas within phytoplankton.

4.4.7 Decoupling of ribosomes, temperature, and N:P

We calculated ribosomal protein fraction by summing the abundance of all ribosomal peptides (regardless of taxonomic origin) then dividing by the total abundance of all matched peptides. This increases certainty in our ribosome abundance measurements, and allows us to examine the overall influence of ribosomal abundance on bulk N:P.

We found that the ribosomal protein fraction was generally lower in BA1 than in BA2 (Figure 4.4A). We also observed that Fe addition increased the investment in ribosomal protein in both bioassays, but less so when Fe and temperature were concurrently increased (Figure 4.4A). Increased ribosomal abundance in the high Fe treatments is consistent with the growth rate hypothesis, linking increased protein synthesis (Figure S4.19) and growth (Figure 4.1) with increased ribosomal abundance (Sterner and Elser, 2002). Interestingly however, ribosomal abundance did not increase synergistically with concurrent increase in Fe and temperature, even though growth did (Figure 4.1). Warming increases translation efficiency per ribosomal unit (Farewell and Neidhardt, 1998), which enables phytoplankton to maintain equivalent (or higher) growth rates with reduced ribosomal abundance within their cells (Woods et al., 2003; Toseland et al., 2013) - this is known as translation compensation. Decreasing the number of highly efficient ribosomes under warming alleviates the energetic and material costs of ribosome synthesis and maintenance. Translation compensation may also explain why we measured more ribosomes in BA2, where the water temperature was colder, than in BA1. Overall, these results reveal high sensitivity of cellular ribosomal allocation to small fluctuations in temperature in the SO, specifically when nutrients are replete.

P-rich ribosomes could play an important role in regulating N:P in phytoplankton (Geider and La Roche, 2002). Toseland et al. (2013) showed that decreased ribosomal

abundance, and hence decreased P requirements, under warming causes an increase in modelled cellular N:P. Other studies have investigated the biogeography of N:P stoichiometry, and found that particulate matter at warmer low latitudes have generally higher N:P ratios than particulate matter from colder high latitudes, and a temperature dependency of N:P specifically at high latitudes (Martiny et al., 2013; Yvon-Durocher et al., 2015; Tanioka et al., 2022). Additionally, when one phytoplankton community in the SO was incubated under cold (0 °C) and warm (4 °C) conditions, its particulate N:P composition was higher in the warmer treatment (Spackeen et al., 2018b). In contrast to these findings, however, we did not observe increased N:P drawdown or particulate accumulation with warming (Figure 4.4B, C). This decoupling between ribosomes, temperature and N:P was also observed in the Ross Sea, where N:P was not impacted by warming despite decreased ribosomal mRNA abundance (Jabre et al., 2021).

Why does ribosomal abundance fail to influence N:P? Here we suggest some mechanisms through which temperature / ribosomal influence on N:P may be buffered in the SO. Phylogenetic variations in organismal N:P (Quigg et al., 2003; Ho et al., 2003) can influence the overall bulk N:P in a mixed phytoplankton community. For example, diatoms have a generally lower N:P composition than *Phaeocystis* (Figure 4.4D), hence, a large diatom fraction within a phytoplankton community could reduce bulk N:P relative to a community with a high *Phaeocystis* fraction. Temperature may also influence N:P differently in different phytoplankton groups. Recently, a metanalysis of *Emiliania huxleyi* elemental composition showed no temperature impact on its N:P stoichiometry (Sheward et al., 2023), and a metanalysis of laboratory studies on cold-adapted species show that N:P increases in *Phaeocystis* and possibly centric diatoms with warming, but not in pennate diatoms (Figure 4.4). This may explain the trends of increased N:P with warming observed in (Spackeen et al., 2018b) where the community was dominated (90%) by *Phaeocystis*. However, when these phytoplankton groups are considered under a mixed community setting, the different ways in which temperature impacts N:P can manifest as a net zero effect on bulk N:P composition.

We also noted that the increased P-rich ribosomal fraction with Fe addition did not co-occur with decreased N:P as expected, but in fact was accompanied by increased N:P in BA2 (Figure 4.4). This again challenges prevailing views on how ribosomal abundance could influence N:P in the ocean. Why did we observe this? Upon Fe addition, the

upregulation of Fe-containing N transport and processing proteins could elevate N uptake substantially (Price et al., 1991; Timmermans et al., 1994). This causes a large influx of N relative to the increase in P-rich ribosomes, which may ultimately cause N:P to increase, even when ribosomal abundance increases. Further, the relative abundance of *Phaeocystis* increased with Fe addition in BA2 (Figure 4.2), which may have also contributed to the increase in N:P, given the relatively high N:P in *Phaeocystis*.

Intracellular storage of N and P could also affect N:P stoichiometry and may dampen changes in N:P when ribosomal abundance fluctuates. It is difficult to measure N and P storage in a microbial community, and it is unknown how much storage plays a role in the SO, where N and P are considered constitutively abundant. However, the high concentrations of dissolved N and P in SO waters are conducive to luxury uptake, which implicate storage as a potentially important regulator of macronutrient stoichiometry. Under a 'high storage scenario' where ribosomal contribution to P quota could be minimal (Geider and La Roche, 2002; Raven, 2013a; Liefer et al., 2019), the changes in ribosomal abundance we observed would have little to negligible impact on N:P. Future studies of macronutrient allocation in polar phytoplankton will help clarify the role of storage, and its influence on N:P in the SO. Together, these data suggest that the seemingly straightforward relationship between ribosomal abundance, temperature, and bulk N:P (Toseland et al., 2013) is highly nuanced by community composition, nutrient storage, and distinct responses to change at the organismal level. Further laboratory experiments combining N:P measurements and ribosomal abundance could drastically improve our understanding of N:P drivers in the ocean.

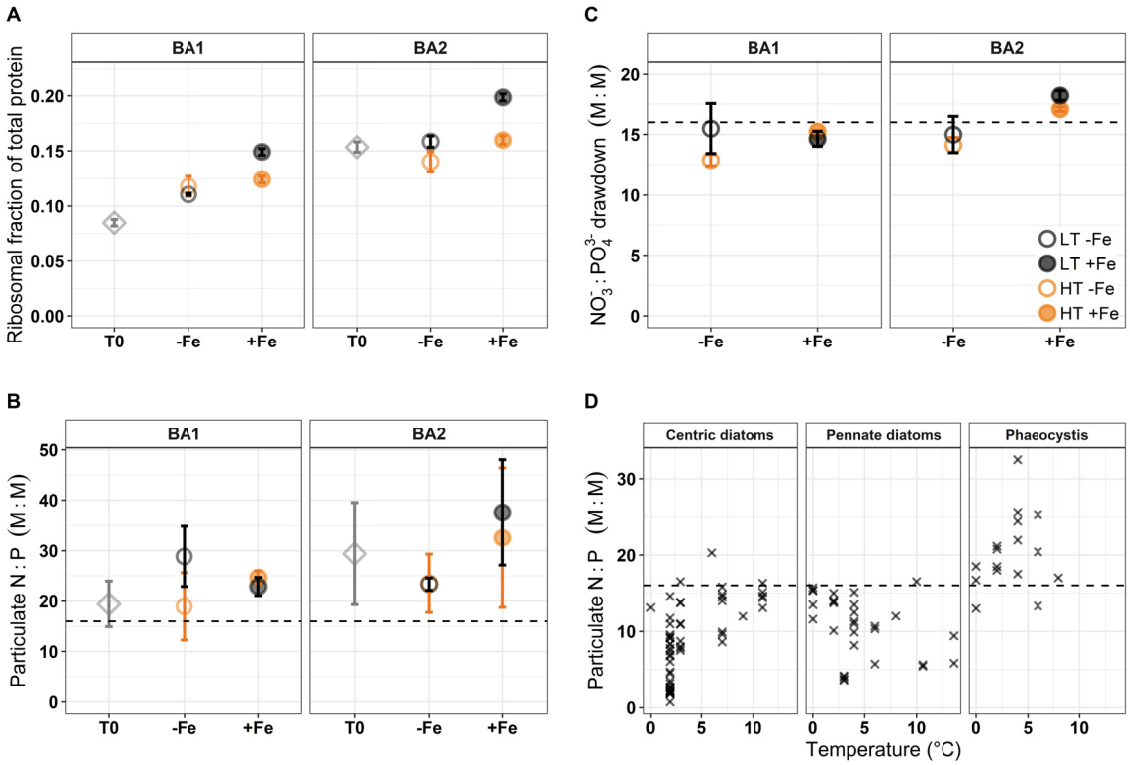

Figure 4.4: Community-wide ribosomal investment is influenced by Fe and temperature, but ribosomal investment is decoupled from N:P. A) Ribosomal protein fraction of total protein abundance (calculated as the sum of all matched peptide intensities). B) Ratio of particulate organic nitrogen to particulate phosphorus at T0 and after 8 days of iron-temperature incubations. C) Ratio of nitrate (NO_3^-) to phosphate (PO_4^{3-}) drawdown (M:M), calculated using NO_3^- and PO_4^{3-} measurements from day 2 and day 8 of iron-temperature incubations. D) Particulate N:P ratios acquired from previously published studies of laboratory cultures grown under nutrient replete conditions and harvested during the exponential phase in semi-continuous or batch growth. See Figure S4.18 for references to all the studies. Centric diatoms include *Thalassiosira* sp., *Chaetoceros* sp., *Skeletonema* sp., and *Odontella* sp. Pennate diatoms include *Pseudo-nitzschia* sp. and *Fragilariopsis* sp. In B, C, and D, dashed horizonal lines represent Redfield N:P ratio of N_{16}:P_1. Error bars represent ± 1 SD and fall within the bounds of points when not visible.

4.4.8 Metaproteomics provides insight into trace metal stoichiometry and utilization strategies

We measured total particulate trace metal (PMetal) concentrations relative to PN to examine trace metal accumulation patterns within the phytoplankton community. As expected, we observed much higher $P^{57}Fe$:PN in the high Fe treatments (Figure 4.5A), showing that the microbial communities consumed a large portion of the Fe we added (Figure S4.20). In BA1, Fe addition did not influence PMn:PN ($p = 0.87$), but caused a significant decrease in PCd:PN ($p = 0.04$), PCu:PN ($p = 0.03$), and PZn:PN ($p < 0.01$). In BA2, Fe addition caused a significant decrease in PMn:PN ($p = 0.01$), PCd:PN ($p = 0.01$), PCu:PN ($p < 0.001$), and PZn:PN ($p < 0.001$). Warming only had a significant effect on PZn:PN in the low Fe treatment in BA1 ($p = 0.04$) (Figure 4.5B-E). Altogether, these trace metal accumulation patterns indicate a generally lower cellular quotas of non-Fe metals under Fe-replete conditions, and vice versa.

Fe and Fe-related protein expression – We observed the upregulation of Fe-containing proteins, including those used in photosynthesis (PSII and PSI proteins, cytochrome b_6f and ferredoxin) and nitrogen metabolism (nitrate and nitrite reductase) after Fe addition (Figure 4.5F, G). These two main protein groups account for a large portion of phytoplankton Fe quotas (Raven, 1988; Raven et al., 1999), and their upregulation after Fe addition is indicative of Fe stress in the in situ community. Additionally, Fe addition caused the downregulation of Fe-stress proteins ISIP-1, ISIP-2 (phytotransferrin) and ISIP-3, which function to improve Fe acquisition and intracellular transport under low Fe (Kazamia et al., 2018; McQuaid et al., 2018; Behnke and LaRoche, 2020). Both non-Fe-containing flavodoxin and rhodopsin proteins were also downregulated after Fe addition (Figure 4.5), suggesting the replacement of Fe-containing proteins with non-Fe containing functional homologs was occurring under low Fe. Previous work has shown that flavodoxin can replace ferredoxin to maintain photosynthesis under low Fe conditions (LaRoche et al., 1996), and rhodopsin may be used to improve photosynthetic efficiency under low Fe (Marchetti et al., 2015), although recent evidence suggests that it may also be involved in nutrient uptake (Bar-Shalom et al., 2023).

Interestingly, we observed the downregulation of a diatom protein cluster annotated as 'fasciclin' after Fe addition (Figure 4.5). That is, both pennate and centric diatoms

produced more of this fasciclin protein when Fe was limited. It has been suggested that fasciclin increases cell surface adhesion in plants and animals, with some evidence suggesting a similar function in diatoms (Huber and Sumper, 1994; Willis et al., 2014; Seifert, 2018). However, its role under Fe stress has not been characterized. We also investigated the global distribution of fasciclin transcripts using The Ocean Gene Atlas v2.0 (Vernette et al., 2022) and found higher fasciclin transcript abundance in the SO and the Equatorial Pacific, both of which are Fe-limited HNLC regions (Figure S4.21). We hypothesize that diatoms invest in fasciclin production under low Fe to increase their adhesion and trapping of micronutrient substrates, similar to how *Phaeocystis* may use exopolysaccharides. Fasciclin may also enhance diatom-bacterial interactions to facilitate Fe uptake from siderophores (Kazamia et al., 2018; Coale et al., 2019; Den et al., 2023), and may improve aggregate formation which increases sinking to more-nutrient rich water. Further investigations of phytoplankton fasciclin and other adhesion molecules will likely yield interesting discoveries regarding their role in mediating nutrient limitation, their influence on phytoplankton-bacterial interactions, and potential impacts on nutrient export and the biological carbon pump.

We then sought to infer the contribution of metalloproteins to trace metal quotas. Recall that we measured specific proteins (e.g. metalloproteins) using relative abundance metrics (i.e. fractions of total protein), but used absolute quantification for trace metal measurements. Here we tested an approach for connecting relative protein abundance with trace metal concentrations using two metalloproteins: 1) Cd-carbonic anhydrase (Cd-CA) and 2) oxygen evolving complex (Mn-cluster) proteins. Cd-CA is involved in the acquisition of inorganic carbon for photosynthesis, and to date, is the only known protein that functions with a Cd cofactor (Lane and Morel, 2000; Lane et al., 2005). Mn-cluster proteins within PSII use Mn to catalyze the splitting of water into O_2, electrons, and protons, which drive photosynthetic electron transport, and ultimately the conversion of solar energy into chemical energy. These two proteins were identified with high confidence within our metaproteomics analyses.

We began by first estimating the concentration of each metalloprotein ($protein_x$) in seawater, using the fractional contribution of the metalloprotein to total protein abundance (Eq. 4.1), where [concentration of $protein_x$] = estimated concentration of metalloprotein in sea water, $\mu g\ L^{-1}$; $protein_x$ = relative abundance of metalloprotein; measured as the total

intensity of all its matching peptides (unitless); total protein = relative abundance of all proteins, measured as the total intensity of all peptides (unitless); [bulkprotein] = bulk protein concentration in sea water in μg L^{-1}, estimated by converting PN to protein using 4.78 g protein / g N, following (Finkel et al. 2016).

$$[concentration\ of\ protein_x] = (protein_x / totalprotein) * [bulkprotein] \quad (4.1)$$

Next, we converted the estimated concentrations of each metalloprotein (μg L^{-1}) into molar concentrations using molar masses from published amino acid sequences. For Cd-CA we used a molar mass based on (Lane et al., 2005). For Mn-cluster, we used an average molar mass based on amino acid sequence in *Fragilariopsis cylindrus* (Mock et al., 2017) and *Thalassiosira pseudonana* (Armbrust et al., 2004). Lastly, we estimated the amount of metal cofactor in each molar amount of metalloprotein by assuming equimolar amount of Cd and Cd-CA (Lane et al., 2005), and four moles of Mn per mole of Mn-cluster protein (Galstyan et al., 2012)

Manganese-containing proteins and Mn quotas – The Mn-cluster in PSII contributes to the majority Mn quota within phytoplankton (Raven et al., 1999; Twining and Baines, 2013). Interestingly, Mn-cluster proteins were upregulated after Fe addition in our experiments (Figure 4.5F, G), even though we did not add Mn, and the dissolved Mn concentrations were very low (Figure S4.7). This Mn-containing protein complex functions in concert with other Fe-containing photosynthetic proteins to drive photosynthesis, and it is therefore likely that its expression is coupled to the expression of Fe-containing photosynthetic proteins by necessity. By this logic, we expect Mn consumption to decrease when Fe availability decreases. However, our data show that this not the case. PMn:PN was not influenced by Fe addition in BA1 and was actually increased under low Fe in BA2 (Figure 4.5B). This indicates that other Mn-containing proteins could play a larger role in phytoplankton Mn quotas under low Fe. Indeed, many phytoplankton taxa rely on Mn-superoxide dismutase (Mn-SOD) for oxidative stress management (Wolfe-Simon et al., 2005), and increase the expression of this protein under Fe limitation (Peers and Price, 2004). The limited number of Mn-SOD peptides detected prevented us from including this

enzyme in our Mn-quota calculations. However, we observed a significant downregulation in Fe-Mn SOD in BA2 after Fe addition, consistent with increased Mn use in SOD under low Fe (it is difficult to disentangle the Fe and Mn isoforms of SOD; it is also possible that the same isoform can use either Fe or Mn depending on availability (Peers and Price, 2004)). We did not observe such an effect in BA1, perhaps due to the very low DMn availability initially. Indeed, our calculations of Mn*, an indicator of Mn-limited growth (Browning et al., 2021), show a lower DMn* in BA1 relative to BA2 (Figure S4.22), indicative of stronger Mn-limitation in BA1 relative to BA2.

Our estimates of metalloprotein contribution to total PMn show that Mn-cluster proteins accounted for virtually all cellular Mn in the high Fe treatments, but less so in the Fe deplete treatment (Figure 4.5H). Further, we estimated a higher abundance of Mn-cluster proteins than could be metalated given the PMn concentrations we measured. While this failure to achieve mass balance may be due to the expected range of error in this type of estimation, we hypothesize that phytoplankton may increase Mn-cluster protein synthesis under Fe-replete conditions, even when Mn availability is low. Increased production of metal-free Mn-cluster proteins could be an anticipatory strategy that primes phytoplankton for growth when Mn becomes available. This also suggests that Mn could increasingly limit primary productivity in the SO if it is not concurrently increased with Fe (Figure S4.22).

Under low Fe, Mn-cluster proteins accounted for 50-80% of cellular Mn (Figure 4.5H). This is consistent with decreased Mn-cluster protein abundance and shows that Mn-SOD, or other Mn-pools, are an important component of the Mn quota when Fe is limited. Intriguingly, these calculations align with estimates in (McCain and Bertrand, 2022) which suggest that Mn-SOD could account for 10-20% of total Mn quota in phytoplankton.

Cd-CA and Cd quotas – Our differential expression analyses showed that Cd-CA (specifically from centric diatoms) was significantly downregulated after Fe addition in both bioassays, consistent with decreased PCd:PN after Fe addition (Figure 4.5C, F, G). Intracellular Cd has been shown to increase under Fe limitation in cultures (Lane et al., 2009) and in the field (Cullen et al., 2003), primarily due to inadvertent uptake through the same Fe-uptake pathways that are upregulated under Fe limitation (Lane et al., 2009). Earlier we showed increased ISIP protein expression under low Fe, which may increase

Cd transport into cells. However, Cd is extremely toxic and phytoplankton must package it safely inside the cell or export it (Ahner et al., 1995; Lee et al., 1996).

In addition to being a potential nuisance, Cd functions as a cofactor in a class of carbonic anhydrases that are essential for inorganic carbon uptake in diatoms. However, our estimates of metalloprotein contribution to total PCd show that Cd-CA contributes to a small amount of total PCd (2-7%) (Figure 4.5I). This raises the question: where does the majority of cellular Cd reside? We are unable to answer this question with our data, but large Cd pools have been shown to exist inside vacuolar polyphosphate granules within *Chlamydomonas*, which help in mediating Cd toxicity (Penen et al., 2017). Further examination of Cd pools within phytoplankton may reveal similar 'safe-storage' strategies, or even novel proteins that use Cd within diatoms or other taxa. Overall, our data also confirm expectations that Cd is unlikely to become a limiting nutrient, given its low requirement relative to supply.

Cu, Zn – We observed exceptionally high PZn:PN ratios in both bioassays, indicating high Zn quotas in SO phytoplankton. Recently, Zn-finger proteins have been shown to play an important role in supporting photosynthetic processes in low-temperature regions (Ye et al., 2022), which, in addition to high Zn availability in SO surface waters (Roshan et al., 2018), could explain the high Zn quotas in our study. Both PZn:PN and PCu:PN were also higher under low Fe, which suggests that phytoplankton use these two metals preferentially under Fe stress. Plastocyanin, a Cu-containing protein, has been shown to replace Fe-containing cytochrome c_6 under low Fe (Peers and Price, 2006), however, we observed constitutive plastocyanin expression in our study, consistent with (Jabre et al., 2021). Thus, the increase in PCu under low Fe indicates a larger role for Cu in Cu-SOD, a protein that was more abundant under low Fe (Figure 4.5). Improved characterization and annotation of metalloproteins (see recent advances in Aptekmann et al. (2022)), could help us identify potentially important proteins that are involved in trace metal use within phytoplankton cells.

Our coupling of protein measurements with trace-metal quotas provided novel field evidence for increased use of non-Fe metals and non-Fe metalloproteins under Fe-limitation. This highlights the utility of metaproteomics in understanding metalloprotein function,

and the dynamics of trace metal use within phytoplankton. Future experiments using standards for absolute quantification of metalloproteins along with trace metal measurements could improve estimates of metalloprotein contribution to metal quotas, which ultimately enhances the utility of proteomics in studying protein-metal dynamics.

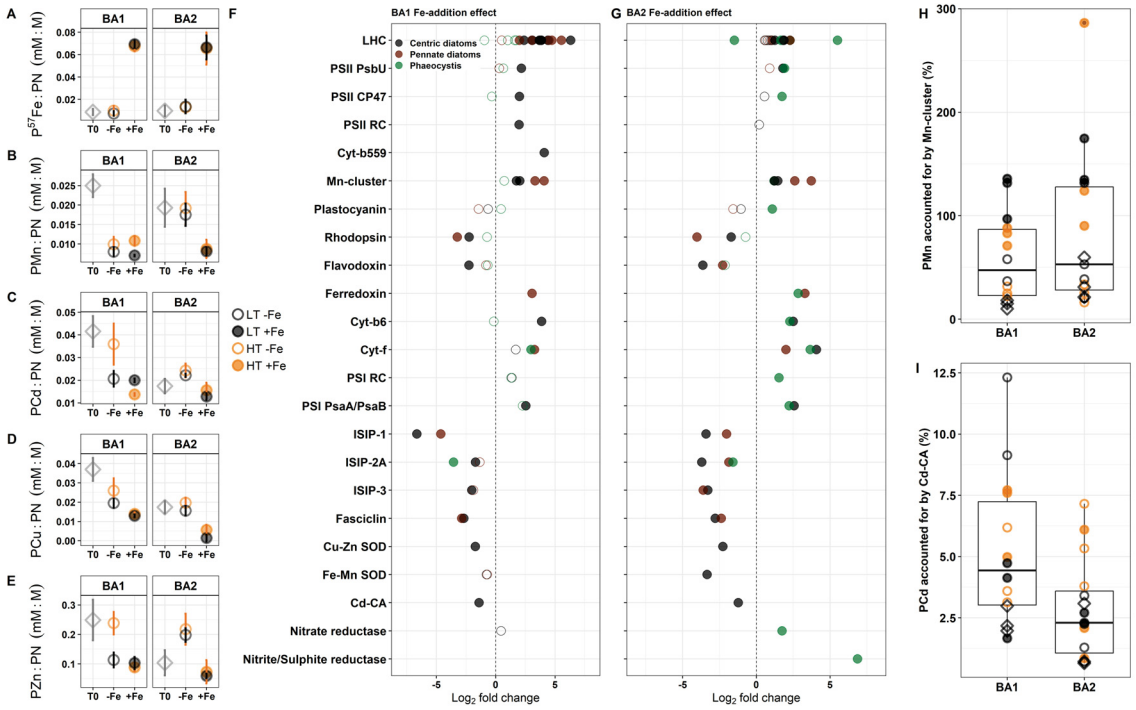

Figure 4.5: Metaproteomics provide a link between trace metal stoichiometry and cellular utilization strategies. Ratio of particulate. A) ^{57}Fe, B) Mn, C) Cd, D) Cu, and E) Zn to particulate N (mM:M) at T0 and after 8 days of iron-temperature incubations. F, G) Differential expression of various metal-related, taxon-specific proteins (protein clusters) of interest after iron addition in Bioassay 1 and Bioassay 2. Filled circles represent statistically significant differential expression (adjusted P-value < 0.05). Positive Log2 fold change represents increased abundance after iron addition, negative Log2 fold change represents decreased abundance after iron addition. H) Contribution of Mn-cluster protein (oxygen evolving complex) to the total particulate Mn measured at T0 and after 8 days or iron-temperature incubations. Boxplots show the median, first and third quartile values for each bioassay, with whiskers showing minimum and maximum values. I) Contribution of cadmium carbonic anhydrase (Cd-CA) protein to the total particulate Cd measured at T0 and after 8 days or iron-temperature incubations. Boxplots show the median, first and third quartile values for each bioassay, with whiskers showing minimum and maximum values. In A-F, error bars represent ± 1 SD and fall within the bounds of points when not visible. In F, LHC = light harvesting complex proteins, PSII = photosystem II, cyt = cytochrome, Mn-cluster = manganese cluster / oxygen evolving complex proteins, PSI = photosystem I, ISIP = iron stress induced protein, SOD = superoxide dismutase, Cd-CA = cadmium carbonic anhydrase.

4.5 Conclusions

In this study, we investigated the responses of two distinct phytoplankton communities in the Weddell Sea to changes in Fe and temperature. We found that slight warming alone, within the bounds of expected temperature fluctuations in the region, had minimal effects on growth, nutrient drawdown, community composition, and protein expression patterns. However, we found that Fe was a strong driver of growth and nutrient drawdown, and influenced the stoichiometry of Si and trace-metal consumption. These findings suggest that changes in Fe availability could have large impacts on nutrient stoichiometry in the SO. The amplified effects of Fe addition and warming on growth and nutrient drawdown indicate that even slight warming could exert substantial influence on ecological and biogeochemical processes in the SO when Fe availability is dynamic.

Our metaproteomics surveys of these communities revealed that ribosomal investment plays an important role in influencing growth, but ribosomal abundance does not influence N:P stoichiometry. This suggests that other mechanisms, such as community composition, nutrient uptake, and storage may play a larger role in influencing N:P stoichiometry in the ocean. In addition, we implemented a novel approach to estimate the trace-metal contribution of metalloproteins using untargeted metaproteomics measurements. This led to new insight into trace metal use within phytoplankton cells, and shed light on potential shifts in trace metal allocation under changing conditions. Altogether, our data underscore the utility of using metaproteomic measurements to understand phytoplankton growth, ecology and biogeochemical processes in today's and future oceans.

4.6 Materials and Methods

4.6.1 Experimental setup

We conducted two Fe-temperature bioassay incubation experiments during the austral summer of 2018-2019 in the Weddell Sea, Southern Ocean. The first bioassay (BA1) was initiated on December 28, 2018, approximately 560 km away from the ice edge at 65 °S 0.038 °E. The second bioassay (BA2) was initiated on January 9, 2019, approximately 70 km from the ice edge at 70.15 °S 11.02 °W (Figure 4.1). For both bioassays, we collected sea water at ca. 21 m depth using a custom built ultraclean CTD sampling system – "Titan" – equipped with PRISTINE high volume samplers (De Baar et al., 2008; Rijkenberg et al., 2015). This depth minimized trace metal contamination from the ship, and coincided with phytoplankton biomass maxima (Figure S4.6). Titan was moved into a dedicated, temperature-controlled, trace-metal-clean (TMC) laboratory container where sea water was used for initial (T0) sampling and to fill triplicate, 20 L, TMC cubitainers for each Fe-temperature treatment.

The treatment matrix included four Fe-temperature conditions: low Fe – low temperature, high Fe – low temperature, low Fe – high temperature, high Fe – high temperature. We did not add any Fe to the low Fe treatments. We supplemented the high Fe treatments with a naturally occurring but rare isotope of ^{57}Fe, which allowed us to differentiate between the added Fe and Fe already present in the water (predominantly ^{56}Fe). For this, we made a 40 μM $^{57}FeCl_3$ stock solution in 0.1 M trace-metal grade HCl, then added 1 mL of this stock to each of the high Fe cubitainers. This resulted in a total initial dissolved ^{57}Fe concentration of 2 nM. We then sealed the cubitainers and placed them inside temperature-controlled deck incubators where the low temperature treatments were incubated under in situ temperature, and the high temperature treatments were incubated under in situ +2 °C (Table 4.1). We note that the incubators could not maintain the frigid in situ temperature in BA2, so we adjusted the temperature by an additional 0.4 °C for all treatments in this bioassay. We used black mesh screens to keep light at 15-20% of incident inside the incubators, which ensured light-saturated growth without inducing photodamage. We maintained the incubations for eight days and subsampled at different time points for various measurements (Table S4.3). When necessary, we followed previously described TMC protocols for cleaning, water collection, and sample processing (Cutter et al., 2017;

van Manen et al., 2022; Tian et al., 2023).

Table 4.1: Temperature and iron treatment matrix for Bioassay 1 (BA1) and Bioassay 2 (BA2). In BA2, temperature was kept at an additional 0.4 °C due to difficulty maintaining in situ temperature (-1.4 °C).

	Treatment	Temperature	Iron added
BA1	Low iron – low temperature	-0.3 °C (in situ)	-
	High iron – low temperature	-0.3 °C (in situ)	+2 nM ^{57}Fe
	Low iron – high temperature	1.7 °C (in situ +2 °C)	-
	High iron – high temperature	1.7 °C (in situ +2 °C)	+2 nM ^{57}Fe
BA2	Low iron – low temperature	-1.0 °C (in situ +0.4 °C)	-
	High iron – low temperature	-1.0 °C (in situ +0.4 °C)	+2 nM ^{57}Fe
	Low iron – high temperature	1.0 °C (in situ +2.4 °C)	-
	High iron – high temperature	1.0 °C (in situ +2.4 °C)	+2 nM ^{57}Fe

4.6.2 Photophysiology

We measured the photosynthetic efficiency of photosystem II (F_v/F_m) using onboard pulse amplitude modulated fluorometry (Heinz Walz GmBH, WATER-PAM, Red LED WATER-ED cuvette version) through a Water-K quartz cuvette. A 3.5 mL sample from each biological replicate was dark acclimated in the cold for 2-4 hours prior to measurement, and the cuvette was rinsed with ultra-pure water between replicates. The WATER-PAM was blanked for each bioassay using 0.2 μm filtered seawater from the respective bioassay locations. The Ft value was kept between 100 and 1000 by adjusting the PM-Gain and blanking was repeated after PM-Gain adjustment. We calculated F_v/F_m as the ratio of variable to maximum fluorescence, where $F_v = F_m - F_0$, and F_0 = minimum fluorescence.

4.6.3 Pigments

We collected samples for chlorophyll a (chl-a) and other pigments using gentle vacuum filtration through GF/F glass microfiber filters (Whatman, 0.7 μm pore size, 47 mm diameter) under dark and cold conditions. Enough water was filtered from each biological replicate to display a green colour on filters (mean volume: 1.1 L, range: 0.54 – 2.65 L).

Filters were double wrapped in aluminium foil, flash frozen in liquid nitrogen and stored at -80 °C until further laboratory analysis.

We freeze dried the filters and extracted pigments in the dark for 48 hours at 4 °C using 5 mL of 90% acetone (van Leeuwe et al., 2006). High-performance liquid chromatography (HPLC) pigment separation was then conducted on a Waters HPLC system (model 2690) using a 3.5 μm particle size Zorbax Eclipse XDB-C8 column, and an autosampler set to 4°C (Van Heukelem and Thomas, 2001). Pigment detection was based on retention time and diode array spectroscopy at 346 nm (Waters 996 Photodiode Array Detector). Pigment quantification was based on standard curves using DHI LAB pigment standards. We then used CHEMTAX v1.95 (Mackey et al., 1996) to determine taxonomic phytoplankton community composition (expressed as fraction of total chl-a) using initial pigment ratios for diatoms, two groups of chlorophyll-c3-containing algae (here called haptophytes and pelagophytes), cryptophytes, chlorophytes, and dinoflagellates (Eich et al., 2022).

4.6.4 Flow cytometry

We collected 2 mL of unfiltered water as well as size fractioned samples from each biological replicate. For the size fractioned samples, we sequentially filtered a 20 mL sample from each replicate through 20, 10, 8, 5, 3, 2, 1, 0.8 and 0.6 μm polycarbonate filters (Isopore, 25 mm diameter) using a plastic syringe and filter holder (Whatman). The filtrate from each size fraction (2 mL) and the unfiltered samples were fixed with formaldehyde-hexamine for 15-30 minutes at 4 °C, then flash frozen in liquid nitrogen and stored at -80 °C until further laboratory analysis.

We performed flow cytometric analyses on a BD-FACSCalibur Flow Cytometer equipped with a 488 nm Argon laser. The average flow rate through a 20 μm inlet filter was 97.3 μL min^{-1}, and the trigger was set on red autofluorescence (Marie et al., 1999). Cell populations were differentiated based on red chl-a autofluorescence and side scatter using FCS Express 5 software (De Novo Software). Cryptophytes were identified by their orange phycoerythrin autofluorescence. We identified a potential *Phaeocystis* sp. (most likely *Phaeocystis antarctica*) group by comparing the chl-a autofluorescence and side scatter patterns from the bioassay samples with those of isolated, broken up *Phaeocystis* colonies. We estimated cell diameter based on filter pore size fractions, and converted these estimates into volume by assuming spherical dimensions for all cells.

4.6.5 Dissolved macronutrients

We measured nitrate, phosphate and silicate (silicic acid) on board the ship using a four-channel Auto-Analyzer (QuAATRo, Seal Analytical, Germany), following the Joint Global Ocean Flux Study protocols described in (Gordon et al., 1993). Briefly, we syringe filtered 125 mL from each biological replicate through 0.2 μm Acrodisc® filters, and collected the filtrate in polyethylene bottles that were rinsed three times with the filtrate before use. When immediate measurements were not possible, we stored the samples in capped bottles at 4 °C for a maximum of five hours. We made ten-point calibration curves daily by diluting stock solutions of the different nutrients in 0.2 μm filtered low-nutrient seawater. We also analyzed a certified reference material (KANSO, Japan) containing known concentrations of nitrate, phosphate, and silicate in Pacific Ocean water with each run. All samples and standards were brought up to 21 °C before measurements were taken.

4.6.6 Particulate macronutrients

We collected samples for particulate organic carbon (POC) and particulate nitrogen (PN) using vacuum filtration through pre-combusted GF/F glass microfiber filters (Whatman, 0.7 μm pore size, 25 mm diameter). We filtered 1 L from each biological replicate, wrapped the filters in aluminum foil, and then stored them at -20 °C until further laboratory analysis. We analyzed POC and PN using a Thermo-Interscience Flash EA1112 Series Elemental Analyzer (Thermo Scientific) with a detection limit of 100 ppm and a precision of 0.3% (Verardo et al., 1990). Briefly, samples were flash combusted with excess oxygen at 900 °C to convert organic carbon and particulate nitrogen into CO_2 and N_2 gas. A helium carrier gas was then used to transfer the CO_2 and N_2 into the elemental analyzer for measurement. We also measured filter and sample handling blanks, and subtracted the blank measurements from sample measurements. The sampling and analysis methods for particulate phosphorus are described in the trace metal measurements section below.

4.6.7 Trace metal measurements

We sampled for both dissolved and particulate trace metals, and measured all metal and particulate phosphorus (P) concentrations using High Resolution Inductively Coupled Plasma Mass Spectrometry (HR-ICP-MS). For this, we followed strict TMC protocols

during sampling and sample processing (Cutter et al., 2017; van Manen et al., 2022; Tian et al., 2023).

Dissolved trace metal sampling and sample processing – To separate the dissolved trace metal fraction from the particulate fraction, we filtered water from each biological replicate through pre-cleaned 0.2 μm filter cartridges (AcroPak). We collected the filtrate in acid cleaned 125 mL LDPE bottles that were rinsed five times with the filtrate before use. We then acidified the samples using trace-metal grade Baseline® HCl (Seastar Chemicals Inc) to a final concentration of 0.024 M HCl, which resulted in a pH of $\sim$1.8. We stored the samples at room temperature until further laboratory analyses.

In the laboratory, we preconcentrated the dissolved trace metals from the acidified samples following methods in (Gerringa et al., 2020; Middag et al., 2023). Briefly, we passed each sample through a SeaFAST-pico preconcentration system (ESI, USA), with two 10 mL loops for a total sample volume of 20 mL. With this, we concentrated each sample into 350 μL of elution acid (double distilled 1.5 M HNO_3) containing rhodium (Rh) as internal standard, and then stored at room temperature until further analysis with HR-ICP-MS.

Particulate trace metal and phosphorus samples – Here we used polyethersulfone (PES) filters (25 mm, 0.45 μm Pall Supor) placed on polypropylene filter holders (Advantec) with polypropylene luer-locks (Cole-Palmer) to capture the particulate trace metal fraction. We pre-cleaned the filters and filter holders by boiling three times in distilled 1.2 M HCl (VWR Chemicals – AnalaR NORMAPUR) at 60 °C for 24 h, then rinsing with ultrapure MQ water 5 times, and eventually storing in ultrapure MQ water before use (Ohnemus et al., 2014). After sampling, we stored the PES filters in acid-cleaned Eppendorf vials at -20 °C until further laboratory analysis.

We digested the particulate trace metal (and P) samples in two successive steps to capture the labile and refractory fractions separately, following methods in (van Manen et al., 2022; Tian et al., 2023). We summed the measurements from these two fractions to get the total particulate metal and P measurements shown in this study. Briefly, we first solubilized the labile fraction by subjecting the PES filters to a weak leach, consisting of 1.8 mL solution of 4.35 M acetic acid (double distilled using PFA Savillex stills, VWR

NORMAPUR) and 0.02 M hydroxylamine hydrochloride (Sigma-Aldrich – 99.999% trace metal basis). The vials were heated to 95 °C for 10 minutes in a water bath and were subsequently cooled down to room temperature. After two hours, the filters were moved to a 30 mL Teflon vial (Savillex), and the remaining leachate was centrifuged at 16000 RCF for 10 minutes to bring any remaining particles to the bottom of the solution in the vials. Next, 1.6 mL of leachate was transferred to a separate 30 mL Teflon vial (Savillex) and 100 μL of concentrated HNO_3 (double distilled, AnalaR NORMAPUR) was added. The vials were then heated to dryness at 110 °C, re-dissolved in 2 mL of 1.5 M HNO_3 with 10 ng mL^{-1} Rh as internal standard, and stored at room temperature for subsequent analysis by HR-ICP-MS.

For the refractory fraction, we transferred the remaining 0.2 mL of leachate from the labile leach vials to the Teflon vials already containing the PES filters – we corrected for the 0.2 mL labile leachate in the refractory fraction. Next, we added a 2 mL solution of 8.0 M HNO_3 (triple distilled, VWR Chemicals – AnalaR NORMAPUR) and 2.9 M HF (Supelco, Ultrapur), and refluxed the capped samples for 4 hours at 110 °C. Afterwards, we cooled the samples to room temperature and poured the contents into secondary Teflon vials (Savillex) without transferring the filters. We then heated the secondary Teflon vials to dryness at 110 °C, redissolved the contents in a 1 mL a solution of 8.0 M HNO_3 and 15% H_2O_2 (Merck – Suprapur), refluxed for second time for 1 hour at 110 °C, and again heated to dryness at 110 °C. Lastly, we redissolved the samples in 2 mL of 1.5 M HNO_3 with 10 ng mL^{-1} Rh as internal standard, and stored them at room temperature for subsequent analysis by HR-ICP-MS.

HR-ICP-MS methods – We analyzed the samples using Thermo Scientific Sector Field High Resolution Element 2 mass spectrometer, with a microFAST introduction system (ESI, USA) equipped with a PFA nebulizer. Detailed HR-ICP-MS methods are described in (Gerringa et al., 2020). We blank-corrected the measurements for contaminants from sample handling, reagents and filters, following (van Manen et al., 2022; Tian et al., 2023). The accuracy and precision of the measurements were determined by measuring GEOTRACES community consensus reference materials SAFE D1, GSC and GSP as well as in-house reference seawater samples. Rh was used as an internal standard and drift standards were measured after every block of 13 samples to correct for drift during the runs. We calculated trace metal and P concentrations using a mixed solution of elemental

standards.

4.6.8 Protein sample preparation

We used a peristaltic pump system to sequentially filter 2-4 L from each biological replicate through 12, 3.0, and 0.2 μm polycarbonate filters (Isopore, 47 mm diameter). Filters were then stored at -80 °C until further laboratory analysis.

We extracted and digested proteins from filters using methods previously described in (Joy-Warren et al., 2022). Briefly, 600 μL of sodium dodecyl sulphate (SDS) lysis buffer (2% SDS, 0.1 M Tris/HCl pH 7.5, 5% glycerol, 5 mM EDTA) was added to each sample, followed by a 10-minute incubation on ice then a 15-minute incubation in a benchtop thermomixer (Eppendorf Thermomixer C) at 95 °C and 350 RPM. Samples were then sonicated on ice for one minute using a QSonica125 microprobe (50% amplitude, 125 W, 15 second on/off pulses) and left at room temperature for an additional 30 minutes. The extracted proteins, which were suspended in SDS lysis buffer at this point, were obtained by removing the filters and centrifuging the samples at 15000 × g for 30 minutes to pellet cellular debris. After this, we acquired the protein-containing supernatant and pooled the three different size fractions from each biological replicate by combining an equal volume from each fraction. We quantified bulk protein concentrations using a Pierce Micro BCA Protein Assay Kit following manufacturer's protocol.

We used S-Trap mini columns (PROTIFI) to remove SDS lysis buffer from the samples and digest the extracted proteins. Samples were first reduced and alkylated using 5 mmol L^{-1} dithiothreitol and 15 mmol L^{-1} iodoacetamide respectively, then denatured using 12% phosphoric acid. Samples were then diluted with S-trap buffer (pH 7.1, 100 mmol L-1 tetraethylammonium bicarbonate in 90% aqueous methanol) (1_{sample}:7_{buffer}, v:v) and loaded onto the S-trap columns. Once on column, we washed each sample 10 times with 600 μL S-trap buffer to remove the SDS. Proteins were then digested on-column using trypsin ($1_{trypsin}$trypsin:$25_{protein}$, μg:μg) at 37 °C for 16 hours. Tryptic peptides were eluted from the S-Trap columns with a series of 50 mmol L^{-1} ammonium bicarbonate, 0.2% aqueous formic acid, and 50% acetonitrile 0.2% formic acid washes. Samples were then desalted on pre-conditioned 50 mg C18 columns (HyperSep), dried using a Vacufuge Plus (Eppendorf), and finally resuspended in a 1% formic acid 3% acetonitrile solution prior to liquid chromatography – tandem mass spectrometry (LC-MS-MS).

4.6.9 LC-MS-MS

We performed duplicate injections for each biological replicate on a Dionex UltiMate 3000 RSLC-nano LC system (Thermo Scientific) coupled to a Q-Exactive hybrid quadrupole-Orbitrap mass spectrometer (Thermo Scientific). Peptides (1 μg per injection) were separated by reverse phase chromatography under a non-linear gradient (Table S4.4) with a self-packed column (50 cm x 0.1 mm ID) containing JUPITER Proteo C18 resin. The mass spectrometer was operated in data-dependent acquisition mode – detailed mass spectrometer settings are shown in (Table S4.5).

4.6.10 Metaproteomics bioinformatics and data analysis

We assessed instrument and acquisition performance by analyzing the unprocessed raw mass spectrometry files using RawTools v2.0.7 (Kovalchik et al., 2019). We then converted the – quality checked – raw files into standardized mzML format using ThermoRawFileParser v1.4.0 (Hulstaert et al., 2020) before further analysis.

Reference database – We used a reference SO metatranscriptome database (Jabre et al., 2021) to match the acquired mass spectra with peptides. Briefly, samples for this database were collected from surface water in the McMurdo Sound, SO, on January 15, 2015 which were subjected to Fe-temperature experimental incubations as described in Jabre et al 2021. Sequencing was performed via Illumina HiSeq, transcript contigs were assembled de novo using CLC Assembly Cell, and open reading frames (ORFs) were predicted using FragGeneScan (Rho et al., 2010). We filtered ORFs to eliminate those with less than 50 reads total across all samples, and annotated for putative function using hidden Markov models and BLAST-p against PhyloDB (Bertrand et al., 2015). ORFs were assigned a taxonomic affiliation based on best Lineage Probability Index (Podell and Gaasterland, 2007; Bertrand et al., 2015). Lastly, we grouped ORFs into protein clusters by sequence similarity using Markov clustering (Enright, 2002), and consensus cluster annotations were based on KEGG, KO, KOG, KOG class, Pfam, TIGRfam, EC, GO. See Jabre et al. (2021) for detailed methods on metatranscriptome sample collection, processing and analysis.

Database searching – We matched the acquired mass spectra with peptide sequences from the reference database using MSGF+ within OpenMS (Kim and Pevzner, 2014;

Röst et al., 2016). We first appended the reference database with a database of common contaminants from the common Repository of Adventitious Proteins (The Global Proteome Machine Organization), and then removed redundant sequences using Python script by P. Wilmarth (github.com/pwilmart/fasta_utilities). We conducted the search using a 10-ppm precursor mass tolerance, and set cysteine carbamidomethylation as a fixed modification, and methionine oxidation and N-terminal glutamate to pyroglutamate conversion as variable modifications. Lastly, we filtered peptide-spectral matches at a 1% false discovery rate using a target-decoy strategy, where 'target' represents all the sequences in the database and 'decoy' represents all the database sequences in reverse (Elias and Gygi, 2007).

Peptide quantification – We grouped the duplicate LC-MS-MS injections for each biological replicate and aligned the retention times within each of these groups using MapAlignerIdentification (Weisser et al., 2013). We then matched unknown features in one injection with identified peptide features from the other injection, which allowed us to improve the number of peptide identifications in each sample. We then calculated feature intensity (i.e. relative peptide abundance) based on MS1 ion intensity using FeatureFinderIdentification (Weisser and Choudhary, 2017).

Peptide annotation – We mapped peptides to corresponding ORFs for protein cluster assignment, and for functional and taxonomic annotations. Peptides mapping to one or more ORFs from the same cluster or functional annotation were annotated with that cluster / function. Peptides mapping to ORFs with different clusters / functional annotations were annotated with "ambiguous cluster" / "ambiguous function". We then assigned a taxonomy string to each peptide by resolving taxonomic affiliation at the genus level, or, when not possible, by gradually progressing through taxonomic rank until a non-ambiguous taxonomic level is found. That is, peptides mapping to one or more ORFs from the same genus (e.g., *Fragilariopsis*) were annotated down to genus (eukaryote-stramenopile-bacillariophyte-pennate-*Fragilariopsis*). Peptides that were ambiguous at the genus level (e.g., mapping to both *Fragilariopsis* (pennate diatom) and *Chaetoceros* (centric diatom) ORFs) were annotated down to the class level as "ambiguous diatom", and so on. Peptides that could not be resolved at the domain level were annotated as "ambiguous domain".

Database suitability – Untargeted metaproteomics experiments like ours generate relative abundance measurements that must be normalized before making comparisons

across samples. Several factors influence these abundance values and complicate their normalization, including the suitability of the reference database and heterogeneity of non-peptide features across samples. Here, we expanded upon previously established methods in (McCain et al., 2022) to test database suitability and to find an appropriate normalization method for our data.

We calculated and correlated three different abundance metrics using our metaproteomics data. I) We calculated the summed total ion current (TIC) for each sample using pyOpenMS (Röst et al., 2014). TIC is a database independent sum of all mass spectral peak intensities measured throughout a run, and therefore includes background noise and contamination, in addition to all measured peptides. II) We identified peptide-like features based on feature resemblance to the isotopic distribution of a theoretical peptide model, "averagine" (Senko et al., 1995), and quantified their total abundance for each sample using Hardklör and Krönik (Hoopmann et al., 2012). The total abundance of peptide-like features is also database independent but is less influenced by background noise and contamination. III) We calculated the abundance of all matched peptides for each sample (see previous methods on database searching and peptide quantification). This approach is database dependent and can therefore be biased by database suitability. A strong correlation between these three metrics would indicate that either one can be used for normalizing our relative abundance measurements. We also used the number of matched peptides and the contribution of matched peptide abundance to the peptide-like feature abundance to evaluate database suitability.

Community composition – We calculated the fractional contribution of various taxonomic groups to the metaproteome by summing the abundance of peptides within each taxonomic group and dividing by the total abundance of all matched peptides (e.g., sum of all centric diatom peptide intensities / sum of all peptide intensities). We focused our analyses at taxonomic resolutions with a high enough number of identified peptides for confident comparison of protein expression across and within treatments (Figure S4.11). These taxa were pennate diatoms, centric diatoms, and *Phaeocystis*.

Proteins and protein group abundances – We first used a coarse-grained clustering approach based on (McCain et al., 2022) to pool peptides into three distinct metabolic categories: light-reaction photosynthetic proteins, RuBisCO and ribosomal proteins. For

this, we searched protein annotations against character strings that capture these groups. The photosynthesis group included all peptides with 'photosyn*' or 'light-harvesting complex' or 'flavodoxin' or 'plastocyanin' in their annotation. The RuBisCO group included all peptides with 'RuBisCO' or 'rubisco' or 'bisphosphate carboxylase' in their annotation. The ribosome group included all peptides with 'ribosom*' in their annotation. The asterisk (*) in the character string represents a wildcard character. We also used a finer grained approach to examine the abundance and differential expression patterns of specific proteins (e.g. Flavodoxin). For this, we searched protein annotations against character strings specific to the proteins of interest, and used MCL clusters to define a protein/protein group.

4.6.11 Statistical analysis and visualization

We performed all statistical analyses and visualizations using various packages in R v4.2.1 (Team, 2022). Differential expression and fold-change analyses were conducted on taxon-normalized protein cluster abundance values using Bayes quasi-likelihood F-tests with the glmQLFTest function in edgeR v4.2 (Robinson et al., 2010). For this, we first filtered that data to remove any protein clusters with fewer than two matched peptides. We then imputed missing values via random forest-based imputation (Jin et al., 2021) using the missForest v1.5 package (Stekhoven and Bühlmann, 2012), and excluded any proteins that were not detected in at least 75% of all samples. Fe effect was determined by comparing the low-Fe to the high-Fe treatments. Temperature effect was determined by comparing the low-temperature to high-temperature treatments under low Fe. Fe-temperature interaction was determined by comparing low-Fe low-temperature treatment to high-Fe high-temperature treatment. An FDR adjusted P-value of 0.05 was used for statistical significance. NMDS ordination analysis was conducted in two dimensions with 1000 maximum random starts using the Vegan v2.6.2 package. We used two-way ANOVA followed by Tukey's HSD testing to examine the effects of Fe and temperature where indicated. The R packages ggplot2 v3.4.1 networkD3 v0.4, cowplot v1.1, and ggOceanMaps v1.2.6 (Vihtakari, 2022) were used for data visualization.

4.6.12 Data and code availability

All proteomics data including the raw mass spectrometry files and processed data files have been deposited to the ProteomeXchange Consortium via the PRIDE partner repository (Perez-Riverol et al. 2021) with the dataset identifier "PXD042627" and "10.6019/PXD042627". All other data will be deposited to a data repository prior to paper submission. All code for bioinformatics analyses, statistical testing, and data visualization is available at `github.com/bertrand-lab/ps117_metaP`.

4.7 Acknowledgments

We thank RV Polarstern captain and crew, Prof Olaf Boebel, Chief Scientist for PS117 expedition, and the entire PS117 science team. We are indebted to Sharyn Ossebaar for taking the dissolved macronutrient measurements onboard the ship, and to John Seccombe from Aquahort for his support in conceiving and building the incubators and for his remote support during the expedition. This study was funded by NSERC Discovery Grant RGPIN-2015-05009 to E.M.B, Simons Foundation Grant 504183 to E.M.B, Simons Foundation CBIOMES Award ID 1001702 to E.M.B, Canada Research Chair Support to E.M.B; ALWPP.2016.020 from the Dutch Research Council (NWO) to R.M, Nova Scotia Graduate Scholarship to L.J.J.

4.8 Supporting Information

4.8.1 Supplemental Figures

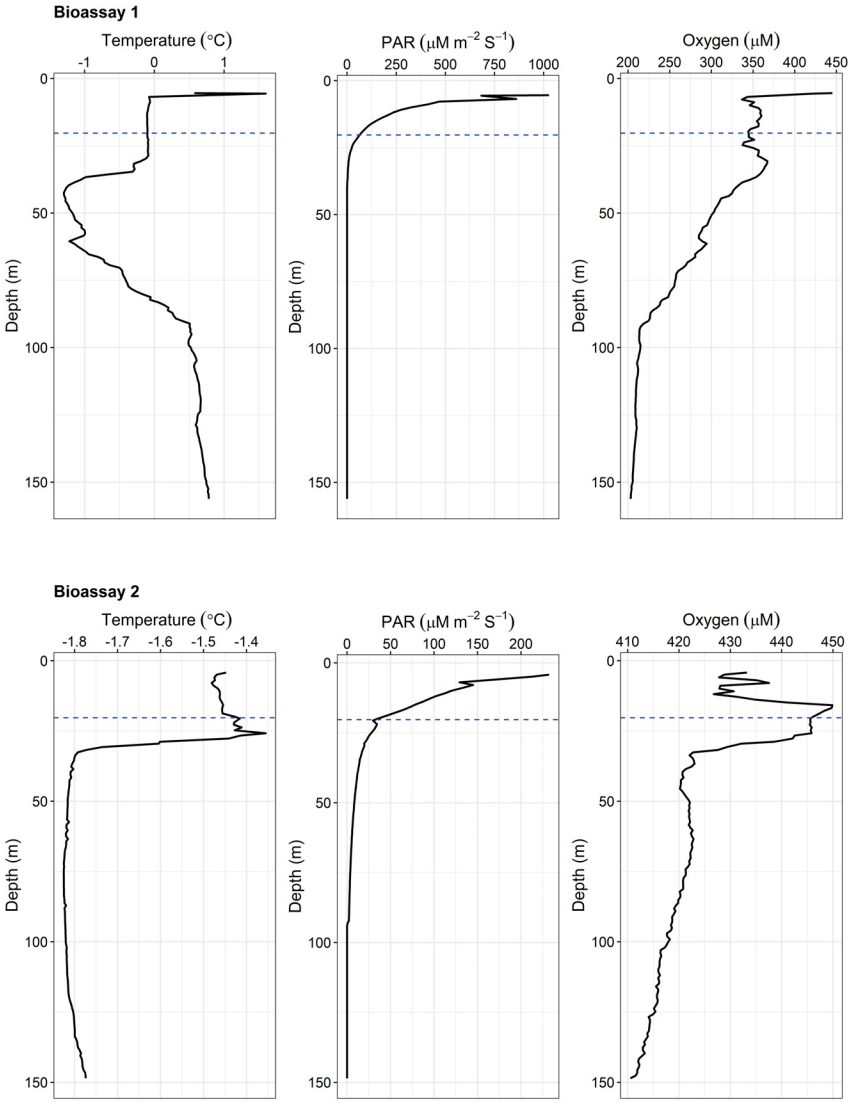

Figure 4.6: Temperature, photosynthetically active radiation (PAR) and oxygen concentration from the CTD instrument downcast prior to water collection for bioassay incubations. Horizontal dashed lines indicate sampling depth for each. Due to the lack of chlorophyll-a sensor data on these casts, we used oxygen measurements as a proxy for photosynthesis to determine phytoplankton biomass maxima.

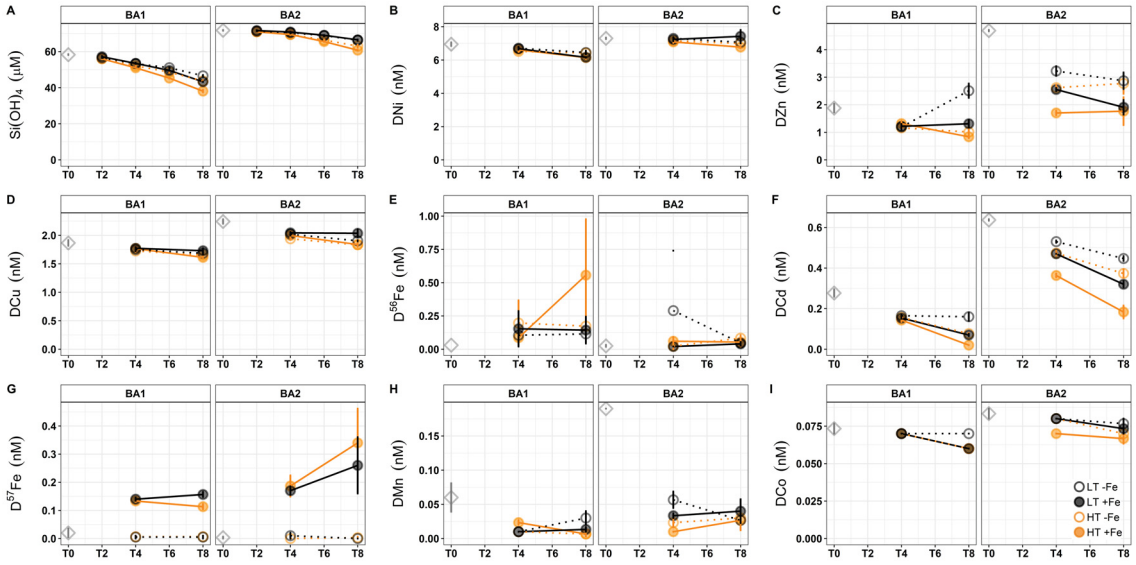

Figure 4.7: Dissolved concentrations of A) silicate, measured as silicic acid ($Si(OH_4)$, B) Nickle, C) Zinc, D) Copper, E) ^{56}Iron (the most abundant iron isotope in the ocean) F) Cadmium, G) ^{57}Iron (the isotope we used in the iron addition treatments), H) Manganese, and I) Cobalt, all taken at different time points during the incubation period in Bioassay 1 and Bioassay 2. Error bars represent ± 1 SD and fall within the bounds of points when not visible.

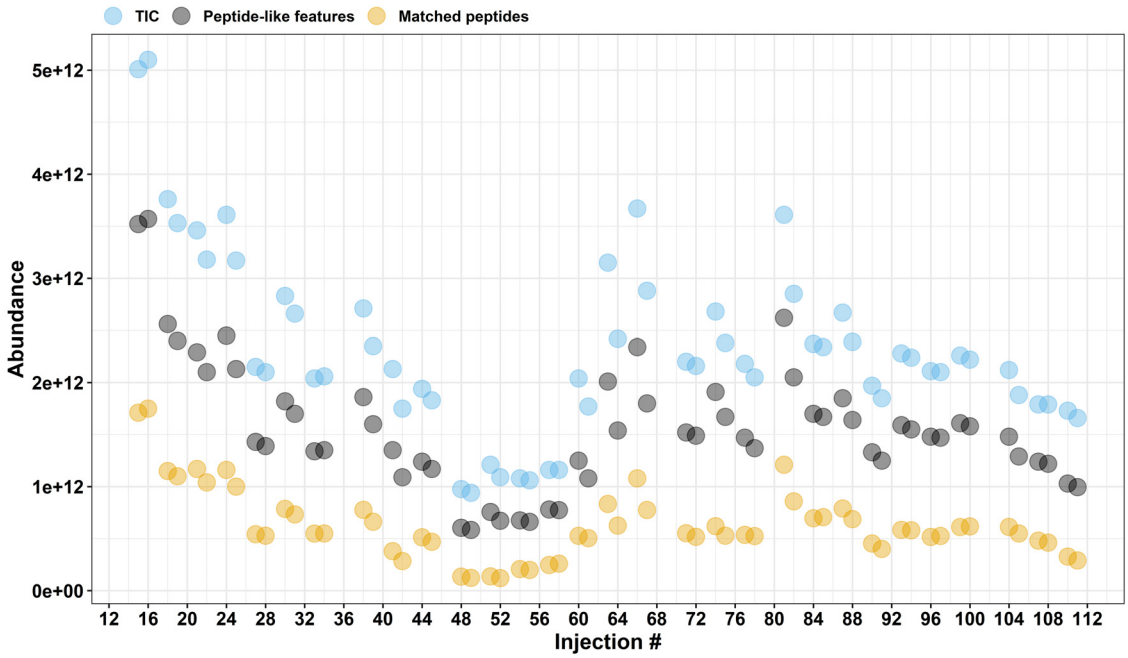

Figure 4.8: Abundance of total ion current (TIC), all peptide-like features, and all matched peptides across all injections. Injection numbers are ordered from earlier to later injections to show the mass spectrometry run progression. Sample details for each injection number are shown in Table S4.2

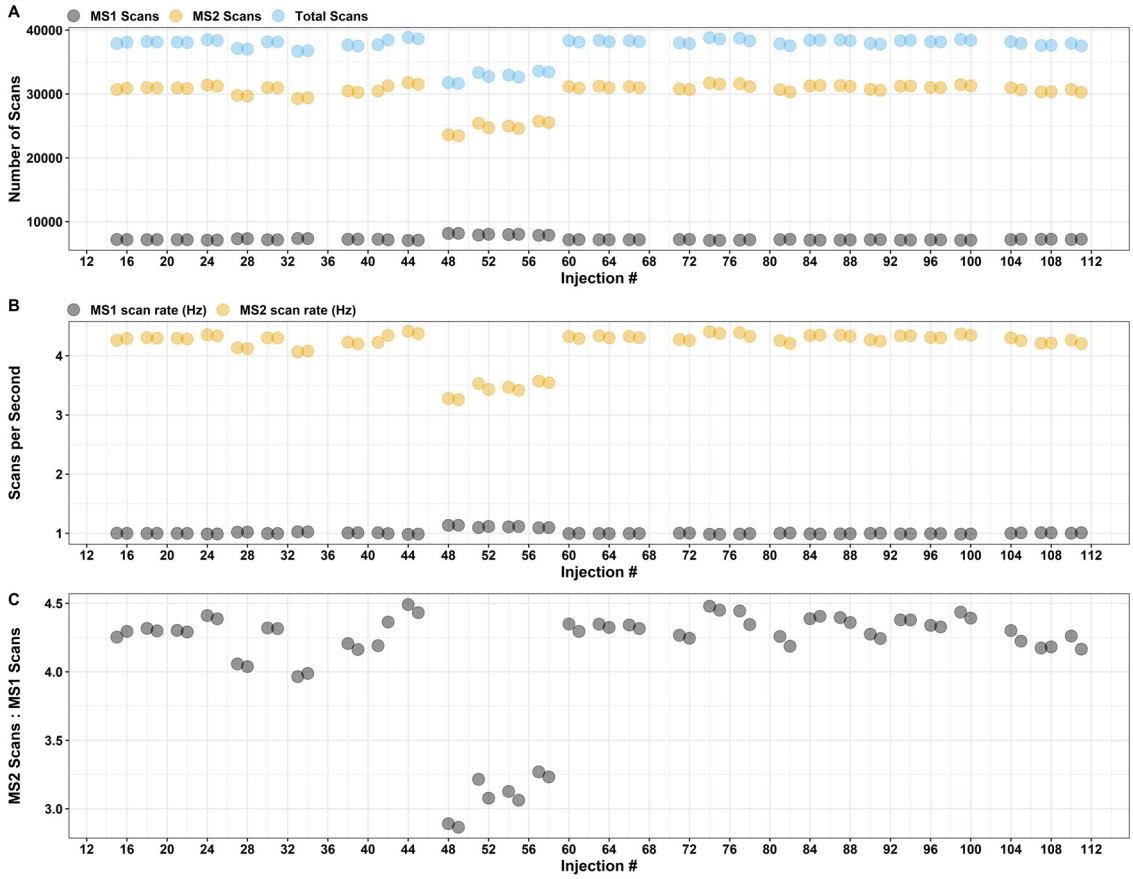

Figure 4.9: A) Number of MS1 and MS2 scans, and total number of both MS1 and MS2 scans. B) MS1 and MS2 can rate per second (Hz). C) Ratio of the number of MS2 scans relative to the number of MS1 scans. In all panels, injection numbers are ordered from earlier to later injections to show the mass spectrometry run progression. Sample details for each injection number are shown in S4.2

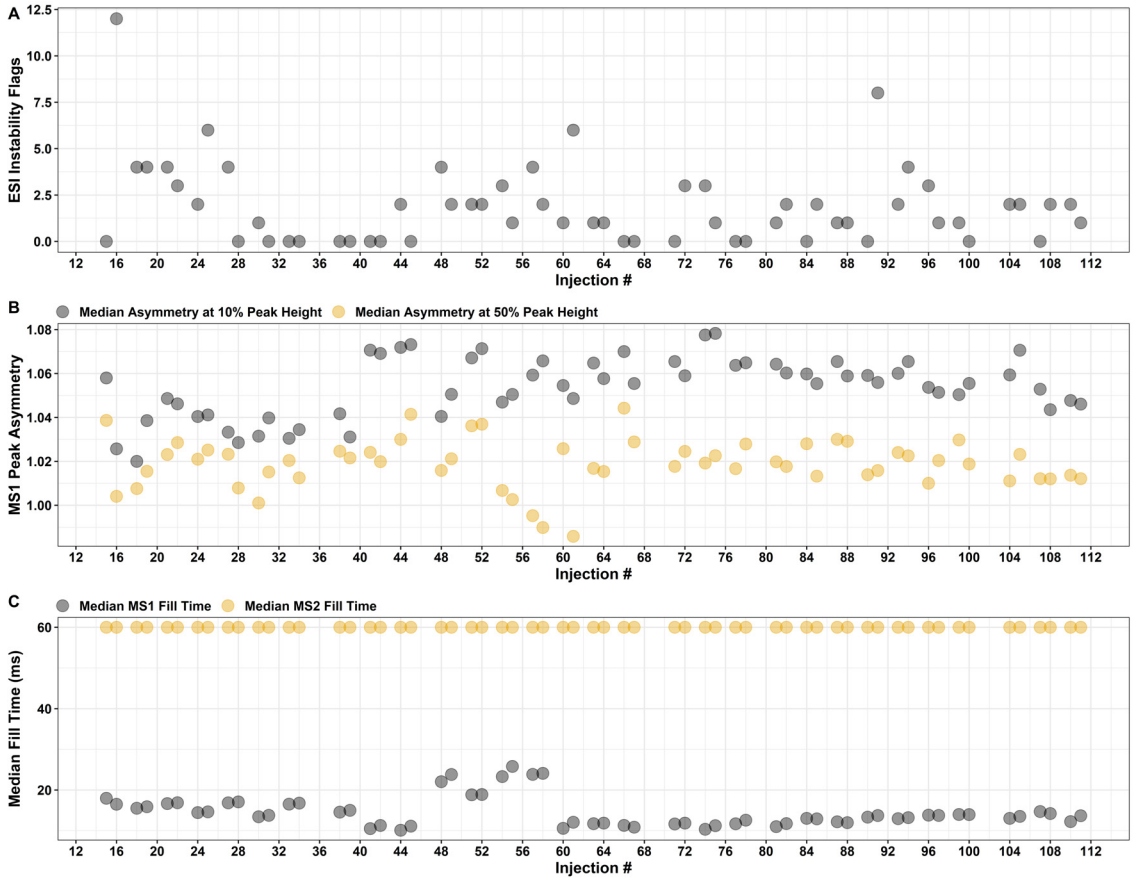

Figure 4.10: A) Number of electron spray instability (ESI) flags in each injection. B) The MS1 peak asymmetry metric calculated at 10% and 50% of peak height. A value of 1.00 represents perfectly symmetrical peaks, a negative value represents peak fronting, and a positive value indicates peak tailing. In all panels, injection numbers are ordered from earlier to later injections to show the mass spectrometry run progression. Sample details for each injection number are shown in Table S4.2 Table.

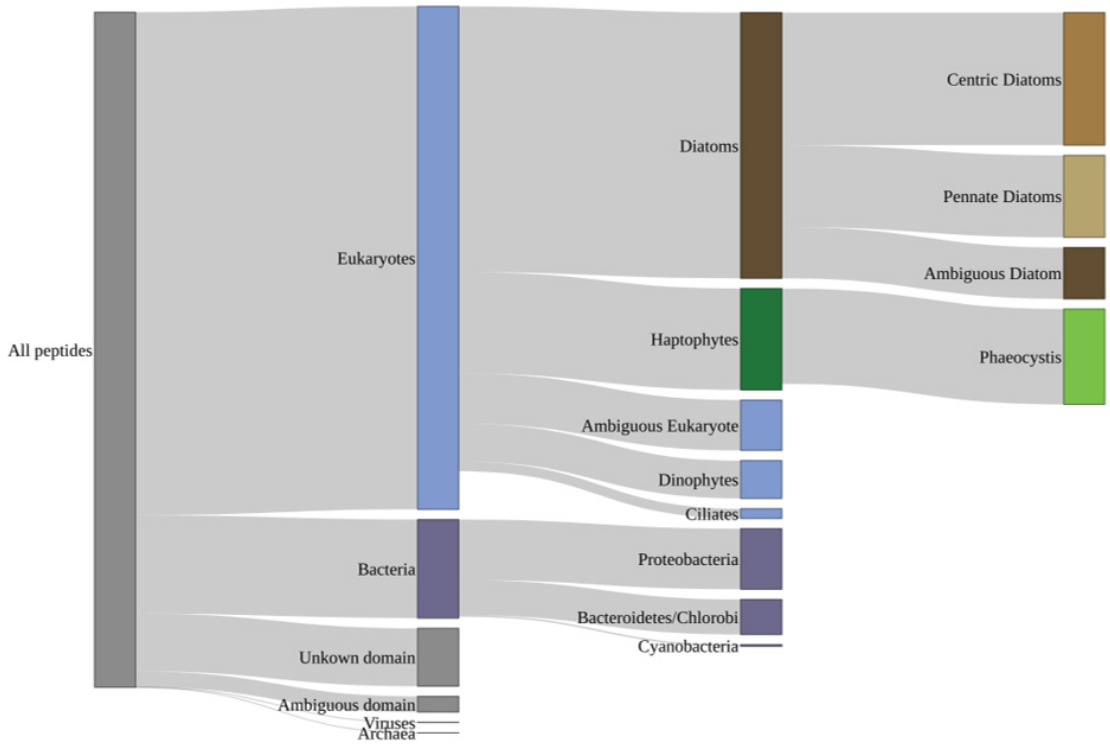

Figure 4.11: From left to right, bar height represents the number of unique peptides assigned to each taxonomic group at different taxonomic resolutions. Note that the number of unique peptides here does not reflect peptide abundance. The number of unique peptides assigned to the main taxonomic groups are as follows: All peptides = 37472, Eukaryotes = 27910, Bacteria = 5466, Unknown domain (peptides that could not be linked to a taxonomic affiliation) = 3208, Diatoms = 14746, Haptophytes = 5622, Centric diatoms = 7353, Pennate Diatoms = 4547, Ambiguous diatoms (diatom peptides that could not be differentiated between pennate and centric origins) = 2846, *Phaeocystis* = 5287.

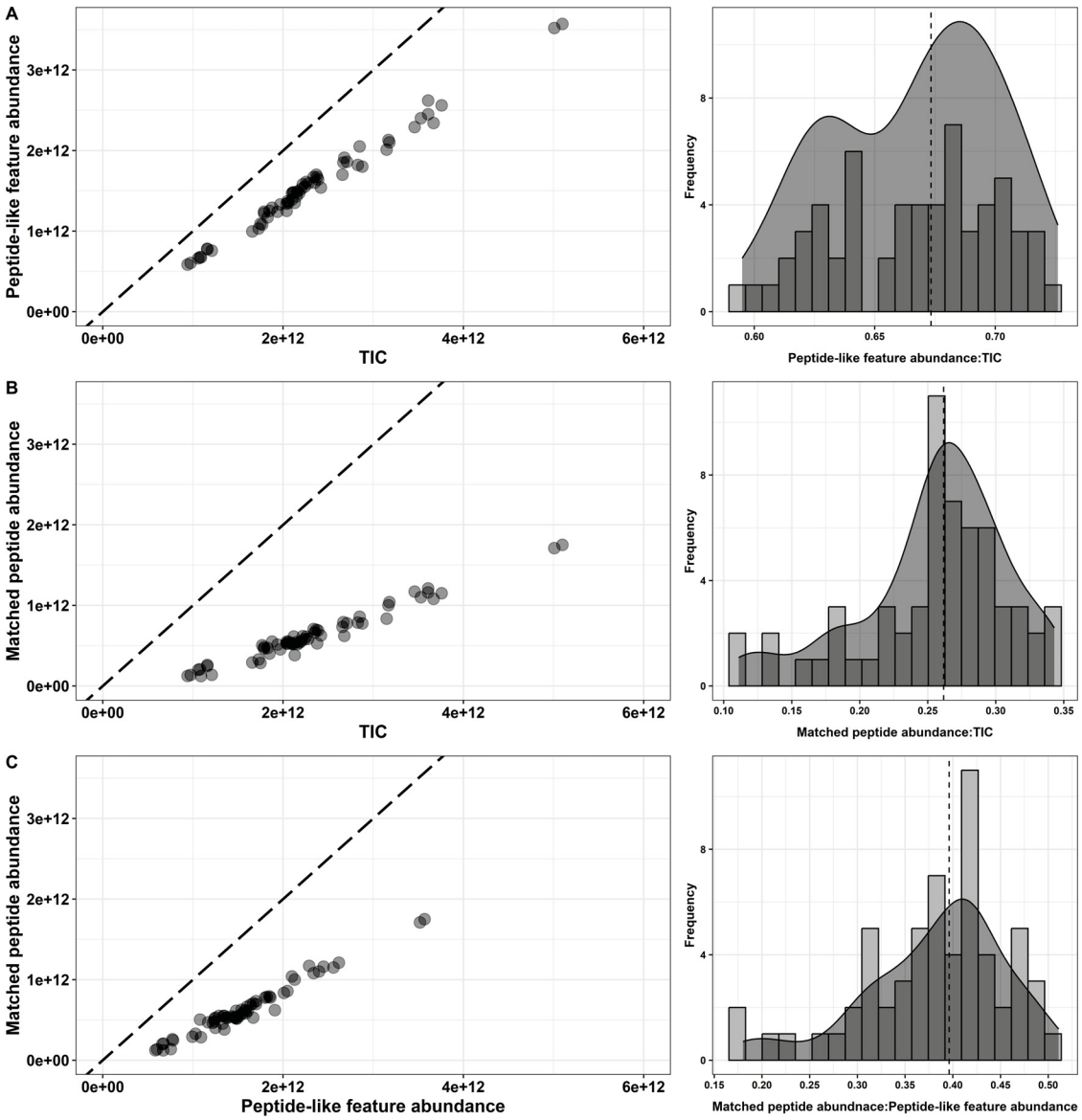

Figure 4.12: Correlations between database dependent and independent normalization factors. A) Peptide-like feature abundance plotted against total ion current (TIC). Frequency histogram shows the number of injections (y-axis) with a given peptide-like feature abundance: TIC ratio (x-axis), calculated up to 4 significant digits. B) Matched peptide abundance (database dependent) plotted against TIC. Frequency histogram shows the number of injections with a given matched peptide abundance:TIC ratio, calculated up to 4 significant digits. C) Matched peptide abundance plotted against peptide-like feature abundance. Frequency histogram shows the number of injections with a given matched peptide abundance: peptide-like feature abundance ratio, calculated up to 4 significant digits. In A, B, and C, each point represents one sample injection. Diagonal dashed lines indicate 1:1 line. Vertical dashed lines indicate the median ratio.

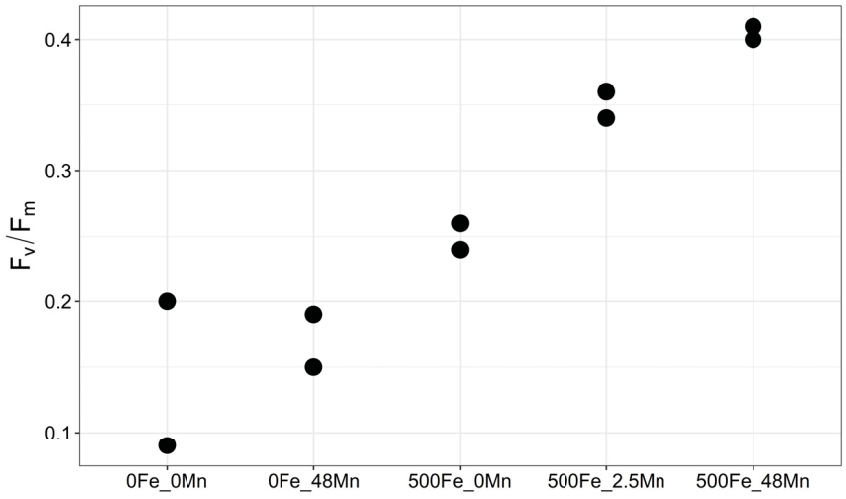

Figure 4.13: Photosynthetic efficiency (F_v/F_m) of *F. cylindrus* cultures grown under saturating light at 3 °C and measured during mid-exponential growth. 0Fe = no added Fe (Fe deplete), 500Fe = 500 nM EDTA-buffered Fe (Fe replete). 0Mn = no added Mn (Mn deplete), 2.5Mn = 2.5 nM EDTA-buffered Mn (medium Mn), 48Mn = 48 nM of EDTA-buffered Mn (Mn replete). Each point represents one biological replicate. See Jabre and Bertrand (2020) for detailed methods.

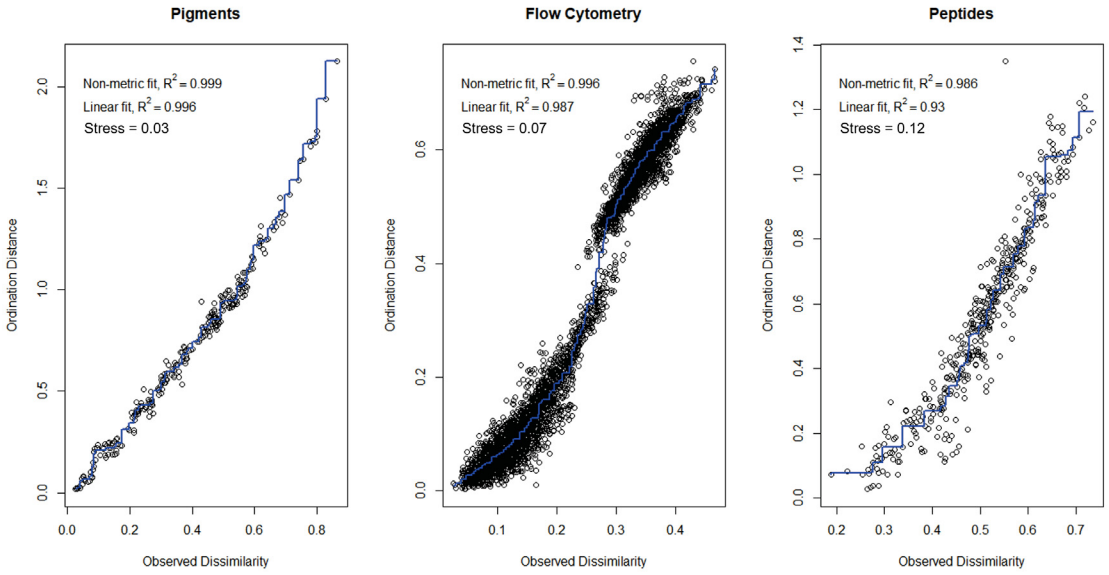

Figure 4.14: Model fit tests for pigment, flow cytometry and peptide NMDS ordinations analyses. A high R^2 (> 0.8) indicates good model fit.

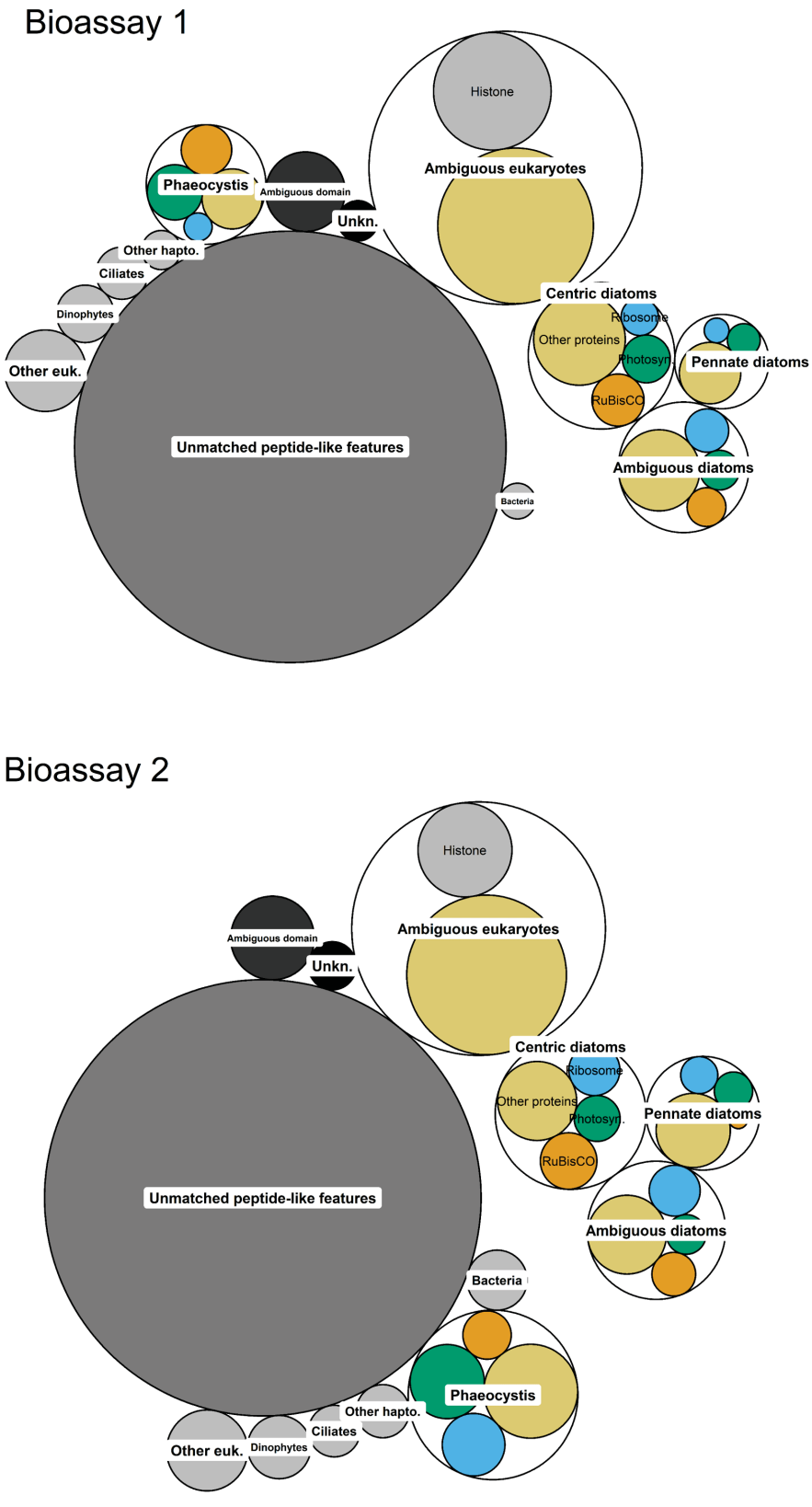
Bioassay 1
Histone
Ambiguous eukaryotes
Phaeocystis
Ambiguous domain
Unkn.
Other hapto.
Ciliates
Dinophytes
Other euk.
Centric diatoms
Ribosome
Other proteins
Photosyn.
RuBisCO
Pennate diatoms
Ambiguous diatoms
Unmatched peptide-like features
Bacteria
Bioassay 2
Histone
Ambiguous eukaryotes
Ambiguous domain
Unkn.
Centric diatoms
Ribosome
Other proteins
Photosyn.
RuBisCO
Pennate diatoms
Ambiguous diatoms
Unmatched peptide-like features
Bacteria
Phaeocystis
Other hapto.
Ciliates
Other euk.
Dinophytes

Figure 4.15

Figure 4.15: Average abundance of major taxa and functional protein groups at T0 in Bioassay 1 and Bioassay 2. Circle size represents taxon or functional protein abundance normalized to total protein in each bioassay. “Unmatched peptide-like features” indicates the abundance of possible peptide-like features that were not matched using our database. “Unkn.” indicates matched proteins with no known function or taxonomic affiliation.

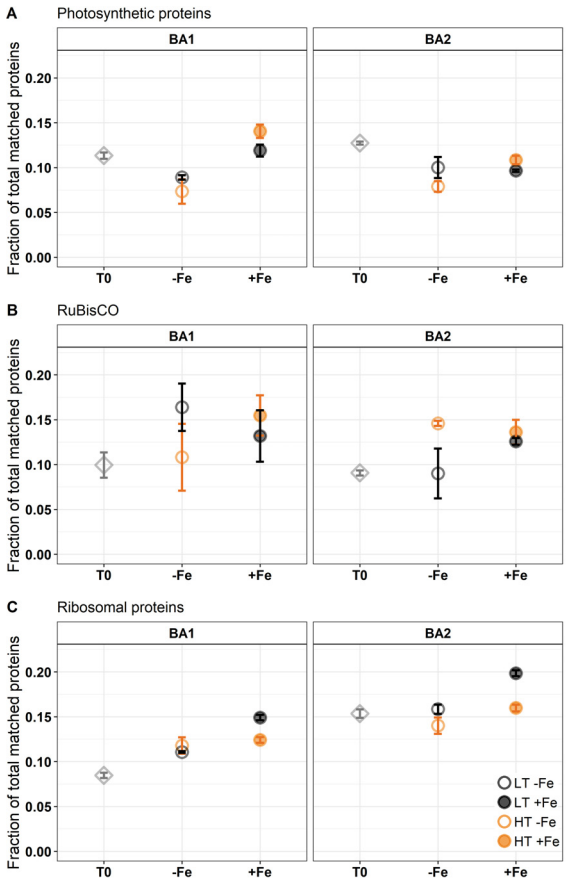

Figure 4.16: A) Photosynthetic protein fraction of the total observed protein abundance at T0 and after eight daysof Fe-temperature incubations. B) RuBisCO protein fraction of the total observed protein abundance at T0 and after eight days of Fe-temperature incubations. C) Ribosomal protein fraction of the total observed protein abundance at T0 and after eight days of Fe-temperature incubations. Error bars represent ± 1 SD and fall within the bounds of points when not visible.

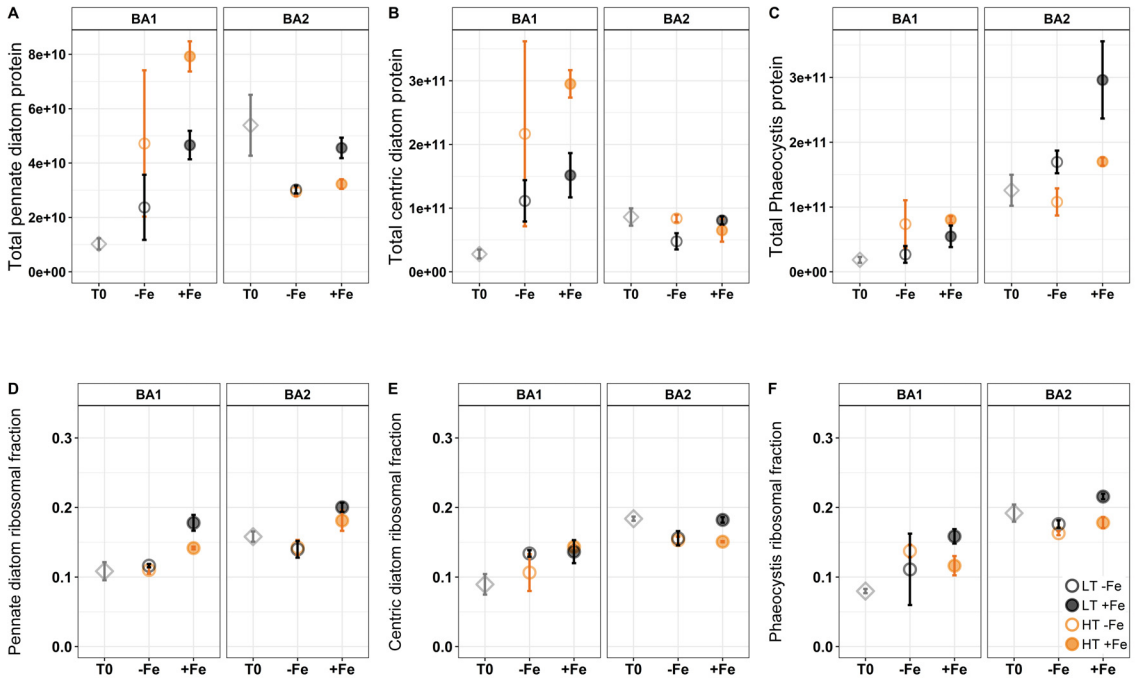

Figure 4.17: Total, unnormalized, taxon-specific protein abundance calculated as sum of all taxon-resolved peptide intensities of A) pennate diatoms, B) centric diatoms, and C) *Phaeocystis* at T0 and after 8 days of iron-temperature incubations. Total taxon protein abundance was calculated as the sum of all taxon-specific peptide intensities. D), E), and F) show taxon-specific ribosomal protein allocations in pennate diatoms, centric diatoms and *Phaeocystis*, respectively. Error bars represent ± 1 SD and fall within the bounds of points when not visible.

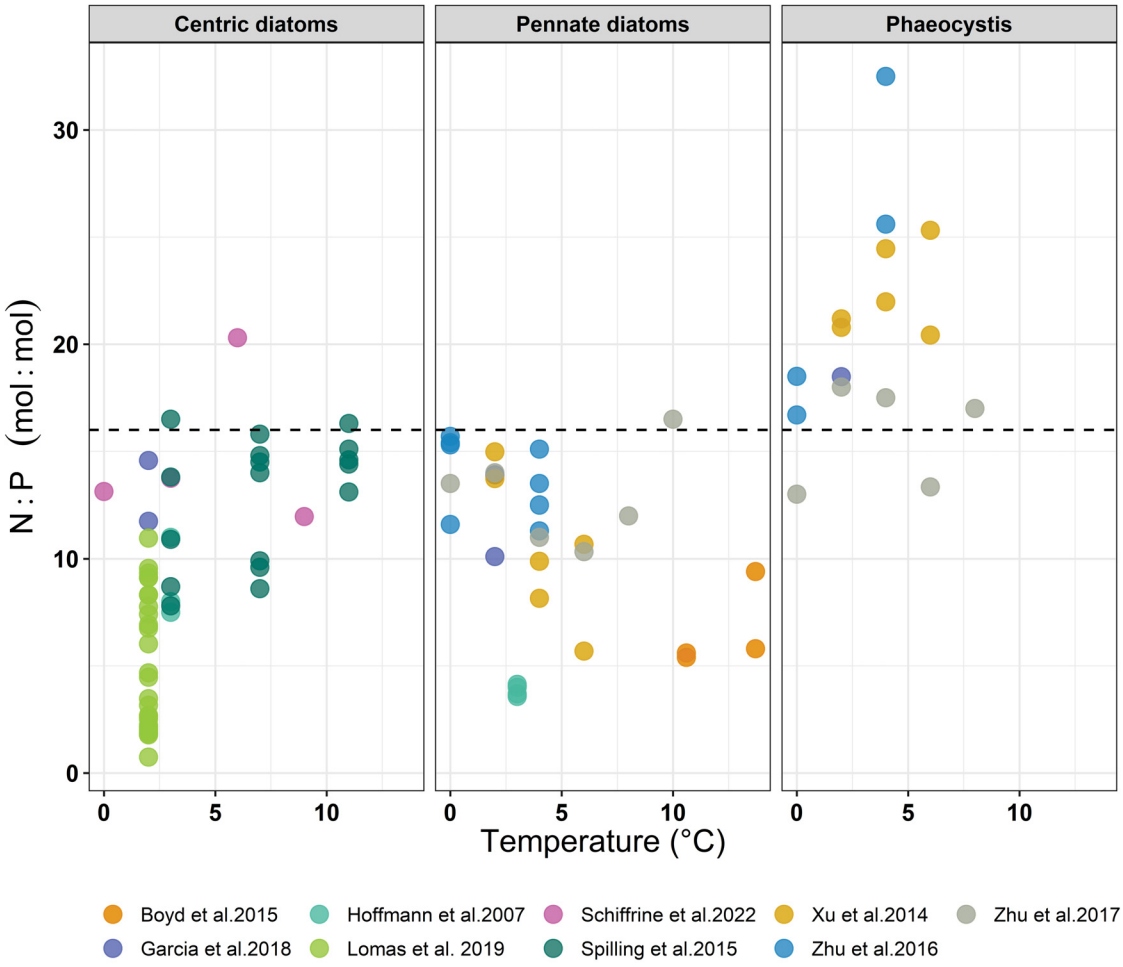

Figure 4.18: Color-coded version of Figure 4.4D, showing N:P ratios acquired from previously published studies of laboratory cultures grown under nutrient replete conditions and harvested during the exponential phase in semi-continuous or batch growth. Centric diatoms include *Thalassiosira* sp., *Chaetoceros* sp., *Skeletonema* sp., and *Odontella* sp. Pennate diatoms include *Pseudo-nitzschia* sp. and *Fragilariopsis* sp. Data were retrieved from the cited studies either directly from text and tables, or from figures using the web tool WebPlotDigitizer (Rohatgi, 2022). Horizontal dashed horizontal lines represent Redfield N:P ratio of 16. The studies used were as follows: Boyd et al. (2015a); Garcia et al. (2018); Hoffmann et al. (2007); Lomas et al. (2019); Schiffrine et al. (2022); Spilling et al. (2015); Xu et al. (2014); Zhu et al. (2016, 2017).

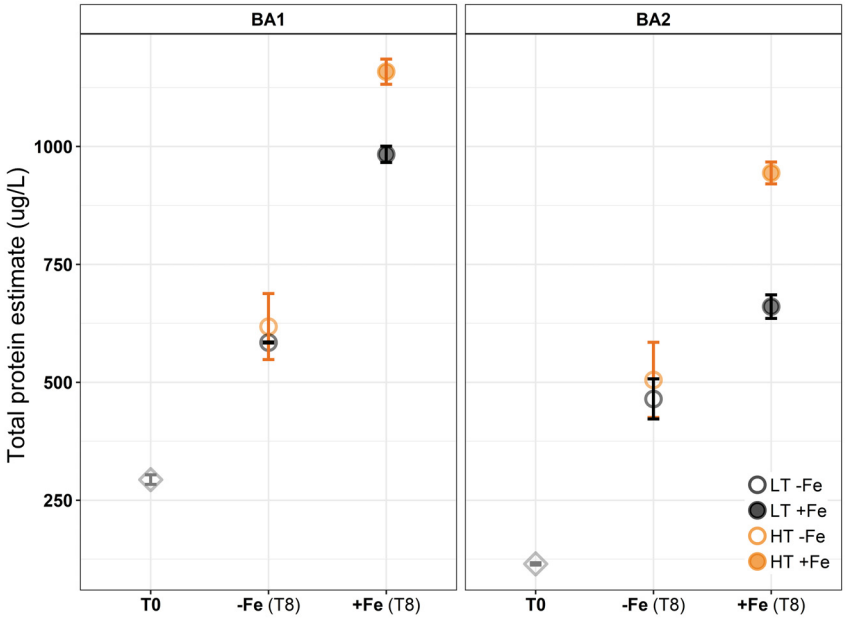

Figure 4.19: Total protein concentrations calculated from particulate nitrogen measurements using PN*4.78 following (Finkel et al., 2016). Iron addition increases total protein production, concurrent iron addition and warming cause a synergistic increase in total protein production.

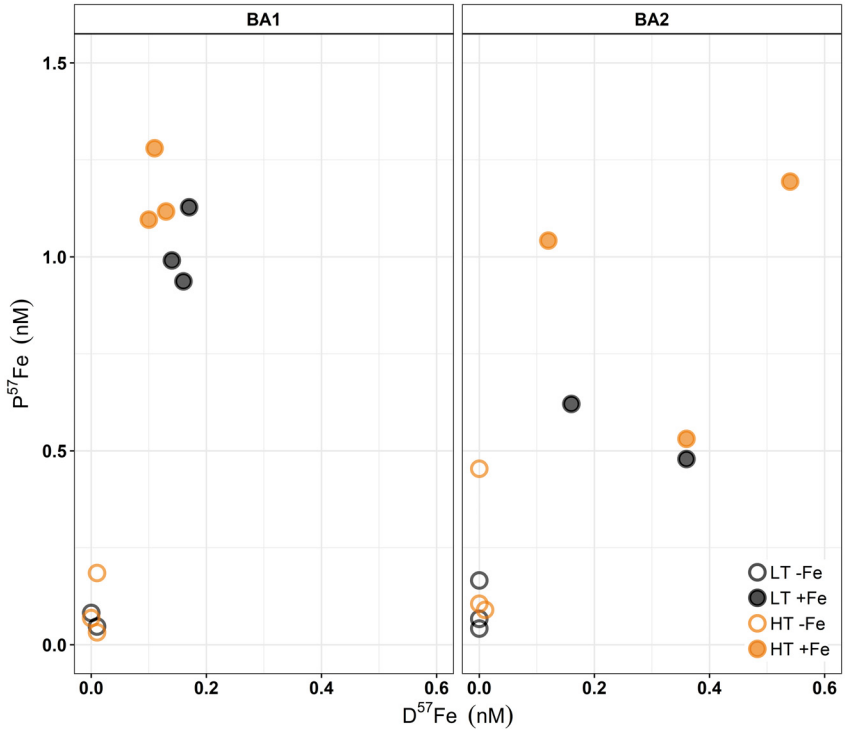

Figure 4.20: Particulate vs dissolved ^{57}Fe (nM) at T8 in both bioassay incubations. This shows that approximately half of the added 2 nM ^{57}Fe was consumed by the microbial community. The ^{57}Fe that is unaccounted for by the particulate and dissolved fractions is likely lost to adsorption to the cubitainer walls or precipitation. Each point represents one biological replicate.

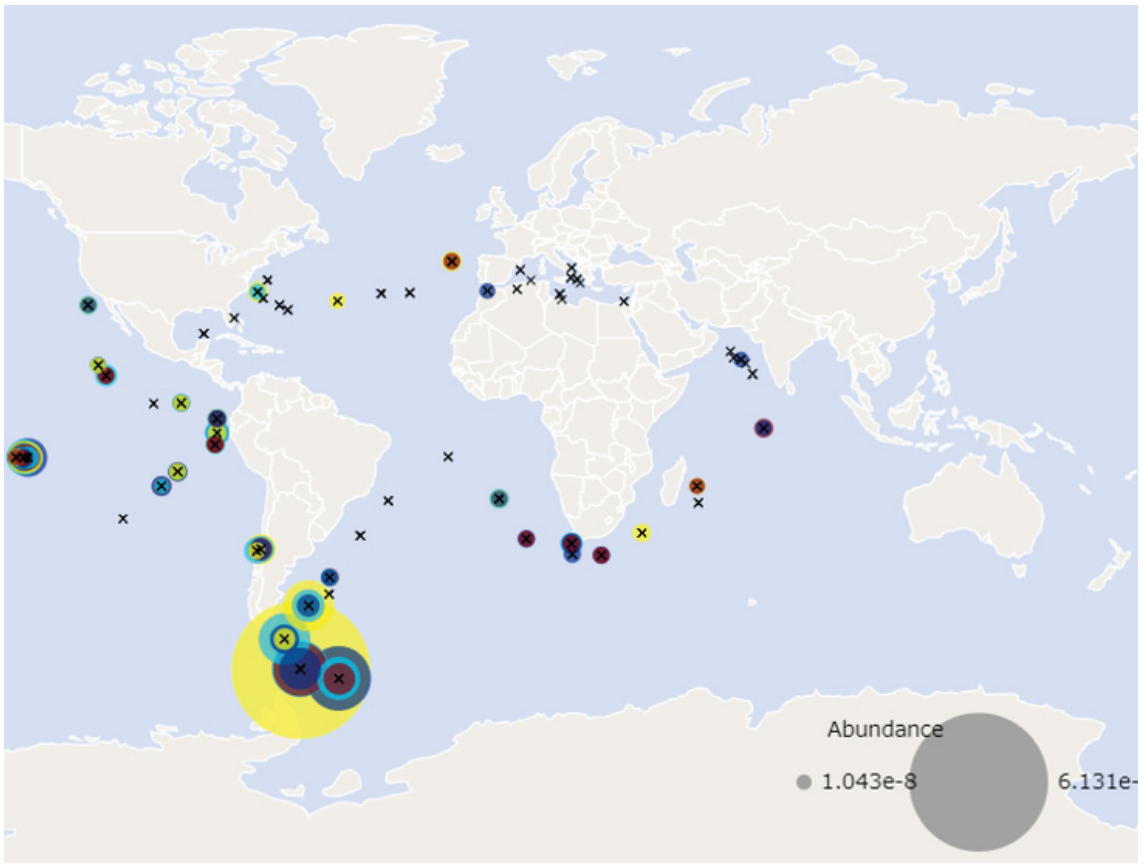

Figure 4.21: Global distribution of Fasciclin transcripts acquired from the Ocean Gene Atlas 2.0 database (Vernette et al., 2022) using a BLAST-p search with 1e-50 threshold. Circle size is proportional to transcript abundance and plotted using surface (<10 m depth) samples only. This shows higher Fasciclin transcript abundance in HNLC Southern Ocean and Equatorial Pacific regions.

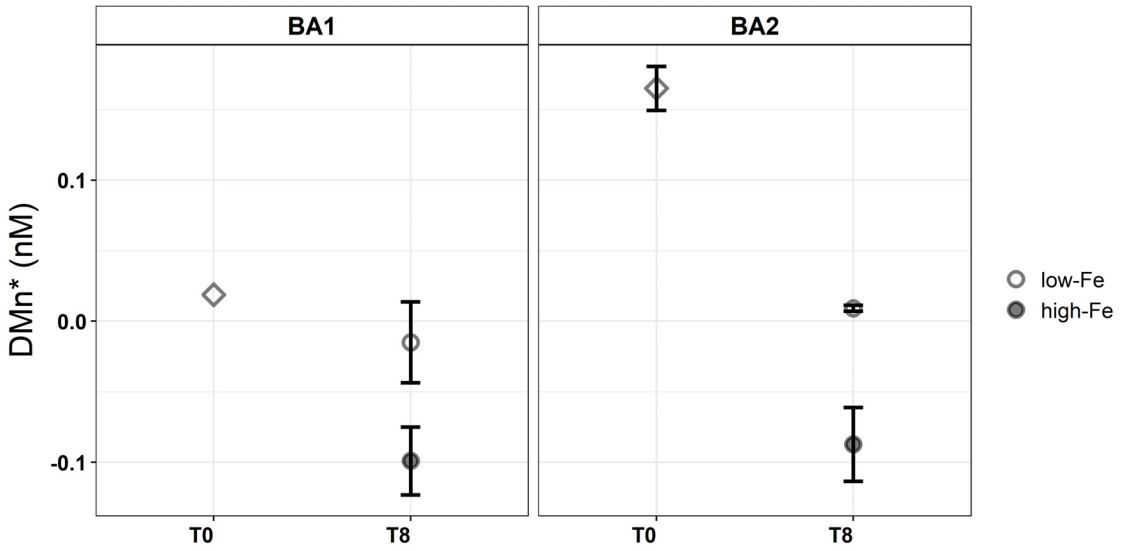

Figure 4.22: DMn* at T0, and after eight days of incubation with and without iron addition. Mn* was calculated following (Browning et al., 2017) as Mn* = [DMn] – [$D^{56}Fe$+$D^{57}Fe$]/2.67. Error bars represent ±1 SD.

4.8.2 Supplemental Tables

Table 4.2: Order of LC-MS-MS injections with corresponding sample information.

Injection	Bioassay	Temperature treatment	Iron treatment	Timepoint	Replicate
15, 16	BA1	HT	-Fe	T8	C
18, 19	BA1	HT	+Fe	T8	A
21, 22	BA1	HT	+Fe	T8	B
24, 25	BA1	HT	+Fe	T8	C
27, 28	BA1	LT	-Fe	T8	C
30, 31	BA1	LT	+Fe	T8	A
33, 34	BA1	LT	+Fe	T8	B
38, 39	BA1	LT	+Fe	T8	C
41, 42	BA1	HT	-Fe	T8	A
44, 45	BA1	HT	-Fe	T8	B
48, 49	BA1	T0	T0	T0	A
51, 52	BA1	T0	T0	T0	B
54, 55	BA1	T0	T0	T0	C
57, 58	BA1	LT	-Fe	T8	B
60, 61	BA2	T0	T0	T0	A
63, 64	BA2	T0	T0	T0	B
66, 67	BA2	T0	T0	T0	C
71, 72	BA2	LT	-Fe	T8	A
74, 75	BA2	LT	-Fe	T8	B
77, 78	BA2	LT	-Fe	T8	C
81, 82	BA2	LT	+Fe	T8	A
84, 85	BA2	LT	+Fe	T8	B
87, 88	BA2	LT	+Fe	T8	C
90, 91	BA2	HT	-Fe	T8	A
93, 94	BA2	HT	-Fe	T8	B
96, 97	BA2	HT	-Fe	T8	C
99, 100	BA2	HT	+Fe	T8	A
104, 105	BA2	HT	+Fe	T8	B
107, 108	BA2	HT	+Fe	T8	C
110, 111	BA1	T0	T0	T0	D

Table 4.3: Time intervals at which subsampling was carried out for various measurements.

	T0	**T2**	**T4**	**T6**	**T8**
Photophysiology	X				X
Pigments	X				X
Flow cytometry	X	X	X	X	X
Dissolved macronutrients	X	X	X	X	X
Particulate macronutrients	X				X
Dissolved trace metals	X		X		X
Particulate trace metals	X				X
Proteomics	X				X

Table 4.4: Liquid chromatography flow rates and solvent composition settings. Arrows indicate linear increase or decreases in Solvent B* and A** composition.

Time (minutes)	**Flow (μL/min)**	**% Solvent B**	**% Solvent A**
0 - 15	0.3	5	95
15.1 - 90	0.25	$5 \rightarrow 30$	$95 \rightarrow 70$
90.1 - 102	0.25	$30 \rightarrow 55$	$70 \rightarrow 45$
102.1 - 106	0.3	$55 \rightarrow 95$	$45 \rightarrow 5$
106.1 - 110	0.3	95	5
111 - 125	0.3	5	95

* Solvent A: H_2O, 0.1% Formic Acid

** Solvent B: Acetonitrile, 0.1% Formic Acid

Table 4.5: Q-Exactive hybrid quadrupole-Orbitrap mass spectrometer settings.

Parameter	**Setting**
TopN	8
Intensity Threshold	8.3 e4
Dynamic Exclusion	30 seconds
MS1 Scan Resolution	140000
MS1 Scan Range	400 to 2000 m/z
MS1 Automatic Gain Control Target	3e6
MS2 Scan Resolution	17500
MS2 Scan Range	200 to 2000 m/z
M2 Automatic Gain Control Target	1 e6
MS2 Isolation Window	2.0 m/z

CHAPTER 5

CONCLUDING REMARKS

This thesis tackles a critical unanswered question: do iron and temperature interactively, or independently, influence phytoplankton growth and physiology? The current conceptions of phytoplankton growth in global ecosystem models largely assume that these variables, along with others, act independently in their impact on growth (Laufkötter et al., 2015). In other words, a change in one variable has no effect on how other variables impact growth. However, this assumption is rooted in a general lack of knowledge of the interactive relationship between iron and temperature in phytoplankton, as most studies have examined these factors in isolation. Here I address this knowledge gap by investigating Southern Ocean phytoplankton growth and underpinning cellular processes under concurrent changes in iron and temperature.

In Chapter 2, I used trace-metal-clean culturing techniques to grow a model Southern Ocean diatom (*Fragilariopsis cylindrus*) under several iron and temperature conditions, and examined growth rates under these conditions. These experiments showed that changes in temperature affect how iron impacts growth - warming reduced the amount of iron required to maintain half maximal growth rates. This new evidence for interactive iron-temperature relationships in marine photoautotrophs highlights an important parameterization that is missing from most current models which use non-interactive (i.e., additive or multiplicative) relationships between growth-controlling factors. These findings also led to new questions: what cellular mechanisms underpin this interactive iron-temperature relationship, and does this interaction happen in other phytoplankton groups?

I address the above questions in Chapter 3, where I used metatranscriptomics to examine gene expression patterns in a Southern Ocean phytoplankton community that

was incubated under different iron and temperature conditions. First, I found that two different pennate diatom groups exhibited different growth patterns under these conditions. One group, *Pseudo-nitzchia* sp., became more abundant under warming even when iron availability was limited, while the other group, *Fragilariopsis* sp. required some additional iron to benefit from warming. The high sequencing depth achieved through metatranscriptomics then allowed for a close examination of the different cellular mechanisms that may have contributed to these differences. I found that *Pseudo-nitzchia* was better equipped to use iron-conserving photosynthetic processes, iron-conserving nitrogen assimilation mechanisms, and increased iron uptake and storage processes under warming. Together, these findings highlight important differences in how iron and temperature influence growth and physiology even in closely related Southern Ocean phytoplankton taxa, and suggest that some phytoplankton groups (like *Pseudo-nitzschia*) may experience a stronger interactive iron-temperature effect on growth. Further, this work provides new insight into the cellular mechanisms (i.e. increased use of iron-conserving processes under warming) that underpin interactive iron-temperature effects on phytoplankton growth. This also led to more new questions: how do changes in phytoplankton growth (Chapter 2) and underpinning molecular processes (Chapter 3) influence phytoplankton element stoichiometry and ultimately ocean biogeochemistry?

I address the above questions in Chapter 4, where I combined metaproteomics with elemental stoichiometry and community growth measurements from another set of iron-temperature incubations in the Southern Ocean. I found an amplification of growth and nutrient drawdown under concurrent warming and increased iron availability, also consistent with what I observed in experiments from Chapters 2 and 3. This further stresses the importance of including interactive/synergistic relationships in marine ecosystem models. I also found that ribosomal abundance could be a possibly useful proteomic trait for understanding phytoplankton growth under different environmental conditions, but showed that our conventional formulations of how ribosomes impact N:P stoichiometry could be nuanced by several other variables. Further, I showed that metaproteomics could be a useful tool for understanding trace metal use and trace metal stoichiometry within phytoplankton by connecting metalloprotein abundance with trace metal quotas.

The work in this thesis has advanced our understanding of the phenomenological and mechanistic processes through which iron and temperature interactively influence

phytoplankton growth. It also raised many new questions, and uncovered new gaps in knowledge that underscore the need for further research.

While evidence is emerging for warming-mediated increase in iron use efficiency (IUE) in nitrogen fixing marine microbes (Yang et al., 2021; Jiang et al., 2018), additional work is still required to confirm whether temperature-mediated IUE applies in non-nitrogen fixing phytoplankton. For instance, the work in Chapter 2 showed that a decrease in the amount of iron required to support growth under warming may be also influenced by decreased cell size. That is, the cellular quota of iron might decrease under warming, but the iron:carbon or iron:biovolume might not be impacted. Does warming then increase IUE of phytoplankton cells regardless of size, or does this depend on changes in cell volume (biomass)? Answering this question is essential for understanding how changes in iron and temperature could influence primary productivity, carbon drawdown, and biogeochemical processes in the ocean. Additional studies combining cell size, iron uptake rates, and elemental stoichiometry measurements (e.g. iron:carbon, iron:nitrogen) would provide valuable insight on how temperature influences iron use efficiency from an organismal and an ecological/biogeochemical perspective.

An interactive iron-temperature relationship appears to be highly beneficial to phytoplankton in regions like the Southern Ocean, where iron availability is low and enzymatic processes are limited by cold water temperatures. Here, the ability to capitalize on small increases in temperature (thermal energy) allows phytoplankton to increase growth and primary productivity. However, should we expect similar interactive relationships in phytoplankton from other regions where iron is replete (e.g. coastal waters), or where water temperatures do not limit enzymatic processes as much (e.g. temperate regions)? It is not clear whether an interactive iron-temperature relationship could be beneficial to phytoplankton in these regions, and if these phytoplankton have evolved the cellular mechanisms to underpin an interactive iron-temperature relationship. Future studies using phytoplankton from various ocean environments could identify more important differences in how iron and temperature (and perhaps other variables) influence phytoplankton growth and physiology throughout the ocean.

Lastly, it is essential to acknowledge that future change scenarios in the Southern Ocean encompass a range of factors like alterations in light exposure, pH, stoichiometry

of nutrient supply, grazing pressure etc. The examination of iron and temperature in isolation may then provide a biased assessment of phytoplankton growth in a changing ocean environment. For example, amplified growth under concurrent warming and increased iron availability may be counteracted by increased grazing or photodamage in a stratified water column. Similarly, changes in trace metal sources (e.g. dust) may alter the stoichiometry iron:manganese availability (Wyatt et al., 2023) in the Southern Ocean, which could lead to changes in primary productivity as iron and manganese interact within cellular processes, and often co-limit phytoplankton growth in the region (Wu et al., 2019; Browning et al., 2021). Multi-factorial experimental designs, which are most suited for laboratory culture studies, would be critical for examining the complex interplay between various environmental variables, and whether other interactive relationships exist between other growth-controlling factors.

5.1 Future Directions

Proteomics vs transcriptomics – Currently, transcriptomic measurements are more accessible and more cost-effective than mass spectrometry-based proteomics measurements. Transcriptomic laboratory and bioinformatics workflows are also more developed, and the sequencing depth achieved by transcriptomics easily surpasses what could be achieved with conventional proteomics methods. Despite these advantages, there are compelling reasons for using proteomics. Protein measurements in cultures or in the ocean (metaproteomics) provide a direct view of the functional machinery (proteins) within cells. This allows us to establish connections between molecular measurements and metabolism, and ultimately ecological and biogeochemical processes. The proteomics field is also on the cusp of transformative technological advances ranging from increased mass spectrometer sensitivity to new methods of measuring proteins such as nanopore and fluorescence de novo sequencing (Timp and Gregory Timp, 2020; Zhang et al., 2021; Reed et al., 2022; Motone and Nivala, 2023). This will likely allow us to make protein expression measurements at a resolution close to what is achieved with transcriptomics, and more importantly, at lower cost and higher accessibility than ever before. These advances could also address many of the current methodological challenges associated with mass spectrometry-based proteomics, such as short peptide sequence lengths and heterogeneous peptide ionization efficiencies, which

complicate protein inference and abundance measurements. Inevitably, the integration of proteomics workflows into phytoplankton research will become increasingly prevalent. It is therefore imperative that we adapt our experimental designs and formulate our research questions to capitalize on these technological advances.

Connecting proteomics with ecosystem processes – In a sense, one of the holy grails of Earth system science is to create a unified theory of ocean metabolism. The idea would be to connect chemical, physical, and biological processes at various scales into a single description of how the ocean functions and interacts with change. Indeed, complex ocean circulation-biogeochemistry-ecosystem models, which include microbial metabolic processes, have been developed (Follows et al., 2007; Dutkiewicz et al., 2009). The majority of these models, however, rely on inflexible parameterizations derived from general phenomenological observations, or theoretical expectations. Advances in omics workflows allow us to examine phytoplankton biology and ecology from mechanistic perspectives, which might be useful for incorporating flexibility into marine ecosystem models that are embedded in Earth system models. The question then becomes: how do we incorporate omics knowledge into these models?

One way is to create detailed cellular models of every microbial type in the ocean and incorporate these into larger scale ecological and biogeochemical processes. Clearly this is implausible, but highlights challenges associated with model complexity. Is it necessary to understand how every protein in every organism connects with cellular and ecosystem processes? Or is it sufficient to have the simplest possible model that is capable of reproducing observations? Perhaps somewhere between the two extremes of complexity is a balanced spot, where a core set of metabolic processes could sufficiently inform Earth system models.

McCain et al. (2022) proposed a course graining approach where measured proteins are binned into functionally informative groups (e.g. ribosomes, photosynthetic proteins) for examining phytoplankton fitness and resource allocation. This grouping of proteins reduces data complexity (in addition to mitigating methodological obstacles), while maintaining a level of information that could be sufficient for informing models (e.g. using proteomics to understand elemental stoichiometry in Chapter 4). It remains unclear how protein measurements could be incorporated into Earth system models – do we treat protein

abundance measurements as “traits”, similar to how cell size or photosynthetic capacity are incorporated into the models? do we treat them as macromolecular pools and build on established macromolecular allocation models that are being incorporated into larger scale models (e.g. (Inomura et al., 2020), or should proteomics data be incorporated into models using completely new frameworks?

As we continue to examine the interplay between proteins and cellular/ecosystem processes (e.g. metalloproteins and trace metal quotas), we will develop a better understanding of which processes can be described with low resolution (e.g. course-graining) approaches, and which processes require higher resolution (e.g. single protein) measurements. For this, the examination of laboratory cultures grown under carefully chosen environmental conditions would serve as a valuable step in connecting molecular processes with metabolic rates and physiology. The testing and confirmation of these laboratory findings in the field would ultimately provide a bridge between observations and numerical descriptions in broader-scale models of ocean processes.

REFERENCES

Ahlgren G. 1987. Temperature functions in biology and their application to algal growth constants. *Oikos*. 49:177.

Ahner BA, Kong S, Morel FMM. 1995. Phytochelatin production in marine algae. 1. An interspecies comparison. *Limnology and Oceanography*. 40:649–657. Tex.eprint: https://aslopubs.onlinelibrary.wiley.com/doi/pdf/10.4319/lo.1995.40.4.0649.

Allen AE, LaRoche J, Maheswari U, Lommer M, Schauer N, Lopez PJ, Finazzi G, Fernie AR, Bowler C. 2008. Whole-cell response of the pennate diatom *Phaeodactylum tricornutum* to iron starvation. *Proceedings of the National Academy of Sciences*. 105:10438–10443.

Amaral-Zettler LA, McCliment EA, Ducklow HW, Huse SM. 2009. A method for studying protistan diversity using massively parallel sequencing of V9 hypervariable regions of small-subunit ribosomal RNA genes. *PLoS ONE*. 4:e6372.

Andersen RA. 2005. Algal culturing techniques. Burlington, Mass.: Elsevier/Academic Press.

Andrew SM, Morell HT, Strzepek RF, Boyd PW, Ellwood MJ. 2019. Iron availability influences the tolerance of Southern Ocean phytoplankton to warming and elevated irradiance. *Frontiers in Marine Science*. 6:681.

Aptekmann AA, Buongiorno J, Giovannelli D, Glamoclija M, Ferreiro DU, Bromberg Y. 2022. mebipred: identifying metal-binding potential in protein sequence. *Bioinformatics (Oxford, England)*. 38:3532–3540. Tex.eprint: https://academic.oup.com/bioinformatics/article-pdf/38/14/3532/49884344/btac358.pdf.

Armbrust EV, Berges JA, Bowler C, et al. (45 co-authors). 2004. The genome of the diatom *Thalassiosira pseudonana*: Ecology, evolution, and metabolism. *Science*. 306:79–86. Tex.eprint: https://www.science.org/doi/pdf/10.1126/science.1101156.

Arrigo K, Robinson DH, Worthen D, Dunbar RB, DiTullio GR, VanWoert M, Lizotte M. 1999. Phytoplankton community structure and the drawdown of nutrients and CO_2 in the Southern Ocean. *Science*. 283:365–367.

Arrigo KR. 2005. Marine microorganisms and global nutrient cycles. *Nature*. 437:349–355.

Arrigo KR, Mills MM, Kropuenske LR, van Dijken GL, Alderkamp AC, Robinson DH. 2010. Photophysiology in two major Southern Ocean phytoplankton taxa: photosynthesis and growth of *Phaeocystis antarctica* and *Fragilariopsis cylindrus* under different irradiance levels. *Integrative and Comparative Biology*. 50:950–966.

Arrigo KR, van Dijken GL, Bushinsky S. 2008. Primary production in the Southern Ocean, 1997–2006. *Journal of Geophysical Research*. 113.

Assmy P, Smetacek V, Montresor M, et al. (24 co-authors). 2013. Thick-shelled, grazer-protected diatoms decouple ocean carbon and silicon cycles in the iron-limited Antarctic Circumpolar Current. *Proceedings of the National Academy of Sciences*. 110:20633–20638.

Atkinson D, Ciotti BJ, Montagnes DJS. 2003. Protists decrease in size linearly with temperature: *ca* . 2.5% $°C^{-1}$. *Proceedings of the Royal Society of London. Series B: Biological Sciences*. 270:2605–2611.

Baer SE, Sipler RE, Roberts QN, Yager PL, Frischer ME, Bronk DA. 2017. Seasonal nitrogen uptake and regeneration in the western coastal Arctic. *Limnology and Oceanography*. 62:2463–2479.

Bar-Shalom R, Rozenberg A, Lahyani M, et al. (12 co-authors). 2023. Rhodopsin-mediated nutrient uptake by cultivated photoheterotrophic *Verrucomicrobiota*. *The ISME Journal*. 17:1063–1073.

Barnett A. 2017. Fireworx. https://sourceforge.net/projects/fireworx/.

Behnke J, LaRoche J. 2020. Iron uptake proteins in algae and the role of Iron Starvation-Induced Proteins (ISIPs). *European Journal of Phycology*. 55:339–360. Publisher: Taylor & Francis tex.eprint: https://doi.org/10.1080/09670262.2020.1744039.

Behrenfeld MJ, Bale A, Kolber Z, Aiken J, Falkowski P. 1996. Confirmation of iron limitations of phytoplankton photosynthesis in the equatorial Pacific Ocean. *Nature*. 383:508–511.

Bertrand EM, Allen AE, Dupont CL, Norden-Krichmar TM, Bai J, Valas RE, Saito MA. 2012. Influence of cobalamin scarcity on diatom molecular physiology and identification of a cobalamin acquisition protein. *Proceedings of the National Academy of Sciences*. 109:E1762–E1771.

Bertrand EM, McCrow JP, Moustafa A, et al. (13 co-authors). 2015. Phytoplankton–bacterial interactions mediate micronutrient colimitation at the coastal Antarctic sea ice edge. *Proceedings of the National Academy of Sciences*. 112:9938–9943.

Bestion E, García-Carreras B, Schaum CE, Pawar S, Yvon-Durocher G. 2018. Metabolic traits predict the effects of warming on phytoplankton competition. *Ecology Letters*. 21:655–664.

Blondeau-Patissier D, Gower JF, Dekker AG, Phinn SR, Brando VE. 2014. A review of ocean color remote sensing methods and statistical techniques for the detection, mapping and analysis of phytoplankton blooms in coastal and open oceans. *Progress in Oceanography*. 123:123–144.

Bokulich NA, Kaehler BD, Rideout JR, Dillon M, Bolyen E, Knight R, Huttley GA, Gregory Caporaso J. 2018. Optimizing taxonomic classification of marker-gene amplicon sequences with QIIME 2's q2-feature-classifier plugin. *Microbiome*. 6:90.

Bolyen E, Rideout JR, Dillon MR, et al. (112 co-authors). 2019. Reproducible, interactive, scalable and extensible microbiome data science using QIIME 2. *Nature Biotechnology*. 37:852–857.

Botebol H, Lesuisse E, Šuták R, et al. (15 co-authors). 2015. Central role for ferritin in the day/night regulation of iron homeostasis in marine phytoplankton. *Proceedings of the National Academy of Sciences*. 112:14652–14657. Tex.eprint: https://www.pnas.org/doi/pdf/10.1073/pnas.1506074112.

Boyd P, Dillingham P, McGraw C, et al. (11 co-authors). 2015a. Physiological responses of a Southern Ocean diatom to complex future ocean conditions. *Nature Climate Change*. 6:207–213.

Boyd P, Hutchins D. 2012. Understanding the responses of ocean biota to a complex matrix of cumulative anthropogenic change. *Marine Ecology Progress Series*. 470:125–135.

Boyd PW. 2019. Physiology and iron modulate diverse responses of diatoms to a warming Southern Ocean. *Nature Climate Change*. 9:148–152.

Boyd PW, Doney SC, Strzepek R, Dusenberry J, Lindsay K, Fung I. 2008. Climate-mediated changes to mixed-layer properties in the Southern Ocean: assessing the phytoplankton response. *Biogeosciences*. 5:847–864.

Boyd PW, Lennartz ST, Glover DM, Doney SC. 2015b. Biological ramifications of climate-change-mediated oceanic multi-stressors. *Nature Climate Change*. 5:71–79.

Boyd PW, Watson AJ, Law CS, et al. (35 co-authors). 2000. A mesoscale phytoplankton bloom in the polar Southern Ocean stimulated by iron fertilization. *Nature*. 407:695–702.

Browning TJ, Achterberg EP, Engel A, Mawji E. 2021. Manganese co-limitation of phytoplankton growth and major nutrient drawdown in the Southern Ocean. *Nature Communications*. 12:884.

Browning TJ, Achterberg EP, Rapp I, Engel A, Bertrand EM, Tagliabue A, Moore CM. 2017. Nutrient co-limitation at the boundary of an oceanic gyre. *Nature*. .

Brunson JK, McKinnie SMK, Chekan JR, et al. (13 co-authors). 2018. Biosynthesis of the neurotoxin domoic acid in a bloom-forming diatom. *Science*. 361:1356–1358.

Brzezinski M. 1985. The Si:C:N ratio of marine diatoms: interspecific variability and the effect of some environmental variables. *Journal of Phycology*. 21:347–357. Tex.eprint: https://onlinelibrary.wiley.com/doi/pdf/10.1111/j.0022-3646.1985.00347.x.

Buck JM, Sherman J, Bártulos CR, et al. (12 co-authors). 2019. Lhcx proteins provide photoprotection via thermal dissipation of absorbed light in the diatom *Phaeodactylum tricornutum*. *Nature Communications*. 10:4167.

Callahan BJ, McMurdie PJ, Rosen MJ, Han AW, Johnson AJA, Holmes SP. 2016. DADA2: High-resolution sample inference from Illumina amplicon data. *Nature Methods*. 13.

Cheng L, Abraham J, Hausfather Z, Kevin E Trenberth. 2019. How fast are the oceans warming? *Science (New York, N.Y.)*. 363:128–129. Tex.eprint: https://www.science.org/doi/pdf/10.1126/science.aav7619.

Cheng Z, Otto GM, Powers EN, Keskin A, Mertins P, Carr SA, Jovanovic M, Brar GA. 2018. Pervasive, coordinated protein-level changes driven by transcript isoform switching during meiosis. *Cell*. 172:910–923.e16.

Coale TH, Moosburner M, Horák A, Oborník M, Barbeau KA, Allen AE. 2019. Reduction-dependent siderophore assimilation in a model pennate diatom. *Proceedings of the National Academy of Sciences*. p. 201907234.

Coello-Camba A, Agustí S. 2017. Thermal thresholds of phytoplankton growth in polar waters and their consequences for a warming polar ocean. *Frontiers in Marine Science*. 4:168.

Cohen NR, A Ellis K, Burns WG, Lampe RH, Schuback N, Johnson Z, Sañudo-Wilhelmy S, Marchetti A. 2017. Iron and vitamin interactions in marine diatom isolates and natural assemblages of the Northeast Pacific Ocean: Iron and vitamin interactions in diatoms. *Limnology and Oceanography*. 62:2076–2096.

Cohen NR, Gong W, Moran DM, McIlvin MR, Saito MA, Marchetti A. 2018a. Transcriptomic and proteomic responses of the oceanic diatom *Pseudo-nitzschia granii* to iron limitation: Intracellular processes of an iron-limited diatom. *Environmental Microbiology*. 20:3109–3126.

Cohen NR, Mann E, Stemple B, Moreno CM, Rauschenberg S, Jacquot JE, Sunda WG, Twining BS, Marchetti A. 2018b. Iron storage capacities and associated ferritin gene expression among marine diatoms: Iron storage and ferritin expression in diatoms. *Limnology and Oceanography*. 63:1677–1691.

Coles VJ, Stukel MR, Brooks MT, et al. (11 co-authors). 2017. Ocean biogeochemistry modeled with emergent trait-based genomics. *Science*. 358:1149–1154. Tex.eprint: https://www.science.org/doi/pdf/10.1126/science.aan5712.

Conil S, Menéndez CG. 2006. Climate fluctuations of the Weddell Sea and its surroundings in a transient climate change scenario. *Climate Dynamics*. 27:83–99.

Cullen JT, Chase Z, Coale KH, Fitzwater SE, Sherrell RM. 2003. Effect of iron limitation on the cadmium to phosphorus ratio of natural phytoplankton assemblages from the Southern Ocean. *Limnology and Oceanography*. 48:1079–1087. Tex.eprint: https://aslopubs.onlinelibrary.wiley.com/doi/pdf/10.4319/lo.2003.48.3.1079.

Cutter G, Casciotti K, Croot P, Geibert W, Heimbürger LE, Lohan M, Planquette H, van de Flierdt T. 2017. *Sampling and Sample-handling Protocols for GEOTRACES Cruises - Version 3*. p. 178.

de Baar H, Buma A, Nolting R, Cadee G, Jacques G, Treguer P. 1990. On iron limitation of the Southern Ocean: experimental observations in the Weddell and Scotia Seas. *Marine Ecology Progress Series*. 65:105–122.

De Baar H, Timmermans K, Laan P, et al. (11 co-authors). 2008. Titan: A new facility for ultraclean sampling of trace elements and isotopes in the deep oceans in the international Geotraces program. *Marine Chemistry*. 111:4–21.

de Baar HJW, Boyd PW, Coale KH, et al. (34 co-authors). 2005. Synthesis of iron fertilization experiments: From the Iron Age in the Age of Enlightenment. *Journal of Geophysical Research: Oceans*. 110. Tex.eprint: https://agupubs.onlinelibrary.wiley.com/doi/pdf/10.1029/2004JC002601.

de Jong J, Schoemann V, Maricq N, Mattielli N, Langhorne P, Haskell T, Tison JL. 2013. Iron in land-fast sea ice of McMurdo Sound derived from sediment resuspension and wind-blown dust attributes to primary productivity in the Ross Sea, Antarctica. *Marine Chemistry*. 157:24–40.

Delmont TO, Gaia M, Hinsinger DD, et al. (54 co-authors). 2022. Functional repertoire convergence of distantly related eukaryotic plankton lineages abundant in the sunlit ocean. *Cell Genomics*. 2:100123.

Den TQ, Neu TR, Sultana S, Giebel HA, Simon M, Billerbeck S. 2023. Distinct glycoconjugate cell surface structures make the pelagic diatom *Thalassiosira rotula* an attractive habitat for bacteria. *Journal of Phycology*. 59:309–322. Tex.eprint: https://onlinelibrary.wiley.com/doi/pdf/10.1111/jpy.13308.

Di Martino Rigano V, Vona V, Lobosco O, Carillo P, Lunn JE, Carfagna S, Esposito S, Caiazzo M, Rigano C. 2006. Temperature dependence of nitrate reductase in the psychrophilic unicellular alga *Koliella antarctica* and the mesophilic alga *Chlorella sorokiniana*. *Plant, Cell and Environment*. 29:1400–1409.

DiTullio GR, Garcia N, Riseman SF, Sedwick PN. 2007. Effects of iron concentration on pigment composition in *Phaeocystis antarctica* grown at low irradiance. In: van Leeuwe MA, Stefels J, Belviso S, Lancelot C, Verity PG, Gieskes WWC, editors, Phaeocystis, major link in the biogeochemical cycling of climate-relevant elements, Dordrecht: Springer Netherlands, pp. 71–81.

DiTullio GR, Smith Jr WO. 1996. Spatial patterns in phytoplankton biomass and pigment distributions in the Ross Sea. *Journal of Geophysical Research: Oceans*. 101:18467–18477. Tex.eprint: https://agupubs.onlinelibrary.wiley.com/doi/pdf/10.1029/96JC00034.

Dobell C. 1932. Antony van Leeuwenhoek and his "Little animals"; being some account of the father of protozoology and bacteriology and his multifarious discoveries in these disciplines. New York, Harcourt, Brace and company, 1932. Pages: 516 tex.copyright: No known copyright restrictions as determined by scanning institution.

Dugdale RC, Wilkerson FP. 1986. The use of ^{15}N to measure nitrogen uptake in eutrophic oceans; experimental considerations. *Limnology and Oceanography*. 31:673–689.

Dutkiewicz S, Follows MJ, Bragg JG. 2009. Modeling the coupling of ocean ecology and biogeochemistry. *Global Biogeochemical Cycles*. 23. Tex.eprint: https://agupubs.onlinelibrary.wiley.com/doi/pdf/10.1029/2008GB003405.

Eich C, Biggs TEG, van de Poll WH, van Manen M, Tian HA, Jung J, Lee Y, Middag R, Brussaard CPD. 2022. Ecological importance of viral lysis as a loss factor of phytoplankton in the amundsen sea. *Microorganisms*. 10. Tex.article-number: 1967 tex.pubmedid: 36296243.

Elias JE, Gygi SP. 2007. Target-decoy search strategy for increased confidence in large-scale protein identifications by mass spectrometry. *Nature Methods*. 4:207–214.

Ellis KA, Cohen NR, Moreno C, Marchetti A. 2017. Cobalamin-independent methionine synthase distribution and influence on vitamin B_{12} growth requirements in marine diatoms. *Protist*. 168:32–47.

Eng JK, Searle BC, Clauser KR, Tabb DL. 2011. A face in the crowd: Recognizing peptides through database search*. *Molecular & Cellular Proteomics*. 10:R111.009522.

Engel BD, Schaffer M, Kuhn Cuellar L, Villa E, Plitzko JM, Baumeister W. 2015. Native architecture of the *Chlamydomonas* chloroplast revealed by in situ cryo-electron tomography. *eLife*. 4:e04889. Publisher: eLife Sciences Publications, Ltd tex.article_type: journal tex.citation: eLife 2015;4:e04889 tex.pub_date: 2015-01-13.

Enright AJ. 2002. An efficient algorithm for large-scale detection of protein families. *Nucleic Acids Research*. 30:1575–1584.

Eppley R. 1972. Temperature and phytoplankton growth in the sea. *Fishery Bulletin*. 70:1063–1085.

Eppley RW, Peterson BJ. 1979. Particulate organic matter flux and planktonic new production in the deep ocean. *Nature*. 282:677–680.

Falcon S, Gentleman R. 2007. Using GOstats to test gene lists for GO term association. *Bioinformatics*. 23:257–258.

Farewell A, Neidhardt FC. 1998. Effect of temperature on in vivo protein synthetic capacity in *Escherichia coli*. *Journal of Bacteriology*. 180:4704–4710.

Field CB, Behrenfeld MJ, Randerson JT, Falkowski P. 1998. Primary production of the biosphere: Integrating terrestrial and oceanic components. *Science*. 281:237–240.

Finkel ZV, Beardall J, Flynn KJ, Quigg A, Rees TAV, Raven JA. 2010. Phytoplankton in a changing world: cell size and elemental stoichiometry. *Journal of Plankton Research*. 32:119–137.

Finkel ZV, Follows MJ, Liefer JD, Brown CM, Benner I, Irwin AJ. 2016. Phylogenetic diversity in the macromolecular composition of microalgae. *PLOS ONE*. 11:e0155977.

Flynn KJ, Raven JA, Rees TAV, Finkel Z, Quigg A, Beardall J. 2010. Is the growth rate hypothesis applicable to microalgae? Questioning the growth rate hypothesis. *Journal of Phycology*. 46:1–12.

Follows MJ, Dutkiewicz S, Grant S, Sallie W Chisholm. 2007. Emergent biogeography of microbial communities in a model ocean. *Science (New York, N.Y.)*. 315:1843–1846. Tex.eprint: https://www.science.org/doi/pdf/10.1126/science.1138544.

Frölicher TL, Sarmiento JL, Paynter DJ, Dunne JP, Krasting JP, Winton M. 2015. Dominance of the Southern Ocean in anthropogenic carbon and heat uptake in CMIP5 models. *Journal of Climate*. 28:862–886.

Galstyan A, Robertazzi A, Knapp EW. 2012. Oxygen-Evolving Mn cluster in photosystem II: The protonation pattern and oxidation state in the high-resolution crystal structure. *Journal of the American Chemical Society*. 134:7442–7449. Publisher: American Chemical Society.

Gao Y, Smith GJ, Alberte RS. 2000. Temperature dependence of nitrate reductase activity in marine phytoplankton: biochemical analysis and ecological implications. *Journal of Phycology*. 36:304–313.

Gao Y, Smith J, Randall A. 1993. Nitrate reductase from the marine diatom *Skeletonema costatum* . *Plant Physiology*. 103:1437–1445.

Garcia NS, Sexton J, Riggins T, Brown J, Lomas MW, Martiny AC. 2018. High variability in cellular stoichiometry of carbon, nitrogen, and phosphorus within classes of marine eukaryotic phytoplankton under sufficient nutrient conditions. *Frontiers in Microbiology*. 9:543.

Geider R, La Roche J. 2002. Redfield revisited: variability of C:N:P in marine microalgae and its biochemical basis. *European Journal of Phycology*. 37:1–17.

Gerringa LJA, Alderkamp AC, van Dijken G, Laan P, Middag R, Arrigo KR. 2020. Dissolved trace metals in the Ross Sea. *Frontiers in Marine Science*. 7.

Geuer JK, Krock B, Leefmann T, Koch BP. 2019. Quantification, extractability and stability of dissolved domoic acid within marine dissolved organic matter. *Marine Chemistry*. 215:103669.

Goldman JC, Carpenter EJ. 1974. A kinetic approach to the effect of temperature on algal growth1: Temperature and algal growth. *Limnology and Oceanography*. 19:756–766.

Gordon LI, Jennings JC, Ross AA, Krest JM. 1993. A Suggested Protocol for Continuous Flow Automated Analysis of Seawater Nutrients (Phosphate, Nitrate, Nitrite and Silicic Acid) in the WOCE Hydrographic Program and the Joint Global Ocean Fluxes Study. *WOCE hydrographic program office, methods manual WHPO*. 68/91:1–52.

Greene RM, Geider RJ, Kolber Z, Falkowski PG. 1992. Iron-induced changes in light harvesting and photochemical energy conversion processes in eukaryotic marine algae. *Plant Physiology*. 100:565–575.

Guillou L, Bachar D, Audic S, et al. (32 co-authors). 2012. The Protist Ribosomal Reference database (PR2): a catalog of unicellular eukaryote Small Sub-Unit rRNA sequences with curated taxonomy. *Nucleic Acids Research*. 41:D597–D604.

Haeckel E. 1904. Kunstformen der Natur. Leipzig: Bibliographisches Institut Leipzig.

Halliwell B, Gutteridge JM. 1992. Biologically relevant metal ion-dependent hydroxyl radical generation An update. *FEBS Letters*. 307:108–112. Tex.eprint: https://febs.onlinelibrary.wiley.com/doi/pdf/10.1016/0014-5793%2892%2980911-Y.

Hama T, Miyazaki T, Ogawa Y, Iwakuma T, Takahashi M, Otsuki A, Ichimura S. 1983. Measurement of photosynthetic production of a marine phytoplankton population using a stable ^{13}C isotope. *Marine Biology*. 73:31–36.

Han X, Aslanian A, Yates JR. 2008. Mass spectrometry for proteomics. *Current Opinion in Chemical Biology*. 12:483–490.

Henley SF, Cavan EL, Fawcett SE, et al. (13 co-authors). 2020. Changing biogeochemistry of the Southern Ocean and its ecosystem implications. *Frontiers in Marine Science*. 7.

Hettich RL, Pan C, Chourey K, Giannone RJ. 2013. *Metaproteomics* : Harnessing the power of high performance mass spectrometry to identify the suite of proteins that control metabolic activities in microbial communities. *Analytical Chemistry*. 85:4203–4214.

Hippmann AA, Schuback N, Moon KM, McCrow JP, Allen AE, Foster LJ, Green BR, Maldonado MT. 2017. Contrasting effects of copper limitation on the photosynthetic apparatus in two strains of the open ocean diatom *Thalassiosira oceanica*. *PLOS ONE*. 12:e0181753.

Ho TY, Quigg A, Finkel ZV, Milligan AJ, Wyman K, Falkowski PG, Morel FMM. 2003. The elemental composition of some marine phytoplankton. *Journal of Phycology*. 39:1145–1159.

Hoffmann LJ, Peeken I, Lochte K. 2007. Effects of iron on the elemental stoichiometry during EIFEX and in the diatoms *Fragilariopsis kerguelensis* and *Chaetoceros dichaeta*. *Biogeosciences (Online)*. 4:569–579.

Holm-Hansen O, Lorenzen CJ, Holmes RW, Strickland JDH. 1965. Fluorometric determination of chlorophyll. *ICES Journal of Marine Science*. 30:3–15.

Hoopmann MR, MacCoss MJ, Moritz RL. 2012. Identification of peptide features in precursor spectra using Hardklör and Krönik. *Current Protocols in Bioinformatics*. 13:bi1318s37.

Huber O, Sumper M. 1994. Algal-CAMs: isoforms of a cell adhesion molecule in embryos of the alga *Volvox* with homology to *Drosophila* fasciclin I. *The EMBO Journal*. 13:4212–4222.

Hudson RJM, Morel FMM. 1990. lron transport in marine phytoplankton: Kinetics of cellular and medium coordination reactions. *Limnology and Oceanography*. 35:1002–1020.

Hulstaert N, Shofstahl J, Sachsenberg T, Walzer M, Barsnes H, Martens L, Perez-Riverol Y. 2020. ThermoRawFileParser: Modular, Scalable, and Cross-Platform RAW File Conversion. *Journal of Proteome Research*. 19:537–542.

Hutchins DA, Boyd PW. 2016. Marine phytoplankton and the changing ocean iron cycle. *Nature Climate Change*. 6:1072–1079.

Hutchins DA, Bruland KW. 1998. Iron-limited diatom growth and Si:N uptake ratios in a coastal upwelling regime. *Nature*. 393:561–564.

Hutchins DA, Hare CE, Weaver RS, et al. (15 co-authors). 2002. Phytoplankton iron limitation in the Humboldt Current and Peru Upwelling. *Limnology and Oceanography*. 47:997–1011.

Hutchins DA, Sañudo-Wilhelmy SA. 2022. The enzymology of ocean global change. *Annual Review of Marine Science*. 14:187–211. Tex.eprint: https://doi.org/10.1146/annurev-marine-032221-084230.

Hutchins DA, Sedwick PN, DiTullio GR, Boyd PW, Quéguiner B, Griffiths FB, Crossley C. 2001. Control of phytoplankton growth by iron and silicic acid availability in the subantarctic Southern Ocean: Experimental results from the SAZ Project. *Journal of Geophysical Research: Oceans*. 106:31559–31572.

Inomura K, Omta AW, Talmy D, Bragg J, Deutsch C, Follows MJ. 2020. A mechanistic model of macromolecular allocation, elemental stoichiometry, and growth rate in phytoplankton. *Frontiers in Microbiology*. 11.

IPCC. 2019. *IPCC Special Report on the Ocean and Cryosphere in a Changing Climate*. .

Jabre L, Bertrand EM. 2020. Interactive effects of iron and temperature on the growth of *Fragilariopsis cylindrus*. *Limnology and Oceanography Letters*. p. lol2.10158.

Jabre LJ, Allen AE, McCain JSP, et al. (11 co-authors). 2021. Molecular underpinnings and biogeochemical consequences of enhanced diatom growth in a warming Southern Ocean. *Proceedings of the National Academy of Sciences*. 118:e2107238118.

Jena B, Bajish CC, Turner J, Ravichandran M, Anilkumar N, Kshitija S. 2022. Record low sea ice extent in the Weddell Sea, Antarctica in April/May 2019 driven by intense and explosive polar cyclones. *npj Climate and Atmospheric Science*. 5:19.

Jiang HB, Fu FX, Rivero-Calle S, Levine NM, Sañudo-Wilhelmy SA, Qu PP, Wang XW, Pinedo-Gonzalez P, Zhu Z, Hutchins DA. 2018. Ocean warming alleviates iron limitation of marine nitrogen fixation. *Nature Climate Change*. 8:709–712.

Jickells T, An Z, Anderson K, et al. (18 co-authors). 2005. Global iron connections between desert dust, ocean biogeochemistry, and climate. *Science, New Series*. 308:67–71.

Jin L, Bi Y, Hu C, Qu J, Shen S, Wang X, Tian Y. 2021. A comparative study of evaluating missing value imputation methods in label-free proteomics. *Scientific Reports*. 11:1760.

Jordan DB, Ogren WL. 1984. The CO_2/O_2 specificity of ribulose 1,5-bisphosphate carboxylase/oxygenase. *Planta*. 161:308–313.

Joy-Warren HL, Alderkamp AC, van Dijken GL, et al. (13 co-authors). 2022. Spring-time phytoplankton responses to light and iron availability along the western Antarctic Peninsula. *Limnology and Oceanography*. 67:800–815. Tex.eprint: https://aslopubs.onlinelibrary.wiley.com/doi/pdf/10.1002/lno.12035.

Kang SH, Fryxell GA. 1992. *Fragilariopsis cylindrus* (Grunow) Krieger: the most abundant diatom in water column assemblages of Antarctic marginal ice-edge zones. *Polar Biology*. 12:609–627.

Kang SH, Fryxell GA. 1993. Phytoplankton in the Weddell Sea, Antarctica: composition, abundance and distribution in water-column assemblages of the marginal ice-edge zone during austral autumn. *Marine Biology*. 116:335–348.

Kazamia E, Sutak R, Paz-Yepes J, et al. (13 co-authors). 2018. Endocytosis-mediated siderophore uptake as a strategy for Fe acquisition in diatoms. *Science Advances*. 4:15.

Keeling PJ, Burki F, Wilcox HM, et al. (81 co-authors). 2014. The marine microbial eukaryote transcriptome sequencing project (MMETSP): Illuminating the functional diversity of eukaryotic life in the oceans through transcriptome sequencing. *PLOS Biology*. 12:1–6. Publisher: Public Library of Science.

Kiene RP, Slezak D. 2006. Low dissolved DMSP concentrations in seawater revealed by small-volume gravity filtration and dialysis sampling: Filtration and dialysis for dissolved DMSP. *Limnology and Oceanography: Methods*. 4:80–95.

Kim S, Pevzner PA. 2014. MS-GF+ makes progress towards a universal database search tool for proteomics. *Nature Communications*. 5:5277.

Koroleff F. 1983. Determination of nutrients. New York: Verlag Chemie.

Kosakowska A, Lewandowska J, Stoń J, Burkiewicz K. 2004. Qualitative and quantitative composition of pigments in *Phaeodactylum tricornutum* (Bacillariophyceae) stressed by iron. *BioMetals*. 17:45–52.

Kovalchik KA, Colborne S, Spencer SE, Sorensen PH, Chen DDY, Morin GB, Hughes CS. 2019. RawTools: Rapid and dynamic interrogation of Orbitrap data files for mass spectrometer system management. *Journal of Proteome Research*. 18:700–708. Publisher: American Chemical Society.

Kraft K, Velhonoja O, Eerola T, et al. (13 co-authors). 2022. Towards operational phytoplankton recognition with automated high-throughput imaging, near-real-time data processing, and convolutional neural networks. *Frontiers in Marine Science*. 9.

Krause G, Weis E. 1991. Chlorophyll fluorescence and photosynthesis: The basics. *Annu. Rev. Plant. Physiol. Plant. Mol. Biol.* 42:313–349.

Kudo I, Miyamoto M, Noiri Y, Maita Y. 2000. Combined effects of temperature and and iron on the growth and physiology of the marine diatom *Phaeodactylum tricornutum* (Bacillariophyceae). *Journal of Phycology*. 36:1096–1102. Tex.eprint: https://onlinelibrary.wiley.com/doi/pdf/10.1046/j.1529-8817.2000.99042.x.

Kumar D, Yadav AK, Dash D. 2017. Choosing an optimal database for protein identification from tandem mass spectrometry data. In: Keerthikumar S, Mathivanan S, editors, Proteome bioinformatics, New York, NY: Springer New York, pp. 17–29.

Kwiatkowski L, Aumont O, Bopp L, Ciais P. 2018. The impact of variable phytoplankton stoichiometry on projections of primary production, food quality, and carbon uptake in the global ocean. *Global Biogeochemical Cycles*. 32:516–528. Tex.eprint: https://agupubs.onlinelibrary.wiley.com/doi/pdf/10.1002/2017GB005799.

Lampe RH, Mann EL, Cohen NR, Till CP, Thamatrakoln K, Brzezinski MA, Bruland KW, Twining BS, Marchetti A. 2018. Different iron storage strategies among bloom-forming diatoms. *Proceedings of the National Academy of Sciences*. 115:E12275–E12284.

Lane ES, Semeniuk DM, Strzepek RF, Cullen JT, Maldonado MT. 2009. Effects of iron limitation on intracellular cadmium of cultured phytoplankton: Implications for surface dissolved cadmium to phosphate ratios. *Marine Chemistry*. 115:155–162.

Lane TW, Morel FMM. 2000. A biological function for cadmium in marine diatoms. *Proceedings of the National Academy of Sciences*. 97:4627–4631. Tex.eprint: https://www.pnas.org/doi/pdf/10.1073/pnas.090091397.

Lane TW, Saito MA, George GN, Pickering IJ, Prince RC, Morel FMM. 2005. A cadmium enzyme from a marine diatom. *Nature*. 435:42–42.

LaRoche J, Boyd PW, McKay M, Geider R. 1996. Flavodoxin as an in situ marker for iron stress in phytoplankton. *Nature*. 382:802–805.

Laufkötter C, Vogt M, Gruber N, et al. (20 co-authors). 2015. Drivers and uncertainties of future global marine primary production in marine ecosystem models. *Biogeosciences*. 12:6955–6984.

Lee JG, Ahner BA, Morel FMM. 1996. Export of cadmium and phytochelatin by the marine diatom *Thalassiosira weissflogii*. *Environmental Science & Technology*. 30:1814–1821. Publisher: American Chemical Society.

Li G, Cheng L, Zhu J, Trenberth KE, Mann ME, Abraham JP. 2020. Increasing ocean stratification over the past half-century. *Nature Climate Change*. 10:1116–1123.

Liefer JD, Garg A, Fyfe MH, Irwin AJ, Benner I, Brown CM, Follows MJ, Omta AW, Finkel ZV. 2019. The macromolecular basis of phytoplankton C:N:P under nitrogen starvation. *Frontiers in Microbiology*. 10:763.

Litchman E, Klausmeier CA. 2008. Trait-based community ecology of phytoplankton. *Annual Review of Ecology, Evolution, and Systematics*. 39:615–639. Tex.eprint: https://doi.org/10.1146/annurev.ecolsys.39.110707.173549.

Liu H, Kelly M, Campbell D, Dong S, Zhu J, Wang S. 2007. Exposure to domoic acid affects larval development of king scallop *Pecten maximus* (Linnaeus, 1758). *Aquatic Toxicology*. 81:152–158.

Liu X, Smith WO. 2012. Physiochemical controls on phytoplankton distributions in the Ross Sea, Antarctica. *Journal of Marine Systems*. 94:135–144.

Liu Y, Beyer A, Aebersold R. 2016. On the dependency of cellular protein levels on mRNA abundance. *Cell*. 165:535–550.

Lomas MW, Baer SE, Acton S, Krause JW. 2019. Pumped up by the cold: Elemental quotas and stoichiometry of cold-water diatoms. *Frontiers in Marine Science*. 6:286.

Lomas MW, Baer SE, Mouginot C, Terpis KX, Lomas DA, Altabet MA, Martiny AC. 2021. Varying influence of phytoplankton biodiversity and stoichiometric plasticity on bulk particulate stoichiometry across ocean basins. *Communications Earth & Environment*. 2:143.

Losh JL, Young JN, Morel FMM. 2013. Rubisco is a small fraction of total protein in marine phytoplankton. *New Phytologist*. 198:52–58.

Louca S, Parfrey LW, Michael Doebeli. 2016. Decoupling function and taxonomy in the global ocean microbiome. *Science (New York, N.Y.)*. 353:1272–1277. Tex.eprint: https://www.science.org/doi/pdf/10.1126/science.aaf4507.

Mackey MD, Mackey DJ, Higgins HW, Wright SW. 1996. CHEMTAX—a program for estimating class abundances from chemical markers: application to HPLC measurements of phytoplankton. *Marine Ecology Progress Series*. 144:265–283. Publisher: Inter-Research Science Center.

Mahowald NM, Baker AR, Bergametti G, Brooks N, Duce RA, Jickells TD, Kubilay N, Prospero JM, Tegen I. 2005. Atmospheric global dust cycle and iron inputs to the ocean. *Global Biogeochemical Cycles*. 19. Tex.eprint: https://agupubs.onlinelibrary.wiley.com/doi/pdf/10.1029/2004GB002402.

Mangoni O, Saggiomo M, Bolinesi F, Castellano M, Povero P, Saggiomo V, DiTullio GR. 2019. *Phaeocystis antarctica* unusual summer bloom in stratified antarctic coastal waters (Terra Nova Bay, Ross Sea). *Marine Environmental Research*. 151:104733.

Mangoni O, Saggiomo V, Bolinesi F, Margiotta F, Budillon G, Cotroneo Y, Misic C, Rivaro P, Saggiomo M. 2017. Phytoplankton blooms during austral summer in the Ross Sea, Antarctica: Driving factors and trophic implications. *PLOS ONE*. 12:e0176033.

Marañón E, Lorenzo MP, Cermeño P, Mouriño-Carballido B. 2018. Nutrient limitation suppresses the temperature dependence of phytoplankton metabolic rates. *The ISME Journal*. 12:1836–1845.

Marchetti A, Catlett D, Hopkinson BM, Ellis K, Cassar N. 2015. Marine diatom proteorhodopsins and their potential role in coping with low iron availability. *The ISME Journal*. 9:2745–2748.

Marchetti A, Parker MS, Moccia LP, Lin EO, Arrieta AL, Ribalet F, Murphy MEP, Maldonado MT, Armbrust EV. 2009. Ferritin is used for iron storage in bloom-forming marine pennate diatoms. *Nature*. 457:467–470.

Marchetti A, Schruth DM, Durkin CA, Parker MS, Kodner RB, Berthiaume CT, Morales R, Allen AE, Armbrust EV. 2012. Comparative metatranscriptomics identifies molecular bases for the physiological responses of phytoplankton to varying iron availability. *Proceedings of the National Academy of Sciences*. 109:E317–E325.

Marie D, Partensky F, Vaulot D, Brussaard C. 1999. Enumeration of phytoplankton, bacteria, and viruses in marine samples. *Current Protocols in Cytometry*. 10:11.11.1–11.11.15. Tex.eprint: https://currentprotocols.onlinelibrary.wiley.com/doi/pdf/10.1002/0471142956.cy1111s10.

Martin J, Fitzwater SE. 1988. Iron deficiency limits phytoplankton growth in the north-east Pacific subarctic. *Nature*. 331:341–343.

Martin JH, Fitzwater SE, Gordon RM. 1990. Iron deficiency limits phytoplankton growth in Antarctic waters. *Global Biogeochemical Cycles*. 4:5–12.

Martin JH, Gordon M, Fitzwater SE. 1991. The case for iron. *Limnology and Oceanography*. 36:1793–1802.

Martin M. 2011. Cutadapt removes adapter sequences from high-throughput reads. *EMBnet.journal*. 17:3.

Martiny AC, Pham CTA, Primeau FW, Vrugt JA, Moore JK, Levin SA, Lomas MW. 2013. Strong latitudinal patterns in the elemental ratios of marine plankton and organic matter. *Nature Geoscience*. 6:279–283.

Maxwell DP, Falk S, Trick CG, Huner N. 1994. Growth at low temperature mimics high-light acclimation in *Chlorella vulgaris*. *Plant Physiology*. 105:535–543.

McCain JSP, Allen AE, Bertrand EM. 2022. Proteomic traits vary across taxa in a coastal Antarctic phytoplankton bloom. *The ISME Journal*. 16:569–579.

McCain JSP, Bertrand EM. 2022. Phytoplankton antioxidant systems and their contributions to cellular elemental stoichiometry. *Limnology and Oceanography Letters*. 7:96–111. Tex.eprint: https://aslopubs.onlinelibrary.wiley.com/doi/pdf/10.1002/lol2.10233.

McCain JSP, Tagliabue A, Susko E, Achterberg EP, Allen AE, Erin M Bertrand. 2021. Cellular costs underpin micronutrient limitation in phytoplankton. *Science Advances*. 7:eabg6501. Tex.eprint: https://www.science.org/doi/pdf/10.1126/sciadv.abg6501.

McQuaid JB, Kustka AB, Oborník M, et al. (11 co-authors). 2018. Carbonate-sensitive phytotransferrin controls high-affinity iron uptake in diatoms. *Nature*. 555:534–537.

Meijers AJS, Le Quéré C, Monteiro PMS, Sallée JB. 2023. Heat and carbon uptake in the Southern Ocean: the state of the art and future priorities. *Philosophical Transactions of the Royal Society A: Mathematical, Physical and Engineering Sciences*. 381:20220071. Tex.eprint: https://royalsocietypublishing.org/doi/pdf/10.1098/rsta.2022.0071.

Middag R, Zitoun R, Conway T. 2023. Trace metals. In: Blasco J, Tovar-Sánchez A, editors, Marine analytical chemistry, Cham: Springer International Publishing, pp. 103–198.

Mock T, Hoch N. 2005. Long-term temperature acclimation of photosynthesis in steady-state cultures of the polar diatom *Fragilariopsis cylindrus*. *Photosynthesis research*. 85:307–317.

Mock T, Otillar RP, Strauss J, et al. (44 co-authors). 2017. Evolutionary genomics of the cold-adapted diatom *Fragilariopsis cylindrus*. *Nature*. 541:536–540.

Moore J, Doney SC, Glover DM, Fung IY. 2001. Iron cycling and nutrient-limitation patterns in surface waters of the World Ocean. *Deep Sea Research Part II: Topical Studies in Oceanography*. 49:463–507.

Moore JK, Braucher O. 2008. Sedimentary and mineral dust sources of dissolved iron to the world ocean. *Biogeosciences*. 5:631–656.

Moore JK, Fu W, Primeau F, Britten GL, Lindsay K, Long M, Doney SC, Mahowald N, Hoffman F, Randerson JT. 2018. Sustained climate warming drives declining marine biological productivity. *Science*. 359:1139–1143.

Moreau S, Hattermann T, de Steur L, et al. (31 co-authors). 2023. Wind-driven upwelling of iron sustains dense blooms and food webs in the eastern Weddell Gyre. *Nature Communications*. 14:1303.

Moreno CM, Lin Y, Davies S, Monbureau E, Cassar N, Marchetti A. 2018. Examination of gene repertoires and physiological responses to iron and light limitation in Southern Ocean diatoms. *Polar Biology*. 41:679–696.

Morrissey J, Sutak R, Paz-Yepes J, et al. (14 co-authors). 2015. A novel protein, ubiquitous in marine phytoplankton, concentrates iron at the cell surface and facilitates uptake. *Current Biology*. 25:364–371.

Motone K, Nivala J. 2023. Not if but when nanopore protein sequencing meets single-cell proteomics. *Nature Methods*. 20:336–338.

Murphy EJ, Johnston NM, Hofmann EE, et al. (22 co-authors). 2021. Global connectivity of Southern Ocean ecosystems. *Frontiers in Ecology and Evolution*. 9.

Nissen C, Vogt M. 2021. Factors controlling the competition between *Phaeocystis* and diatoms in the Southern Ocean and implications for carbon export fluxes. *Biogeosciences*. 18:251–283.

Nunn BL, Faux JF, Hippmann AA, Maldonado MT, Harvey HR, Goodlett DR, Boyd PW, Strzepek RF. 2013. Diatom proteomics reveals unique acclimation strategies to mitigate Fe limitation. *PLoS ONE*. 8:e75653.

Ohnemus DC, Auro ME, Sherrell RM, Lagerström M, Morton PL, Twining BS, Rauschenberg S, Lam PJ. 2014. Laboratory intercomparison of marine particulate digestions including Piranha: a novel chemical method for dissolution of polyethersulfone filters. *Limnology and Oceanography: Methods*. 12:530–547.

Olson R, Sosik H, Chekalyuk A, Shalapyonok A. 2000. Effects of iron enrichment on phytoplankton in the Southern Ocean during late summer: active fluorescence and flow cytometric analyses. *Deep Sea Research Part II: Topical Studies in Oceanography*. 47:3181–3200.

Orsi A, Johnson G, Bullister J. 1999. Circulation, mixing, and production of antarctic bottom water. *Progress in Oceanography*. 43:55–109.

Oxborough K, Moore CM, Suggett DJ, Lawson T, Chan HG, Geider RJ. 2012. Direct estimation of functional PSII reaction center concentration and PSII electron flux on a volume basis: a new approach to the analysis of Fast Repetition Rate fluorometry (FRRf) data: Analysis of FRRf data: a new approach. *Limnology and Oceanography: Methods*. 10:142–154.

Pankowski A, McMinn A. 2009a. Development of immunoassays for the iron-regulated proteins ferredoxin and flavodoxin in polar microalgae. *Journal of Phycology*. 45:771–783.

Pankowski A, McMinn A. 2009b. Iron availability regulates growth, photosynthesis, and production of ferredoxin and flavodoxin in Antarctic sea ice diatoms. *Aquatic Biology*. 4:273–288.

Parslow JS, Harrison PJ, Thompson PA. 1984. Development of rapid ammonium uptake during starvation of batch and chemostat cultures of the marine diatom *Thalassiosira pseudonana*. *Marine Biology*. 83:43–50.

Parsons T, Maita Y, Lalli C. 1984. A manual of chemical and biological methods for seawater analysis. New York: Pergamon Press.

Pauly D, Christensen V. 1995. Primary production required to sustain global fisheries. *Nature*. 374:255–257.

Pedregosa F, Varoquaux G, Gramfort A, et al. (13 co-authors). 2011. Scikit-learn: Machine learning in Python. *J. Mach. Learn. Res.* 12.

Peers G, Price NM. 2004. A role for manganese in superoxide dismutases and growth of iron-deficient diatoms. *Limnology and Oceanography*. 49:1774–1783.

Peers G, Price NM. 2006. Copper-containing plastocyanin used for electron transport by an oceanic diatom. *Nature*. 441:341–344.

Penen F, Isaure MP, Dobritzsch D, Bertalan I, Castillo-Michel H, Proux O, Gontier E, Le Coustumer P, Schaumlöffel D. 2017. Pools of cadmium in *Chlamydomonas reinhardtii* revealed by chemical imaging and XAS spectroscopy. *Metallomics : integrated biometal science*. 9:910–923. Tex.eprint: https://academic.oup.com/metallomics/article-pdf/9/7/910/34732293/c7mt00029d.pdf.

Petrou K, Doblin MA, Ralph PJ. 2011. Heterogeneity in the photoprotective capacity of three Antarctic diatoms during short-term changes in salinity and temperature. *Marine Biology*. 158:1029–1041.

Petrou K, Ralph P. 2011. Photosynthesis and net primary productivity in three Antarctic diatoms: possible significance for their distribution in the Antarctic marine ecosystem. *Marine Ecology Progress Series*. 437:27–40.

Petrucciani A, Moretti P, Ortore MG, Norici A. 2023. Integrative effects of morphology, silicification, and light on diatom vertical movements. *Frontiers in Plant Science*. 14.

Pierella Karlusich JJ, Lombard F, Irisson JO, Bowler C, Foster RA. 2022. Coupling imaging and omics in plankton surveys: State-of-the-art, challenges, and future directions. *Frontiers in Marine Science*. 9.

Podell S, Gaasterland T. 2007. DarkHose: a new method for genome-wide prediction of horizontal gene transfer. *Genome Biology*. 8:R16.

Price NM, Andersen LF, Morel FM. 1991. Iron and nitrogen nutrition of equatorial Pacific plankton. *Deep Sea Research Part A. Oceanographic Research Papers*. 38:1361–1378.

Price NM, Harrison GI, Hering JG, Hudson RJ, Nirel PM, Palenik B, Morel FM. 1988. Preparation and chemistry of the artificial algal culture medium Aquil. *Biological Oceanography*. 6:20.

Primeau FW, Holzer M, DeVries T. 2013. Southern Ocean nutrient trapping and the efficiency of the biological pump. *Journal of Geophysical Research: Oceans*. 118:2547–2564. Tex.eprint: https://agupubs.onlinelibrary.wiley.com/doi/pdf/10.1002/jgrc.20181.

Quigg A, Finkel ZV, Irwin AJ, Rosenthal Y, Ho TY, Reinfelder JR, Schofield O, Morel FMM, Falkowski PG. 2003. The evolutionary inheritance of elemental stoichiometry in marine phytoplankton. *Nature*. 425:291–294.

Quéguiner B. 2013. Iron fertilization and the structure of planktonic communities in high nutrient regions of the Southern Ocean. *Deep Sea Research Part II: Topical Studies in Oceanography*. 90:43–54.

Quéré CL, Rödenbeck C, Buitenhuis ET, et al. (12 co-authors). 2007. Saturation of the southern ocean CO_2 sink due to recent climate change. *Science*. 316:1735–1738. Tex.eprint: https://www.science.org/doi/pdf/10.1126/science.1136188.

Raes EJ, Bodrossy L, Van De Kamp J, Bissett A, Ostrowski M, Brown MV, Sow SLS, Sloyan B, Waite AM. 2018. Oceanographic boundaries constrain microbial diversity gradients in the South Pacific Ocean. *Proceedings of the National Academy of Sciences*. 115.

Raven J. 2013a. RNA function and phosphorus use by photosynthetic organisms. *Frontiers in Plant Science*. 4.

Raven JA. 1988. The iron and molybdenum use efficiencies of plant growth with different energy, carbon and nitrogen sources. *New Phytologist*. 109:279–287.

Raven JA. 2013b. Iron acquisition and allocation in stramenopile algae. *Journal of Experimental Botany*. 64:2119–2127.

Raven JA, Evans MCW, Korb RE. 1999. The role of trace metals in photosynthetic electron transport in O_2-evolving organisms. *Photosynthesis Research*. 60:111–149.

Raven JA, Geider RJ. 1988. Temperature and algal growth. *New Phytologist*. 110:441–461.

Reay DS, Nedwell DB, Priddle J, Ellis-Evans JC. 1999. Temperature dependence of inorganic nitrogen uptake: Reduced affinity for nitrate at suboptimal temperatures in both algae and bacteria. *Applied and Environmental Microbiology*. 65:2577–2584.

Reed BD, Meyer MJ, Abramzon V, et al. (82 co-authors). 2022. Real-time dynamic single-molecule protein sequencing on an integrated semiconductor device. *Science (New York, N.Y.)*. 378:186–192. Tex.eprint: https://www.science.org/doi/pdf/10.1126/science.abo7651.

Rhee GY, Gotham IJ. 1981. The effect of environmental factors on phytoplankton growth: Temperature and the interactions of temperature with nutrient limitation. *Limnology and Oceanography*. 26:635–648.

Rho M, Tang H, Ye Y. 2010. FragGeneScan: predicting genes in short and error-prone reads. *Nucleic Acids Research*. 38:e191–e191.

Rickard G, Behrens E. 2016. CMIP5 Earth System Models with biogeochemistry: a Ross Sea assessment. *Antarctic Science*. 28:327–346.

Rijkenberg MJ, de Baar HJ, Bakker K, et al. (13 co-authors). 2015. "PRISTINE", a new high volume sampler for ultraclean sampling of trace metals and isotopes. *Marine Chemistry*. 177:501–509.

Robinson MD, McCarthy DJ, Smyth GK. 2010. edgeR: a Bioconductor package for differential expression analysis of digital gene expression data. *Bioinformatics*. 26:139–140.

Rohatgi A. 2022. Webplotdigitizer: Version 4.6.

Rose JM, Feng Y, DiTullio GR, et al. (13 co-authors). 2009. Synergistic effects of iron and temperature on Antarctic phytoplankton and microzooplankton assemblages. *Biogeosciences*. 6:3131–3147.

Roshan S, DeVries T, Wu J, Chen G. 2018. The internal cycling of zinc in the ocean. *Global Biogeochemical Cycles*. 32:1833–1849. Tex.eprint: https://agupubs.onlinelibrary.wiley.com/doi/pdf/10.1029/2018GB006045.

Ryderheim F, Grønning J, Kiørboe T. 2022. Thicker shells reduce copepod grazing on diatoms. *Limnology and Oceanography Letters*. 7:435–442. Tex.eprint: https://aslopubs.onlinelibrary.wiley.com/doi/pdf/10.1002/lol2.10243.

Röst HL, Sachsenberg T, Aiche S, et al. (27 co-authors). 2016. OpenMS: a flexible open-source software platform for mass spectrometry data analysis. *Nature Methods*. 13:741–748.

Röst HL, Schmitt U, Aebersold R, Malmström L. 2014. pyOpenMS: A Python-based interface to the OpenMS mass-spectrometry algorithm library. *PROTEOMICS*. 14:74–77. Tex.eprint: https://analyticalsciencejournals.onlinelibrary.wiley.com/doi/pdf/10.1002/pmic.201300246.

Sackett O, Petrou K, Reedy B, De Grazia A, Hill R, Doblin M, Beardall J, Ralph P, Heraud P. 2013. Phenotypic plasticity of Southern Ocean diatoms: Key to success in the sea ice habitat? *PLoS ONE*. 8:e81185.

Saito MA, Bertrand EM, Duffy ME, et al. (20 co-authors). 2019. Progress and challenges in ocean metaproteomics and proposed best practices for data sharing. *Journal of Proteome Research*. 18:1461–1476.

Sarmiento JL, Gruber N, Brzezinski MA, Dunne JP. 2004. High-latitude controls of thermocline nutrients and low latitude biological productivity. *Nature*. 427:56–60.

Schaum CE, Barton S, Bestion E, et al. (11 co-authors). 2017. Adaptation of phytoplankton to a decade of experimental warming linked to increased photosynthesis. *Nature Ecology & Evolution*. 1:0094.

Schiffrine N, Tremblay J, Babin M. 2022. Interactive effects of temperature and nitrogen source on the elemental stoichiometry of a polar diatom. *Limnology and Oceanography*. p. lno.12235.

Schmieder R, Lim YW, Edwards R. 2012. Identification and removal of ribosomal RNA sequences from metatranscriptomes. *Bioinformatics*. 28:433–435.

Schoffman H, Lis H, Shaked Y, Keren N. 2016. Iron–nutrient interactions within phytoplankton. *Frontiers in Plant Science*. 7.

Scholin CA, Gulland F, Doucette GJ, et al. (26 co-authors). 2000. Mortality of sea lions along the central California coast linked to a toxic diatom bloom. *Nature*. 403:80–84.

Schuback N, Schallenberg C, Duckham C, Maldonado MT, Tortell PD. 2015. Interacting effects of light and iron availability on the coupling of photosynthetic electron transport and CO_2-assimilation in marine phytoplankton. *PLOS ONE*. 10:e0133235.

Scott F, Marchant H, editors. 2005. Antarctic Marine Protists. ABRS, Canberra and Australian Antarctic Division.

Seifert G. 2018. Fascinating fasciclins: A surprisingly widespread family of proteins that mediate interactions between the cell exterior and the cell surface. *International Journal of Molecular Sciences*. 19:1628.

Senko MW, Beu SC, McLafferty FW. 1995. Determination of monoisotopic masses and ion populations for large biomolecules from resolved isotopic distributions. *Journal of the American Society for Mass Spectrometry*. 6:229–233.

Sheward RM, Liefer JD, Irwin AJ, Finkel ZV. 2023. Elemental stoichiometry of the key calcifying marine phytoplankton *Emiliania huxleyi* under ocean climate change: A meta-analysis. *Global Change Biology*. Tex.eprint: https://onlinelibrary.wiley.com/doi/pdf/10.1111/gcb.16807.

Silver MW, Bargu S, Coale SL, Benitez-Nelson CR, Garcia AC, Roberts KJ, Sekula-Wood E, Bruland KW, Coale KH. 2010. Toxic diatoms and domoic acid in natural and iron enriched waters of the oceanic Pacific. *Proceedings of the National Academy of Sciences*. 107:20762–20767.

Smith SR, Dupont CL, McCarthy JK, et al. (18 co-authors). 2019. Evolution and regulation of nitrogen flux through compartmentalized metabolic networks in a marine diatom. *Nature Communications*. 10:4552.

Smith WO, Tozzi S, Long MC, Sedwick PN, Peloquin JA, Dunbar RB, Hutchins DA, Kolber Z, DiTullio GR. 2013. Spatial and temporal variations in variable fluoresence in the Ross Sea (Antarctica): Oceanographic correlates and bloom dynamics. *Deep Sea Research Part I: Oceanographic Research Papers*. 79:141–155.

Spackeen J, Sipler R, Bertrand E, Xu K, McQuaid J, Walworth N, Hutchins D, Allen A, Bronk D. 2018a. Impact of temperature, CO_2, and iron on nutrient uptake by a late-season microbial community from the Ross Sea, Antarctica. *Aquatic Microbial Ecology*. 82:145–159.

Spackeen JL, Bronk DA, Sipler RE, Bertrand EM, Hutchins DA, Allen AE. 2018b. Stoichiometric N:P ratios, temperature, and iron impact carbon and nitrogen uptake by Ross Sea microbial communities. *Journal of Geophysical Research: Biogeosciences*. 123:2955–2975.

Spilling K, Ylöstalo P, Simis S, Seppälä J. 2015. Interaction effects of light, temperature and nutrient limitations (N, P and Si) on growth, stoichiometry and photosynthetic parameters of the cold-water diatom *Chaetoceros wighamii*. *PLOS ONE*. 10:e0126308.

Stekhoven DJ, Bühlmann P. 2012. MissForest—non-parametric missing value imputation for mixed-type data. *Bioinformatics*. 28:112–118.

Sterner R, Elser JJ. 2002. Ecological stoichiometry : the biology of elements from molecules to the biosphere. Princeton: Princeton University Press.

Strass VH, Rohardt G, Kanzow T, Hoppema M, Boebel O. 2020. Multidecadal warming and density loss in the deep Weddell Sea, Antarctica. *Journal of Climate*. 33:9863 – 9881. Place: Boston MA, USA Publisher: American Meteorological Society.

Strzepek RF, Boyd PW, Sunda WG. 2019. Photosynthetic adaptation to low iron, light, and temperature in Southern Ocean phytoplankton. *Proceedings of the National Academy of Sciences*. 116:4388–4393.

Strzepek RF, Hunter KA, Frew RD, Harrison PJ, Boyd PW. 2012. Iron-light interactions differ in Southern Ocean phytoplankton. *Limnology and Oceanography*. 57:1182–1200.

Strzepek RF, Maldonado MT, Hunter KA, Frew RD, Boyd PW. 2011. Adaptive strategies by Southern Ocean phytoplankton to lessen iron limitation: Uptake of organically complexed iron and reduced cellular iron requirements. *Limnology and Oceanography*. 56:1983–2002.

Sunda W. 1989. Trace metal interactions with marine phytoplankton. *Biological Oceanography*. 6:411–422.

Sunda W. 2012. Feedback interactions between trace metal nutrients and phytoplankton in the ocean. *Frontiers in Microbiology*. 3.

Sunda W, Huntsman S. 2003. Effect of pH, light, and temperature on Fe–EDTA chelation and Fe hydrolysis in seawater. *Marine Chemistry*. 84:35–47.

Sunda WG, Huntsman SA. 1995a. Cobalt and zinc interreplacement in marine phytoplankton: Biological and geochemical implications. *Limnology and Oceanography*. 40:1404–1417.

Sunda WG, Huntsman SA. 1995b. Iron uptake and growth limitation in oceanic and coastal phytoplankton. *Marine Chemistry*. 50:189–206.

Sunda WG, Huntsman SA. 2011. Interactive effects of light and temperature on iron limitation in a marine diatom: Implications for marine productivity and carbon cycling. *Limnology and Oceanography*. 56:1475–1488.

Sunda WG, Price NM, Morel FM. 2005. Trace metal ion buffers and their use in culture studies. In: Anderson R, editor, Algal Culturing Techniques, Burlington, Mass: Elsevier/Academic Press, pp. 35–63. OCLC: ocm57349072.

Tada K, Suksomjit M, Ichimi K, Funaki Y, Montani S, Yamada M, Harrison PJ. 2009. Diatoms grow faster using ammonium in rapidly flushed eutrophic Dokai Bay, Japan. *Journal of Oceanography*. 65:885–891.

Taddei L, Stella GR, Rogato A, et al. (14 co-authors). 2016. Multisignal control of expression of the LHCX protein family in the marine diatom *Phaeodactylum tricornutum*. *Journal of Experimental Botany*. 67:3939–3951.

Tagliabue A, Aumont O, DeAth R, et al. (14 co-authors). 2016. How well do global ocean biogeochemistry models simulate dissolved iron distributions?: GLOBAL IRON MODELS. *Global Biogeochemical Cycles*. 30:149–174.

Tagliabue A, Bowie AR, Boyd PW, Buck KN, Johnson KS, Saito MA. 2017. The integral role of iron in ocean biogeochemistry. *Nature*. 543:51–59.

Tagliabue A, Sallée JB, Bowie AR, Lévy M, Swart S, Boyd PW. 2014. Surface-water iron supplies in the Southern Ocean sustained by deep winter mixing. *Nature Geoscience*. 7:314–320.

Takahashi T, Sutherland SC, Sweeney C, et al. (12 co-authors). 2002. Global sea–air CO_2 flux based on climatological surface ocean pCO_2, and seasonal biological and temperature effects. *Deep Sea Research Part II: Topical Studies in Oceanography*. 49:1601–1622.

Takeda S. 1998. Influence of iron availability on nutrient consumption ratio of diatoms in oceanic waters. *Nature*. 393:774–777.

Tanca A, Palomba A, Fraumene C, et al. (11 co-authors). 2016. The impact of sequence database choice on metaproteomic results in gut microbiota studies. *Microbiome*. 4:51.

Tanioka T, Garcia CA, Larkin AA, Garcia NS, Fagan AJ, Martiny AC. 2022. Global patterns and predictors of C:N:P in marine ecosystems. *Communications Earth & Environment*. 3:271.

Tatters AO, Schnetzer A, Xu K, et al. (15 co-authors). 2018. Interactive effects of temperature, CO_2 and nitrogen source on a coastal California diatom assemblage. *Journal of Plankton Research*. 40:151–164.

Team RC. 2022. R: A language and environment for statistical computing.

Tian HA, van Manen M, Wille F, et al. (12 co-authors). 2023. The biogeochemistry of zinc and cadmium in the Amundsen Sea, coastal Antarctica. *Marine Chemistry*. 249:104223.

Timmermans KR, Stolte W, de Baar HJW. 1994. Iron-mediated effects on nitrate reductase in marine phytoplankton. *Marine Biology*. 121:389–396.

Timp W, Gregory Timp. 2020. Beyond mass spectrometry, the next step in proteomics. *Science Advances*. 6:eaax8978. Tex.eprint: https://www.science.org/doi/pdf/10.1126/sciadv.aax8978.

Tomas C. 1997. Identifying Marine Phytoplankton. San Diego: Academic Press, San Diego.

Toseland A, Daines SJ, Clark JR, et al. (11 co-authors). 2013. The impact of temperature on marine phytoplankton resource allocation and metabolism. *Nature Climate Change*. 3:979–984.

Trask BJ, van den Engh GJ, Elgershuizen JHBW. 1982. Analysis of phytoplankton by flow cytometry. *Cytometry*. 2:258–264. Tex.eprint: https://onlinelibrary.wiley.com/doi/pdf/10.1002/cyto.990020410.

Tréguer P, Bowler C, Moriceau B, et al. (16 co-authors). 2018. Influence of diatom diversity on the ocean biological carbon pump. *Nature Geoscience*. 11:27–37.

Turner J, Colwell SR, Marshall GJ, Lachlan-Cope TA, Carleton AM, Jones PD, Lagun V, Reid PA, Iagovkina S. 2005. Antarctic climate change during the last 50 years. *International Journal of Climatology*. 25:279–294.

Twining BS, Baines SB. 2013. The trace metal composition of marine phytoplankton. *Annual Review of Marine Science*. 5:191–215.

Van Heukelem L, Thomas CS. 2001. Computer-assisted high-performance liquid chromatography method development with applications to the isolation and analysis of phytoplankton pigments. *Journal of Chromatography A*. 910:31–49.

van Leeuwe M, Villerius L, Roggeveld J, Visser R, Stefels J. 2006. An optimized method for automated analysis of algal pigments by HPLC. *Marine Chemistry*. 102:267–275.

van Leeuwe MA, Stefels J. 2007. Photosynthetic responses in *Phaeocystis antarctica* towards varying light and iron conditions. *Biogeochemistry*. 83:61–70.

van Manen M, Aoki S, Brussaard CP, et al. (14 co-authors). 2022. The role of the Dotson Ice Shelf and Circumpolar Deep Water as driver and source of dissolved and particulate iron and manganese in the Amundsen Sea polynya, Southern Ocean. *Marine Chemistry*. 246:104161.

van Oijen T, van Leeuwe MA, Gieskes WW, de Baar HJ. 2004. Effects of iron limitation on photosynthesis and carbohydrate metabolism in the Antarctic diatom *Chaetoceros brevis* (Bacillariophyceae). *European Journal of Phycology*. 39:161–171. Publisher: Taylor & Francis tex.eprint: https://doi.org/10.1080/0967026042000202127.

van Tol HM, Amin SA, Armbrust EV. 2017. Ubiquitous marine bacterium inhibits diatom cell division. *The ISME Journal*. 11:31–42.

Vaughan DG, Marshall GJ, Connolley WM, Parkinson C, Mulvaney R, Hodgson DA, King JC, Pudsey CJ, Turner J. 2003. Recent rapid regional climate warming on the Antarctic Peninsula. *Climatic Change*. 60:243–274.

Verardo DJ, Froelich PN, McIntyre A. 1990. Determination of organic carbon and nitrogen in marine sediments using the Carlo Erba NA-1500 analyzer. *Deep Sea Research Part A. Oceanographic Research Papers*. 37:157–165.

Vernet M, Geibert W, Hoppema M, et al. (29 co-authors). 2019. The weddell gyre, southern ocean: Present knowledge and future challenges. *Reviews of Geophysics*. 57:623–708. Tex.eprint: https://agupubs.onlinelibrary.wiley.com/doi/pdf/10.1029/2018RG000604.

Vernette C, Lecubin J, Sánchez P, Coordinators TO, Sunagawa S, Delmont TO, Acinas SG, Pelletier E, Hingamp P, Lescot M. 2022. The Ocean Gene Atlas v2.0: online exploration of the biogeography and phylogeny of plankton genes. *Nucleic Acids Research*. 50:W516–W526. Tex.eprint: https://academic.oup.com/nar/article-pdf/50/W1/W516/44376169/gkac420.pdf.

Vihtakari M. 2022. ggOceanMaps: Plot data on oceanographic maps using 'ggplot2'. *R package version 1.3.7*. .

Violle C, Navas ML, Vile D, Kazakou E, Fortunel C, Hummel I, Garnier E. 2007. Let the concept of trait be functional! *Oikos (Copenhagen, Denmark)*. 116:882–892. Tex.eprint: https://onlinelibrary.wiley.com/doi/pdf/10.1111/j.0030-1299.2007.15559.x.

Volk T, Hoffert MI. 1985. Ocean carbon pumps: Analysis of relative strengths and efficiencies in ocean-driven stmospheric CO_2 changes. In: Sundquist E, Broecker W, editors, Geophysical Monograph Series, Washington, D. C.: American Geophysical Union, pp. 99–110.

Waite AM, Nodder SD. 2001. The effect of in situ iron addition on the sinking rates and export flux of Southern Ocean diatoms. *Deep Sea Research Part II: Topical Studies in Oceanography*. 48:2635–2654.

Weisser H, Choudhary JS. 2017. Targeted feature detection for data-dependent shotgun proteomics. *Journal of Proteome Research*. 16:2964–2974.

Weisser H, Nahnsen S, Grossmann J, et al. (11 co-authors). 2013. An automated pipeline for high-throughput label-free quantitative proteomics. *Journal of Proteome Research*. 12:1628–1644. Tex.eprint: https://doi.org/10.1021/pr300992u.

Willis A, Eason-Hubbard M, Hodson O, Maheswari U, Bowler C, Wetherbee R. 2014. Adhesion molecules from the diatom *Phaeodactylum tricornutum* (Bacillariophyceae): genomic identification by amino-acid profiling and in vivo analysis. *Journal of Phycology*. 50:837–849. Tex.eprint: https://onlinelibrary.wiley.com/doi/pdf/10.1111/jpy.12214.

Wolfe-Simon F, Grzebyk D, Schofield O, Falkowski PG. 2005. The role and evolution of superoxide dismutases in algae. *Journal of Phycology*. 41:453–465. Tex.eprint: https://onlinelibrary.wiley.com/doi/pdf/10.1111/j.1529-8817.2005.00086.x.

Woods HA, Makino W, Cotner JB, Hobbie SE, Harrison JF, Acharya K, Elser JJ. 2003. Temperature and the chemical composition of poikilothermic organisms. *Functional Ecology*. 17:237–245. Tex.eprint: https://besjournals.onlinelibrary.wiley.com/doi/pdf/10.1046/j.1365-2435.2003.00724.x.

Wu M, McCain JSP, Rowland E, Middag R, Sandgren M, Allen AE, Bertrand EM. 2019. Manganese and iron deficiency in Southern Ocean *Phaeocystis antarctica* populations revealed through taxon-specific protein indicators. *Nature Communications*. 10:3582.

Wu Y, Jeans J, Suggett DJ, Finkel ZV, Campbell DA. 2014. Large centric diatoms allocate more cellular nitrogen to photosynthesis to counter slower RUBISCO turnover rates. *Frontiers in Marine Science*. 1.

Wyatt NJ, Birchill A, Ussher S, et al. (12 co-authors). 2023. Phytoplankton responses to dust addition in the Fe–Mn co-limited eastern Pacific sub-Antarctic differ by source region. *Proceedings of the National Academy of Sciences*. 120:e2220111120. Tex.eprint: https://www.pnas.org/doi/pdf/10.1073/pnas.2220111120.

Xu K, Fu FX, Hutchins DA. 2014. Comparative responses of two dominant Antarctic phytoplankton taxa to interactions between ocean acidification, warming, irradiance, and iron availability. *Limnology and Oceanography*. 59:1919–1931.

Yang N, Merkel CA, Lin YA, et al. (11 co-authors). 2021. Warming iron-limited oceans enhance nitrogen fixation and drive biogeographic specialization of the globally important cyanobacterium *Crocosphaera*. *Frontiers in Marine Science*. 8:628363.

Ye N, Han W, Toseland A, et al. (47 co-authors). 2022. The role of zinc in the adaptive evolution of polar phytoplankton. *Nature Ecology & Evolution*. 6:965–978.

Young JN, Goldman JAL, Kranz SA, Tortell PD, Morel FMM. 2015. Slow carboxylation of Rubisco constrains the rate of carbon fixation during Antarctic phytoplankton blooms. *New Phytologist*. 205:172–181.

Yvon-Durocher G, Dossena M, Trimmer M, Woodward G, Allen AP. 2015. Temperature and the biogeography of algal stoichiometry. *Global Ecology and Biogeography*. 24:562–570.

Zhang S, Huang G, Versloot RCA, Bruininks BMH, de Souza PCT, Marrink SJ, Maglia G. 2021. Bottom-up fabrication of a proteasome–nanopore that unravels and processes single proteins. *Nature Chemistry*. 13:1192–1199.

Zhu SH, Green BR. 2010. Photoprotection in the diatom *Thalassiosira pseudonana*: Role of LI818-like proteins in response to high light stress. *Biochimica et Biophysica Acta (BBA) - Bioenergetics*. 1797:1449–1457.

Zhu Z, Qu P, Gale J, Fu F, Hutchins DA. 2017. Individual and interactive effects of warming and CO_2 on *Pseudo-nitzschia subcurvata* and *Phaeocystis antarctica*, two dominant phytoplankton from the Ross Sea, Antarctica. *Biogeosciences (Online)*. 14:5281–5295.

Zhu Z, Xu K, Fu F, Spackeen J, Bronk D, Hutchins D. 2016. A comparative study of iron and temperature interactive effects on diatoms and *Phaeocystis antarctica* from the Ross Sea, Antarctica. *Marine Ecology Progress Series*. 550:39–51.

Zinser ER, Johnson ZI, Coe A, Karaca E, Veneziano D, Chisholm SW. 2007. Influence of light and temperature on *Prochlorococcus* ecotype distributions in the Atlantic Ocean. *Limnology and Oceanography*. 52:2205–2220.